UNIVERSIDADE DE LISBOA

Faculdade de Medicina

Impact of adipose tissue colonization by *Trypanosoma brucei* during infection

Henrique Pedro Pereira da Silva Amaral Machado

Orientadora: Prof. Doutora Luísa Miranda Figueiredo

Tese especialmente elaborada para obtenção do grau de Doutor em Ciências Biomédicas na especialidade de Microbiologia e Parasitologia

2022

UNIVERSIDADE DE LISBOA
Faculdade de Medicina

Impact of adipose tissue colonization by *Trypanosoma brucei* during infection

Henrique Pedro Pereira da Silva Amaral Machado
Orientadora: Prof. Doutora Luísa Miranda Figueiredo

Tese especialmente elaborada para obtenção do grau de Doutor em Ciências Biomédicas na especialidade de Microbiologia e Parasitologia

Júri:
Presidente:
– Doutor Mário Nuno Ramos de Almeida Ramirez, Professor Associado com Agregação e Vice-Presidente do Conselho Científico da Faculdade de Medicina da Universidade de Lisboa.
Vogais:
– Doctor Philipp Erich Scherer, Professor da University of Texas Southwestern Medical Center (USA);
– Doctor Terry Kenneth Smith, Professor da University of St. Andrews, School of Biology (UK);
– Doutora Raquel Ângela Silva Soares Lino, Professora Catedrática da Faculdade de Medicina da Universidade do Porto;
– Doutora Julie Cécile Caroline Ribot, Staff Scientist do Instituto de Medicina Molecular - João Lobo Antunes, unidade de investigação associada à Faculdade de Medicina da Universidade de Lisboa;
– Doutora Luísa Miranda Figueiredo, Professora Associada Convidada da Faculdade de Medicina da Universidade de Lisboa (Orientadora);
– Doutor Rui Miguel Prudêncio da Cunha Pignatelli, Professor Associado Convidado da Faculdade de Medicina da Universidade de Lisboa.

Lisbon BioMed International PhD Program – Biomedical and Clinical Research – Fundação para a Ciência e Tecnologia PD/BD/128286/2017.

2022

As opiniões expressas nesta publicação são da exclusiva responsabilidade do seu autor.

A impressão desta tese foi aprovada pelo Conselho Científico da Faculdade de Medicina de Lisboa em reunião de 18 de outubro de 2022.

Table of contents

Table of contents i
List of figures iii
List of abbreviations v
Acknowledgements vii
Resumo viii
Summary xii
Introduction 1
1. Etiology of African trypanosomiasis 2
2. Life cycle 2
3. Epidemiological evolution of HAT 4
4. Pathology and treatment 5
5. Extravascular colonization 6
5.1. CNS colonization 6
5.2. Skin colonization 7
5.3. Adipose tissue colonization 7
6. Adipose tissue biology 8
6.1. White adipocytes 9
6.2. Brown adipocytes 10
6.3. Beige adipocytes 10
7. Adipocyte lipid anabolism 11
8. Adipocyte lipid catabolism 12
8.1. Exocytosis of TAG-carrying EVs 13
8.2. Lipolysis 13
8.3. Adipocyte lipolysis in pathogenesis 18
9. Immunity and immune evasion 21
9.1. Immune response to *T. brucei* 21
Aims 27
Methods 29
Part 1: Adipose tissue immunity during a *T. brucei* infection 43
Results of Part 1 44
1. Transcriptome of infected adipose tissue reveals a strong inflammatory response 46
2. Adipose tissue shows a gradual accumulation of immune cells during infection. 50
3. Adipose tissue is populated by effector innate and adaptive immune cells 54
4. Adipose tissue presents a strong humoral response 59

5. Parasite load in adipose tissue depends on systemic effectors 63
Discussion of Part 1 68
Adipose tissue immunity against *T. brucei* 69
How do parasites evade the immune response in the AT? 71
Part 2: Adipose tissue metabolism during a *T. brucei* infection 73
Results of Part 2 74
1. Effect of *T. brucei* infection on adipocyte lipid metabolism 75
1.1. *T. brucei* infection induces loss of adipose tissue weight and adipocyte area 75
1.2. Adipocyte lipolysis is increased during a *T. brucei* infection 77
2. Effect of adipocyte-specific lipase deficiency in infection 79
2.1. ATGL-dependent lipolysis prolongs host survival 79
2.2. Fat mass loss is dependent on adipocyte ATGL activity 81
3. Upstream signals of *T. brucei* induced lipolysis 86
3.1. Infection-induced lipolysis does not depend on feeding behavior 86
3.2. Infection-induced lipolysis requires immune cues but not sympathetic innervation . 89
3.3. Parasite-adipocyte interactions induce lipolysis 93
3.4. Adipocyte lipolysis is induced by a secreted *T. brucei* factor 94
4. Effect of adipocyte lipolysis on parasite burdens 97
4.1. Adipocyte lipolysis contributes to the reduction of adipose tissue parasite burden .. 97
4.2. Chemical induction of adipocyte lipolysis prevents *T. brucei* growth 98
Discussion of Part 2 102
Impact of ATGL-dependent adipocyte lipolysis on body fat 103
Induction of adipocyte lipolysis 105
Effect of adipocyte lipolysis on pathology 106
Local parasite burden control by adipocyte lipolysis 106
General Discussion 109
References 113
Annexes 137

List of figures

Introduction

Figure 1: Simplified *T. brucei* life cycle

Figure 2: Geographical distribution of HAT cases in the tsetse belt

Figure 3: Adipose tissue distribution in humans and mice

Figure 4: Morphological and phenotypic adipocyte properties

Figure 5: Post-translational regulation of neutral lipolysis

Figure 6: Transcriptional regulation of neutral lipolysis

Methods

Figure 7: Immune cell flow cytometry gating strategy

Figure 8: Parasite flow cytometry gating strategy

Part 1 – Results

Figure 9: Transcriptome of *T. brucei* infected AT shows a strong immune response

Figure 10: Immune activatory and suppressive transcriptomic signature

Figure 11: Dynamics of *T. brucei* parasites and immune cells throughout infection

Figure 12: Inflammatory cell response in the adipose tissue

Figure 13: Dynamics of immune cells during infection

Figure 14: Organ mass and T cell dynamics

Figure 15: Comparison of flow cytometry and immuCC data

Figure 16: Purified soluble VSG identification

Figure 17: Dynamics of immunoglobulins, B cells and plasmocytes during infection

Figure 18: Assessment of the role of immune cells/factors in parasite control

Figure 19: Assessment of the role of PD-1 expression in parasite control

Part 2 – Results

Figure 20: Dynamics of adipose tissue mass and adipocyte size during infection

Figure 21: Increased *ex vivo* lipolysis during a *T. brucei* infection

Figure 22: Effect of adipocyte-specific lipase deficiency in infection

Figure 23: Effect of adipocyte-specific ATGL deficiency in body composition and skeletal muscle pathology

Figure 24: ATGL deficiency prevents *T. brucei* induced lipolysis and loss of lipid adipocyte area

Figure 25: Feeding synchronization does not prevent *T. brucei* induced adipocyte lipolysis

Figure 26: Disease induced hypophagia is not responsible for *T. brucei* induced adipocyte lipolysis

Figure 27: *T. brucei* induced loss of fat mass is dependent on an adaptive immune response

Figure 28: *T. brucei*-adipocyte interactions are sufficient to induce ATGL-dependent lipolysis

Figure 29: Soluble *T. brucei* factors are sufficient to induce adipocyte lipolysis

Figure 30: ATGL-dependent adipocyte lipolysis impacts adipose tissue parasite burden

Figure 31: Chemical induction of adipocyte-lipolysis impairs *T. brucei* growth

Figure 32: Adipocyte lipolysis does not promote stumpy differentiation

General Discussion

Figure 33: A coordinated immuno-metabolic response protects the host at the expense of fat mass

List of abbreviations

AAT	animal African trypanosomiasis
AC	adenylate cyclases
AMP	adenosine monophosphate
APC	antigen presenting cell
APOAI	apolipoprotein A-I
APOL1	apolipoprotein L-1
AT	adipose tissue
ATF	adipose tissue form
ATGL	adipose tissue triglyceride lipase
BES	bloodstream expression site
BSF	bloodstream form
C3	complement component 3
CAC	cancer associated cachexia
cAMP	cyclic adenosine monophosphate
CD	cluster of differentiation
CGI-58	comparative gene identification-58
CNS	central nervous system
COA	coenzyme A
CR	complement receptor
CTLA4	cytotoxic T-lymphocyte associated protein 4
DAG	diacylglycerol
DMEM	Dulbecco's modified eagle medium
ELISA	Enzyme-linked immunosorbent assay
ERK	extracellular-signal regulated kinase
FasL	Fas ligand
FASN	fatty acid synthase
FBS	fetal bovine serum
FELASA	Federation of European Laboratory Animal Science
FFA	free fatty acid
FOXO1	forkhead box protein O-1
FP	flagellar pocket
GFP	green fluorescent protein
HAT	Human African trypanosomiasis
HPR	haptoglobin-related protein
HSL	hormone sensitive lipase
IFNγ	interferon gamma
Ig	immunoglobulin
IL	interleukin
Jht	joining heavy targeted mutation
KO	knockout
LAL	lysosomal acid lipase
LPL	lipoprotein lipase
MAG	monoacylglycerol

MAPK	mitogen-activated protein kinase
mg	milligram
MGL	monoacylglycerol lipase
MHC	major histocompatibility complex
NEFA	non-esterified fatty acid
OHDA	hydroxydopamine hydrobromide
PBS	phosphate buffered saline
PD-1	programmed cell death protein 1
PD-L1	programmed cell death ligand 1
PI3K	phosphatidylinositol-3 kinase
PKA	protein kinase A
PPAR	peroxisome proliferator-activated receptor
qPCR	quantitative polymerase chain reaction
Rag2	recombination activation gene 2
RPMI	Roswell Park Memorial Institute
SRA	serum resistance associated
STAT5	signal transducer and activator of transcription
TAG	triacylglycerol
TCA	tricarboxylic acid
TCR	T cell receptor
TEM	transmission electron microscopy
TGFβ	transforming growth factor beta
Th	T helper
TLF	trypanosome lytic factor
TNFα	tumor necrosis factor alpha
Treg	T regulatory
UCP	uncoupling protein
VSG	variant surface glycoprotein
WAT	white adipose tissue
WT	wild-type

Acknowledgements

To my supervisor, Luísa I am exceedingly grateful for the opportunity you granted me and for the effort you have always made not only to move our projects forward, but also to make me a better scientist. Wherever the path ahead may lead me, I will always carry the many lessons you've taught me and, in many things, you are indeed a model I will always seek to emulate. On a lighter note, something has to be done about the increasing number of FC Porto supporters in our group!

To the many great friends and colleagues I've met along the way. Building a PhD would have been a truly bleak experience without so many brilliant and kind hearted people around me. Fortunately, you are far too many to name individually, but from past and present "Figueirencio" lab members, to my Lisbonbiomed classmates and the remainder of iMM's parasitology community – thank you.

To my family, I am forever grateful for all the support you have always given me and for always doing your very best, even at great personal sacrifice, to give me the best possible chance to achieve my goals.

To Filipa, my wife, I cannot overstate how central you have been to all aspects of my life, academic and otherwise, for the past 10 years. As you know all too well, the trials and tribulations of a PhD are not always too kind. I was beyond fortunate to always know that at the end of the day you would always be there with a smile and a kind word to help me put everything into perspective and to muster the will to carry on through.

Resumo

A tripanossomíase africana é uma doença infeciosa causada por vários parasitas unicelulares e extracelulares da família *Trypanosomatidae*, incluindo o parasita *Trypanosoma brucei.* Esta doença afeta múltiplas espécies de mamíferos, incluído humanos. Em humanos, a doença é denominada de tripanossomíase humana africana, ou doença do sono, e tripanossomíase animal africana nos restantes hospedeiros. Uma apresentação clínica comum da tripanossomíase africana é a perda acentuada de volume adiposo seguido de perda de músculo esquelético. Na maioria dos contextos estudados, a perda de volume adiposo deve-se a alterações no metabolismo lipídico dos adipócitos, sendo estas as células responsáveis por armazenar gordura no tecido adiposo na forma de triglicerídeos. Neste caso, um aumento do catabolismo lipídico na forma de lipólise neutra leva à hidrólise sequencial de triglicerídeos em ácidos gordos livres e glicerol, que são posteriormente libertados para a circulação. Este processo de lipólise neutra é levado a cabo por três lípases: lípase de triglicéridos do tecido adiposo (ATGL), lípase sensível a hormonas (HSL) e lípase de monoglicerídeos (MGL). Quando um aumento de lipólise neutra não é compensado por um aumento proporcional de síntese de triglicéridos no adipócito (lipogénese), ocorre uma perda de volume adiposo. Dentro do hospedeiro mamífero, o parasita *T. brucei* coloniza tanto espaços intravasculares como extravasculares. Dentro dos espaços extravasculares estudados até à data em modelos de roedores, o *T. brucei* apresenta uma colonização desproporcionalmente elevada no tecido adiposo quando comparado com a maioria dos restantes órgãos. Contudo, como esta colonização contribui para a perda de volume adiposo característica da tripanossomíase africana, ou como o microambiente metabólico e/ou imunológico do tecido adiposo permite a acumulação de números tão elevados de parasitas é ainda incompreendida.

Neste trabalho demonstramos que o tecido adiposo não é um órgão imunologicamente privilegiado durante uma infeção com *T. brucei*. Neste órgão, à medida que a infeção progride, ocorre a acumulação de uma resposta imune constituída por todos os componentes considerados necessários para eliminar o parasita. Especificamente, a análise do transcriptoma do tecido adiposo revelou

uma marcada assinatura imunológica em ratinhos infetados quando comparada à de controlos não infetados. Esta assinatura imunológica é sugestiva do recrutamento e ativação de células imunes inatas e adaptativas, e a sua intensidade aumentou com o decorrer da infeção. Em seguida, confirmamos esta previsão através de uma caracterização por citometria de fluxo e imuno-histoquímica das células imunes presentes no tecido adiposo ao longo da infeção. Verificamos que durante a infeção existe uma acumulação significativa de neutrófilos, monócitos, macrófagos, linfócitos T CD4+, linfócitos T CD8+, linfócitos T CD4+ reguladores, linfócitos B (incluído plasmócitos produtores de imunoglobulinas). Uma vez confirmada a presença de uma resposta imune celular ativa no tecido adiposo, aferimos se uma resposta humoral contra antigénios do parasita também era montada nos espaços intersticiais do tecido adiposo. Verificamos que tal como o que acontece no sangue, quantidades progressivamente mais elevadas das imunoglobulinas IgM e IgG específicas para a glicoproteína variante de superfície do parasita. Uma vez demonstrada a presença no tecido adiposo dos componentes celulares e humorais necessários à eliminação do parasita, procedemos à investigação da contribuição relativa de vários destes fatores para a eliminação de parasitas do tecido adiposo recorrendo a modelos de ratinho geneticamente modificados. Apuramos que ratinhos deficientes para linfócitos T e B (*Rag2*$^{-/-}$), deficientes apenas para linfócitos B (*Jht*$^{-/-}$) ou deficientes para a citocina pró-inflamatória interferão-gama (*Ifng*$^{-/-}$) não foram capazes de controlar a carga parasitária no sangue, no tecido adiposo, e em outros órgãos não adiposos. Estes resultados sugerem que a eliminação do parasita no tecido adiposo utiliza mesmos mecanismos gerais previamente descritos como necessários para eliminar *T. brucei* intravascular. Contudo, verificamos que ratinhos deficientes para componente do complemento 3 (*C3*$^{-/-}$), necessário para o reconhecimento e fagocitose de parasitas opsonizados com IgM, foram menos eficientes a eliminar parasitas do tecido adiposo que ratinhos tipo selvagem (WT). Esta mesma redução de eficiência não foi observada no sangue ou baço dos mesmos animais, sugerindo que a eliminação de parasitas no tecido adiposo, e possivelmente de outros espaços extravasculares, é particularmente dependente do sistema do complemento.

Para além do estudo da resposta imune contra *T. brucei* no tecido adiposo, interrogamos também que alterações metabólicas geradas pela infeção com este

parasita poderiam levar à perda de massa adiposa, e por sua vez como é que estas alterações metabólicas impactam a patologia desenvolvida. Verificamos que tecidos adiposos brancos recolhidos de diferentes localizações anatómicas sofrem uma progressiva redução de tamanho ao longo da infeção, e que esta redução de tamanho está correlacionada com a diminuição do tamanho da gotícula lipídica dos adipócitos. Em seguida, mostramos que o tecido adiposo de ratinhos infetados liberta níveis significativamente elevados de ácidos gordos e glicerol em vários dias de infeção, comparativamente a controlos não infetados. Esta libertação aumentada de produtos de lipólise deve-se a um aumento da atividade da enzima ATGL, uma vez que o tecido adiposo de ratinhos com adipócitos deficientes para esta enzima (*Adipoq*$^{Cre/+}$-*Atgl*$^{fl/fl}$) foram incapazes de aumentar a libertação de ácidos gordos e glicerol durante a infeção. Adicionalmente, mostramos que ratinhos *Adipoq*$^{Cre/+}$-*Atgl*$^{fl/fl}$ sofrem uma menor perda de percentagem de massa gorda total durante a infeção, e que os seus adipócitos retêm um maior volume da sua gotícula lipídica quando comparados com ratinhos controlo *Atgl*$^{fl/fl}$ infetados. Esta lipólise mediada pela enzima ATGL exerce uma função protetora para o hospedeiro, uma vez que na sua ausência ratinhos sucumbem mais cedo à infeção com *T. brucei* por um mecanismo ainda a explorar. Para além de prolongar a sobrevivência do hospedeiro, demonstramos que elevados níveis de lipólise no adipócito levam a uma diminuição da carga parasitária. Este resultado é evidenciado de duas formas distintas: animais *Adipoq*$^{Cre/+}$-*Atgl*$^{fl/fl}$ apresentam maior carga parasitária no tecido adiposo; indução química de lipólise em co-culturas de adipócitos e *T. brucei* reduz significativamente o crescimento do parasita. No futuro, o mecanismo pelo qual a lipólise de adipócitos reduz a carga parasitária será alvo de investigação adicional. Finalmente, investigamos que sinais oriundos do hospedeiro ou do parasita poderiam estar por trás da indução de lipólise. Utilizando um sistema de adipócitos diferenciados *in vitro*, verificamos que co-cultura destes adipócitos com *T. brucei*, ou tratamento com lisados totais do parasita, é suficiente para a indução de lipólise. Paralelamente, verificamos que ratinhos *Rag2*$^{-/-}$ registam uma perda de massa gorda total significativamente mais baixa do que controlos WT, apesar de apresentarem maior carga parasitária. Adicionalmente, adipócitos tratados *in vitro* com soro recolhido de ratinhos WT infetados mostraram uma maior libertação de ácidos gordos do que adipócitos tratados com soro de ratinhos WT não infetados ou ratinhos *Rag2*$^{-/-}$ infetados. Coletivamente, estes resultados indicam que fatores

oriundos tanto do parasita como do próprio hospedeiro poderão contribuir para a ativação da lipólise e subsequente perda de massa gorda durante uma infeção com *T. brucei*. De particular relevância, num contexto *in vivo* o efeito da resposta imune gerada contra o parasita parece ser predominante na indução da perda de massa gorda, que poder-se-á dever a um ou vários fatores solúveis indutores de lipólise derivados de linfócitos T e/ou B.

Em conclusão, neste trabalho demonstramos que a colonização extensiva do tecido adiposo por parte do parasita *T. brucei* não se deve à ausência de uma resposta imune. Mostramos também que, conjuntamente com sinais derivados do parasita, esta resposta imune é capaz de induzir lipólise do adipócito, levando à perda de massa gorda. Finalmente, mostramos que esta lipólise é dependente da atividade da lípase ATGL e que a sua atividade prolonga a sobrevivência do hospedeiro ao mesmo tempo que ajuda a controlar a quantidade de parasitas presentes no tecido adiposo.

Summary

African trypanosomiasis is an infectious disease caused by unicellular and extracellular parasites of the Trypanosomatidae family, including *Trypanosoma brucei*. Both Human and animal African trypanosomiasis are characterized by a pronounced loss of fat and skeletal muscle mass. *T. brucei* occupies both intravascular and extravascular compartments of the mammalian host. In the mouse model of infection, *T. brucei* colonizes the adipose tissue in disproportionately high numbers when compared with most other organs. The properties of the adipose tissue microenvironment, immunological and others, which enable such extensive colonization, are still incompletely understood. Moreover, the impact of adipose tissue colonization on the loss of fat mass observed during natural infections, and the impact of fat mass loss itself on disease pathology are unknown. Here, we show that during infection the adipose tissue acquires a marked transcriptomic immune signature. This correlated with the accumulation of both innate and adaptive immune cells consistent with a T helper (Th) 1 response. Moreover, as observed for the serum, we found increasingly higher titers of IgM and IgG specific for the parasite's surface variant glycoprotein in the adipose tissue's interstitial fluid. Similar to the blood, parasite clearance from the adipose tissue was dependent on T and B cells and the hallmark Th1 cytokine interferon gamma. Interestingly, while the complement system was dispensable to eliminate circulating parasites, mice lacking the complement component 3 showed reduced elimination of parasites from the adipose tissue. This suggests that the complement system may play an important role in the clearance of highly parasitized extravascular compartments.

In addition to studying the immunological surveillance of the adipose tissue, we also studied how adipocyte metabolism is modulated by a *T. brucei* infection. Here, we show that during infection, white adipose tissue depots progressively reduce in size and that this reduction correlates with loss of adipocyte lipid droplet volume (*i.e.* fat containing organelle). In turn, this loss of adipose tissue weight is preceded by an increase in *ex vivo* adipocyte lipolysis. This increase in lipolysis proved to be central in loss of fat mass, as adipocyte-specific adipose tissue triglyceride lipase deficient (*Adipoq*$^{Cre/+}$-*Atgl*$^{fl/fl}$) mice, which have reduced lipolysis, were more resistant to loss of total fat mass and kept higher adipocyte lipid droplet volumes than wild-type (WT)

littermate controls (*Atgl*$^{fl/fl}$). Moreover, adipocyte lipolysis showed host-protective effects, as *Adipoq*$^{Cre/+}$*-Atgl*$^{fl/fl}$ mice succumbed earlier to infection than *Atgl*$^{fl/fl}$ controls. In addition to increased survival, our data suggest that increased lipolysis improves local parasite burden control. On one hand, *Adipoq*$^{Cre/+}$*-Atgl*$^{fl/fl}$ mice present transiently higher adipose tissue parasite burdens than *Atgl*$^{fl/fl}$ controls. On the other hand, chemical induction of adipocyte lipolysis in an *in vitro* adipocyte-*T. brucei* co-culture system significantly reduces parasite growth. Lastly, we shed light on the upstream signals that induce adipocyte lipolysis. Here, we found that *T. brucei* promotes lipolysis in *in vitro* grown co-cultured adipocytes. In addition to parasite cues, we found that T and B cells are central in the induction of fat mass loss and that serum factor produce by these cells are able to induce adipocyte lipolysis.

Overall, in this work we show that during a *T. brucei* infection a trypanocydal immune response is mounted in the adipose tissue and that as infection progresses a loss of fat mass occurs through host-protective ATGL-dependent adipocyte lipolysis.

Introduction

1. Etiology of African trypanosomiasis

African trypanosomiasis is an infectious disease caused by several unicellular and extracellular protozoan parasites of the Trypanosomatidae family[1,2]. This disease affects humans and other mammals (*e.g.* domestic cattle) and is thus divided as Human African trypanosomiasis (HAT) and animal African trypanosomiasis (AAT). HAT is caused by two distinct *T. brucei* subspecies, namely *T. brucei gambiense* and *T. brucei rhodesiense*[1]. On the other hand, AAT is caused by multiple Trypanosoma species, including *T. congolense*, *T. vivax* and *T. brucei*[2]. The latter includes the non-human infective subspecies *T. brucei brucei*[2,3].

2. Life cycle

As the sole etiological agent of HAT, *T. brucei* is the most studied African trypanosome. *T. brucei* undergoes a complex lifecycle, alternating between a mammalian host and the tsetse fly (*Glossina* spp.) arthropod vector[1] (Fig. 1). Within the mammalian host, the parasite alternates between two morphologically distinct forms. These are the highly replicative slender form and the cell-cycle arrested stumpy form[4].

High levels of parasitemia trigger a process of quorum sensing that promotes slender to stumpy parasite differentiation[5]. Although incompletely understood, this process involves the release of parasite peptidases that cleave extracellular host proteins[6]. In turn, the newly generated oligopeptides are taken up by the parasite's through the surface receptor TbGPR89, leading to downstream signaling that culminates in stumpy differentiation[7]. This differentiation self-limits the parasite virulence and prolongs host survival[8,9]. Moreover, the resulting stumpy forms are pre-adapted to the conditions found within the Tsetse fly vector and as such are considered to be more efficiently transmitted from the mammalian to the arthropod host[10]. Interestingly, recent work has shown that stumpy forms may not be essential for transmission and that slender forms are indeed capable of surviving and differentiating inside the Tsetse fly[11]. Upon being taken up during a blood meal, the bloodstream forms of *T. brucei* are transported to the mid-gut of the Tsetse fly[4]. Here, they differentiate into proliferative procyclic forms and cross the peritrophic matrix on their way to the proventriculus where they differentiate into proliferative

epimastigotes[4]. These parasites then migrate to the salivary glands where they undergo a final round of differentiation into mammalian-infective metacyclic forms[4].

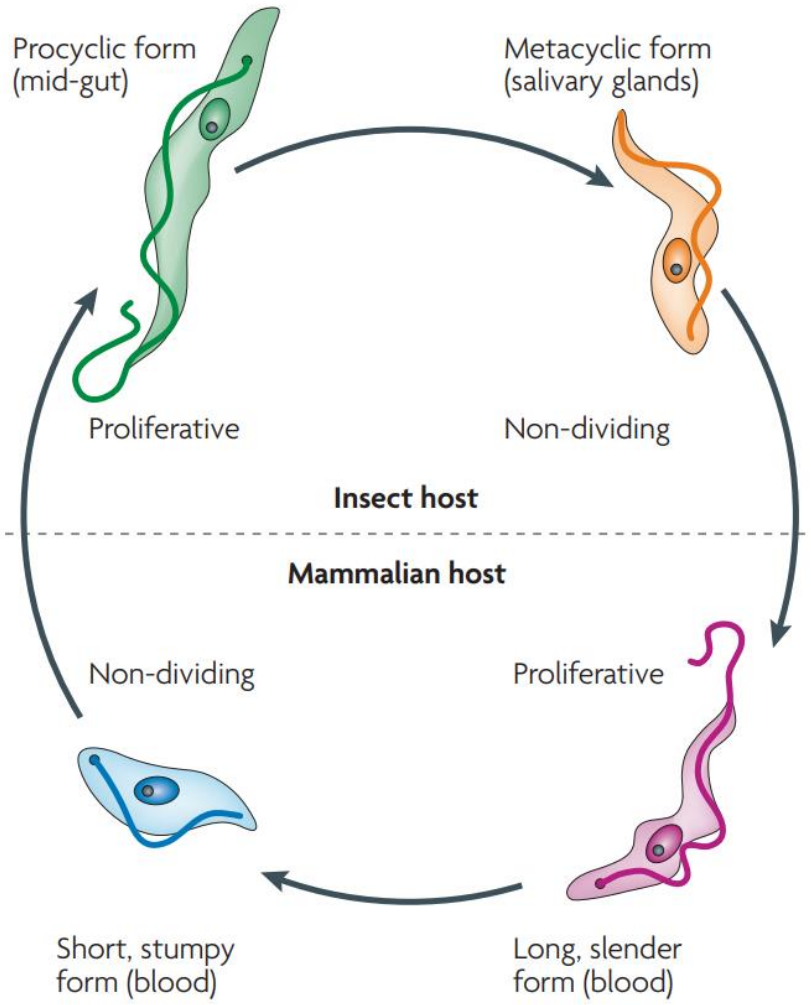

Figure 1 – Simplified *T. brucei* life cycle: The parasite alternates between a mammalian host (such as humans and cattle) and a tsetse fly (*Glossina spp.*). Within the mammalian host the parasite has two distinct forms: replicative long slender form (pink) and a non-dividing stumpy form (blue). Within the tsetse fly proliferative procyclic forms (green) are found in the mid-gut and mammalian infective metacyclic forms (orange) are found the salivary glands. Epimastigotes and other intermediate forms found within the tsetse fly are not depicted. Originally from Lee et al. 2007.[12]

Upon a new blood meal, these metacyclic parasites are deposited on the dermis of the host where they will differentiate into slender forms and repeat its life cycle anew[4].

3. Epidemiological evolution of HAT

HAT is geographically restricted to 36 nations in sub-Saharan African where the Tsetse fly vector can be found in the wild, hence it is commonly referred to as the Tsetse belt (Fig. 2)[1]. Despite 65 million people being considered to be at risk of developing HAT, the number of reported cases has been in steady decline in the past two decades[1,13,14]. Although likely underreported, in 2020 a record low 663 HAT cases were reported by the World Health Organization (WHO).

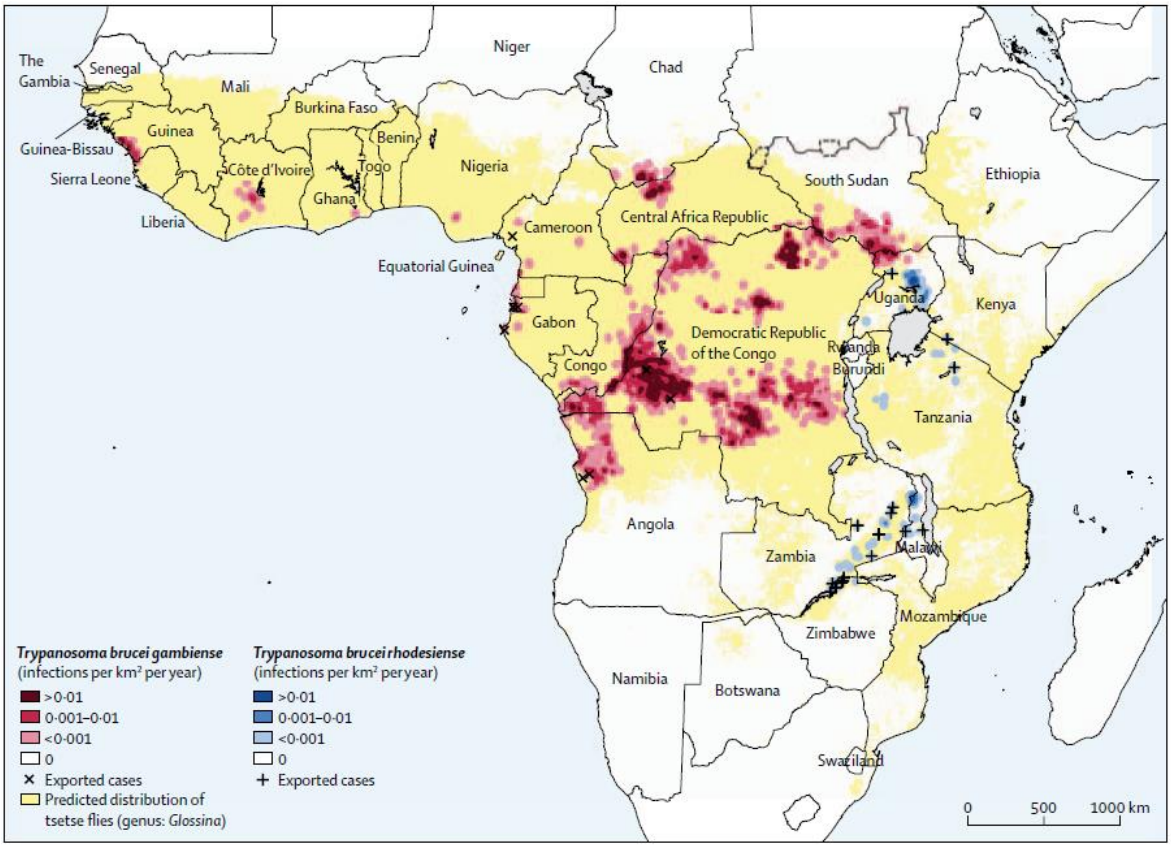

Figure 2 – Geographical distribution of HAT cases in the tsetse belt: Reported cases per km^2 per year of *T. brucei gambiense* (in red) and *T. brucei rhodesiense* (in blue) between 2010 and 2014. Geographical distribution of tsetse flies is depicted in yellow. Originally from Büscher et al. 2017.[1]

This presents a sharp contrast to the more than 50.000 cases per year in the early 1940s[13], when yearly HAT case numbers started being reported by the WHO. In the following two decades, control measures aimed at curbing transmission achieved a reduction of over 90% in new HAT cases. A significant part of this enormous

progress in HAT control was reversed in the ensuing decades. This regression of HAT control coincided with a period of social instability and often armed conflict in many African countries in the wake of independence from colonial rule, which hindered HAT control efforts. Indeed, by the end of the 1990s more than 30.000 HAT cases were reported per year, with estimates increasing this number to as high as 300.000[13]. The reestablishment of HAT-control programs has led to the record low in new cases currently observed and set the groundwork to achieve the WHO goal to eliminate HAT by 2030[15]. However, the resurgence of HAT in the 1970s serves as a cautionary tale of how quickly HAT can re-emerge if left unchecked.

4. Pathology and treatment

HAT is a lethal disease if left untreated and it is classically divided into two main stages. These are the initial hemolymphatic stage, characterized by the presence of the parasite in the blood and lymphatic vessels and the subsequent meningoencephalitic stage in which the parasite is also present in the central nervous system (CNS). During the hemolymphatic stage the host experiences a wide array of clinical presentations which include fever, nausea, severe weight loss, skin lesions, lymphadenopathy, myalgia, headaches, and nocturnal hyperhidrosis[16]. After colonizing the CNS, the meningoencephalitic stage begins. In this stage the patient experiences extensive neurological symptoms, which generate motor, psychiatric and sleep disorders. These can include apathy, motor discoordination, aggressiveness, uncontrollable tremors, and the disruption of sleep/wake cycles due to which HAT is commonly referred to as “sleeping sickness”[16]. Unlike the hemolymphatic stage, the meningoencephalitic stage occurs mainly in *T. brucei gambiense* infected patients, as *T. brucei rhodesiense*-infected patients typically succumb before the onset of neurological symptoms.

Until recently, treatment of HAT relied exclusively on intravenous administration of pentamidine and suramin for patients in the hemolymphatic stage and melarsoprol, eflornithine and nifurtimox for patients in the meningoencephalitic stage[14,16]. Treatment for meningoencephalitic stage HAT patients presents many serious side effects and its administration is logistically challenging. Recently, oral administration of fexinidazole has been used to treat both hemolymphatic and low-grade meningoencephalitic HAT[14].

5. Extravascular colonization

Classically, *T. brucei* has been regarded as a predominantly bloodborne pathogen. In the past decade a wealth of knowledge has begun to shift this blood-centric paradigm. Indeed, numerous extravascular spaces of different mammalian hosts can be colonized by *T. brucei*[17]. Interestingly, these different tissues appear to support markedly distinct amounts of parasites. In the mouse model, organs like the adipose tissue (AT) and pancreas show disproportionately high numbers of *T. brucei* when compared to other organs, suggesting tissue-specific tropism[18,19]. The implications of extravascular colonization are just beginning to be elucidated, however the access to distinct extracellular milieus may endow the parasite with selective advantages, by modulating transmission, survival, and proliferation[17,20]. Moreover, drug bioavailability may vary throughout tissues and as such certain extravascular niches may contribute to disease recrudescence[17,20]. Lastly, tissue colonization further disrupts host homeostasis and may contribute to disease progression and outcome.

5.1. CNS colonization

The CNS is the quintessential example of an extravascular niche for *T. brucei* colonization[21–23]. The colonization of the CNS and ensuing inflammatory response is directly correlated with the onset of neurological disorders, which associate with a poor prognosis for the host[16]. The advantage for CNS colonization for *T. brucei* is unclear. It has been hypothesized that the parasite benefits from reduced immune surveillance in the CNS, as this considered an “immune privilege” site where immune activation is tightly limited to prevent irreversible damage to vital structures[24]. Accordingly, the stable maintenance of CNS-occupying *T. brucei* may egress to the blood stream to re-establish systemic infection after blood-occupying parasites have been eliminated by the immune system. Another possible advantage for CNS colonization is that of increased transmission. In this instance, the induction of a lethargic state and the increased sleeping time during the day (*i.e* active time of most *Glossinidae*) provides undisturbed access for tsetse fly bloodmeals[25].

5.2. Skin colonization

The skin is first solid organ encountered by *T. brucei* during a natural infection, as metacyclic parasites are deposited in the dermis before differentiation into proliferative slender forms that migrate to the blood.

Extensive skin pathology has long been described as a common clinical presentation in HAT patients[26]. These have since been attributed to parasite colonization of the dermis[27]. No molecular mechanism has thus far been attributed to *T. brucei* invasion of the skin. The biological relevance of *T. brucei* colonization in the skin is likely related to increased transmission potential. Indeed, how *T. brucei* is capable of being transmitted despite inducing low parasitemia during the majority of infection has been a long-standing paradox. Accordingly, it is has been suggested that *T. brucei* should have gone extinct if transmission relied solely on the uptake of infected blood by the tsetse fly[28]. Here, the skin may play a pivotal role in transmission. The bite of a tsetse fly induces significant skin damage resulting from its “slash and sucking” feeding behavior. In this process, the tsetse fly’s serrated proboscis displaces significant pieces of epidermis and dermis tissue, which may then may then be ingested[28]. Moreover, recent work has shown that *T. brucei* could be detected in skin biopsies of asymptomatic individuals and that *T. brucei* cultured in artificial skin following a natural route of infection could acquire a quiescent phenotype[27,29]. These observations suggest that the skin may be pivotal in the establishment of asymptomatic infections and for the maintenance of *T. brucei* transmission.

5.3. Adipose tissue colonization

The AT was recently described as a major target for *T. brucei* colonization in rodents. Here, *T. brucei* parasites were ubiquitously found in the interstitial spaces of visceral and subcutaneous AT depots[19], as well as in close proximity to individual dermal adipocytes[27]. Parasite numbers in the AT are higher than those of other internal organs and often higher than the blood. A myriad of factors may contribute to this disproportionately high accumulation of parasites. On the one hand, a selective mechanism of parasite tropism towards the AT tissue may result in a continuous egress of *T. brucei* from the bloodstream into the interstitial spaces of

the AT. Indeed, while several endothelial adhesion molecules (*e.g.* E-selectin, P-selectin and CD54) are required for overall tissue invasion, CD36 has been shown to be specifically required for AT colonization[18]. In addition to AT-specific tropism, the immune surveillance mechanisms responsible for eliminating the parasite may show decreased efficacy within the AT, promoting parasite accumulation. Lastly, tissue specific adaptations of the parasite may contribute to increased survival and/or proliferation. Interestingly, parasites extracted from the AT of infected mice show a distinct transcriptomic profile when compared with their bloodstream counterparts (≈20% of genes differentially expressed)[19]. These adipose tissue forms (ATFs) of the parasite are able to use local fatty acids as a carbon source through β-oxidation[19], unlike their bloodstream form (BSF) counterparts which rely exclusively on glycolysis[30]. In addition to these parasite adaptations, the modulation of the AT itself may play an important role in disease pathology, as this organ is a major player in metabolic homeostasis and endocrine regulation. These important functions, together with the fact that loss of AT mass is a common clinical finding in both HAT and AAT warrant further investigation of the relevance of AT colonization.

6. Adipose tissue biology

Research in the middle of the 20th century identified the AT as a site of energy storage in the form of lipids that would provide the organism with free fatty acids (FFAs) during periods of fasting[31]. For a long time, it was believed that energy storage was the sole function of the AT. This dogmatic view was contested upon the discovery that the AT secretes a myriad of signaling proteins, collectively known as adipokines[31,32]. These bioactive molecules include cytokines, hormones, and enzymes. Adipokines such as tumor necrosis factor alpha (TNFα), interleukin (IL)-6, leptin, adiponectin and adipsin (complement factor D) can exert endocrine, paracrine, and autocrine functions, and as such can play important roles in disease settings[33–35].

Unlike most tissues, the AT is distributed into discrete depots across the mammalian organism (Fig. 3). The majority of these depots fall within two categories depending on their anatomical location: visceral and subcutaneous[36,37]. The distribution of these depots varies significantly between species and even within species according to sex[36–38]. Indeed, although most AT in humans is subcutaneous, men

typically present higher visceral adiposity than women[38], which is associated with poorer metabolic health[31,36–38].

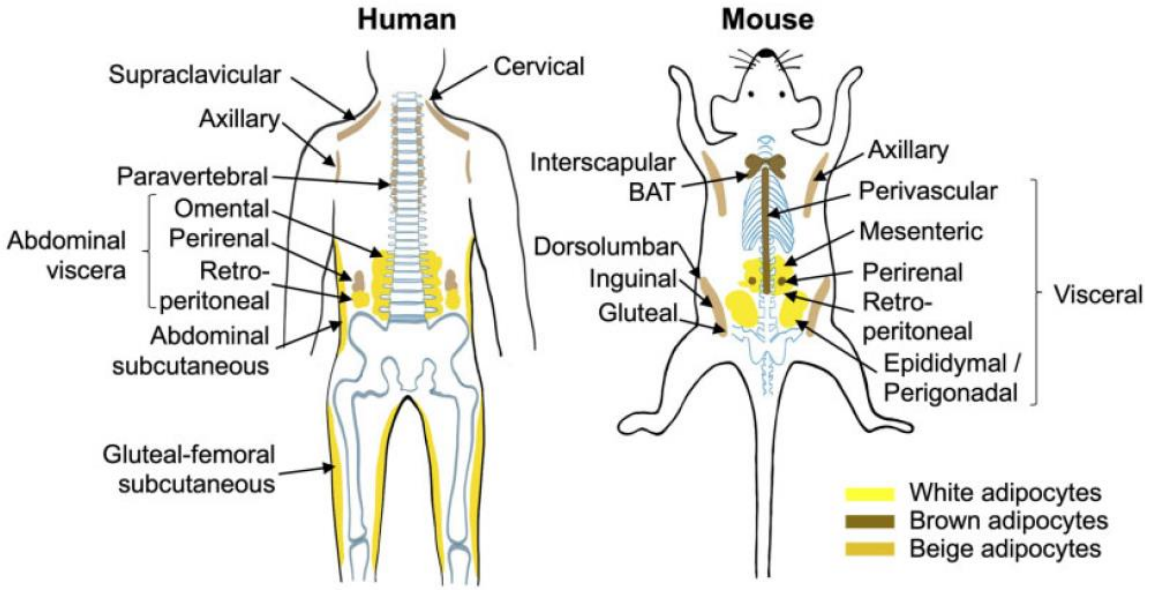

Figure 3 – Adipose tissue distribution in humans and mice: Discrete adipose tissue depots divided according to anatomical location (visceral and subcutaneous) and thermogenic capacity (white, brown and beige). Originally from Cheong et al. 2021.[39]

Each AT depot is composed by a complex mixture or distinct cells, which include adipocytes, immune cells, endothelial cells, neurons, glial cells and stem-cells. Adipocytes are large cells composed mainly of triacylglycerol (TAG)-containing lipid droplets[37]. These cells show phenotypical diversity and can be classified as three classes: white, brown and beige adipocytes (Fig. 4).

6.1. White adipocytes

White adipocytes are the predominant adipocyte class. They are the main component of most AT depots. These adipocytes present a single lipid droplet that accounts for over 80% of the cells' volume. These cells are essential for the maintenance of metabolic homeostasis. Specifically, during times of positive energy balance they generate and store TAG through lipogenesis and *de novo* lipogenesis[40,41]. Conversely, during periods of negative energy balance (*e.g.* fasting) the store TAG e broken down and its hydrolysis products are exported to peripheral tissues where they are further metabolized for energy production[42].

6.2. Brown adipocytes

Unlike their white counterparts, brown adipocytes have a multilocular morphology, showing multiple small lipid droplets. Due to their high mitochondrial (and consequentially iron) content, these cells present a macroscopic brownish hue[31]. Although these cells are also rich in TAG content, their primary role is not that of energy storage. Instead, brown adipocyte use the FFAs resulting from TAG hydrolysis to produce heat[43]. To achieve this, FFAs undergo mitochondrial β-oxidation in mitochondria with uncoupled electron transfer chains. This uncoupling occurs through the action of the specialized uncoupling protein (UCP)-1[44]. This process divert proton pumping through ATP-synthase and consequent storage of energy in the form of a chemical bond in ATP and instead forces the energy generated by crossing proton to dissipate in the form of heat[43,44]. This process is known as non-shivering thermogenesis and together with shivering-thermogenesis (*i.e.* in skeletal muscle) is important for optimal temperature regulation in mammals[43,45].

6.3. Beige adipocytes

Beige adipocytes are a plastic cell type found predominantly in white subcutaneous ATs[46]. Upon appropriate induction, such as through sympathetic stimuli, these cells upregulate UCP-1 and perform thermogenic functions[46]. Under steady state conditions these cells can also accumulate lipids in the form of TAG. Beige adipocytes are generally considered an intermediate phenotype between white and brown adipocytes[46,47].

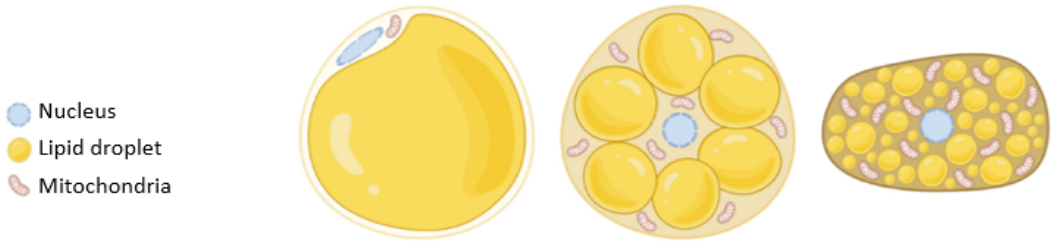

	White adipocyte	Beige adipocyte	Brown adipocyte
UCP1 expression	Negative	Positive	Positive
Mitochondria density	Low	Medium	High
Morphology of lipid droplet	One large droplet	Small multiple droplets	Small multiple droplets
Function	Store energy as fat	Heat generation	Heat generation

Figure 4 – Morphological and phenotypic adipocyte properties: Three main adipocyte categories classified based on their expression of UCP1, mitochondrial density, lipid droplet morphology and main function. UCP-1 (uncoupling protein 1); Adapted from Lee et al. 2021.[48]

7. Adipocyte lipid anabolism

Limiting the amount of circulating and extracellular FFAs is of significant importance for mammals. Failure to efficiently limit the amount of extracellular FFAs results in systemic inflammation, ectopic fat accumulation (*i.e.* in non-adipose organs) as well as cellular oxidative and endoplasmic reticulum stress[49]. In turn, these contribute the development and progression of insulin resistance, cardiovascular and hepatic diseases[49–52]. White adipocytes are specialized in lipid uptake and their *de novo* synthesis, thus removing toxic lipids from circulation. This enables the safe storage of lipids as acylglycerol species inside lipid droplets until adipocytes become hypertrophied and their storage capacity is exceeded[53].

To remove circulating lipids, adipocytes secret lipoprotein lipase (LPL) which is ultimately transported to the lumen of neighboring capillary endothelial cells[54]. Here, LPL hydrolyzes TAG carried by chylomicrons and very-low density lipoproteins and the resulting FFAs and monoacylglycerol MAG are transported to the interstitial spaces of the AT and then internalized by adipocytes. Once intracellular, these FFAs are converted by acyl coenzyme A (CoA) synthetase (ACS) into FA-CoAs[55,56]. In turn, these are converted to lysophosphatidic acids by glycerol-3-phosphate

acyltransferase, which are then converted to phosphatidic acids through the addition of one more FA-CoA by acylglycerolphosphate acyltransferase [57]. These intermediate species are then converted to diacylglycerol (DAG) through phosphatidic acid phosphatase activity[57]. To a lesser extent, FA-CoA and monoacylglycerol can be converted to DAG by MAG acyltransferase [58]. DAG molecules and additional acylated FAs are then converted to TAGs by DAG acyltransferase (DGAT)[59]. Overall, uptake and re-esterification of FFAs is the major source of adipocyte TAG[60].

In addition to re-esterification of FFAs, adipocytes also synthesize TAGs through *de novo* lipogenesis. Here, adipocytes import interstitial glucose through glucose transporter type 4[61]. Glucose is then converted to pyruvate through glycolysis which is then shuttled to the mitochondrion and incorporated in the tricarboxylic acid (TCA) cycle. Citrate, a TCA intermediate, is exported to the cytoplasm where it is re-converted into CoA by ATP-citrate lyase[61]. The resulting CoA is converted to malonyl-CoA by acetyl-CoA carboxylase, which is then used to synthesize palmitate (C-16) by FA synthase (FASN)[61]. In turn, palmitate can be used to synthesize longer FAs or to synthesize TAG through the pathway described above for FFAs obtained via LPL activity.

Collectively these lipogenic pathways promote fat accumulation and adipocyte volume expansion.

8. Adipocyte lipid catabolism

In periods of negative energy balance or after specific stimulation, adipocytes mobilize their stored energy to meet whole-organism energy demands. However, there are no TAG transporters to enable its export from the intracellular compartments of the adipocyte to the extracellular milieu. To enable the export of lipid stores the adipocyte employs two distinct strategies. These are extracellular vesicle (EV)-mediated TAG export and lipolysis[42].

8.1. Exocytosis of TAG-carrying EVs

EV-mediated TAG export has been reported in sebocytes[62], cuboidal epithelial cells (*i.e.* in lactating mammary glands)[63] and more recently in adipocytes[64]. In this process, the adipocyte sheds EVs composed by a phospholipid bilayer originating from the plasma membrane, an inner phospholipid monolayer made originating for the lipid droplet membrane and a central core rich in TAG[64]. Most of these EVs are readily internalized by local macrophages and accounts for approximately 2% of total lipid daily lipid export from adipocytes[64]. Accordingly, whether these EVs can be exported to other tissues and how they contribute to whole-organism metabolic homeostasis remains to be elucidated.

8.2. Lipolysis

The other, and more relevant, mechanism to mobilize fat stores is lipolysis. Here, TAG molecules are first hydrolyzed into individual FFAs and glycerol molecules, which are then exported through plasma membrane transporters. Adipocyte lipolysis occurs through two major pathways: acid and neutral lipolysis[65].

8.2.1. Neutral lipolysis

Neutral lipolysis is the major mechanism of fat mobilization from adipocytes. This process is catalyzed by three lipases: adipose tissue triglyceride lipase (ATGL), hormone-sensitive lipase (HSL) and monoacylglycerol lipase (MGL)[42,65]. ATGL converts TAG into DAG and a FFA[66]. Hormone-sensitive lipase converts DAG into MAG and a FFA, and to a lesser extent is also able to convert TAG into DAG[67,68]. Lastly, MGL hydrolyses MAG into a FFA and a glycerol molecule[69–71].

8.2.1.1. Regulation of neutral lipolysis

Regulation of adipocyte neutral lipolysis is essential to maintain metabolic homeostasis. In conditions of positive energy balance (*i.e.* fed state) adipocyte neutral lipolysis occurs at very low rates. This state lipolytic state is known as basal lipolysis. During periods of negative energy balance (*i.e.* fasting), adipocyte neutral lipolysis is activated, a status known as induced lipolysis. A myriad of stimuli activate neutral adipocyte lipolysis. Indeed, sympathetic nervous system input (*i.e.*

norepinephrine)[72], inflammatory mediators (*e.g.* TNFα, IL-6)[73–76] hormonal queues (*e.g.* epinephrine, T3/T4)[72,77] and toll-like receptor agonists are known inducers of adipocyte neutral lipolysis in humans and rodents. Conversely, insulin which is secreted by pancreatic β-cells after feeding, is a potent inhibitor of adipocyte neutral lipolysis[78].

8.2.1.2. Post-translational regulation

Activation of adipocyte neutral lipolysis occurs mainly through post-translational modifications of neutral lipases (Fig. 5). Arguably, the most studied mechanism of adipocyte neutral lipolysis induction is through catecholamines (*i.e.* epinephrine and norepinephrine). Here, catecholamines bind to β-adrenergic receptors and activate G-protein-coupled receptors which activate downstream adenylate cyclases (ACs)[79,80]. These ACs quickly convert adenosine triphosphate (ATP) into cyclic adenosine monophosphate (cAMP) inducing protein kinase A (PKA). Activated PKA phosphorylates multiple serine residues of HSL[81] and perilipin(PLIN)-1[82]. One the one hand, HSL phosphorylation promotes its activation and translocation to the lipid droplet's surface. On the other hand, PLIN1 phosphorylation induces its dissociation from comparative gene identification (CGI)-58. The released CGI-58 is then able to bind lipid droplet-bound ATGL, activating its enzymatic activity. Unlike ATGL and HSL, no post-translational modifications have been identified for MGL.

Phosphorylation of HSL can also be promoted through the mitogen-activated protein kinase (MAPK) pathway[83]. In this instance, cytokines such as TNFα and IL-6 or bacterial products such as lipopolysaccharide and peptidoglycans activate their cognate receptors of the surface of adipocytes, leading to phosphorylation of extracellular-signal regulated kinase (ERK) 1 and 2[76,84–87].

Inhibition of adipocyte neutral lipolysis occurs primarily through reduction of intracellular levels of PKA-activating cAMP. The best-described physiological inhibitor of adipocyte neutral lipolysis is insulin[78,88–91]. Insulin binds to the insulin receptor resulting in phosphorylation of the insulin receptor substrate and subsequent phosphorylation of phosphatidylinositol-3 kinase (PI3K)[90,91]. Activation of PI3K induces downstream activation of the phosphoinositide-dependent kinase 1 and protein kinase B (*i.e.* also known as serine/threonine kinase or AKT) [90,91]. This

signaling cascade culminates with the activation of phosphodiesterase 3B which converts cAMP into AMP, thus deactivating the lipolysis inducing PKA[91].

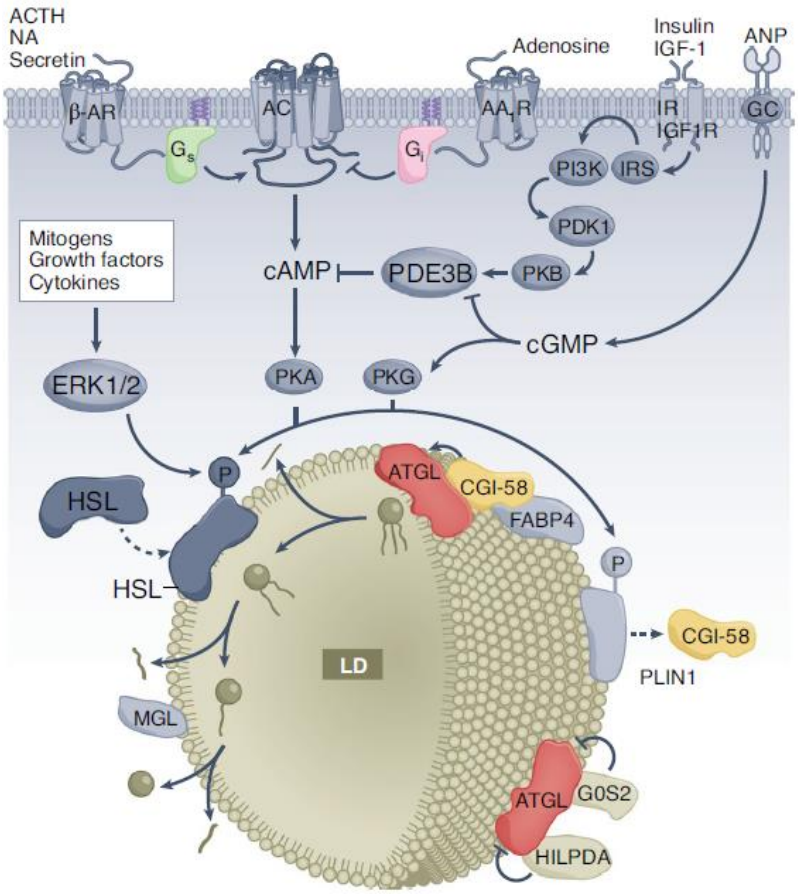

Figure 5 – Post-translational regulation of neutral lipolysis: AC and GC are activated downstream of β-AR and ANP receptor activation respectively, resulting in increased cAMP and cGMP and downstream activation of PKA and PKG. Activated PKA and PKG phosphorylate HSL and PLIN1, resulting in HSL translocation to the lipid droplet and dissociation of CGI-58 from PLIN1. Alternatively, ERK1/2 activated downstream of mitogen and cytokine signaling may also phosphorylate HSL. Dissociated CGI-58 binds to ATGL increasing its activity, which is further enhanced by interactions between CGI-58 and FABP4. ATGL is inhibited by interactions with the transcriptionally regulated proteins G0S2 and HILPDA. Insulin and IGF1 receptor activation inhibits lipolysis through sequential activation of IRS, PI3K, PKB and PDE3B. PDE3B converts cAMP into AMP preventing PKA activation. Adenosine activates AA1R which inhibits AC, decreasing cAMP levels. AC (adenylate cyclase); GC (guanylate cyclase); β-AR (β-adrenergic receptor); ANP (atrial natriuretic peptide); cAMP (cyclic adenosine monophosphate); cGMP (cyclic guanosine monophosphate); PKA (protein kinase A); PKG (protein kinase G); HSL (hormone sensitive lipase); PLIN1 (perilipin-1); LD (lipid droplet); CGI-58 (comparative gene identification-58); ERK (extracellular-signal regulated kinase); ATGL (adipose triglyceride lipase); FABP4 (fatty acid binding protein 4); G0S2 (G0/G1 Switch 2); HILPDA (hypoxia inducible lipid droplet associated); IGF (insulin-like growth factor-1); IRS (insulin receptor substrate); PI3K (phosphatidylinositol-3-kinase); PDK-1 (phosphoinositide-dependent kinase-1); PKB (protein kinase B); PDE3B (phosphodiesterase 3B); AA1R (adenosine A1 receptor). Originally from Garbner et al. 2021.[42]

8.2.1.3. Transcriptional regulation

Regulation of transcript abundance of neutral lipases and their regulatory elements plays a significant, yet poorly understood, role in the regulation of adipocyte neutral lipolysis (Fig. 6). In addition to inducing HSL phosphorylation, activation of ERK1 and 2 results in decreased expression of the genes coding for G0/G1 switch gene 2 and fat-specific protein-27, two potent inhibitors of ATGL activity[92–94]. Moreover, although no reports show PLIN 1 phosphorylation by ERK1/2, the activation of this MAPK pathway induces downregulation of PLIN1. In turn, this reduces the overall quantity of PLIN 1 available to buffer CGI-58[95], which may contribute to ATGL activation.

Activation of other MAPK signaling pathways through Janus kinase 2 and ERK3 result in the activation of two transcription factors: signal transducer and activator of transcription (STAT) 5 and forkhead box protein O-1 (FOXO1). In turn, activation of STAT5 and FOXO-1 leads to increase *Pnpla2* (ATGL coding gene)[96,97].

Conversely, insulin dependent PKB and cyclin-dependent kinase-1 phosphorylation of FOXO-1 prevents its translocation to the nucleus[98]. This inhibitory mechanism is amplified during states of high nutrient abundance through PKB activation by mechanistic target of rapamycin complex 2[99]. Moreover, insulin activates the Snail1 transcription factor, which suppresses *Pnpla2* transcription by binding the E2-box sequences in the *Pnpla2* promoter[100].

Other modulators of *Pnpl2* and *Lipe* (coding for HSL) expression are suggested by a multitude of studies. These include the peroxisome proliferator-activated receptor (PPAR) and CCAAT/enhancer binding protein α, which induce a net increase in *Pnpla2* and *Lipe* transcript levels[89,101,102]. On the other hand, the transcription factors specificity protein 1 and transcription factor E3 exert a net decrease in *Pnpla2* and *Lipe* transcript levels[101,103]. Moreover, *Lipe* transcript levels have been shown to be increased by the transcription factors sterol regulatory element-binding protein 1c, liver X receptor and retinoid X receptor[104,105].

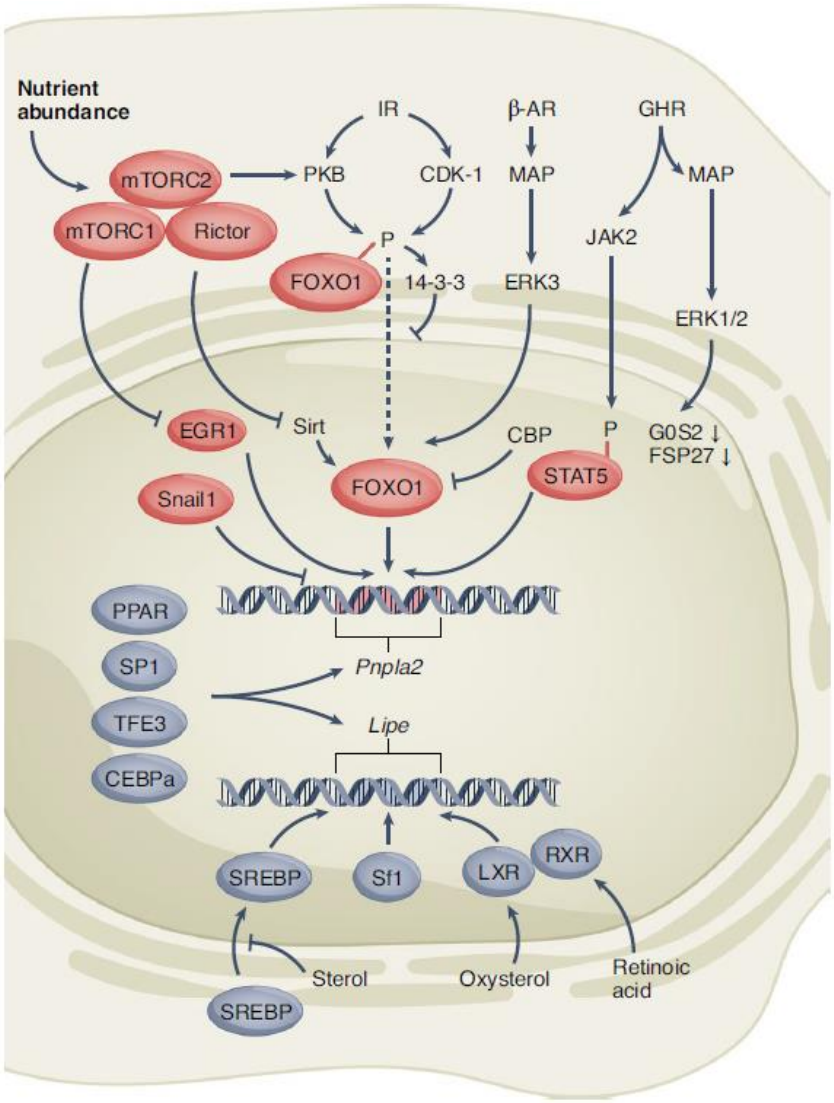

Figure 6 – Transcriptional regulation of neutral lipolysis: *Pnpla2* (ATGL) is inhibited by Snail1, SP1, TFE3 and activated by phosphorylated STAT5, FOXO1, EGR1, PPAR, CEBPα. *Lipe* (HSL) is inhibited by SP1, TFE3 and activated by PPAR, CEBPα, LXR and RXR. GHR activation activates MAP-ERK1/2 pathway, leading to decreased transcript levels of G0S2 and FSP27. STAT5 is phosphorylated by JAK2, which is activated following GHR activation. Nutrient abundance inhibits *Pnpla2* expression through EGR1 inhibition by mTORC1 and by preventing FOXO1 deacetylation through Rictor-mediated Sirt inhibition. IR and mTORC2 activation of PKB and CDK-1 promote FOXO1 phosphorylation, preventing its nuclear translocation by interacting with 14-3-3 protein. SP1 (specificity protein 1); TFE3 (transcription factor E3); STAT5 (signal transducer and activator of transcription 5); FOXO1 (forkhead box protein O-1); EGR1 (early growth response protein-1); PPAR (peroxisome proliferator-activated receptor); CEBPα (CCAAT/enhancer binding protein); LXR (liver X receptor); RXR (retinoid X receptor); GHR (growth hormone receptor); MAP (mitogen activated protein); ERK (extracellular-signal regulated kinase); G0S2 (G0/G1 Switch 2); FSP27 (fat-specific protein 27); JAK2 (Janus kinase 2); mTORC (mechanistic target of rapamycin complex); Rictor (rapamycin-insensitive companion of mTOR); Sirt (sirtuin) PKB (protein kinase B); CDK-1 (cyclin-dependent kinase 1). Originally from Garbner et al. 2021.[42]

8.2.2. Acid lipolysis

Acid lipolysis occurs during macrolipophagy and microlipophagy (*i.e.* forms lipid autophagy). In macrolipophagy portions of the lipid droplet are engulfed by portions of the endoplasmic reticulum containing microtubule-associated protein 1A/1B-light chain 3[106]. These lipoautophagosomes then fuse with lysosomes containing lysosomal acid lipase (LAL) forming acidified autolysosomes. In microlipophagy, TAG is transferred directly between the lipid droplet and the lysosome through Ras-related in brain proteins[42,65,107]. In both macrolipophagy and microlipophagy, TAG is hydrolyzed into three FFAs and a glycerol molecule within acidified compartments by LAL[40,63]. Unlike neutral lipolysis, the extracellular release of lipolytic generated during acid lipolysis does not require membrane transporters. Instead, lysosomal membranes fuse with the plasma membrane and release the lysosomal contents into the extracellular milieu through lysosomal exocytosis[108].

8.2.2.1. Regulation of acid lipolysis

Unlike its neutral lipase counterparts, known regulation of *Lipa* (LAL coding gene) relies mainly on transcriptional control. Here, transcription factors known to induce *Pnpla2* and *Lipe* transcription also induce *Lipa* expression. During starvation, activation of AMP-activated protein kinase and inhibition of mechanistic target of rapamycin signaling lead to the translocation of several transcription factors to the nucleus. Among these, FOXO-1, transcription factor EB and PPARs are positive modulators of *Lipa* expression[109–112].

8.3. Adipocyte lipolysis in pathogenesis

Cytosolic lipolysis has been increasingly studied in different pathologies, having both beneficial and deleterious effects depending on the context. One such pathology is cachexia, a progressive hyper-catabolic wasting syndrome in which the afflicted individual experiences extensive loss of fat mass before undergoing skeletal muscle loss[113–115]. This disorder cannot be reversed solely through nutritional interventions and constitutes a poor prognosis factor observed in the late stage of many diseases[113]. In the context of cancer associated cachexia (CAC),

activation of ATGL and HSL-dependent lipolysis has been associated with the development of cachexia[116].

In conditions of overweight and obesity, visceral adipocytes become hypertrophied and exhaust their fat storage capacity[117]. This leads to excessive fatty acid efflux, resulting in ectopic fat accumulation, especially in insulin sensitive tissues such as the liver and skeletal muscle. In turn, this disruption in lipid homeostasis is associated with an increase in insulin resistance and a decrease in glucose tolerance, which are hallmarks of type 2 diabetes mellitus[118]. Moreover, continuous hepatic uptake of adipocyte's lipolytic products leads to non-alcoholic fatty liver disease[119]. This highly prevalent condition is predominantly asymptomatic but may progress into nonalcoholic steatohepatitis and ultimately lethal hepatic cirrhosis and malignancies.

8.3.1 Adipocyte lipolysis in infection

Activation of adipocyte lipolysis is frequently observed in the context of infectious diseases. Indeed, this has been described in the context of bacterial, viral and parasitic diseases and is likely implicated in the loss of fat mass often observed during infections.

Several intracellular pathogens have been shown to induce intracellular lipolysis to fuel their replication. This body of work has been generated in a plethora of different host cells with few studies using adipocytes as the host cell. One such study has shown that *in vitro* infection of 3T3-L1 adipocytes with *Chlamydia pneumoniae* results in an HSL-dependent increased secretion of glycerol and FABP4[120,121]. Chemical inhibition or genetic ablation of HSL results in impaired *C. pneumoniae* growth[121]. Interestingly, this induction of adipocyte lipolysis may be a contributing factor to the clinical link between *C. pneumoniae* infection and metabolic syndrome prevalence[122,123].

Mycobacterium tuberculosis, another highly prevalent bacterial pathogen, has been shown to colonize and modulate the AT[124,125]. This modulation includes increased adipocyte lipolysis, which was associated with the development of insulin resistance[126]. Despite this negative impact of AT modulation, mice devoid of a

functional AT present higher lung bacterial burdens and pathology, suggesting a net protective role for the AT during *M. tuberculosis* infection[127].

It has been a long-standing observation that HIV infected individuals develop severe lipoatrophy associated with general lipodystrophy. While the wider lipodystrophy phenotype has been associated with the use of earlier generation thymidine analogue nucleoside reverse transcriptase inhibitors[128], the lipoatrophy phenotype had been documented prior to the introduction of these drugs and is still observed in people treated with new generation anti-retroviral therapy[129–131]. This can be partially explained by the adipose dysfunction induced by viral protein R encoded by HIV, which promotes adipocyte *Pnpla2* (ATGL) expression and induces lipolysis[132]. The impact of adipocyte lipolysis on viral load and host resistance remains to be elucidated.

Unlike *T. brucei*, *T. cruzi* is able to infect host cells and proliferate intracellularly. Although macrophages are the preferred target cell for *T. cruzi*, it is well established that this parasite is also able to infect and proliferate within adipocytes[133–136]. Concomitant to this AT colonization, a progressive reduction of adipocyte size and increased immune infiltration is observed[137]. Moreover, modulation of AT metabolism has been shown to worsen cardiac pathology[138]. Although these presentations suggest an increase in adipocyte lipolysis, to date no study has reported the release of lipolytic products from *T. cruzi* infected AT. In fact, AT from *T. cruzi* infected mice present a simultaneous reduction in the expression of lipolytic and lipogenic genes[137,138].

Despite not colonizing the AT, the large extracellular parasite *Echinococcus granulosus* is able to modulate adipocyte metabolism. Specifically, transcriptomic analysis of the subcutaneous WAT of *E. granulosus* infected mice suggested an upregulation of adipocyte lipolysis concomitant with a reduction of *de novo* lipogenesis which correlated with a decrease in overall adipocyte volume[139].

9. Immunity and immune evasion

During infection, host and parasite perform a continuous arms race that balances parasite proliferation and elimination. The mammalian host employs innate and adaptive cellular and humoral immune responses to eliminate the majority of *T. brucei* parasites. Although this complex immune response has a high trypanocidal capacity, the parasite has developed a series of virulence mechanisms that prevent its complete elimination[140].

9.1. Immune response to *T. brucei*

A natural *T. brucei* infection begins with the deposition of metacyclic parasites in the dermis of the host during a tsetse fly blood meal. In the dermis, metacyclic parasites encounter host phagocytes, namely neutrophils and macrophages. In this early stage of infection, these phagocytic cells lack proper activation stimuli. This, together with low concentration of *T. brucei*-binding opsonins results in a very low phagocytic efficiency. Accordingly, only parasites with reduced motility and viability are seen internalized by these phagocytic cells in the dermis[141]. The low rate of trypanosome killing in the dermis enables *T. brucei* to differentiate from cell-cycle arrested metacyclic forms to bloodstream slender forms, which then invade and quickly proliferate in the blood. In the bloodstream, *T. brucei* encounters innate and adaptive humoral responses. In non-primate mammalians hosts this response relies on the production of antibodies and complement factors, while several primates employ an additional innate trypanosome lytic factor (TLF).

9.1.1. Trypanosome Lytic Factor

It is a long-standing observation that many animal-infective *T. brucei* parasites lyse soon after being incubate with human blood or serum. As such, since the early 20th century it has been recognized that human sera contain a TLF[142].

TLF is a high-density lipoprotein which contains apolipoprotein L-1 (APOL1), apolipoprotein A-I (APOAI) and hemoglobin binding haptoglobin-related protein (HPR)[143]. Upon endocytosis, APOL1 is trafficked in acidic endosomal compartments. Here, it forms inactive cation-selective channels in the endosomal membranes. Upon fusion of these endosomes with the plasma membrane during

endosomal recycling, these channels are activated by pH-neutralization and enable potassium efflux concomitants with the influx of chloride and water[143]. The resulting osmotic imbalance leads to swelling and cell lysis. This highly efficient trypanolytic mechanism grants sterile immunity of TLF-expressing primates (*e.g.* humans) to TLF-susceptible Trypanosomes (*e.g. T. brucei brucei*)[144,145].

Human-infective *T. brucei gambiense* and *T. brucei rhodesiense* have developed distinct strategies to inactivate TLF. *T. brucei gambiense* increases endosomal membrane stiffness through the expression of a *T. brucei gambiense*-specific glycoprotein (TgsGP), preventing APOL1 insertion[146,147]. *T. brucei rhodesiense* synthesizes an APOL1-binding protein encoded by the serum resistance associated (SRA) gene. This binding prevents APOL1 endosomal insertion[148,149].

9.1.2. Immunoglobulins and complement

In the case of TLF-competent hosts infected with TLF resistant *T. brucei*, or in TLF-deficient hosts, control of the parasite relies instead in the synergistic humoral response by antibodies and the complement system. Here, a strong antibody response against the parasite's variant surface glycoprotein (VSG) is required for parasite elimination[150]. VSG is a glycosylphosphatidylinositol-anchored protein tightly packed on the parasite's surface and is the most abundant *T. brucei* protein, with each parasite presenting approximately 10 million VSG molecules on its surface[151]. This humoral response begins with a largely T cell-independent proliferation of B cells in the spleen and lymph nodes[152]. These B cells produce a polyclonal anti-VSG immunoglobulin M (IgM) response that is essential to control parasitemia[153], by enabling host phagocytes to recognize and internalize the parasite[154]. This elimination is dependent on phagocytosis, particularly by host macrophages, as evidenced by the increased susceptibility of mice to *T. brucei* following macrophage depletion with clodronate-loaded liposomes[155,156]. However, macrophages lack the FcμR required for IgM-binding[157,158] and instead rely on classical activation of the complement system[159]. This results in deposition of complement factors on VSG-bound IgM followed by conversion of complement component 3 (C3) into C3a and C3b. The latter is a potent opsonin which binds to several macrophage receptors, such as complement receptor 1 (CR1), CR3, CR4 and CRIg, promoting phagocytosis[160]. Mice deficient for C5, which are unable to

form membrane attack complexes, are equally capable of controlling *T. brucei* as complement competent mice[161,162]. Accordingly, opsonization and pleotropic immune-activating properties are the mechanisms that enable optimal trypanocidal activity.

Shortly after this initial IgM response, a T-cell dependent B cell response takes place. Here, cluster of differentiation 4 (CD4) positive T follicular helper cells enable B cells to undergo antibody class switch recombination and subsequent affinity maturation[163]. This results in the production of highly specific IgGs, that enable parasite phagocytosis through FcγR binding[164].

9.1.3. Antigenic variation

To avoid sterilization by this humoral immune response, the parasite has developed an immune evasion strategy to reduce antibody effectiveness. To this end, *T. brucei* employs 2000 genes and gene-fragments capable of encoding antigenically distinct VSGs, encompassing roughly 30% of the parasite's genome[150]. During *T. brucei* expansion, a low frequency and likely stochastic event enables the switch from expressing one VSG to an alternative one. VSG switching can take place by replacing the VSG gene at the active dedicated expression locus (called bloodstream expression site, BES) or by transcriptionally silencing the active BES and activation of a second BES[150,165]. Thus, the antigen-specific immune response mounted against the *T. brucei* parasites expressing the population-dominant VSG are unable to target and eliminate parasites presenting this new VSG coat. This process is classically known as antigen variation and it is essential for parasite virulence, as individual parasites expressing the initially dominant VSG are negatively selected by the host's immune response.

9.1.4. Immunocomplex endocytosis

Another major virulence mechanism employed by *T. brucei* to circumvent the host's immune response relies on active removal of VSG-bound antibodies. Antibody binding to VSG, especially bulky IgMs, creates a large VSG-Ig immunocomplex[166]. The high surface area of these immunocomplexes generates a molecular sail effect, where a hydrodynamic drag force generated during the parasite's forward swimming motion propels the immunocomplex towards the flagellar pocket (FP). In the FP,

these complexes are endocytosed and then eliminated. This process is modulated by multiple biophysical properties, such as the VSG-Ig complex size, the milieu's viscosity and the parasite's forward swimming velocity[166,167]. As a result of the fast elimination of surface bound antibodies, a higher antibody titer is required before a critical Ig concentration is reached and the parasite eliminated. Although this mechanism of antibody clearance is central in the evasion of *T. brucei* to the humoral immune response, recent work has suggested that primate hosts may also exploit this mechanism to efficiently deliver TLF to the parasite. Here, germline-encoded polyreactive IgMs bind simultaneously VSG and TLF (*i.e.* HPR portion), forming an IgM-VSG-TLF immunocomplex that is rapidly endocytosed in the FP[168] and consequently killing TLF-sensitive parasites.

9.1.5. Phagocytes

Antibody responses by themselves have no lytic capacity against *T. brucei*. To achieve parasite elimination, the host requires phagocyte activity. These phagocytes comprise macrophages, monocytes, and neutrophils. Unlike macrophages and monocytes, neutrophils appear to exert no overt protective role in *T. brucei* infections and are even reported to promote early dissemination following intradermal infections[141]. Indeed, macrophages/monocytes are essential for *T. brucei* elimination and their depletion using chlodronate-containing liposomes results in increased parasitemia and reduced survival[155,156]. They achieve parasite elimination through the production and release of highly trypanocidal nitric oxide and phagocytosis[169–171].

9.1.6. T cell response

T cell responses are essential for host resistance to *T. brucei*. These can be divided into two categories: cytotoxic or helper T (Th) cell responses. Cytotoxic T cell responses are carried out by CD8+ T cells and specialize on the elimination of intracellular pathogens[172]. They target cells that present non-self antigens in a major histocompatibility complex class I (MHC-I) context cognate to their T cell receptor (TCR). This interaction induces CD8+ T cell release perforins and granzymes and enables Fas-Fas ligand (FasL), resulting in apoptosis of infected cells. Owing to the nature of *T. brucei* as an exclusively extracellular parasite, no direct cytotoxic activity

of CD8+ T cells contribute to parasite clearance[172]. Moreover, CD8 deficient mice infected with *T. brucei* present an overall reduction in parasitemia and increased survival, suggesting a detrimental role for CD8+ T cells during a *T. brucei* infection[173,174].

Th responses are carried out by phenotypically diverse CD4+ T cells. Depending on the activation stimuli leading to the activation of these CD4+ T cells, they will acquire different effector functions. These functions are determined by the release of specific cytokines and through the expression of immunomodulatory surface molecules. The study of Th heterogeneity has so far yielded seven distinct Th types: Th1, Th2, Th9, Th17, Th22, T follicular helper (Tfh) and regulatory T (Treg) cells[175]. Each Th type has a distinct function, ranging from the elimination of unicellular pathogens to large helminths, as well as playing pivotal roles in tissue repair and direct B cell support[175].

CD4+ T cells have no known direct trypanocidal capacity. Instead, they are essential for optimal activation both innate immune cells and B cells. Specifically, a T helper 1 (Th1) response is protective during a *T. brucei* infection. This response is characterized by the production of high levels of TNFα and IFNγ, promoting the differentiation of macrophages into a protective nitric oxide-producing M1 phenotype and promoting class-switch recombination of IgM-producing into IgG2a and IgG3-producing B cells[176–178]. Indeed, mice deficient for TNFα (*i.e.* particularly its membrane-bound form), IFNγ or CD4+ T cells show reduced parasite control[173,174,179–182].

Although parasite elimination by the immune system is a desirable outcome, it occurs at the cost of extensive immunopathology. This consists in extensive tissue secondary damage resulting from the immune response primed against *T. brucei*. Immunopathology, and not pathogen load *per se*, is often the main contributor to overall disease severity and ultimately host death[183]. As such, the immune system attempts to limit the intensity of immune responses to prevent excessive damage to self. To this end, Treg cells limit immune cell effector functions by release the anti-inflammatory cytokines interleukin (IL)-10 and transforming growth factor beta (TGFβ)[184,185]. Moreover, Tregs are able to suppress antigen-presenting cell (APC) activity through direct cell-cell interactions by binding APC surface CD80 with

cytotoxic T-lymphocyte associated protein 4 (CTLA4). Experimental activation of Treg cells has been shown to prolong survival of *T. brucei* infected mice[186]. Conversely, mice deficient for IL-10, a cytokine produced abundantly by Tregs and other cells, succumb to severe immunopathology early during infection[187]. Accordingly, fine-tuning of pro and anti-inflammatory pathways is required to achieve good pathogen elimination in the absence of excessive immunopathology.

Aims

T. brucei has evolved multiple strategies to avoid elimination by the host's immune system while simultaneously self-limiting its growth in order to prolong its host's survival and consequently increase the likelihood of transmission. To achieve this, *T. brucei* employs mechanisms of antigenic variation, quorum sensing and immunocomplex clearance. Although essential to the parasite's survival and transmission, these may be only part of the strategies employed by *T. brucei* to maintain its transmission across hosts.

The recent re-appreciation of extravascular spaces of tissues as major targets of colonization by *T. brucei* has raised several important questions on the relevance of tissue colonization in parasite survival, transmission and pathology. This extravascular colonization is not homogeneous between different organs. Of note, the AT harbors particularly high amounts of *T. brucei* parasites when compared to most other organs. In turn, this raises questions on which properties of the AT enable such high parasite accumulation and how this accumulation *per se* modulates normal AT function and ultimately pathology.

Accordingly, the work presented in this dissertation aims at understanding two major questions: First, we aimed to understanding whether a permissive immune environment is responsible for the extensive colonization of the AT. Second, we aimed to understating if and how a *T. brucei* infection modulates AT metabolism and in turn how this affects pathology and parasite growth. Thus, our aims are to:

I. Characterize the accumulation of cellular and humoral components of the immune response in the AT, and how this compares to the blood.
II. Identify any immune factor differentially involved in parasite elimination from the AT but not from other organs and/or blood.
III. Identify metabolic pathways responsible for the loss of AT weight during infection, and assess how these pathways are modulated.
IV. Characterize the impact of these metabolic alterations on pathology and parasite behavior.

Methods

Ethics statement

All experimental animal work was performed in accordance with the Federation of European Laboratory Animal Science Associations (FELASA) guidelines and was approved by the Animal Care and Ethical Committee of the Instituto de Medicina Molecular João Lobo Antunes (under the licenses AWB_2016_07_LF_Tropism and AWB_2021_11_LF_TrypColonization).

Animals

In vivo experiments were performed with male C57BL/6J mice, from Charles River Laboratories International, unless otherwise stated. Rag2-deficient (Rag2-/-) and Jht-deficient (Jht-/-) mice, generated on a C57BL/6J background, were obtained from Instituto Gulbenkian de Ciência (IGC, Portugal). Ifng-deficient (Ifng-/-), generated on a C57BL/6J background, were kindly provided by Bruno Silva-Santos laboratory from Instituto de Medicina Molecular (iMM, Portugal). C3-deficient (C3-/-), generated on a C57BL/6J background, were kindly provided by Miguel Prudêncio laboratory from Instituto de Medicina Molecular (iMM, Portugal). Adipocyte-specific ATGL deficient (*Adipoq*$^{Cre/+}$-*Atgl*$^{fl/fl}$) mice, adipocyte-specific HSL deficient (*Adipoq*$^{Cre/+}$-*Hsl*$^{fl/fl}$) mice and respective *Atgl*$^{fl/fl}$ and *Hsl*$^{fl/fl}$ control mice were kindly provided by Rudolf Zechner (University of Graz, Austria). All experimental mice were 7–12 weeks old, unless otherwise stated. Jht-deficient mice were 9–21 weeks old, as well as the WT controls in such experiment. Mice were housed in a Specific-Pathogen-Free barrier facility, at iMM, under standard laboratory conditions: 21 to 22°C ambient temperature and a 12h light/12h dark cycle. Chow and water were available *ad libitum*.

Infection

T. brucei cryostabilates were thawed and parasite viability by its motility was confirmed under an optic microscope. Mice were infected by intraperitoneal (i.p.) injection of 2000 *T. brucei* parasites. At selected time-points post-infection, animals were euthanized by CO2 narcosis and immediately perfused transcardially with pre-warmed heparinised saline (50 mL phosphate buffered saline (PBS) with 250 µL of 5000 I.U./mL heparin). Organs were collected and either snap frozen in liquid nitrogen; used immediately to prepare single cell suspensions for flow cytometry

staining; or immersion-fixed in formalin or glutaraldehyde for histopathology or electron microscopy, respectively.

Feeding synchronization

Feeding synchronization was achieved by fasting mice for 7 h from 0 am to 7 am. Afterwards, access to food was re-established for 2 h after which mice were euthanized.

Pair feeding

Mice were individually housed, and their food intake monitored daily. To each infected mouse a non-infected control was assigned (*i.e*. pair-fed control). Every 24 h, pair-fed controls were provided with the same amount of food consumed by their respective infected pair in the previous 24 h.

Body composition analysis

Mouse total fat mass, lean mass and free body fluid mass were determined using a 6.2 MHz time-domain nuclear magnetic resonance based Minispec LF65 (Bruker) apparatus. Live unanesthetized were restrained, weighed and then inserted into the Minispec apparatus. Each measurement lasted for approximately one minute.

Antibody treatment

To block PD-1/PD-L1 axis, mice were injected intravenously (i.v.) with 300µg of αPD-1 (clone RMP1-14, InVivoMab, BioXcell), immediately before infection and at days 3, 5 and 7 post-infection.

Chemical sympathectomy

Chemical sympathectomy was performed by i.p. administration of 200 mg/kg of 6-hydroxydopamine hydrobromide (6-OHDA) in PBS containing 0.4% ascorbic acid as stabilizer[188]. Mice were treated with either 6-OHDA or with PBS containing 0.4% ascorbic acid (sham controls) 72 and 24 h prior to infection.

Parasite lines

Mouse and *in vitro* infections were performed using parasites derived from *T. brucei* AnTat 1.1E, a pleomorphic clone derived from the EATRO1125 strain. AnTat 1.1E 90–13 is a transgenic cell-line encoding the tetracyclin repressor and T7 RNA

polymerase[189]. AnTat1.1E 90–13 GFP::PAD1utr derives from AnTat1.1E 90–13 in which the green fluorescent protein (GFP) is coupled to PAD1 3'UTR. Monomorphic bloodstream form Lister 427 parasites (MITat1.2, clone 221a) were used for *in vitro* infections. All parasite cell lines were propagated and maintained in HMI-11 medium at 37°C in a 5% CO_2 atmosphere [190].

Ex vivo lipolysis assay

Follow euthanasia and systemic re-perfusion as previously described, AT depots were collected, rinsed with PBS and kept at 37°C in low-glucose (1 g/L) DMEM (Gibco, Thermo Fisher Scientific Inc.) without serum until processing. Next, AT depots were cut into ≈ 20 mg explants and incubated for 2 h at 37°C in 96-well plates containing 200 µL low glucose DMEM with 5% (w/v) fatty acid-free BSA and 5 µM of Triacsin C (Sigma, T4540) per well. Afterwards, these supernatants were collected and replaced with similar medium containing 20 µM of forskolin (Abcam, ab120058) and the explants were incubated for an additional hour. Up to 5 explants were used per AT depot. Next, free fatty acid (C8 and longer) and glycerol concentrations were assessed using commercially available colorimetric kits (MAK044 and MAK117, Sigma) according to the manufacturer's instructions. Concentration of fatty acids and glycerol was normalized to each explant's protein content. Protein contents were quantified by first delipidating the explants for 1 hour in 1 mL of 2:1 chloroform-methanol and 1% acetic acid solution at 37°C under vigorous agitation on a benchtop thermomixer. Afterwards, delipidated explants were lysed overnight in 500 µL of a 0.3M NaOH and 0.1% (w/v) SDS solution at 56°C under vigorous agitation. Lysate protein quantification was performed using a BCA Protein Assay Kit (A53225, Thermo Fisher Scientific Inc.) according to the manufacturer's instructions. *Ex vivo* lipolysis rates are expressed as: Nanomoles of metabolite released per mg or protein per hour.

In vitro lipolysis assay

Culture media from axenically grown 3T3-L1 adipocytes or co-cultured with *T. brucei* was replaced with 500 µL or 250 µL low glucose DMEM with 5% (w/v) fatty acid-free BSA and 5 µM of Triacsin C (Sigma, T4540) per well in 12-well and 24-well plates, respectively. As described above for the *ex vivo* lipolysis assays, this medium is then replaced by a similar medium containing 20 µM of forskolin (Abcam,

ab120058) and incubated for an additional hour followed by metabolite quantification. *In vitro* lipolysis rates are expressed as: Nanomoles of metabolite released per well per hour.

3T3-L1 cell culture

Murine 3T3-L1 pre-adipocytes (CL-173^{TM}; American Type Culture Collection, USA) were grown in 4.5 g/L glucose DMEM supplemented with GlutaMAX™, pyruvate and 10% iron supplemented calf serum (Sigma, C8056) on tissue culture-treated 100 mm dishes (Corning, 353003) at 37°C in a 5% CO_2 atmosphere. For routine passages, cells were kept below 70% confluence and re-plated at 5x10^4 cells/mL. For differentiation into adipocytes 3T3-L1 cells were grown to confluence for 92 h and media was refreshed 48 h after plating. Afterwards, media was replaced by 4.5 g/L glucose DMEM supplemented with GlutaMAX™, pyruvate, 10% fetal bovine serum (FBS), 1 µM dexamethasone (Sigma, D4902), 0.5 mM 3-isobutyl-1-methylxanthine (Sigma, I7018), 1 µg/mL insulin (Sigma, I9278) and 2 µM rosiglitazone (Santa Cruz, sc-202795). Cells were incubated for 48 h and then this step was repeated once to promote better differentiation. Next, medium was replaced by media was replaced by 4.5 g/L glucose DMEM supplemented with GlutaMAX™, pyruvate, 10% FBS and 1 µg/mL insulin for 48 h. Cells were then kept in 4.5 g/L glucose DMEM supplemented with GlutaMAX™, pyruvate and 10% FBS, which was refreshed every 48 h, until cells were used.

Histopathology and Electron Microscopy

Formalin-fixed gonadal adipose tissue was paraffin-embedded and sectioned at 4 µm. Immunohistochemistry for the identification of trypanosomes and inflammatory cells (macrophages and T cells) was performed using a non-purified rabbit serum anti-*T. brucei* VSG13 antigen (cross-reactive with most *T. brucei* VSGs because it is not CRD-depleted, produced in-house), anti-F4/80 antibodies (Abcam, ab6640), anti-CD3 (Dako, A0452), and anti-CD138 (BD, 553712) following conventional protocols. Briefly, antigen retrieval slides was performed in PT Link module (DAKO) at low-Ph, followed by incubation with the primary antibodies. EnVision Link horseradish peroxidase/DAB visualization system (DAKO) was used and counterstained with Harris hematoxylin. For Transmission Electron Microscopy, samples were fixed with a solution containing 2.5% glutaraldehyde (Electron

Microscopy Sciences, EMS) plus 0.1% formaldehyde (Thermo Fisher Scientific Inc.) in 0.1 M cacodylate buffer (Sigma), pH 7.3 for 1 h. After fixation, these were washed and treated with 0.1% Millipore filtered cacodylate buffered (Sigma), post-fixed with 1% Millipore-filtered osmium tetroxide (EMS) for 30 min, and stained *en bloc*, with 1% Millipore-filtered uranyl acetate (Agar Scientific). Samples were dehydrated in increasing concentrations of ethanol, infiltrated and embedded in EMBed-812 medium (EMS). Polymerization was performed at 60°C for 2 days, and ultrathin sections were cut in a Reichert supernova microtome, stained with uranyl acetate and lead citrate (Sigma) and examined in a H-7650 transmission electron microscope (Hitachi) at an accelerating voltage of 100 kV. Electron micrographs were obtained using a XR41M bottom mount AMT digital camera (Advanced Microscopy Techniques Corp). Acquisition of immunohistochemistry images was done in a Nanozoomer-SQ (Hamamatsu Photonics) and analysed using NDP.view2 (Hamamatsu Photonics).

Adipocyte lipid droplet area quantification

Images of hematoxylin and eosin stained slides of gonadal AT were acquired in a Nanozoomer-SQ (Hamamatsu Photonics) with a magnification of 20x. Afterwards, at least 6 random fields per slide were analysed with imageJ using the Adiposoft (version 1.16) plugin[191]. Only adipocytes with a diameter between 10 and 100 µm were considered in this analysis.

Parasite quantification in blood and organs

For parasitemia quantification, blood samples were taken daily from the tail vein and diluted 1:150. Parasites were counted manually in a Neubauer haemocytometer (0.1 mm^3, detection limit is $3.75x10^5$ parasites per mL of blood). When applicable, the total number of parasites was determined by multiplying by the total volume of blood, considering that a mouse has 58.5 mL of blood per kg of bodyweight.

For parasite quantification in organs, genomic DNA (gDNA) was extracted using NZY tissue gDNA isolation kit (NZYTech, Portugal). The amount of *T. brucei* 18S rDNA was measured by quantitative PCR (qPCR), using the primers 5'-ACGGAATGGCACCACAAGAC–3' and 5'–GTCCGTTGACGGAATCAACC–3', and converted into number of parasites using a calibration curve, as previously described by Trindade et al.[19]. Number of parasites per mg of organ (parasite

density) was calculated by dividing the number of parasites by the mass of organ used for qPCR. The total amount of parasites in the organ was estimated by multiplying parasite density by the total mass of the organ. Parasite burden normalized to tissue mass and corresponding organ masses are available in Files S3 and S5 of the annex section.

Preparation of single cell suspensions

Gonadal AT samples were incubated at 37°C in Dulbecco's Modified Eagle Medium (DMEM, GIBCO) with Collagenase I (0.4 mg/mL, Whortington LS004196), Collagenase IV (1 mg/mL, Whortington LS004188) and DNAse (10 µg/mL) for 30 min, under 1100 rpm agitation. Single cell suspensions from the spleen, heart and digested gonadal AT were obtained by sieving them through a 40µm-pore-size nylon cell strainer (BD Biosciences) with a syringe plunger. Spleen cells were treated with erythrocyte lysis buffer (BioLegend 420301) to lyse red blood cells. Both spleen and gonadal AT cells were resuspended in complete Roswell Park Memorial Institute medium (cRPMI, RPMI supplemented with 1% sodium pyruvate 100mM, 1% MEM non-essential amino acids, 1% HEPES 1M, 1% Pen-Strep, 0.1% gentamycin 50 mg/mL, 0.1% β-mercaptoethanol 50 mM and 10% fetal calf serum (all from Gibco)) to use for flow cytometry analysis. Live cells in single cell suspensions were counted after trypan blue staining in a haemocytometer.

Single cell suspensions containing AnTat1.1E 90–13 GFP::PAD1utr parasites were prepared for analysis of PAD1 expression by flow cytometry. Parasites co-cultured with 3T3-L1 cells were recovered by mechanically resuspending the co-cultures through repeated pipetting. Parasite ATFs were recovered by incubating the gonadal AT of infected mice in 5 mL of HMI-11 medium within 50 mL conical tubes under gentle agitation at 37°C for 30 min. Afterwards, cell suspensions were centrifuged at 2000 rpm, washed with PBS, fixed with 2% formaldehyde for 20 min, washed with PBS.

Flow cytometry

Stainings of myeloid and lymphoid cells were performed separately. In isolated spleen cells, stainings were performed in $5x10^6$ cells. Stainings of cells isolated from the gonadal AT were performed with the highest number of cells possible, by diving the cell suspension equally between each staining (never exceeding $5x10^6$ cells).

For myeloid staining of surface determinants, cells were incubated for 45 min at 25°C in cRPMI, in the presence of 5% normal mouse serum (NMS), with the following antibodies: F4/80-FITC (clone BM8, BioLegend), Ly6G-PerCP/Cy5.5 (clone 1A8, BioLegend), CD274-PE/Cy7 (PD-L1, clone 10F.9G2, BioLegend), CD11b-APC/Cy7 (clone M1/70, BioLegend), CD45-Brilliant Violet (BV) 510 (clone 30-F11, BioLegend) and Ly6C-BV605 (clone HK1.4, BioLegend). To stain non-viable cells, Zombie Violet Fixable Viability Kit (BioLegend) was used, incubating cells in PBS with 5% NMS, for 15 min at 25°C. Finally, stained cells were resuspended in cRPMI for flow cytometry acquisition.

For lymphoid staining, cells were first incubated in cRPMI with phorbol 12-myristate 13-acetate (20 ng/mL, PMA) and ionomycin (1 µg/mL) to stimulate cytokine production by T cells, for 1h45 at 37°C. Next, to block cytokine secretion, brefeldin A (10 µg/mL) and monensin (5 µM), were added for the final 1h at 37°C of incubation. Staining of surface determinants was performed by incubating cells for 45 min at 25°C in cRPMI with 5% NMS and the following antibodies: CD3-FITC (clone 17A2, BioLegend), CD279-PE (PD-1, clone J43, eBioscience), CD45-BV510 (clone 30-F11, BioLegend), CD4-BV605 (clone RM4-5, BioLegend) and CD8-BV711 (clone 53–6.7, BioLegend). To stain non-viable cells, LIVE/DEAD Fixable Near-IR Dead Cell Stain Kit (Invitrogen) was used, incubating cells in PBS with 5% NMS, for 15 min at 4°C. For staining of intracellular antigens, fixation and permeabilization of cells was performed using Foxp3/Transcription Factor Staining Buffer Set (eBioscience) and the following antibodies: IFN-γ-PerCP/Cy5.5 (clone XMG1.2, BioLegend), Foxp3-APC (clone FJK-16s, eBioscience) and TNF-α-eFluor450 (clone MP6-XT22, eBioscience). Finally, stained cells were resuspended in cRPMI for flow cytometry acquisition.

For staining of B cell surface determinants, cells were incubated for 45 min at 25°C in cRPMI, in the presence of 5% normal mouse serum (NMS), with the following antibodies: CD45-BV510 (clone 30-F11, BioLegend), IgD-APC (clone 12-26c, eBioscience) and CD19-APC/Cy7 (clone 6D5, Biolegend). For staining of intracellular antigens, fixation and permeabilization of cells was performed using Foxp3/Transcription Factor Staining Buffer Set (eBioscience) and the following antibody Ki67-PE (clone 16A8, eBioscience).

Cell suspensions containing formaldehyde-fixed AnTat1.1E 90–13 GFP::PAD1utr parasites were stained with a PBS solution containing 0.005 mg/mL Hoechst 33342 (Thermo Fisher Scientific) for 20 min at 4°C.

Samples were passed through a 40µm-pore-size nylon cell strainer (BD Biosciences) and then analysed on a BD LSRFortessa flow cytometer with FACSDiva 6.2 Software. All data were analysed using FlowJo software version 10.0.7r2. Schematics of the gating strategies used for immune cell and parasite analyses are represented in Figure 7 and Figure 8, respectively. Immune cell populations normalized to tissue mass and corresponding organ masses are available in the Files S3 and S4 in the annex section.

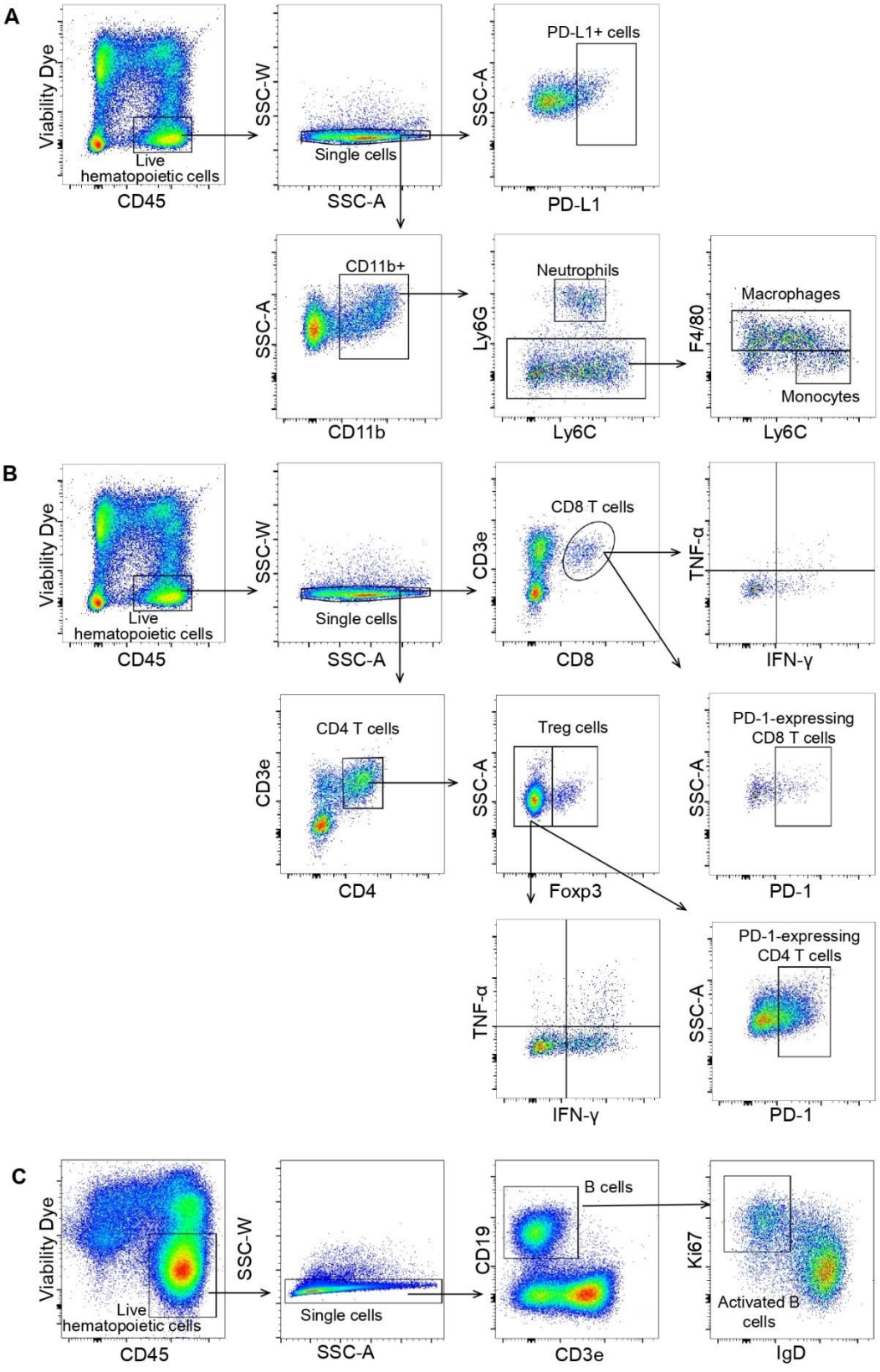

Figure 7 – Immune cell flow cytometry gating strategy. (A) Myeloid gating strategy: live immune cells were gated based on positive expression of CD45 and absence of viability

dye signal. Single cells were then identified using SSC-W vs SSC-A gating. Total myeloid cells were selected based on CD11b expression and then subdivided into neutrophils and other myeloid cells based on Ly6G gating. Within the remaining myeloid cells, macrophages and monocytes were identified using F4/80 vs Ly6C gating. **(B)** Lymphoid gating strategy: single live immune cells were identified as described above and then T cells were identified based on the co-expression of CD3 and CD4 or CD3 and CD8. CD4+ T cells were further subdivided into conventional CD4+ T cells or regulatory T cells based on FoxP3 expression. Effector T cells were identified by gating single or dual expression of TNF-α and IFN-γ within CD3+CD4+FoxP3- or CD3+CD8+ cells **(C)** B cell gating strategy: Live immune cells were identified as before and then B cells were identified based on expression of CD19 and lack of CD3 expression. Activated B cells were identified based on positive Ki67 expression and absence of IgD expression.

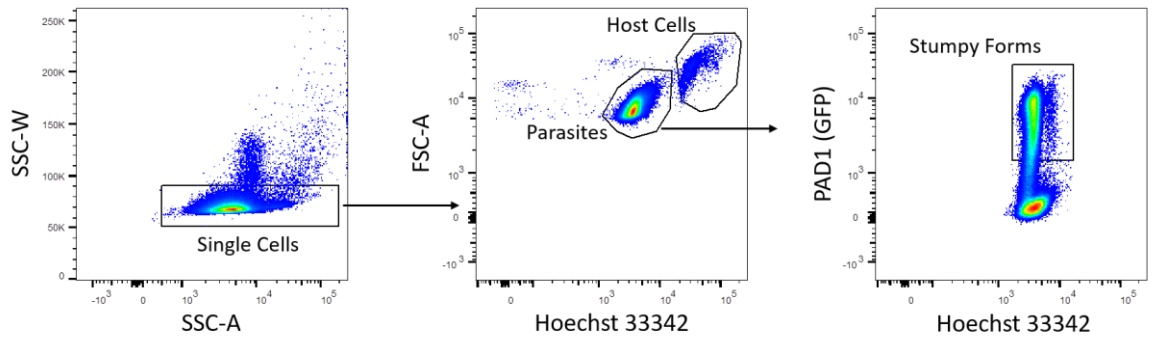

Figure 8 – Parasite flow cytometry gating strategy. Single cells were identified using SSC-W vs SSC-A gating. Parasites and host cells were then differentiated based on Hoechst 33342 intensity. Stumpy forms of the parasite were identified based on PAD1 (GFP) expression.

Soluble VSG isolation and identification

Approximately 5x10^8 AnTat1.1E parasites cultured in HMI-11 were centrifuged at 2500g at 4°C for 10 min and washed twice in trypanosome dilution buffer (TDB). Trypanosomes were then resuspended and incubated for 3 min at 37°C in 3 mL of 10mM sodium phosphate (NaH2PO4) buffer pH 8.0 containing a protease inhibitor cocktail (P8340, Sigma). Cells were then incubated for 3 min on an ice water bath, centrifuged at 4000g for 5 min and the supernatant purified through a diethylaminoethyl Sepharose column (GE Healthcare). Protein quantification was performed using a BCA Protein Assay Kit (A53225, Thermo Fisher Scientific Inc.) according to the manufacturer's instructions.

The protein sample was run through SDS-PAGE, stained with Coomassie blue and the protein band of interest was isolated, destained, reduced, alkylated and digested with trypsin (Promega) overnight at 37°C. The tryptic peptides were desalted and

concentrated using POROS C18 (Empore, 3M) and eluted directly onto the MALDI plate using 1 µL of in 50% (v/v) acetonitrile and 5% (v/v) formic acid. The data were acquired in positive reflector MS and MS/MS modes using a 5800 MALDI-TOF/TOF (AB Sciex) mass spectrometer and using TOF/TOF Series Explorer software v.4.1.0 (Applied Biosystems). External calibration was performed using a CalMix5 standard (Protea). The 25 most intense precursor ions from the MS spectra were selected for MS/MS analysis. The raw MS and MS/MS data were analysed using Protein Pilot software v.4.5 (ABSciex) with the Mascot search engine (MOWSE algorithm). For the search parameters were as follows: monoisotopic peptide mass values were considered, maximum precursor mass tolerance (MS) of 50 ppm and a maximum fragment mass tolerance (MS/MS) of 0.3 Da. The search was performed against the SwissProt protein sequence database without taxonomy restriction. Carboxyamidomethylation of cysteines was set as fixed modifications, oxidation of methionines and N-Pyro Glu of the N-terminal Q were set as variable modifications. Protein identification was accepted only when significant protein homology scores were obtained ($P < 0.05$) and at least one peptide was fragmented with a significant individual ion score ($P < 0.05$). The MS data were generated by the Mass Spectrometry Unit (UniMS), ITQB/iBET, Oeiras, Portugal.

Antibody quantification

Antigen-specific antibody titers were determined by ELISA. Assay plates (423501, BioLegend) were coated overnight with 2 µg/mL purified VSG AnTat1.1 (10 mM sodium phosphate buffer, pH 8.0) at 4°C. Assay plates were blocked with blocking buffer (3% BSA in PBS with 0.05% Tween20). Secondary antibody solutions were prepared by diluting 1:1000 anti-mouse IgM-HRP (lab0372, Covalab), anti-mouse IgG-HRP (lab0365, Covalab) and anti-mouse IgA-biotin (clone RMA-1, BioLegend). Wells with biotinylated antibodies were incubated with SAv-HRP (BioLegend). Assay plates were developed with TMB substrate set (BioLegend), subsequently stopped with a 1M sulfuric acid solution and the OD 450 nm values were read in a TECAN Infinite M200 microplate reader using 570 nm as the reference wavelength. All washing steps were performed with PBS with 0.05% Tween20. The OD cut-off value used for antibody titer was determined according to the formula [Cut-off = Xneg+ 0.13(Xpos)], where Xneg is the average of the assay wells loaded with PBS and Xpos is the average of the wells loaded with the most concentrated samples

from mice infected for 9 days Antibody titers for AT, kidney and spleen were normalized to the organ masses used to prepare cell-free suspensions.

RNA isolation and RNA-Seq analysis

Mice infected for 0, 6 and 26 days were euthanized and perfused, gonadal fat depots were collected, RNA extracted by TRIzol (Invitrogen) and its integrity assessed by TapeStation (Agilent). Poly-A mRNA library was prepared as recommended by the manufacturer (Illumina TruSeq) and the samples were sequenced in Illumina HiSeq2000 platform (EMBL and BGI). Sequenced reads were 49bp single-end for samples D0.1, D6.1, D26.1 and D26.2 and 100bp paired-end for the remaining ones. To reduce differences between single and paired-end RNA-Seq datasets, the second read of each mate-pair in paired-end samples was discarded. Also, the first read of each mate-pair was trimmed to the first 49 bases using Trimmomatic (version 0.38)[192].

Read quality was evaluated with FastQC quality control tool (version 0.11.5)[193] and raw reads were trimmed to improve mapping with SolexaQA (version 3.1.7.1)[194]. First, reads were cropped to their longest continuous segment whose PHRED score was higher than 28 and then reads smaller than 25 bp were discarded. Trimmed reads were aligned to the *T. brucei* TREU927 genome (TriTrypDB version 33)[195] using HISAT2 (version 2.0.0-beta)[196] without spliced alignments. Reads mapping to *T. brucei* were discarded and the unmapped reads aligned to the M. musculus genome (GRCm38 release 92)[197] using HISAT2 with default parameters. Unique read counts were computed using featureCounts (version 1.6.2)[198] and lowly expressed genes were discarded by keeping genes having a minimum of 10 read counts in at least 2 replicates of the same condition (D0, D6 or D26). In total, 19,488 genes were used to perform differential expression analysis by DESeq2 (version 1.18.1)[199], edgeR (version 3.20.9)[200] and limma (version 3.34.9)[201] from Bioconductor (version 3.5)[202] in the R software environment (version 3.4.4)[203]. Genes having an adjusted p-value < 0.01 in at least 2 algorithms and a fold-change > 2 in all were considered differentially expressed.

GO term overrepresentation on differentially expressed genes was performed with the topGO (version 2.30.1)[204] R package, using the weight01 algorithm and Fisher's exact test (p-value < 0.01) for terms with at least 5 annotated genes.

Heat maps were created using the package ComplexHeatmap (version 1.17.1)[205] and ggplot2 (version 3.0.0)[206] was used to create the remaining plots.

Relative immune cell compositions in infected AT were estimated with seq-ImmuCC deconvolution tool[207]. As in differential expression analysis, only genes having a minimum of 10 read counts in at least 2 replicates of the same condition were used. Then, read counts were processed following the authors script in Github[207]: the read counts of each V, D and J gene segments in both T and B cell receptors merged and a quantile normalization performed. The quantile normalized read counts were uploaded in ImmuCC server using the SVR algorithm.

RNA-Seq data from the samples of day 6 post-infection AT were made publicly available in the ArrayExpress database under the accession number E-MTAB-4061. The remaining RNA-Seq sequence data have also been submitted to the ArrayExpress database under the accession number E-MTAB-7596.

Statistical analysis

The values presented are mean ± SEM. Parasite and immune cell numbers were transformed into their respective Log base 10 values to achieve linearization prior to statistical analysis. Statistical differences were assessed using two-way ANOVA and one-way ANOVA with Sidak's test for multiple comparisons. P values lower than 0.05 were considered to be statistically significant.

Part 1: Adipose tissue immunity during a *T. brucei* infection

Results of Part 1

The results presented in this section were generated in part by Tiago Bizarra Rebelo and others and are partially included in his MSc thesis under the name "Deciphering parasite persistence in adipose tissue", available at: https://repositorio.ul.pt/handle/10451/31880. A detailed list of my contributions to this part of the work is available in the annexes section of this document.

The relevance of tissue invasion and colonization by *T. brucei* is only now being elucidated in the context of pathogenesis, persistence, and drug resistance. Each tissue presents a specific immune environment that may impact a pathogen's ability to colonize and persist in each anatomical location. The increasing evidence of persistence of evolutionarily diverse pathogens in the AT raises the question of its immune competence. Given the extensive accumulation of *T. brucei* in the AT we sought to elucidate whether an effective immune response was mounted in this tissue and how different it was from the better described systemic responses observed in the blood and spleen (where the parasites also reside).

1. Transcriptome of infected adipose tissue reveals a strong inflammatory response

A local immune response typically consists in the accumulation of myeloid and lymphoid cells sensing determinants of inflammation and/or determinants specific to the pathogen in order to control the infection and regulate the immune response itself. Given that the signature profile of immune cells is unique and different from all other resident cells of AT (adipocytes, endothelial cells, and mesenchymal stromal cells)[208,209], we postulated that a transcriptome analysis of infected versus non-infected AT should provide a first glimpse of the type of immune response that is mounted in this tissue.

We performed RNA sequencing (RNA-Seq) analysis of mice gonadal AT depots at early and late stages of infection. Total RNA was extracted from this tissue at day 0 (n = 3), 6 (n = 3) and 26 (n = 2) post-infection. Most sequence reads mapped to the mouse genome (between 86% and 96%) and the 1%-10% of reads that mapped to the parasite were not considered in this analysis (S1 Table, annex).

Unbiased clustering of the expression profiles of the analysed samples showed that non-infected and infected AT clustered separately. Furthermore, the cluster of infected AT was divided in 2 sub-clusters separating samples of early and late infection time points (Fig. 9A). This indicates significant alterations of transcript abundances in AT upon and during a *T. brucei* infection. To identify the genes differentially expressed, we used three distinct algorithms. Genes significant in at

least 2 of them (adjusted p-value < 0.01) and having a fold-change higher than 2 were considered differentially expressed.

At day 6 post-infection, 2678 genes were differentially expressed compared with non-infected AT. From these, 1770 genes were upregulated while the remaining 908 were downregulated at day 6 post-infection (S1C File, annex). When comparing AT at day 26 post-infection with non-infected AT, 3684 genes were differentially expressed, from which 2264 were upregulated and 1420 downregulated (S1D File, annex).

Between AT at day 6 and day 26 post-infection, we identified 941 differentially expressed genes, 503 upregulated and 438 downregulated at day 26 post-infection (S1E File, annex).Gene ontology (GO) enrichment analysis was conducted to determine which GO terms were over-represented among the differentially expressed genes (Fisher's exact test, p-value < 0.01).

Enrichment tests on the upregulated genes in infected AT (both on day 6 and day 26 versus day 0) revealed a strong inflammatory profile, with 84.7% of the top 150 (127/150) most significant Biological Process GO-terms related to immunity (Fig. 9B and S2 File, annex). Also, the median fold-change of the genes associated to the top 20 Biological Process GO-terms in infected versus non-infected AT (p-value < $1x10^{-5}$) increased from day 6 to day 26 (Fig. 9C), suggesting that the immune response taking place in AT increases in magnitude as infection progresses.

Conversely, most downregulated genes were involved in metabolite biosynthesis (*e.g.* fatty acid biosynthetic processes) and other metabolic changes (*e.g.* fatty acid beta-oxidation) (S1 and S2D and S2E Files, annex).

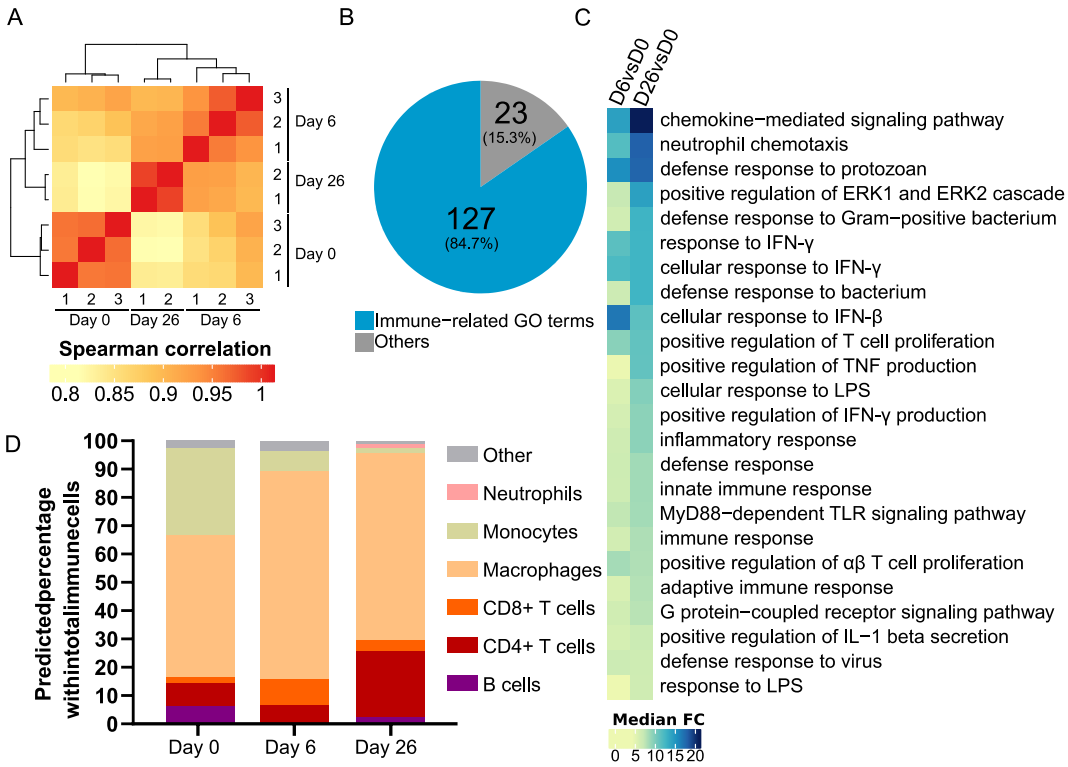

Figure 9 - Transcriptome of *T. brucei* infected AT shows a strong immune response. **(A)** Heat map of hierarchical clustering of Spearman correlations of Reads per kilobase per million mapped reads (RPKM) levels from non-infected (D0), n = 3 and infected AT at early (D6), n = 3 and late (D26), n = 2 time points. **(B)** Pie chart of most significant biological processes GO term families. **(C)** Heat map view of median fold change (FC) of genes associated to the top 20 Biological Process GO terms in day 6 and day 26 of infection versus non-infected AT (D6 vs D0 and D26 vs D0, respectively) **(D)** Prediction of immune cell distribution based on immuCC RNA-seq deconvolution.

Interestingly, differential expression analysis showed a marked and significant upregulation of T helper 1 (Th1) signature genes (*e.g. Tbx21*, *Eomes*, *Il12r1b*, *Ifng*, *Tnf*, *Nos2*, *Stat1*, *Stat4*) both on day 6 and day 26 versus day 0 (Fig. 10 and S1C and S1D File, annex), which are associated with a protective immune response against *T. brucei*. This profile was not observed for non-protective Th2 response associated genes (*e.g. Gata3*, *Il4*, *Il5*, *Il13*, *Stat5*, *Stat6*), which were either not detected or not differentially expressed in all conditions assessed (Fig. 10 and S1 File, annex). In addition to Th1 signature genes, the infected AT showed an overall upregulation of pro-inflammatory genes such as *Gzma*, *Gzmb*, *Il1a* and *Il6* (Fig. 10). In turn, this was accompanied by the upregulation of genes such as *Il10*, *Il10ra*,

Ctla4, *Foxp3* and *Pdcd1*, which are associated with the suppression of an active immune response (Fig. 10).

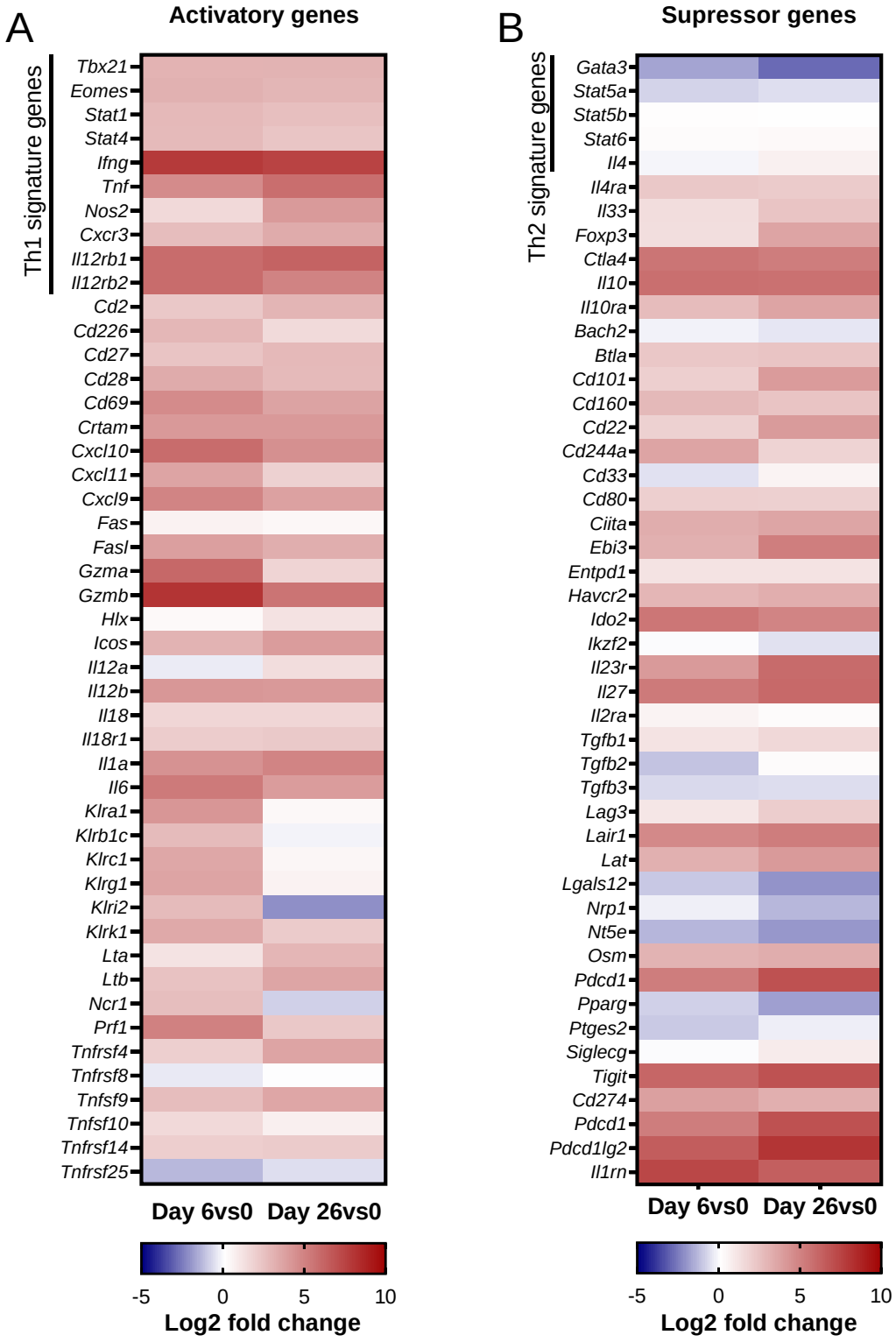

Figure 10 - Immune activatory and suppressive transcriptomic signature. Heat map of the differential expression of genes associated with immune response **(A)** activation and **(B)** suppression at days 6 and 26 post-infection relative to non-infected. Gene expression change in Log2 units is denoted in red for up-regulation and in blue for down-regulation.

To assess whether the changes in transcriptomic profile of the AT could be due to an alteration of the cellular makeover of the tissue, we performed a cellular deconvolution analysis using the immuCC algorithm[207]. This analysis predicted that during a *T. brucei* infection the relative proportions of innate and adaptive immune cells were variable (Fig. 9D). Specifically, these data predicted a relative increase of macrophages and CD8+ T cells between days 0 and 6 post-infection, while the prediction for monocytes and B cells was a relative decrease in the same period. Lastly, by day 26 post-infection this deconvolution model predicted a sizeable increase of the CD4+ T cell response, with a predicted 3 to 4-fold relative increase when compared to days 0 and 6 post-infection. Overall, the transcriptome of the AT of infected mice revealed signs of intense inflammation and an ongoing active immune response.

2. Adipose tissue shows a gradual accumulation of immune cells during infection.

Bulk RNA-seq provides a strong indication of broad changes in the inflammatory profile immune cell milieu of the AT, however it does not allow to identify the absolute accumulation of immune cells and determine their selective *in situ* effector functions. To investigate this, and to compare the extent of systemic to AT immune responses, we quantified the number of parasites and immune cells in the spleen and the AT. The spleen was used as a proxy for the systemic immune response as it filters bloodborne pathogens and is a major site for lymphocyte activation and proliferation. Quantifications were performed at key time-points of the murine *T. brucei* infection, encompassing the formation and resolution of the first and second peaks of parasitemia as well as the chronic stage of infection.

In the blood, the progression of parasitemia throughout infection exhibited its characteristic pattern (Fig. 11A): a first peak around day 5 post-infection; undetectable parasitemia between days 9 and 13 post-infection; followed by a fluctuating number of parasites that differs in each mouse until day 28 post-infection. In the spleen, the number of parasites reached the peak at day 5 post-infection and dropped 32-fold from 6 to 9 days post-infection, when the lowest parasite load was detected (Fig. 11B).

From day 14 post-infection, the number of parasites fluctuated at around 10^5 parasites per organ. Remarkably, in the gonadal AT, the number of parasites peaked at day 6 post-infection (one day later than in blood/spleen) and it suffered only a 6-fold reduction from 6 to 9 days post-infection (Fig. 11B). From day 14 post-infection onward, the number of parasites fluctuated at around 10^6 parasites, which is an approximate constant 10-fold more than in the spleen or any other organ assessed, as we have previously reported[19].

At the same key time-points of infection, immune cells from spleen and AT were analysed by flow cytometry. Using an anti-CD45 antibody to gate all immune cells (Fig. 7), we observed a striking gradual accumulation in the gonadal AT with a 16-fold increase in the number of immune cells per tissue from days 0 to 28 post-infection (Fig. 11C). Conversely, and despite a large increase in spleen mass (Fig. 14A), no significant changes were observed in the total number of splenic immune cells. This suggests that the increase in spleen weight may be largely due to the accumulation of damaged red blood cells undergoing eythrophagocytosis[210], which is known to occur during *T. brucei*-induced anemia[211]. Interestingly, while the number of parasites in the AT peaks on day 6 post-infection and oscillates afterwards, the immune cells are recruited and/or proliferate in AT with different dynamics, increasing steadily as infection progresses. The fact that the spleen has a higher proportion of immune cells than the AT is not surprising due to its nature as a secondary lymphoid organ.

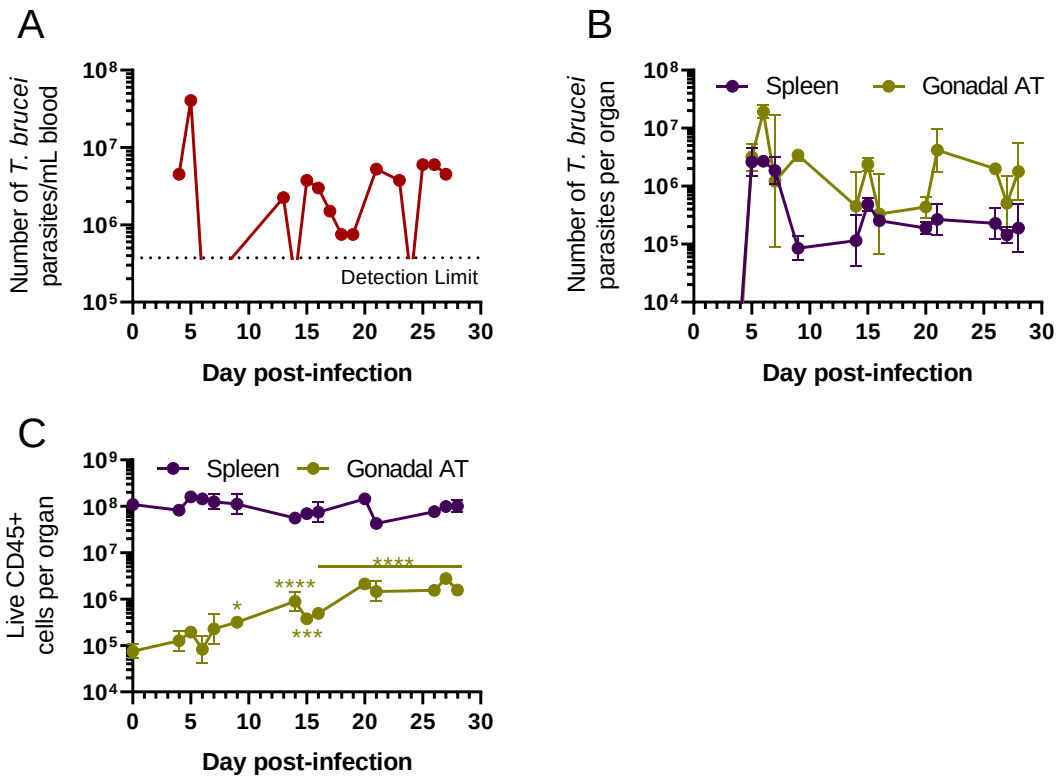

Figure 11 - Dynamics of *T. brucei* parasites and immune cells throughout infection. **(A)** Number of *T. brucei* parasites per mL of blood of a single representative mouse, quantified using a hemocytometer. Dashed line represents the detection limit ($3.75x10^5$ parasites/mL of blood). **(B)** Total number of *T. brucei* parasites in the spleen and gonadal AT, quantified by qPCR. **(C)** Number of live immune cells in spleen and gonadal AT. **(B-C)** Error bars represent the standard error of the mean (SEM) (n = 2–6 mice per group). Statistical analysis was performed with a two-way analysis of variance (ANOVA) using Sidak's test for multiple comparisons. * refers to statistical differences within the groups in each time-point and the non-infected group. *, P<0.05; **, P<0.01; ***, P<0.001; ****, P<0.0001.

To assess the distribution of the inflammatory cell infiltrates and the morphological changes of the AT, we performed immunohistochemistry for parasites (anti-VSG antibody), macrophages (anti-F4/80 antibody) and T cells (anti-CD3 antibody) in sections of gonadal AT on days 6 and 26 post-infection. Consistent with the analysis by flow cytometry, a significant increase was observed in the number of infiltrating macrophages and T cells, mainly during the later time-points of infection (Fig. 12A). Inflammatory cells were distributed diffusely in the tissue, often associated with parasites or parasite debris. By transmission electron microscopy (TEM), parasites were also detected intracellularly, in the cytoplasm of phagocytes (most likely macrophages) (Fig. 12B).

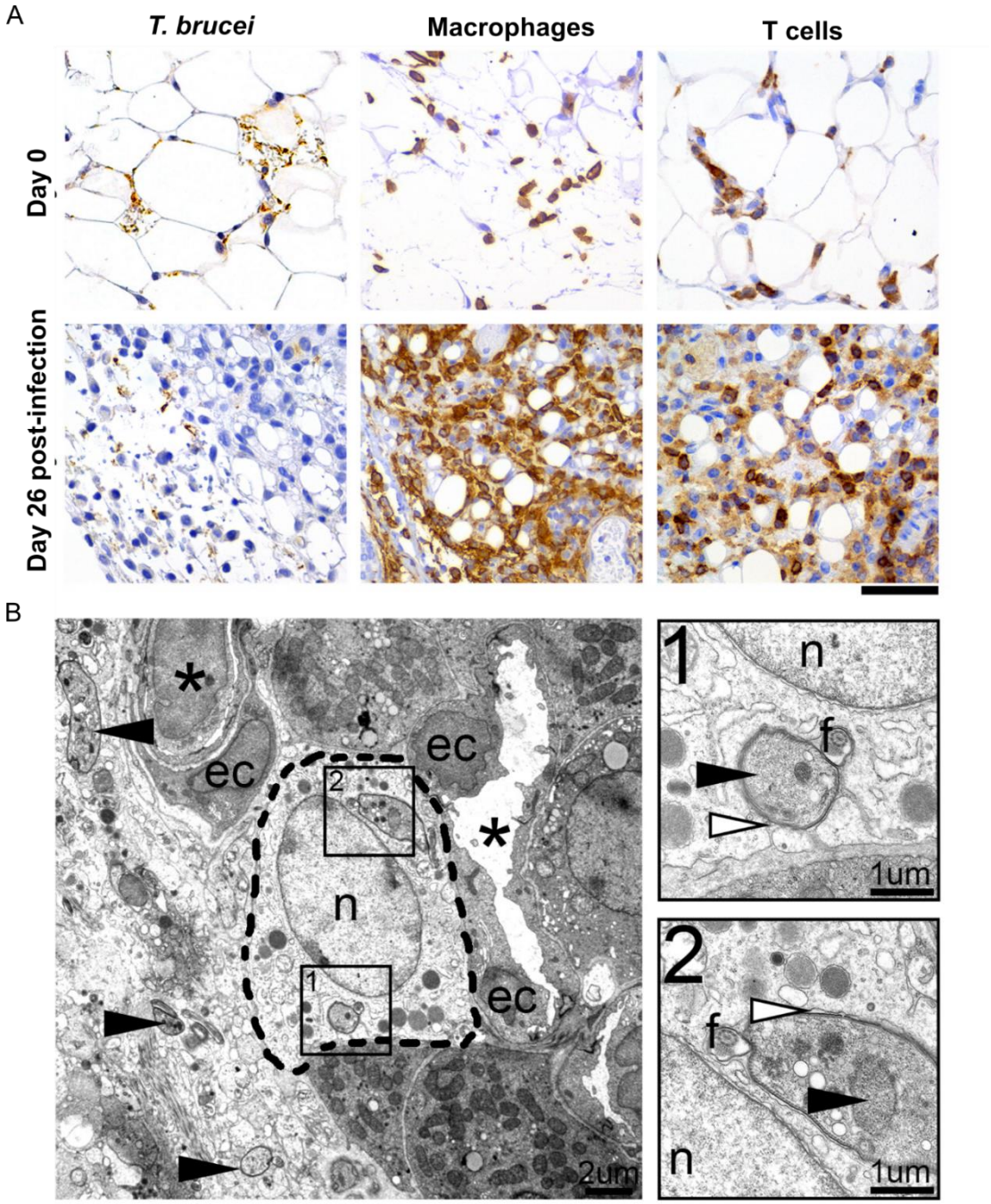

Figure 12- Inflammatory cell response in the adipose tissue. **(A)** Immunohistochemistry reveals a large number of *T. brucei* parasites (anti-VSG antibody) accompanied by marked infiltration by macrophages (anti-F4/80 antibody) and moderate infiltration by T cells (anti-CD3 antibody), at a later stage post-infection (day 26). (n = 4–6 per time-point); DAB counterstained with hematoxylin, original magnification 40x (Scale bar, 50µm). **(B).** Representative electron micrograph of the perirenal adipose tissue of the mouse, 26 days post-infection, showing various extracellular tangential and cross-sectional profiles of trypanosomes (arrowhead) and also intracellular parasites, in the cytoplasm of a phagocyte [most probably a macrophage (inside dashed line)]. Asterisk, vessel; ec, endothelial cell; n, nucleus, f, flagellum. **B-1, B-2.** Insets of the phagocytized trypanosomes, with well-defined nucleus (black arrowhead) and pseudopodia (white arrowhead), consisting of multiple membranous whorls extended by the phagocyte around the parasite.

These intracellular parasites were often surrounded by membranous whorls, suggesting they had been phagocytosed. In conclusion, our analysis shows that the AT is not an immune silent tissue, but instead that it actively responds to a *T. brucei* infection. It is important to mention that these data were acquired in an intraperitoneal infection model and that Tsetse fly transmitted or intradermally injected *T. brucei* may lead to significant differences in immune response.

3. Adipose tissue is populated by effector innate and adaptive immune cells

To experimentally characterize the immune response that is mounted against *T. brucei* in the AT, we isolated gonadal fat pads and spleen of infected animals at different time-points of the infection, and we identified and quantified the main immune cell subsets by flow cytometry. On the one hand we followed the dynamics of neutrophils, monocytes, and macrophages to assess the innate myeloid immunity branch. On the other hand, to assess the adaptive immunity branch, we followed T cell subsets (helper T cells (CD4+) and killer T cells (CD8+)) and evaluated whether these T cells were activated and responding to the infection by assessing their expression of two main pro-inflammatory cytokines, IFN-γ and TNF-α. Additionally, we analysed the frequency of Treg cells, a key immunosuppressive subset. The gating strategies for all the populations are presented in the Figure 7.

As infection progressed, while the total number of immune cells of all subtypes assessed increased in the AT, the same was not observed for the spleen (Fig. 13). As expected for the innate immune response, neutrophils (Fig. 13A) and monocytes (Fig. 13B) are the first to be recruited to the AT, presenting an increase of 68-fold and 49-fold from days 6 to 9 post-infection, respectively.

Few neutrophils were detected in the gonadal AT prior to infection with $8.45x10^2$ cells, however they increased nearly 100-fold by day 28 post-infection (Fig. 13A). Similarly, the number of neutrophils in the spleen increased significantly, presenting a 38-fold increase from days 0 to 28 post-infection (Fig. 13A). Prior to infection, few monocytes were present in the spleen and AT. During *T. brucei* infection, monocytes

accumulated in both tissues, increasing 39-fold in the spleen and 12-fold in the gonadal AT by day 28 post-infection (Fig. 13B).

Macrophages were the most abundant myeloid population in both tissues in control mice. Interestingly, this population was kept at relatively stable numbers throughout infection in the spleen, as the only significant change observed was a moderate 2.7-fold increase by day 28 post-infection (Fig. 13C). In the gonadal AT, the number of macrophages was significantly increased from day 20 post-infection onward, presenting a 10-fold increase by day 28 post-infection (Fig. 13C). CD4+ and CD8+ T cell subsets showed a similar overall increase in the AT, while the spleen showed no changes in CD4+ T cells and an overall decrease for CD8+ T cells (Fig. 14B and 14C).

Within the total pool of T cells, we assessed the fraction that differentiated into effector T cells expressing IFN-γ, TNF-α or both pro-inflammatory cytokines. During the infection, we observed that the number of effector CD4+ T cells presented a modest incremental trend in the spleen, reaching a 3.8-fold increase by day 28 post-infection (Fig. 13D). A higher relative increase in effector CD4+ T cells was observed in gonadal AT, with significant accumulation from day 14 post-infection onwards, showing a 14.6-fold increase by day 28 post-infection (Fig. 13D).

A distinct profile between the spleen and gonadal AT was observed for effector CD8+ T cells. There was a trend for a modest reduction in number of this effector cell in the spleen (Fig. 13E). In contrast, a significant increase in the number of effector CD8+ T cells in the gonadal AT was observed from day 16 post-infection onwards, reaching a 8.7-fold increase by day 28 post-infection. This profile of effector T cells is in agreement with the high expression of TNF-α and IFN-γ in gonadal AT revealed at the transcriptomic level (Fig. 10 and S1C and S1D Files, annex), confirming the accumulation of effector T cells in the AT and propagating a Th1 type of response. The number of Treg cells showed an overall decrease in the spleen while increasing 4-fold in gonadal AT (Fig. 13F), which is in agreement with the increased expression of FOXP3, CTLA-4 and IL-10 at the transcriptomic level (Fig. 10 and S1C and S1D Files, annex).

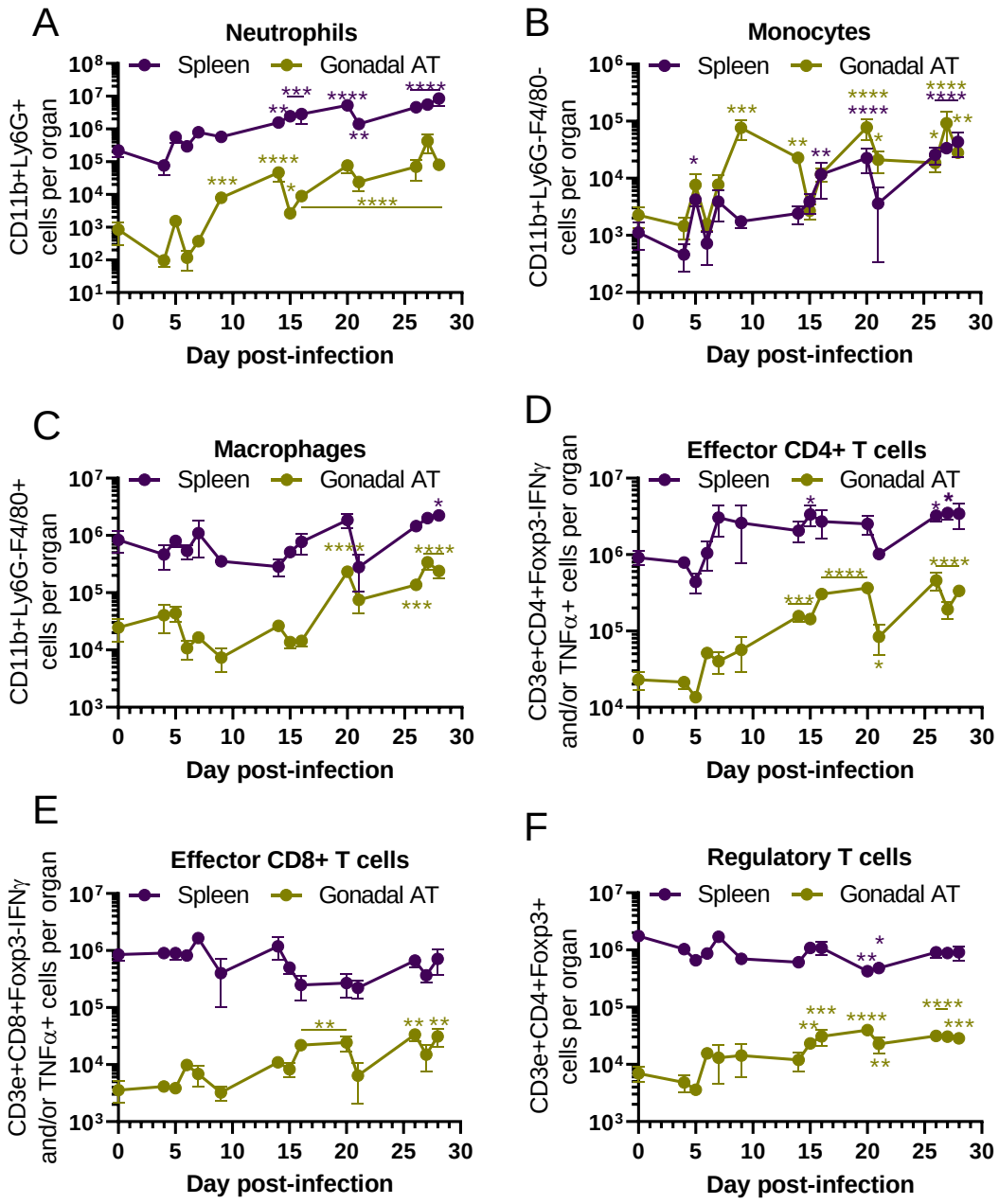

Figure 13 - Dynamics of immune cells during infection. (A-F) Number of **(A)** neutrophils, **(B)** monocytes, **(C)** macrophages, **(D)** effector CD4+ T cells, **(E)** effector CD8+ T cells and **(F)** regulatory T cells in the spleen and gonadal AT. Error bars represent the SEM (n = 2–6 mice per group). Statistical analysis was performed with a two-way ANOVA using Sidak's test for multiple comparisons. * refers to statistical differences within the groups in each time-point and the non-infected group. *, P<0.05; **, P<0.01; ***, P<0.001; ****, P<0.0001.

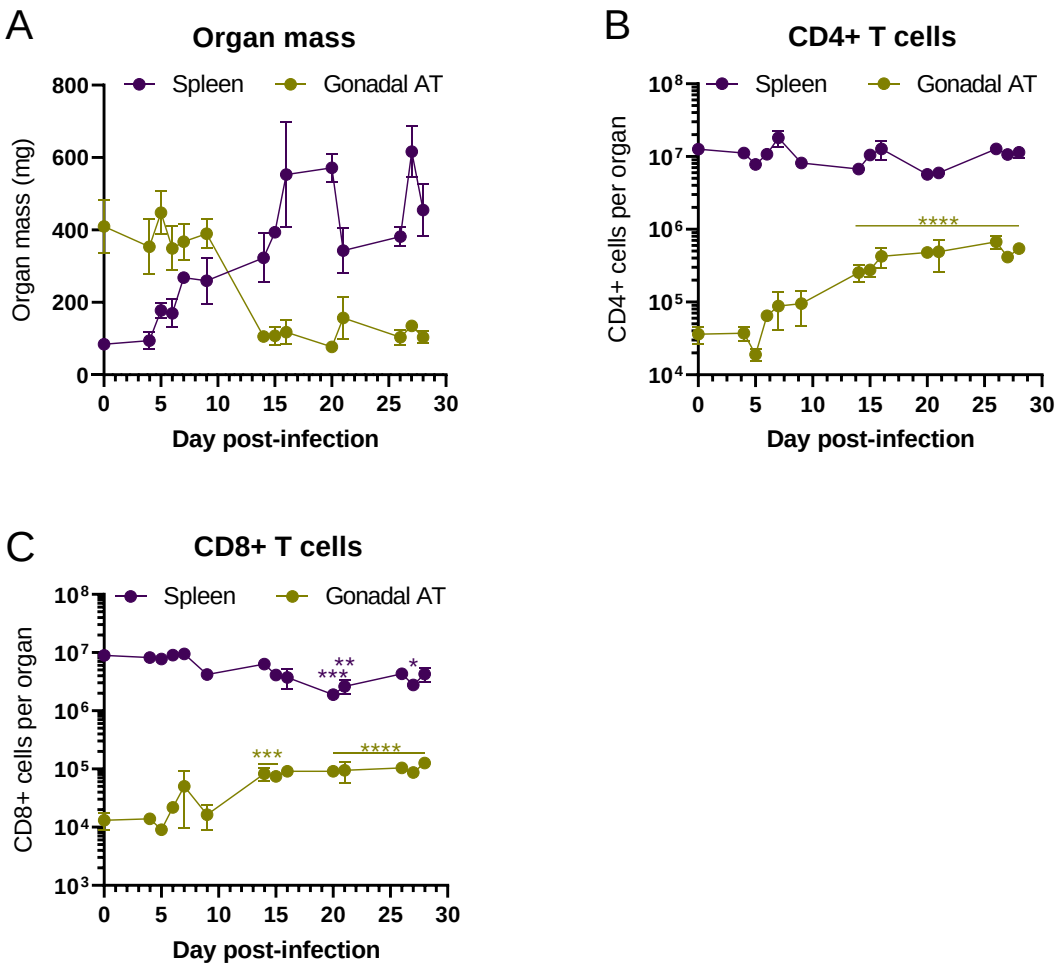

Figure 14 - Organ mass and T cell dynamics. (A) Spleen and gonadal AT mass. **(B)** CD4+ T cells. **(C)** CD8+ T cells. Error bars represent the standard error of the mean (n = 2–6 mice per group). Statistical analysis was performed with a two-way ANOVA using Sidak's test for multiple comparisons. * refers to statistical differences between the group in each time-point and the non-infected group. *, P<0.05; **, P<0.01; ***, P<0.001; ****, P<0.0001.

This suggests that Treg cells recruited to AT may contribute to control an excessive inflammatory response and could favor the persistence of *T. brucei* parasites in AT. This flow cytometry analysis in the AT is mostly consistent with changes observed in transcriptomic data (Fig. 9C) and predicted by immuCC (Fig. 9D). Specifically, we confirmed a similar relative variation for many immune subsets such as CD4+ T cells, CD8+ T cells, monocytes and neutrophils. Macrophages were the only population for which flow cytometry did not confirm the immuCC predictions (Fig. 15). This overestimation of the macrophage population by immuCC could be due to

the fact that immune activation of adipocytes unlocks a gene expression signature that highly resembles that of macrophages[212].

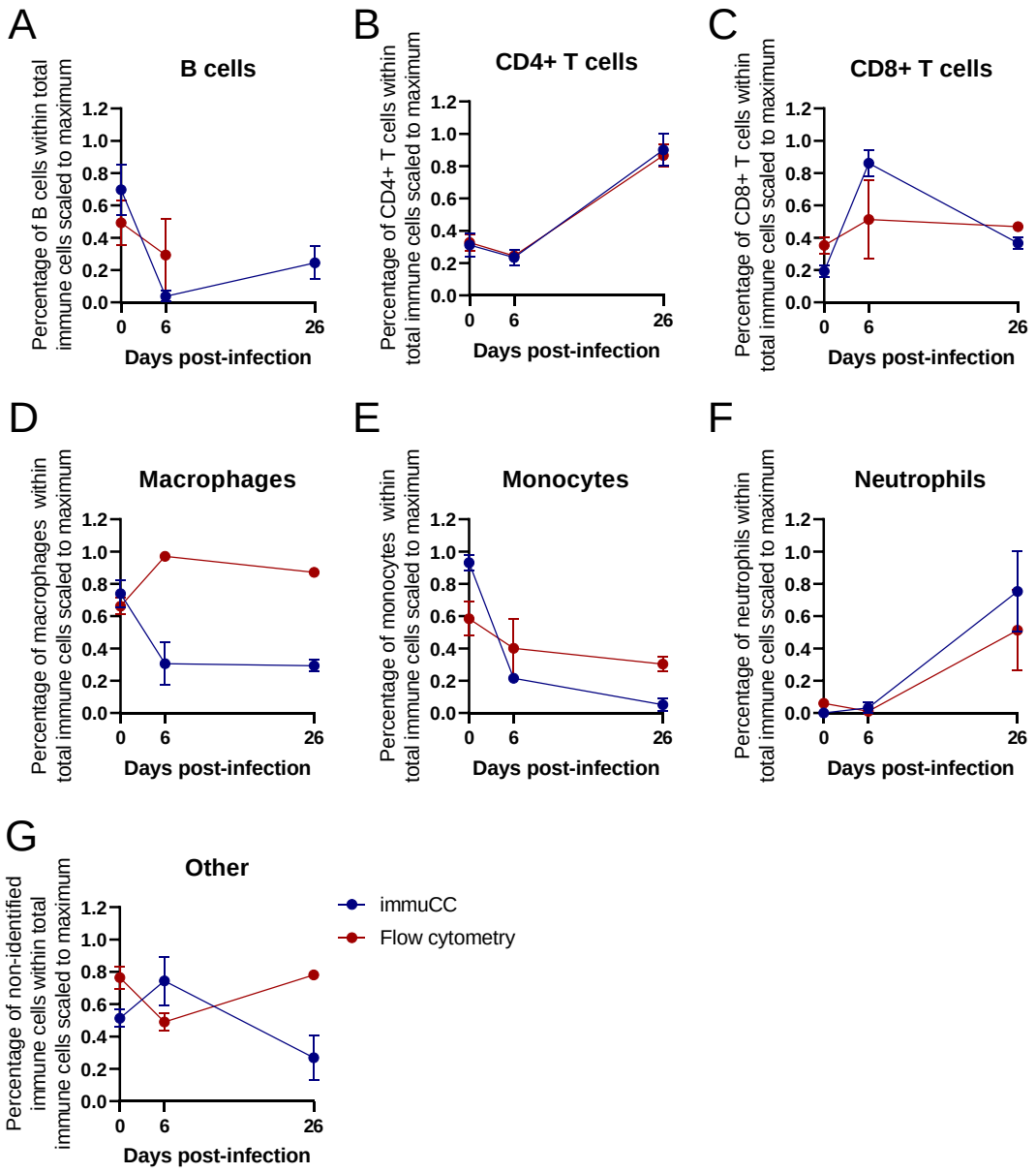

Figure 15 - Comparison of flow cytometry and immuCC data. Variation of immune cell subsets between days 0, 6 and 26 post-infection. Data are scaled between 0 and 1, where 1 corresponds to the highest percent value within each group. **(A)** B cells, **(B)** CD4+ T cells, **(C)** CD8+ T cells, **(D)** Macrophages, **(E)** monocytes, **(F)** neutrophils and **(G)** other immune cells.

Overall, during a *T. brucei* infection the AT accumulates cells of the innate and adaptive immunity branches. Importantly, there is a significant increase of immune cells described as protective against a *T. brucei* infection (*i.e.* IFN-γ+CD4+Th1 cells and macrophages).

4. Adipose tissue presents a strong humoral response

Effective immunity against *T. brucei* requires a humoral immune response in addition to a strong cellular immune response[152]. The importance of antibody-mediated *T. brucei* clearance is well documented. Indeed, B cell and antibody deficiencies lead to increased susceptibility to *T. brucei*[153] and passive transfer of VSG-specific antibodies grants variant-specific protection[164,213].

To assess if a humoral response was ongoing in solid tissues and in AT in particular, we quantified the levels of antigen-specific IgM, IgG and IgA by ELISA, using plates coated with purified VSG AnTat1.1 (Fig. 16). A series of 10-fold dilutions of serum samples and 2-fold dilutions of cell-free suspensions from tissues were tested for anti-VSG AnTat1.1 immunoglobulins. For each sample, the antibody titer was determined as the highest dilution with an OD450nm higher than the cutoff value (0.13x average of positive control + average of negative control) (Fig. 16D)[214].

We collected samples from mice on days 0, 6 and 9 post-infection from the serum (reference of circulating immunoglobulins), spleen (reference of an active site of immunoglobulin production), AT and kidney (an example of low parasitised organ). These time-points were chosen because in wild-type (WT) mice there is a significant drop in AT parasite burden between days 6–9 (Fig. 11B) and we questioned if B cell responses could play a local role.

As expected, circulating antibodies against VSG AnTaT1.1 increased in infected mice when compared to non-infected mice (*i.e.* 10 to 100-fold increase (Fig. 17A). This effect was also observed in the interstitial fluid, albeit in an organ specific manner. Specifically, the antibody titer of IgM in the AT increased upon infection but was lower than in the kidney and spleen at day 6 post-infection (6.6 and 88-fold respectively) and to a lesser extent at day 9 post-infection (4.6 and 6.3-fold). Moreover, the antibody titer for IgG in the AT was similar that of the kidney at day 6 post-infection but was 107-fold lower than that of the spleen. By day 9 post-infection the AT presented a 3-fold lower anti-VSG IgG titer compared to the kidney and 14-fold lower than the spleen. Additionally, anti-VSG IgA was not detected in the AT and presented low titers in the spleen. Interestingly, kidney titers for anti-VSG IgA were high but were independent of infection, as titers from non-infected mice were equally elevated as those of infected mice.

A

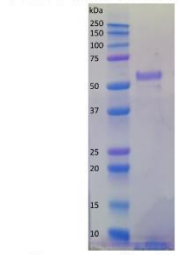

B

```
  1 MVTKERNAAL KIVMLVASAL TLHPQQALAQ TAGRPLADVV GKTLCTYSKT
 51 AKRQAANLAQ TLQRASSAAK QSRQAQQLAA LALAKLPDYK EAAATLLIYA
101 THKIQDAQAS IENWTGENTK LVGQAMYSSG RIDELMLLLE GHREDGANGQ
151 DKTCLGAAAG GNTVNEFVKT ECDTESGHNI EADNSNIGQA ATTLSQESTD
201 PEASGGASCK ITANLATDYD SHANELPLLG GLLTIHNAGG FKTGQSLQTA
251 APTNKLISAL KNKGAGVAAK LATVTSAAPT SKQELKTLLA SKGERAKLQA
301 ANDEYNNWKP GAKPEDFDAH IKKVFGAEDG KDSAYAIALE GISIEAPLGG
351 GQTQNKQLYS MQPKDLMAAL IGTIAELQTA AATKPACPGH KQTTTESDAL
401 CSKIKDANEC NSKHFCSYNG TETDSAKKCK YNATKASASD APVTQAQTTS
451 RSETPAEKCT GKKKDDCKDG CKWEAETCKD SSILLTKNFA LSVVSAALVA
501 LLF
```

C

Protein Hits	Protein Score	Sequence Coverage (%)	Identified Peptides
Variant surface glycoprotein AnTaT 1.1 UniProtKB/Swiss-Prot ID: P06015	376	27	R.QAANLAQTLQR.A R.IDELMLLLEGHR.E R.ASSAAKQSRQAQQLAALALAK.L R.IDELMLLLEGHREDGANGQDK.T K.DLMAALIGTIAELQTAAATKPACPGHK.Q K.LQAANDEYNNWKPGAKPEDFDAHIKK.V K.ITANLATDYDSHANELPLLGGLLTIHNAGGFK.T

D

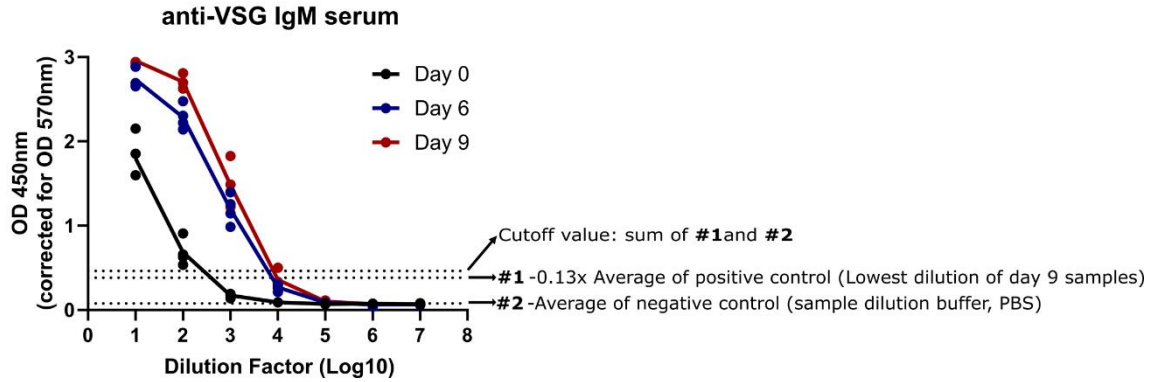

Figure 16 - Purified soluble VSG identification. (A) Coomassie stained SDS-PAGE of purified soluble VSG solution denoting a single preeminent band within the predicted size range of VSG. **(B)** Best peptide match within the SwissProt database (sp|P06015|VSA1_TRYBB, Variant surface glycoprotein AnTaT 1.1 OS = *Trypanosoma brucei brucei* OX = 5702 PE = 2 SV = 1) with matching peptides depicted in bold red. **(C)** Summary of protein identification. Protein score is -10*Log(P), where P is the probability that the observed match is a random event. Protein scores greater than 70 are significant ($p<0.05$). Protein scores are derived from ions scores as a non-probabilistic basis for ranking protein hits. (D) Measurement of anti-VSG IgM titers by ELISA depicting optical density (OD) curves and antibody titer cut off determination.

Next, we assessed whether this humoral response in the AT was accompanied by a local B cell response. There was an increase in the numbers of B cells in spleen and AT (Fig. 17E), as well as an increase in the number of activated, (IgD-CD19+ cells), and proliferating (Ki67+) B cells (Fig. 17F). Specifically, by day 9 post-infection total B cells showed a 3.55-fold increase in the spleen and a 8.45-fold increase in the AT, relative to non-infected controls. This increase was also

observed for activated B cells, as their number presented a 16.29-fold increase in the spleen and a 9.24-fold increase in the AT in the same period. We then assessed whether plasmocytes (*i.e.* main immunoglobulin producing cells) were present in the AT. CD138 (also known as syndecan-1) is an excellent marker of plasmacytic differentiation, however it is sensitive to the collagenase treatment used for flow cytometry analysis of AT digestion, and thus we applied immunohistochemistry to AT (Fig. 17G–17I). Relative to non-infected mice, the number of CD138+ cells increased 3.7-fold and 17.4-fold at days 6 and 9 post-infection, respectively (Fig. 17J), indicating that the AT harbors plasmocytes that secrete immunoglobulins.

Collectively, these data show that a humoral response takes place in the AT and suggest that the increase of immunoglobulin levels is likely the result of the infiltration of circulating immunoglobulins (serum), but also partially due to increased local production by antibody producing plasmocytes in the AT. Altogether, we conclude that the components of a protective immune response against *T. brucei* are present in the AT.

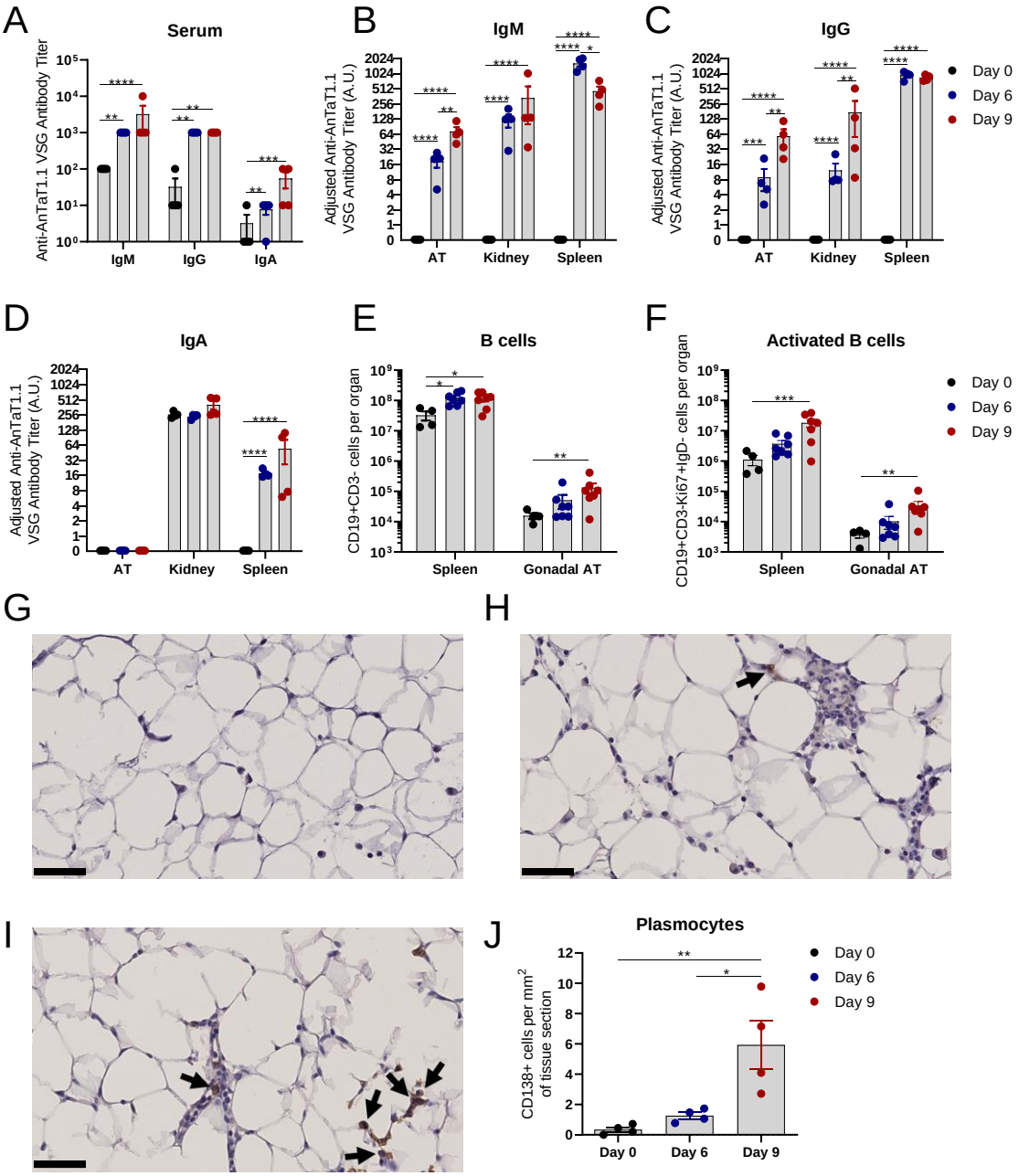

Figure 17 - Dynamics of immunoglobulins, B cells and plasmocytes during infection. **(A)** Antibody titers of anti-AnTaT1.1 VSG in the serum. Antibody titer normalized to tissue mass used to prepare cell-free suspensions in arbitrary units (A.U.) of **(B)** IgM, **(C)** IgG and **(D)** IgA. Number of **(E)** total B cells and **(F)** activated B cells in the spleen and gonadal AT. Immunohistochemistry detection of (anti-CD138 antibody) plasmocytes at days **(G)** 0, **(H)** 6 and **(I)** 9 post-infection. **(J)** Quantification of plasmocytes in tissue sections. **(G-I)** Black arrows indicate CD138+ cells and scale bars represent 50 µm, original magnification 40x. Statistical analysis was performed with **(A-F)** two-way ANOVA and **(J)** one-way ANOVA using Sidak's test for multiple comparisons. *, P<0.05; **, P<0.01; ***, P<0.001; ****, P<0.0001.

5. Parasite load in adipose tissue depends on systemic effectors

Parasites infiltrate and accumulate in the AT, even though a host-protective acute (that turns chronic) immune response is mounted in response to the infectious agent, as revealed by the dramatic accumulation of myeloid cells and lymphoid effector subsets (Fig. 12 and 13). Thus, we decided to undertake a systematic approach and test the importance of several immune cells and soluble factors key in the control of *T. brucei*. For this, we performed infections in several immunocompromised mouse mutants, and collected organs on days 6 and 9 post-infection. Specifically, we infected mice that lack T and B lymphocytes (deficient in the recombination activation gene 2 (*Rag2*-/-)), (Fig. 18A and 18B) mice that lack selectively B lymphocytes (*Jht*-/-) (Fig. 18C and 18D), mice that lack IFN-γ (*Ifng*-/-) (Fig. 18E and 18F), and mice that lack complement component 3 (*C3*-/-) (Fig. 18G and 18H). These cells or factors have been previously implicated in the parasite's elimination. Here, we hypothesized that if one of these factors was ineffective solely in the clearance of parasites in the AT, its absence would have little impact on the elimination of AT parasites, but it would prevent parasite elimination in the blood and other organs.

Upon infection with *T. brucei*, in both *Rag2*-/- and *Jht*-/- mice, parasitemia increased until day 6 post-infection, but instead of undergoing a quick reduction, parasite numbers persisted at very high levels (Fig. 18A and 18C). While WT mice were able to reduce parasite burden from the spleen and AT between days 6 and 9 by roughly 10-fold, neither *Rag2*-/- nor *Jht*-/- showed a significant decrease in the parasite burden of these organs in the same period (Fig. 18B and 18D). These data show that efficient parasite elimination between days 6 and 9 post-infection in the AT requires a B and T cell responses, similarly to parasitemia clearance in the blood.

Given that the infection promoted the generation of a high frequency of IFN-γ-producing CD4+ and CD8+ T effectors in AT (Fig. 13D and 13E), the contribution of IFN-γ was assessed by infecting *Ifng*-/- mice. Unlike WT controls, *Ifng*-/- mice were not able to eliminate parasites from the blood nor from all tested solid tissues (Fig. 18E and 18F). These results suggest that *T. brucei* is controlled by IFN-γ both systemically and within the tissues, highlighting the key role of Th1-dependent immune response in the control of the infection. As previously shown, albeit with

different kinetics[215], mice with defective complement system (*C3*-/-), were able to control the first peak of *T. brucei* parasitemia, suggesting that complement opsonization is not essential in the blood (Fig. 18G) between days 6 and 9 post-infection. These results suggest that the complement system may have a more active role in parasite elimination from some tissues than from the blood. Interestingly, these mutant mice were partially impaired in controlling the number of parasites in the AT, between days 6 and 9 post-infection (4.3-fold reduction vs 32-fold reduction in WT mice) (Fig. 18H). This impairment was also observed in the heart, where *C3*-/- showed virtually no parasite elimination (1.6-fold) whereas WT mice presented an 8.4-fold decrease.

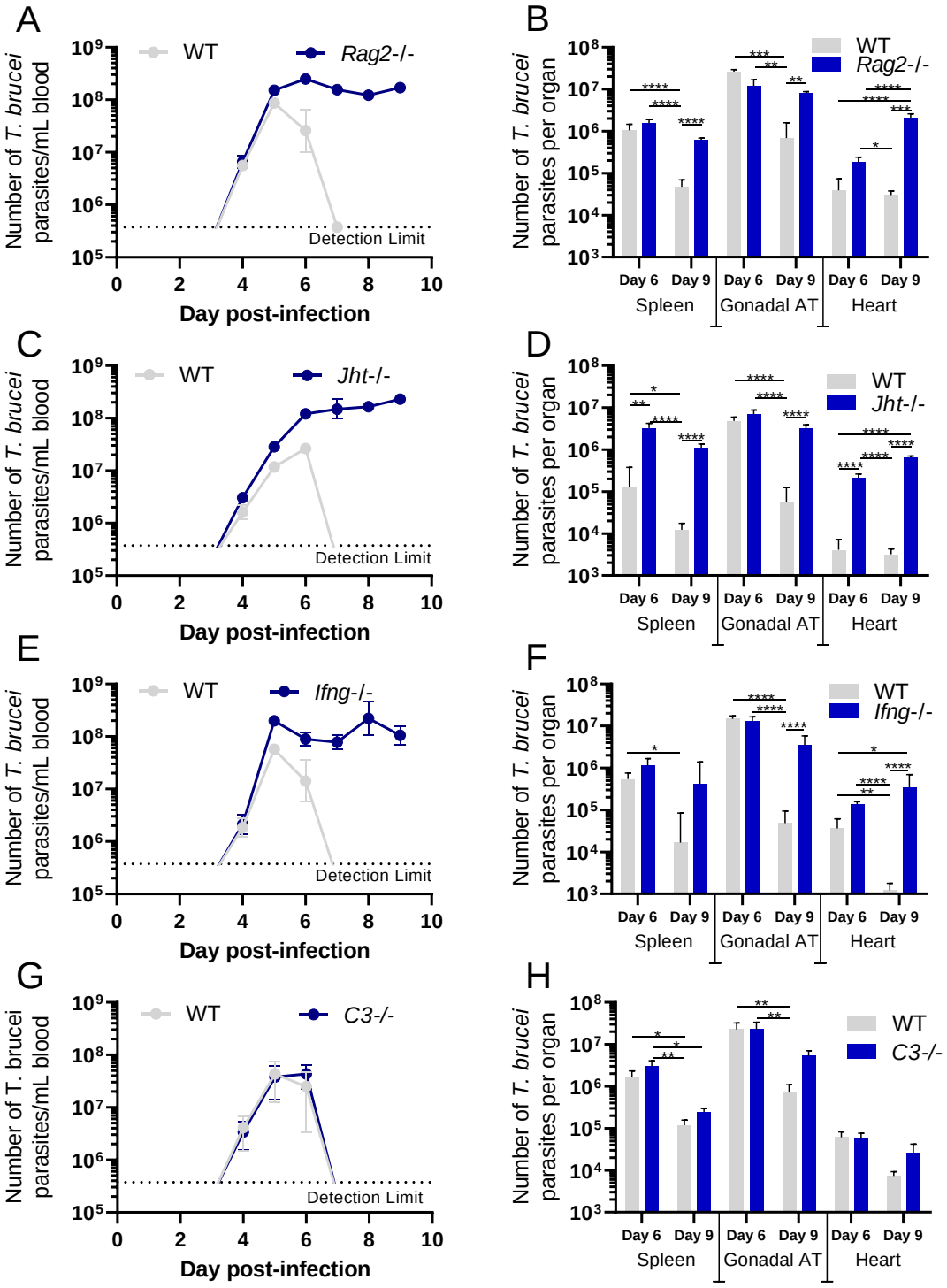

Figure 18 - Assessment of the role of immune cells/factors in parasite control. Infection of WT and **(A-B)** *Rag2-/-*, **(C-D)** *Jht-/-*, **(E-F)** *Ifng-/-*, **(G-H)** *C3-/-* **(A-H)** Error bars represent the SEM (n = 3–7 mice per group). (Left) Parasitemia of mice infected with *T. brucei*, quantified in a hemocytometer. Dashed line represents the limit of detection ($3.75x10^5$ parasites/mL of blood). (Right) Number of *T. brucei* parasites quantified by qPCR in spleen, gonadal AT and heart, 6 and 9 days post-infection. Statistical analysis was

performed with a two-way ANOVA using Sidak's test for multiple comparisons. *, P<0.05; **, P<0.01; ***, P<0.001; ****, P<0.0001.

We then questioned whether an overarching immunosuppressive mechanism was reducing overall parasite clearance and allowing for higher parasite accumulation in the AT, when compared to other organs. Among these, the programmed cell death protein 1 (PD-1) and the programmed cell death ligand 1 (PD-L1) interactions are well described as inhibitors of T cell effector functions in several contexts, including infection[216]. The interaction between PD-1 on the surface of a T cell and PD-L1 on the surface of an antigen presenting cell, leads to the decreased activation, proliferation and cytokine secretion of the T cell. Although we observed by flow cytometry an upregulation of PD-1 in both CD4+ and CD8+ T cells (Fig. 19A and 19B) and in *Pdcd1* gene expression (Fig. 10B and S1C File, annex) during the acute phase of infection, its antibody-mediated blockade failed to enhance parasite clearance in AT (Fig. 19C and 19D).

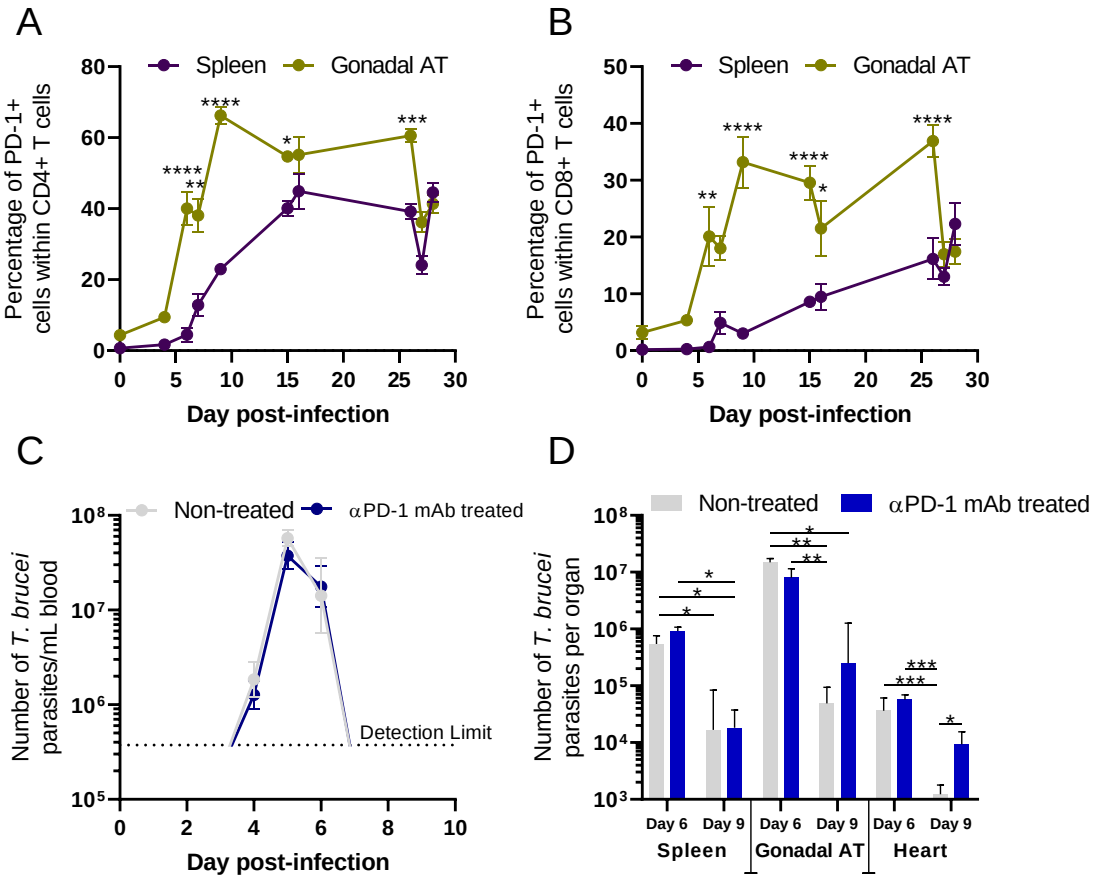

Figure 19 - Assessment of the role of PD-1 expression in parasite control. Percentage of PD1+ **(A)** CD4+ T cells and **(B)** CD8+ T cells. Effect of anti-PD-1 treatment on **(C)** parasitemia of mice infected with *T. brucei*, quantified in a hemocytometer and **(D)** number of *T. brucei* parasites quantified by qPCR in spleen, gonadal AT and heart, 6 and 9 days

post-infection. Error bars represent the SEM (n = 5 mice per group). Statistical analysis was performed with a two-way ANOVA using Sidak's test for multiple comparisons. (A-B) * refers to statistical differences between groups. *, P<0.05; **, P<0.01; ***, P<0.001; ****, P<0.0001

Overall, the infections in immunocompromised mice revealed the parasite burden in the AT depends on several systemic components (B cells, T cells, IFN-γ and complement system). We conclude that the AT does not provide a niche devoid of immune surveillance for *T. brucei*.

Discussion of Part 1

Adipose tissue immunity against *T. brucei*

Here, we show that upon *T. brucei* infection the AT acquires a marked immune transcriptomic phenotype. Within this immune phenotype, a marked Th1 signature is observed, which unlike a Th2 signature, is associated with protection against *T. brucei*. This shift in transcriptomic profile is likely the result of *in situ* activation of resident immune cells as well as of the recruitment of additional immune cells throughout infection. Accordingly, during infection we observed both by immunohistochemistry and flow cytometry a large accumulation of myeloid and lymphoid cells. Indeed, although with distinct kinetics, similar accumulations of neutrophils[217], monocytes[217,218] and T cells[186,219] have been reported for other active sites of *T. brucei*, such as the skin[217], liver[186,218]and brain[219].

Comparison of the AT and spleen leukocyte accumulation kinetics reveals a sharp contrast between these tissues. The AT presents an overall sustained increase throughout time of all the immune cell types assessed. While starting with a much higher number of immune cells, the spleen shows an overall maintenance of the total number of immune cells (Fig. 11C). This maintenance of the total number of splenic immune cells does not represent a static immune environment and it is in fact the result of opposing variations in individual immune subsets.

Among the few similarities found between the spleen and AT is the overall increase in monocyte and neutrophil numbers (Fig. 13A and 13B), which is in accordance with previously published data for the spleen[220]. Although an active immune response is taking place in both the spleen and AT, the differences in their immune kinetics, especially in the T cell compartment, suggest that parasites in the spleen and in AT may be subjected to distinct immune responses.

The immune response mounted in the AT is likely to actively participate in the reduction of the number of parasites. Classically, parasites are described to be eliminated by antibody-dependent phagocytosis that can be assisted by IgM-mediated complement opsonization[140].

Our observation by TEM of phagocytosed parasites in the AT suggests that local elimination of the parasite is ongoing. This phagocytic clearance is consistent with the accumulation of antigen-specific IgM and IgG (Fig. 17B and 17C) in the tissue,

and macrophages that are activated by innate signals delivered by the presence of the parasite as well as adaptive signals such as the local production of IFN-γ by CD4+ Th1 cells (Fig. 13D). This is supported by the observed abrogation of parasite clearance from the AT in infected mice deficient for T and/or B cells, or IFN-γ (Fig. 18).

Given the hyperparasitemia presented by these mutant mice, we cannot exclude the possibility that the high number of parasites in AT 9 days post-infection is partially due to a spill in effect from circulating parasites (although in some mutants and in some organs a tendency for higher parasite load is already detectable 6 days post-infection). However, the inability to remove immune cells/factors exclusively from the AT prevents the study of the contribution of circulating parasites that may excessively cross into tissues.

The dynamics of anti-VSG immunoglobulins show a protective humoral response in the AT, although at significantly lower levels than the spleen. Compared to the kidney, the AT shows comparable anti-VSG IgG titers and modestly lower IgM titers. Interestingly, while the AT shows no detectable anti-VSG IgA titer, the kidney has elevated titers even in non-infected mice. These are likely natural polyreactive IgAs[221] whose relevance in Trypanosomiasis, if any, remains to be elucidated. Although our data show the presence of plasmocytes and thus suggest that local immunoglobulin production in the AT is likely occurring (Fig. 17G–17J), how important this production is for the overall humoral response requires further investigation.

The observation that *C3*$^{-/-}$ mice are not as efficient at reducing parasite load in non-lymphoid solid tissues on day 9 is intriguing (Fig. 18G and 18H). It has been previously reported that, while the parasite is at least partially resistant to complement-mediated lysis[166,222,223], the complement system is important for *T. brucei* opsonization and killing via phagocytosis[154,223]. In the absence of complement opsonization, macrophages can still phagocytose *T. brucei*, albeit less efficiently[223–225].

Classical activation of the complement system requires IgM or IgG binding the parasite to initiate binding of complement components to the Fc-region. Unlike IgG, opsonization by IgM alone does not promote macrophage phagocytosis, as these

cells lack the FcμR[157]. Hence, IgM-promoted phagocytosis requires opsonization by the complement system. Given that in the AT, anti-VSG IgM and IgG titers are significantly lower than in the spleen (a proxy for the blood) (Fig. 17), it is tempting to speculate that the parasite control in AT (and perhaps other solid organs) is more dependent on complement opsonization, while in the spleen the faster accumulation of specific IgG could reduce complement-dependency.

Further studies are required to better understand the role of the complement system in *T. brucei* infection, including a quantitative analysis of the complement components and immunoglobulins in multiple tissue types throughout infection.

Parasite immune evasion in the AT could also be achieved by an increased activity of immunosuppressive effectors when compared to other organs. Our transcriptomic data show an upregulation of multiple immune-suppressive genes (Fig. 10B), which is further validated by a progressive accumulation of Treg cells (Fig. 13F). This suppressive response serves to prevent over-activation of the immune system and reduce immunopathology but can be exploited by pathogens to reduce immune pressure on them.

In this scenario it is possible that one or multiple of these suppressive mechanisms prevent sterile tissue immunity. As such, we sought to disrupt the immunosuppressive PD-1/PD-L1 axis which shows evidence of being upregulated in the AT during infection. This disruption led to no significant alterations in the number of parasites in the AT (Fig. 19D). Thus, it is unlikely that this immunosuppressive axis is a determining factor for parasite colonization of the AT.

How do parasites evade the immune response in the AT?

Antigenic variation is the hallmark immune evasion strategy used by African trypanosomes. At any given time during infection a small subset of VSGs is dominant among the BSF population[226], leading to the mounting of VSG-specific IgM responses. These IgM responses are efficient at eliminating parasites expressing their cognate VSG but exert no effect on parasites expressing a different VSG coat. It is possible that when parasites colonize solid tissues, they adapt VSG gene regulation to fine tune antigenic variation. If for example, VSG switching occurred more frequently, perhaps the tissues could be the source of new VSG

variants that escape more efficiently the immune response. This hypothesis remains to be investigated.

Another immune evasion strategy employed by *T. brucei* is its ability to remove VSG-bound antibodies through endocytosis of the VSG-Ig complex. This process requires a hydrodynamic drag force to propel the VSG-Ig complex towards the parasite's flagellar pocket and protects the parasite from Ig-mediated opsonization until a critical antibody threshold is reached[166]. Factors affecting this hydrodynamic drag force include the milieu's viscosity, the parasites swimming speed and the interstitial fluid's flow speed[166,167].

It is possible that these and other biophysical factors may vary between the blood and interstitia of different organs[167], thus granting the parasite a varying capacity to neutralize antibody responses. This could confer to parasites an immune-independent resistance to antibody-mediated phagocytosis.

In summary, we show that an active immune response is mounted in the AT against *T. brucei*, where parasite burden is controlled using the same overarching components of the systemic immune response. Whether these host-protective components are as effective in the AT as in other tissues and the blood requires further study.

Part 2: Adipose tissue metabolism during a *T. brucei* infection

Results of Part 2

1. Effect of *T. brucei* infection on adipocyte lipid metabolism

Natural infections of *T. brucei* induce a marked debilitation of overall physical condition of mammalian hosts. This includes a progressive loss volume of AT depots, which has classically been interpreted as part of the progressive wasting phenotype observed in African trypanosomiasis. However, these changes in the AT of infected hosts may be more than a systemic consequence of disease progression and may in fact be the result of local (*i.e.* within tissue) insults.

Indeed, we now know that these AT depots harbor high numbers of tissue-adapted parasites and that a progressive accumulation of immune cells occurs in the AT. These leukocytes and parasites may play an active role in modulating the local adipocyte metabolism. In turn, disruption of AT metabolic homeostasis may induce significant changes in whole-organism bioenergetics as well as reciprocal modulation of local parasite growth/survival and immune response efficacy. Accordingly, studying the AT of *T. brucei* infected hosts may reveal novel biology of host-pathogen interactions and AT biology in disease.

1.1. *T. brucei* infection induces loss of adipose tissue weight and adipocyte area

First, we sought to study the dynamics of AT weight loss in detail using C57BL/6J mice infected with pleomorphic *T. brucei* via intraperitoneal injection. These mice were then euthanized at different time-points post-infection and 4 distinct AT depots were harvest and weighed. These were: visceral gonadal (white) AT; visceral retroperitoneal (white) AT; inguinal subcutaneous (white/beige) AT; interscapular (brown) AT.

Infected mice show a progressive loss of weight of individual white AT depots. Indeed, by day 10 post-infection a 40% loss of gonadal AT mass (*i.e.* largest visceral white AT depot) was observed, which progressed to a 61% and 70% loss by days 16 and 30 post-infection, respectively (Fig. 20A). A similar weight loss was observed for the retroperitoneal AT and the inguinal AT. Specifically, the retroperitoneal AT presented a 45% mass reduction by day 10 post-infection and was no longer macroscopically identified by day 30 post-infection.

Among the tested AT depots, the inguinal AT presented the fastest loss of overall mass, showing a reduction of approximately 40% between days 4 and 6 post-infection and was no longer macroscopically identifiable by day 10 post-infection. Interestingly, loss of AT weight appears to be specific to white AT depots, as the interscapular (brown) AT depot remained relatively stable throughout infection, presenting a maximum of 25% weight reduction by day 30 post-infection (Fig. 20A).

To assess whether the observed loss of AT weight was associated with a reduction in adipocyte size, we analysed H&E-stained sections of the gonadal AT at different time-points post-infection. A progressive reduction in lipid droplet size was observed concomitant with the accumulation of inflammatory infiltrates (Fig. 20B). Quantification of lipid droplet areas revealed an average reduction of 20%, 44%, 54%, and 64%, by days 6, 10, 16 and 30 post-infection, respectively (Fig. 20C).

Overall, these data show that during infection white AT depots undergo a progressive weight loss that is correlated with a reduction of individual adipocyte sizes. In turn, this suggests that a *T. brucei* infection disrupts the balance between lipid anabolism and lipid catabolism of white adipocytes. This imbalance should favor the mobilization of stored intracellular fat over lipogenesis, leading to a reduction in adipocyte volume.

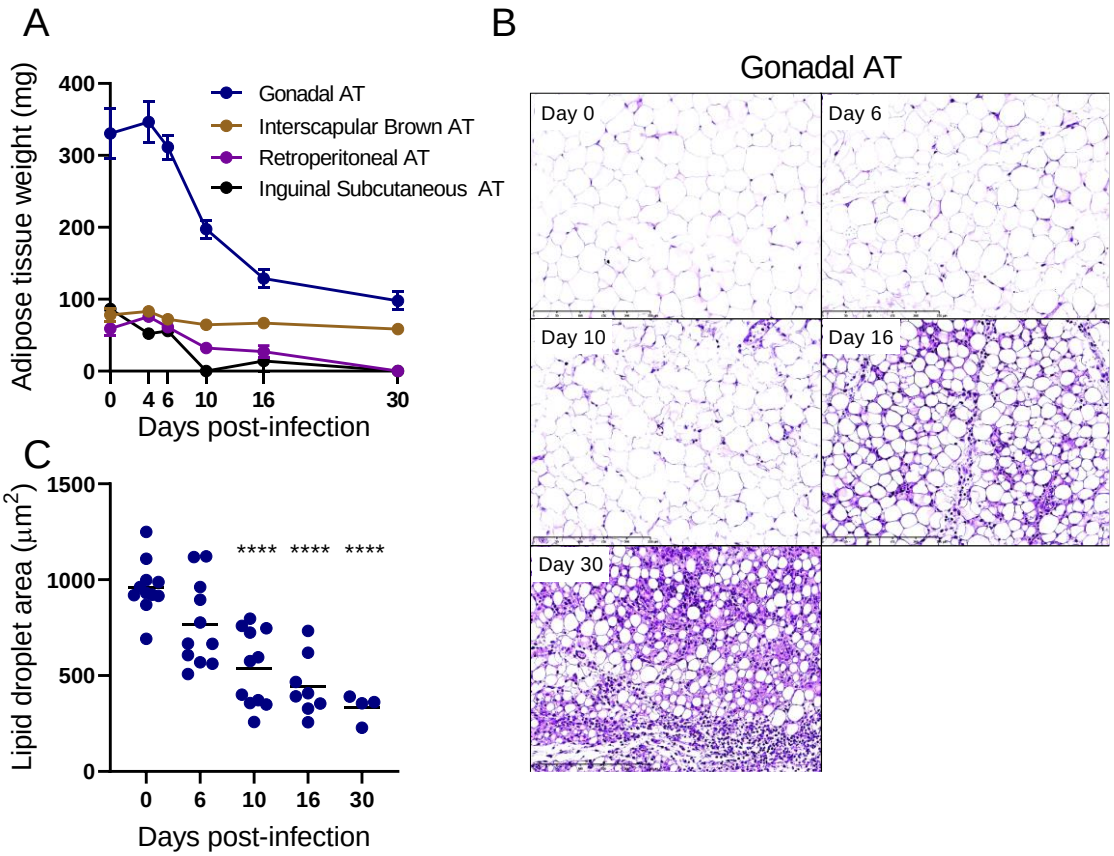

Figure 20 – Dynamics of adipose tissue weight and adipocyte size during infection. **(A)** Weight of gonadal, interscapular brown, retroperitoneal and inguinal subcutaneous adipose tissues throughout infection. **(B)** Representative hematoxylin & eosin micrographs of gonadal AT at different time-points post-infection. Scale bar length = 250 µm, magnification = 20x. **(C)** Quantification of lipid droplet area of the gonadal AT at different time-points post-infection. Error bars represent the SEM (n = **(A)** 5-12 or **(C)** 4-10 mice per group). Statistical analysis was performed with one-way ANOVA using Sidak's test for multiple comparisons. *, P<0.05; **, P<0.01; ***, P<0.001; ****, P<0.0001.

1.2. Adipocyte lipolysis is increased during a *T. brucei* infection

Next, we sought to identify whether adipocyte lipolysis (*i.e.* a major player of fat mobilization) is activated during *T. brucei* infection. Gonadal AT from infected and control mice was harvested at different time-points post-infection and incubated *ex vivo* to allow for the release of lipolytic products (*i.e.* fatty acids and glycerol), which were subsequently quantified (Fig. 21A). A significant increase in fatty acid release was observed from the gonadal AT of mice infected for 6 and 9 days (Fig. 21B). At day 16 post-infection the opposite was observed, as on average fewer fatty acids

were release from the AT of infected mice when compared to non-infected controls (Fig. 21B).

Likewise, an increase in glycerol release was observed by days 6 and 9 post-infection, but not by day 16 post-infection (Fig. 21C). On average the fold increase was for glycerol was higher than that observed for fatty acids. This difference may in part be due to glycerol secreted by the parasite. Indeed, significant amounts of glycerol are produced by *T. brucei* during glycolysis, especially under hypoxic conditions[227,228].

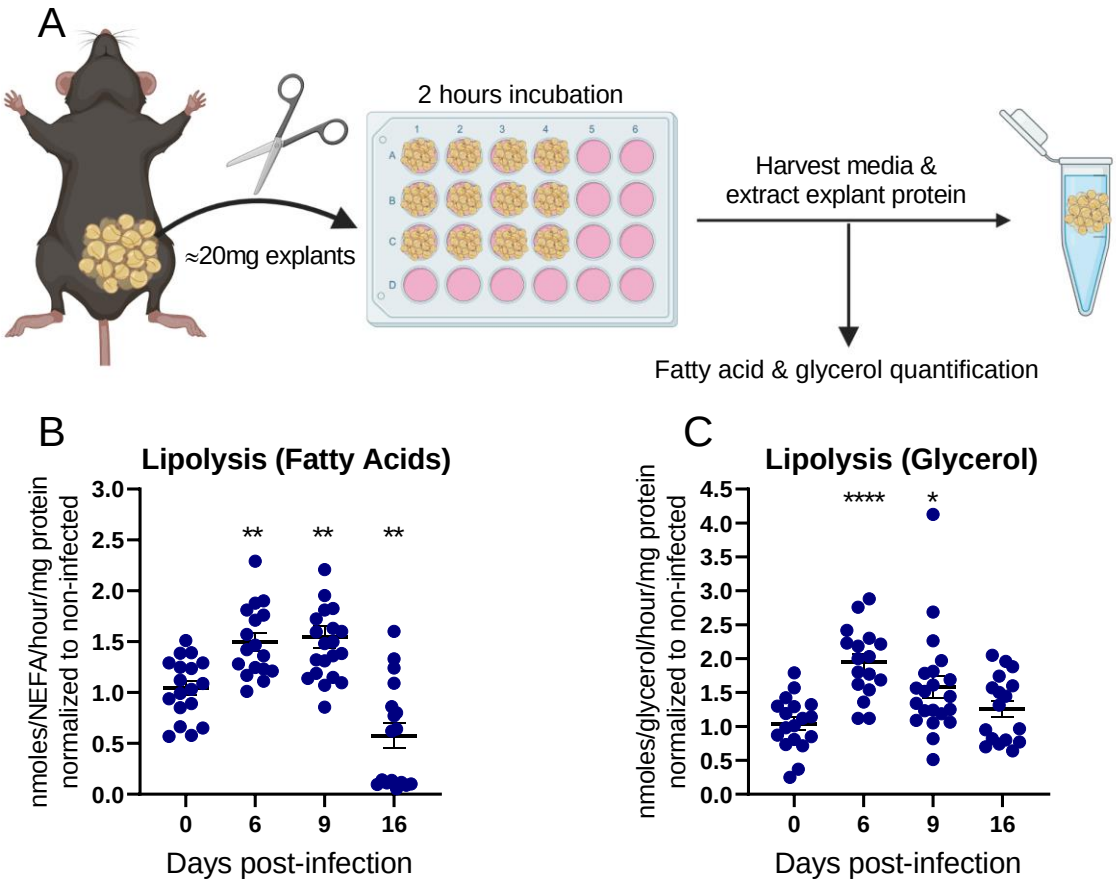

Figure 21 – Increased *ex vivo* lipolysis during a *T. brucei* infection. (A) Schematic representation of an *ex vivo* lipolysis assay using AT explants (figure created using BioRender.com). Release of **(B)** fatty acids and **(C)** glycerol from AT explants. Error bars represent the SEM (n = 17-18 mice per group, pooled data from 3 independent experiments). Statistical analysis was performed with one-way ANOVA using Sidak's test for multiple comparisons. *, P<0.05; **, P<0.01; ***, P<0.001; ****, P<0.0001.

2. Effect of adipocyte-specific lipase deficiency in infection

2.1. ATGL-dependent lipolysis prolongs host survival

After establishing that adipocyte lipolysis is increased during a *T. brucei* infection, we questioned whether its activation affects disease progression. To assess this, we infected adipocyte-specific lipase deficient mice, which express a Cre recombinase under the control of the adiponectin promoter and have loxP sites flanking either the Pnpla2 (ATGL) or Lipe (HSL) gene. Thus, these mice should show no expression of ATGL or HSL in cells that express adiponectin (*i.e.* adipocytes).

Infected adipocyte-specific ATGL deficient (*Adipoq*$^{Cre/+}$-*Atgl*$^{fl/fl}$) mice showed significantly shorter survival than their WT littermate controls (*Atgl*$^{fl/fl}$) (Fig. 22A), suggesting a protective role for ATGL-mediated lipolysis during infection. Conversely, infected adipocyte-specific HSL (*Adipoq*$^{Cre/+}$-*Hsl*$^{fl/fl}$) deficient mice were equally susceptible to infection as their WT littermate controls (*Hsl*$^{fl/fl}$) (Fig. 22C). Absence of either lipase had no significant effect on the control of the first peak of parasitemia or on late-stage (*i.e.* 10 days preceding death) (Fig. 22B and 22D).

Necropsy of moribund mice revealed significantly larger gonadal AT depots in *Adipoq*$^{Cre/+}$-*Atgl*$^{fl/fl}$ mice when compared to *Atgl*$^{fl/fl}$, *Hsl*$^{fl/fl}$ and *Adipoq*$^{Cre/+}$-*Hsl*$^{fl/fl}$ mice (Fig. 22E and 22F). This suggests that AT mass loss during infection is primarily dependent on ATGL activity in the AT.

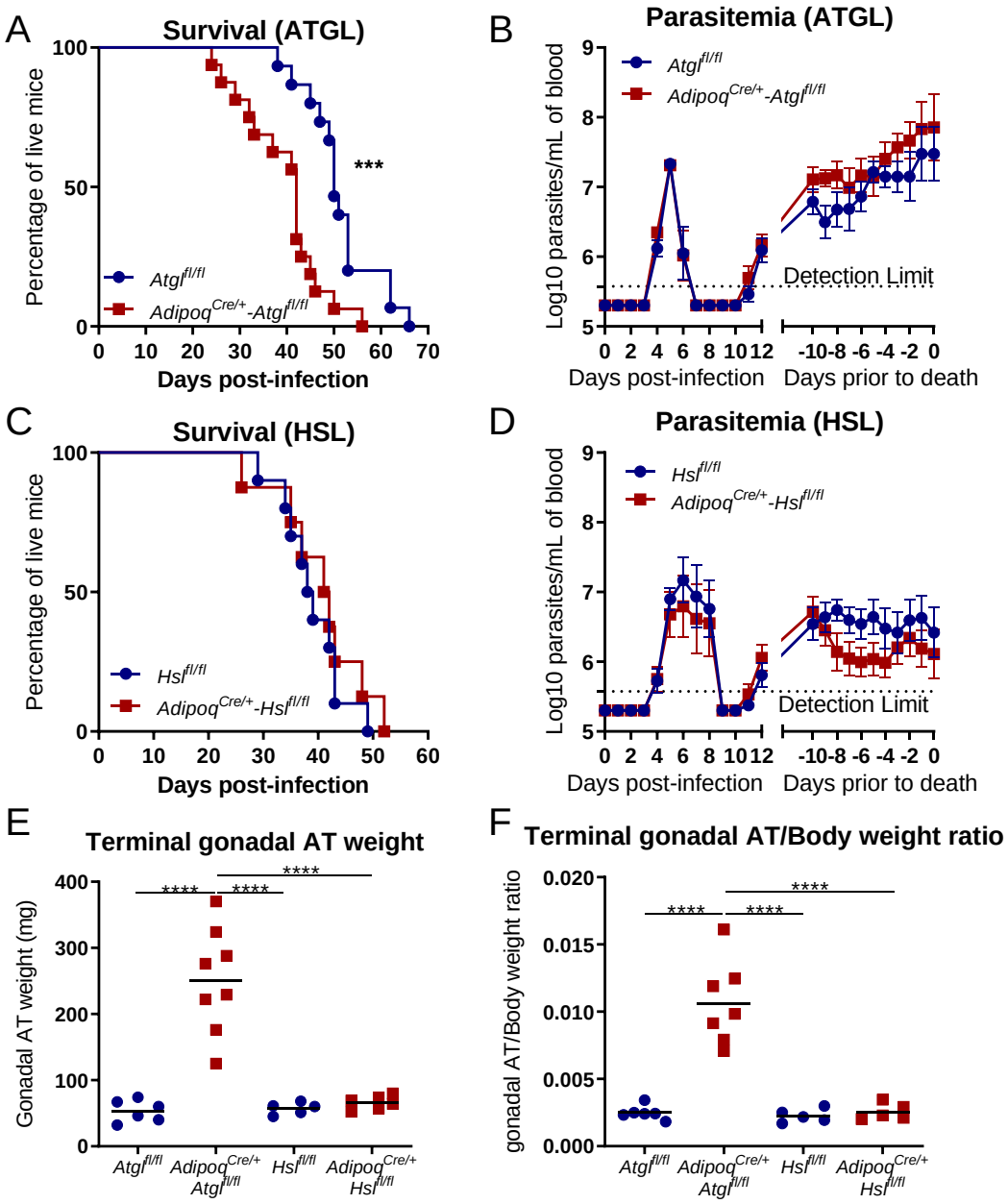

Figure 22 – Effect of adipocyte-specific lipase deficiency in infection. Survival curves of *T. brucei* infected **(A)** *Adipoq*$^{Cre/+}$*-Atgl*$^{fl/fl}$ or **(C)** *Adipoq*$^{Cre/+}$*-Hsl*$^{fl/fl}$ and respective WT littermate controls. Log10 parasitemia numbers in the first twelve and last ten days of infection in **(B)** *Adipoq*$^{Cre/+}$*-Atgl*$^{fl/fl}$ or **(D)** *Adipoq*$^{Cre/+}$*-Hsl*$^{fl/fl}$ and respective WT littermate controls. Terminal **(E)** gonadal AT mass and **(F)** gonadal AT mass to body weight ratio of *Adipoq*$^{Cre/+}$*-Atgl*$^{fl/fl}$ and *Adipoq*$^{Cre/+}$*-Hsl*$^{fl/fl}$ respective WT littermate controls. Error bars represent the SEM (**(B/D)** n= 8-10 and **(E/F)** n=5-9 mice per group). Statistical analysis was performed with **(A/C)** Log-rank (Mantel-Cox) test and **(E/F)** one-way ANOVA using Sidak's test for multiple comparisons. *, P<0.05; **, P<0.01; ***, P<0.001; ****, P<0.0001. **(A)** Pooled data from two independent experiments.

2.2. Fat mass loss is dependent on adipocyte ATGL activity

Next, we questioned how ATGL-deficiency may impact mouse whole body composition. Specifically, we hypothesized that in the absence of ATGL activity infected mice would be unable to mobilize energy stored in the form of TAG within adipocytes. In turn, this could potentially be compensated by skeletal muscle proteolysis which would precipitate the hallmark cachexia phenotype observed during natural infections and thus account for the shorter lifespan observed in infected *Adipoq*$^{Cre/+}$*-Atgl*$^{fl/fl}$ mice. To assess this, we performed a longitudinal study of body composition by nuclear magnetic resonance, which allowed us to follow total body weight, free fluid, fat and lean mass.

Total body weight of *Atgl*$^{fl/fl}$ and *Adipoq*$^{Cre/+}$*-Atgl*$^{fl/fl}$ followed a similar profile with a trend for increased loss of total weight in the absence of ATGL activity in adipocytes. Both groups showed an initial loss of approximately 5% of total body weight during the first peak of parasitemia (*i.e.* days 5-7 post-infection), followed by a rapid recovery and relative stability until day 20 post-infection (Fig. 23A). Afterwards, total body weight declined for both WT and KO mice, with a trend for *Adipoq*$^{Cre/+}$*-Atgl*$^{fl/fl}$ to show lower total weight during the latest stages of infection (*i.e.* by day 30 post-infection) (Fig. 23A).

During infection, a clear increase in free fluid mass was observed in both WT and KO mice (Fig. 23B), which was likely due to the formation of widespread edema that stems from the increased vascular leakage known to occur during *T. brucei* infection[18].

As expected, *Adipoq*$^{Cre/+}$*-Atgl*$^{fl/fl}$ mice present significantly increased retention of fat when compared to *Atgl*$^{fl/fl}$ mice (Fig. 23C). By day 8 post-infection, while *Atgl*$^{fl/fl}$ mice lost over 40% of total fat mass, *Adipoq*$^{Cre/+}$*-Atgl*$^{fl/fl}$ mice presented only a modest 8% loss (Fig. 23C). Afterwards, *Adipoq*$^{Cre/+}$*-Atgl*$^{fl/fl}$ mice steadily lost fat mass, reaching an average 33% loss by day 30 post-infection – significantly less than the 49% experienced by *Atgl*$^{fl/fl}$ mice. This suggests that both ATGL-dependent and ATGL-independent mechanisms contribute to fat loss during a *T. brucei* infection.

Lastly, lean mass progression showed a similar profile to total body weight progression. Both experimental groups showed an initial decrease in overall lean

mass by day 6 post-infection, which was followed by an increase in total lean mass in the following days, peaking by day 12 post-infection at levels above baseline (Fig. 23D). This increase in total lean mass likely stems from hepatomegaly and splenomegaly observed during *T. brucei* infections[229]. After this peak, both groups progressively lost lean mass, with an overall trend for *Adipoq*$^{Cre/+}$*-Atgl*$^{fl/fl}$ mice to show lower lean mass retention than *Atgl*$^{fl/fl}$ mice. To further characterize the changes in total lean mass, we performed histopathology analysis of several skeletal muscles, which represent the major source of lean mass.

To assess whether adipocyte ATGL activity modulates myofiber size and overall immunopathology, we performed histopathology analysis of the heart, diaphragm and hindlimb muscle at different time-points post-infection In addition, we also analysed the lungs of these mice, as respiratory distress is a commonly observed in moribund animal of this experimental model. If adipocyte-ATGL activity exerts a protective role on skeletal muscle, we would expect that *Adipoq*$^{Cre/+}$*-Atgl*$^{fl/fl}$ mice would present higher and earlier skeletal muscle pathology than *Atgl*$^{fl/fl}$ controls.

All analysed tissues, regardless of host genotype, showed inflammatory infiltrates. These were mostly mononuclear in nature, comprised by macrophages, plasma cells and lymphocytes. In the case of the hindlimb muscle, numerous neutrophils were also visible. In the heart, inflammatory infiltrates were present mostly in the subepicardium and atrium as well as in the adjacent AT. In the lung the inflammatory infiltrates were perivascular, peribronchial and interstitial. In the diaphragm, the infiltrates were interstitial (*i.e.* between muscle fibers). Lastly, in the hindlimb muscles, the infiltrates were predominantly interstitial but were also present in perineural and perivascular regions, as well as in the adjacent AT.

Surprisingly, no overt changes in myofiber diameter (*i.e.* indicative of cachexia) were observed in either *Atgl*$^{fl/fl}$ or *Adipoq*$^{Cre/+}$*-Atgl*$^{fl/fl}$ mice. Moreover, semi-quantitative pathology analysis of the assayed tissues revealed no significant differences between *Atgl*$^{fl/fl}$ and *Adipoq*$^{Cre/+}$*-Atgl*$^{fl/fl}$ mice at any of the time-points assessed (Fig. 23E).

In summary, ATGL activity in adipocytes during infection promotes loss of fat mass which is not correlated with significant changes lean mass retention nor modulation of skeletal muscle pathology.

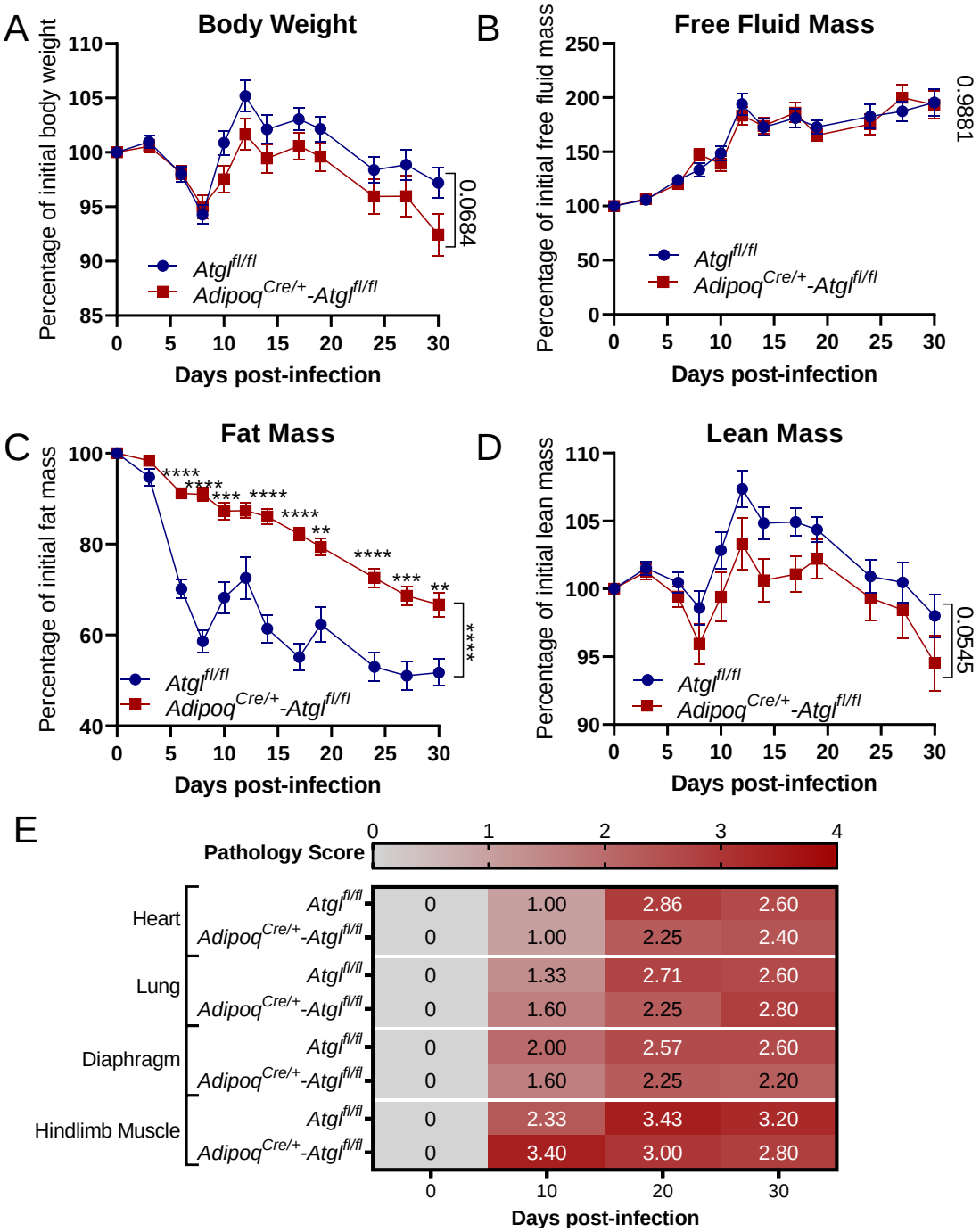

Figure 23 – Effect of adipocyte-specific ATGL deficiency in body composition and skeletal muscle pathology. (A) Total body weight, **(B)** free fluid mass, **(C)** fat mass and **(D)** lean mass relative to baseline. **(E)** Heatmap of pathology score (n=4-7 mice per group). Error bars represent the SEM (**(A-D)** n= 27-32 mice per group). Statistical analysis was performed with **(A-E)** mixed-effects Two-way ANOVA using Sidak's test for multiple comparisons. *, P<0.05; **, P<0.01; ***, P<0.001; ****, P<0.0001. **(A-D)** pooled data from four independent experiments.

As *Adipoq*$^{Cre/+}$*-Atgl*$^{fl/fl}$ mice showed a slower loss of fat mass during infection we decided to further characterize the impact on adipocyte ATGL activity within the AT.

First, to confirm that *ex vivo* lipolysis observed in WT mice was indeed dependent on ATGL activity we compared fatty acid and glycerol release from the gonadal AT of infected and non-infected *Atgl*$^{fl/fl}$ and *Adipoq*$^{Cre/+}$-*Atgl*$^{fl/fl}$ mice (Fig. 24A and 24B). As expected, by day 6 post-infection *Atgl*$^{fl/fl}$ but not *Adipoq*$^{Cre/+}$-*Atgl*$^{fl/fl}$ mice presented a significant increase in both fatty acid and glycerol release when compared to the non-infected controls (Fig. 24A and 24B). Interestingly, high variability was observed for glycerol release in infected *Adipoq*$^{Cre/+}$-*Atgl*$^{fl/fl}$ mice, suggesting that this metabolite is being produced by alternative pathways or by the parasite itself.

We further confirmed that ATGL-dependent lipolysis is central in *T. brucei* induced lipid droplet size reduction, as *Adipoq*$^{Cre/+}$-*Atgl*$^{fl/fl}$ mice maintain a stable average adipocyte size (*i.e.* ≈900 μm^2) while *Atgl*$^{fl/fl}$ mice experience a progressive reduction in adipocyte size of up to 75% by day 30 post-infection (Fig. 24C and 24D).

Collectively, these data show that, during a *T. brucei* infection, adipocyte lipolysis occurs mainly through ATGL activation and that in the absence of this lipase, adipocytes are able to retain their lipid droplet size.

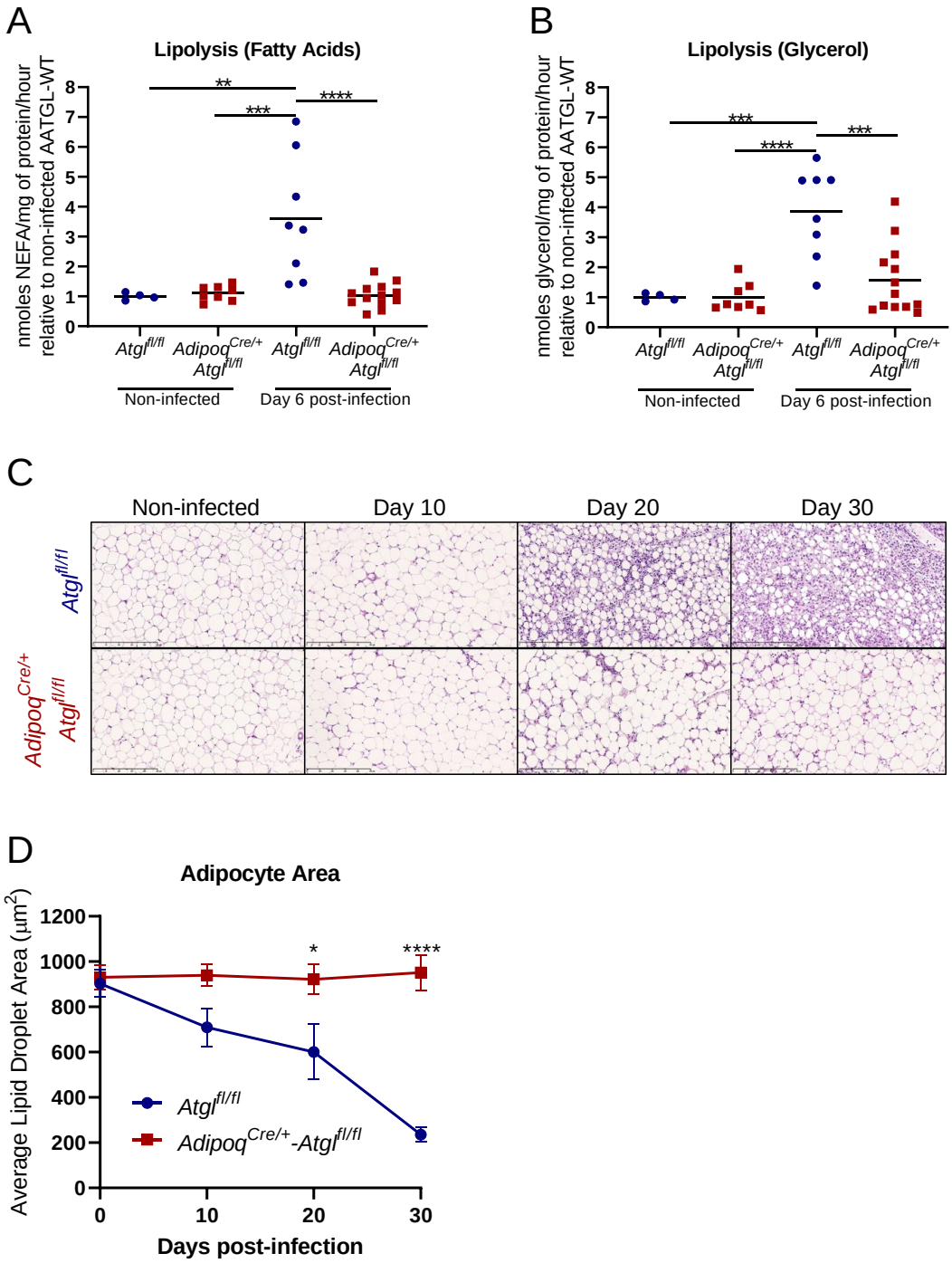

Figure 24 – ATGL deficiency prevents *T. brucei* induced lipolysis and loss of lipid adipocyte area. Release of **(A)** fatty acids and **(B)** glycerol from gonadal AT explants of infected and non-infected *Atgl*$^{fl/fl}$ and *Adipoq*$^{Cre/+}$-*Atgl*$^{fl/fl}$ mice. **(C)** Representative gonadal AT hematoxylin and eosin micrographs (20x magnification, scale bar 250 µm). **(D)** Quantification of lipid droplet area of the gonadal AT at different time-points post-infection. Error bars represent the SEM (**(A-B)** n= 4-12 and **(D)** n=3-6 mice per group). Statistical analysis was performed with **(A-B)** One-way ANOVA or **(D)** Two-way ANOVA using Sidak's test for multiple comparisons. *, P<0.05; **, P<0.01; ***, P<0.001; ****, P<0.0001. **(A-B)** pooled data from two independent experiments.

3. Upstream signals of *T. brucei* induced lipolysis

After establishing that a *T. brucei* infection induces ATGL-dependent adipocyte lipolysis, we sought to understand the upstream signal(s) underlying this activation. A multitude of distinct stimuli may contribute to the induction of adipocyte lipolysis. These include immune, neuronal and hormonal signals[42]. Accordingly, we used *in vivo* and *in vitro* models in which several of these factors were modulated and assessed whether upregulation of adipocyte lipolysis and/or loss of fat mass would no longer occur.

3.1. Infection-induced lipolysis does not depend on feeding behavior

Adipocyte lipolysis is tightly regulated by whole-organism energy balance, which in turn is highly dependent on feeding behavior. We thus investigated whether the increase in adipocyte lipolysis during a *T. brucei* infection stems from a reduction in food intake. This is especially relevant as our group has previously shown that infected mice undergo a transient period of hypophagia around the first peak of parasitemia (*i.e.* days 4 to 10 post-infection)[19].

To test the impact of food intake in *T. brucei* induced adipocyte lipolysis we synchronized the food intake of infected and control mice prior to sacrifice. To achieve this, mice were forced to fast for 7 h during peak activity time and then allowed to re-feed for 2 h prior to sacrifice (Fig. 25A). This experimental setup ensures that both infected and non-infected mice were under a fed status when euthanized. Analysis of *ex vivo* release of lipolytic products from gonadal AT of infected mice showed and overall increase in fatty acid and glycerol release between days 6 and 12 post-infection, albeit with significant biological variability across infected mice (Fig. 25B and 25C). A significant difference in fatty acid release was observed by days 6 post-infection, showing an approximate 1.5-fold increase of fatty acid release from the AT of infected mice when compared to non-infected controls. Additionally, a significant 2.4-fold decrease was observed in fatty acid release by day 16 post-infection. Moreover, glycerol levels released from gonadal AT of infected mice were significantly increased (*i.e.* 1.8 to 2.5-fold) between days 8 and 12 post-infection (Fig. 25C).

As shown above (Fig. 20B and 20C), during the course of infection, adipocyte's lipid droplets become progressively smaller, reducing the overall lipid content of the AT. Concomitantly, a progressive immune infiltration alters the cellular makeup of the AT[230]. Together, these changes result in a significant enrichment of the AT's protein content. In turn, this may constitute a confounding factor in the assessment of the *ex vivo* lipolytic rate, as protein content is one of the variables used to calculate this rate. Accordingly, we quantified the ratio between total AT explant mass and its protein content throughout infection. Here, by day 12 post-infection we observed a 2-fold positive increase in relative protein content, which progressed to 2.4 and 4-fold increase in protein content by days 14 and 16 post-infection, respectively (Fig. 25D), which may lead to underestimation of lipolytic rates later in infection.

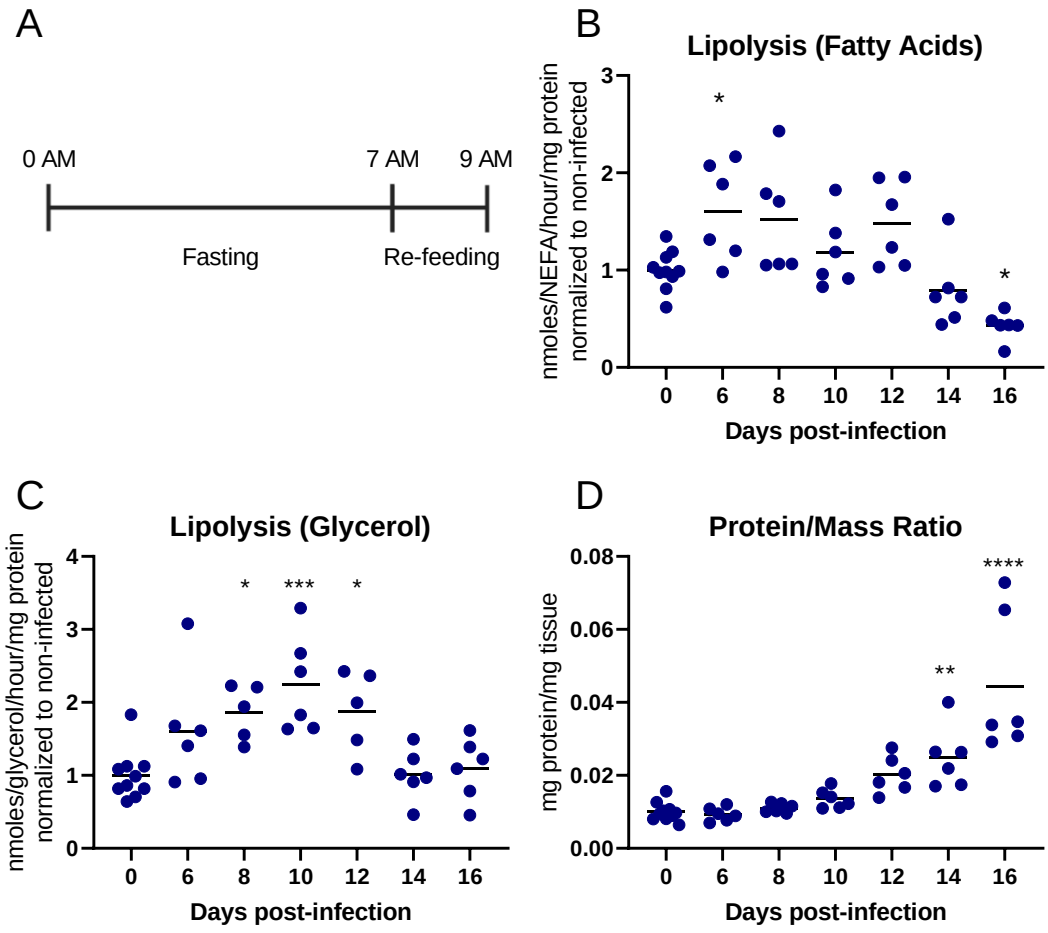

Figure 25 – Feeding synchronization does not prevent *T. brucei* induced adipocyte lipolysis. Schematic representation of the fasting and re-feeding experimental layout. Release of **(B)** fatty acids and **(C)** glycerol from gonadal AT explants of infected and non-infected WT mice, normalized to non-infected mice. **(D)** Explant protein to total mass ratio. Error bars represent the SEM (**(B-C)** n= 5-10 mice per group). Statistical analysis was performed with **(B-D)** One-way ANOVA using Sidak's test for multiple comparisons. *, P<0.05; **, P<0.01; ***, P<0.001; ****, P<0.0001.

To further demonstrate that reduced food intake is not the primary inducer of adipocyte lipolysis during a *T. brucei* infection, we performed a paired-feeding experiment. Here, individually housed infected and control mice were allowed to feed *Ad libitum* (AL) and their food intake was registered daily. An additional group of non-infected and pair-fed (PF) mice was established. In this group, the amount of food provided to each mouse was limited to the amount of food consumed by its pre-arranged infected counterpart in the previous 24 h (Fig. 26A). As previously reported[19], infected mice show an hypophagia phenotype early during infection (Fig. 26B). As early as day 4 post-infection, we observed a significant 17% reduction in food intake.

This hypophagia phenotype progressively worsened, reaching a 27% and then 50% decrease in food intake by days 6 and 8 post-infection (Fig. 26B). This hypophagia phenotype was not sufficient to significantly increase *ex vivo* release of fatty acids by when compared to day 6 or 8 infected mice (Fig. 26C and 26D).

Overall, these data suggest that disease-induced hypophagia is not the main cause of increased adipocyte lipolysis during a *T. brucei* infection.

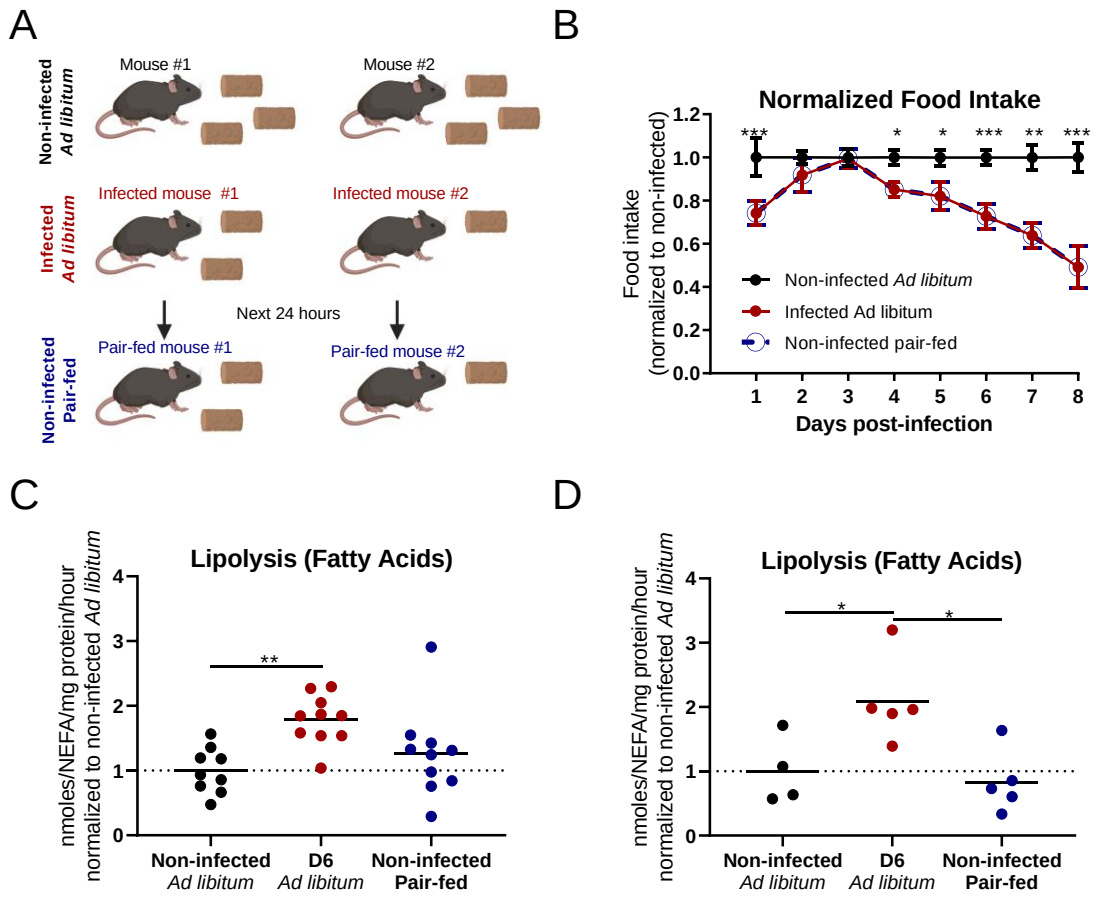

Figure 26 – Disease induced hypophagia is not responsible for *T. brucei* induced adipocyte lipolysis. (A) Schematic representation of the paired-feeding experimental layout. **(B)** Daily food intake normalized to non-infected *ad libitum* fed mice. **(C-D)** Release of fatty acids from gonadal AT explants of infected and non-infected WT mice, normalized to ad libitum fed non-infected mice. Error bars represent the SEM (**(B-D)** n= 4-9 mice per group). Statistical analysis was performed with **(B)** Two-way ANOVA and (**C-D)** One-way ANOVA using Sidak's test for multiple comparisons. *, P<0.05; **, P<0.01; ***, P<0.001; ****, P<0.0001. **(C-D)** Pooled data from two independent experiments.

3.2. Infection-induced lipolysis requires immune cues but not sympathetic innervation

As hypophagia is not the main inducer of adipocyte lipolysis during a *T. brucei* infection, next we investigated neuronal and immune cues known to induce adipocyte lipolysis.

The nervous system is also a central player in the regulation o adipocyte lipolysis. The sympathetic nervous system responds to stimuli such as cold, fasting and even

leptin produced in the AT. In turn, sympathetic neurons release noradrenaline in the AT, which will bind to β3-adrenergic receptors on the surface of adipocytes leading to the activation of lipolysis. To test whether sympathetic innervation contributed to *T. brucei* induced fat loss, we infected mice chemically sympathectomized with 6-hydroxydopamine (6-OHDA), a neurotoxic analogue of dopamine.

Contrary to our hypothesis, body composition analysis revealed a transiently faster loss of fat mass in the 6-OHDA treated group when compared to sham controls (*i.e.* 16% higher loss of fat mass by day 6 post-infection) (Fig. 27A). However, this difference was not kept at later time-points, as by day 12 post-infection both groups presented similar losses of fat mass. These data suggest that differential sympathetic input is not involved in *T. brucei* induced loss of fat mass, and likely in lipolysis induction.

Next, we tested whether immune factors were responsible for increased adipocytes lipolysis during a *T. brucei* infection. To test this, we infected *Rag2*$^{-/-}$ mice, which are highly immunosuppressed lacking both B and T cells and usually succumb to infection by day 15 post-infection[231].

Body composition analysis of infected *Rag2*$^{-/-}$ mice revealed a clear reduction in the loss of overall fat mass when compared to infected WT controls (Fig. 27B). Indeed, by day 6 post-infection while WT mice presented a 25% reduction in total fat mass, *Rag2*$^{-/-}$ mice showed no significant loss of fat mass. As infection progressed, *Rag2*$^{-/-}$ mice showed a modest loss of fat mass. Specifically, by day 12 post-infection *Rag2*$^{-/-}$ mice had lost 14% of total fat mass, significantly less than the 37% loss of fat mass exhibited by infected WT mice at the same time.

To assess whether this higher retention of fat mass in infected *Rag2*$^{-/-}$ mice correlated with a failure to upregulate adipocyte lipolysis, we assessed the release rate of fatty acids from gonadal AT explants of infected *Rag2*$^{-/-}$ mice and compared it to both infected and non-infected WT controls (Fig. 27C). Indeed, unlike WT infected mice, infected *Rag2*$^{-/-}$ mice failed to upregulate adipocyte lipolysis, suggesting that in these mice higher fat mass retention is correlated with reduced adipocyte lipolysis.

We then investigated whether the lipolysis-inducing immune factor was present in the serum of infected mice. To assess this, plasma was harvested from WT and

Rag2$^{-/-}$ mice after 6 days of infection, as well as non-infected WT controls, and was then added to an *in vitro* culture of 3T3-L1 adipocytes. While the plasma from WT infected mice was able to induce an increase in the release of fatty acids (Fig. 27D), serum from *Rag2*$^{-/-}$ infected mice failed to elicit an increase in the release of fatty acids. These data suggest that during infection, a soluble factor likely released by B or T cells is able to induce adipocyte lipolysis.

A fitting candidate that is produced by T cells and is known to induce adipocyte lipolysis is TNF-α[230,232]. This pro-inflammatory cytokine binds to the TNF-receptor 1 on the surface of adipocytes and is able to activate adipocytes lipolysis through ERK1/2 and PKA mediated mechanisms[76,87]. Moreover, this cytokine has been extensively associated with highly catabolic scenarios, such as cachexia[115,233]. To test whether TNF-α drives the loss of fat mass during a *T. brucei* infection, we infected *Tnfa*$^{-/-}$ and followed their body composition for 12 days (Fig. 27E). These mice showed small delay in fat mass loss when compared to WT controls. Specifically, by day 6 post-infection *Tnfa*$^{-/-}$ showed a 16% reduction in fat mass whereas WT mice had lost 39% of total fat mass. However, from day 9 post-infection onwards, overall loss of fat mass was similar between the two experimental groups.

As previously performed with sera from *Rag2*$^{-/-}$ infected mice, we stimulated 3T3-L1 adipocytes with sera isolated from *Tnfa*$^{-/-}$ and WT infected controls. Unlike sera from infected *Rag2*$^{-/-}$ mice, sera extracted from *Tnfa*$^{-/-}$ mice was able to induce the release of fatty acids to a similar extent as sera from infected WT mice (Fig. 27F). Collectively, these data show that TNF-α is not necessary for *T. brucei* induced lipolysis.

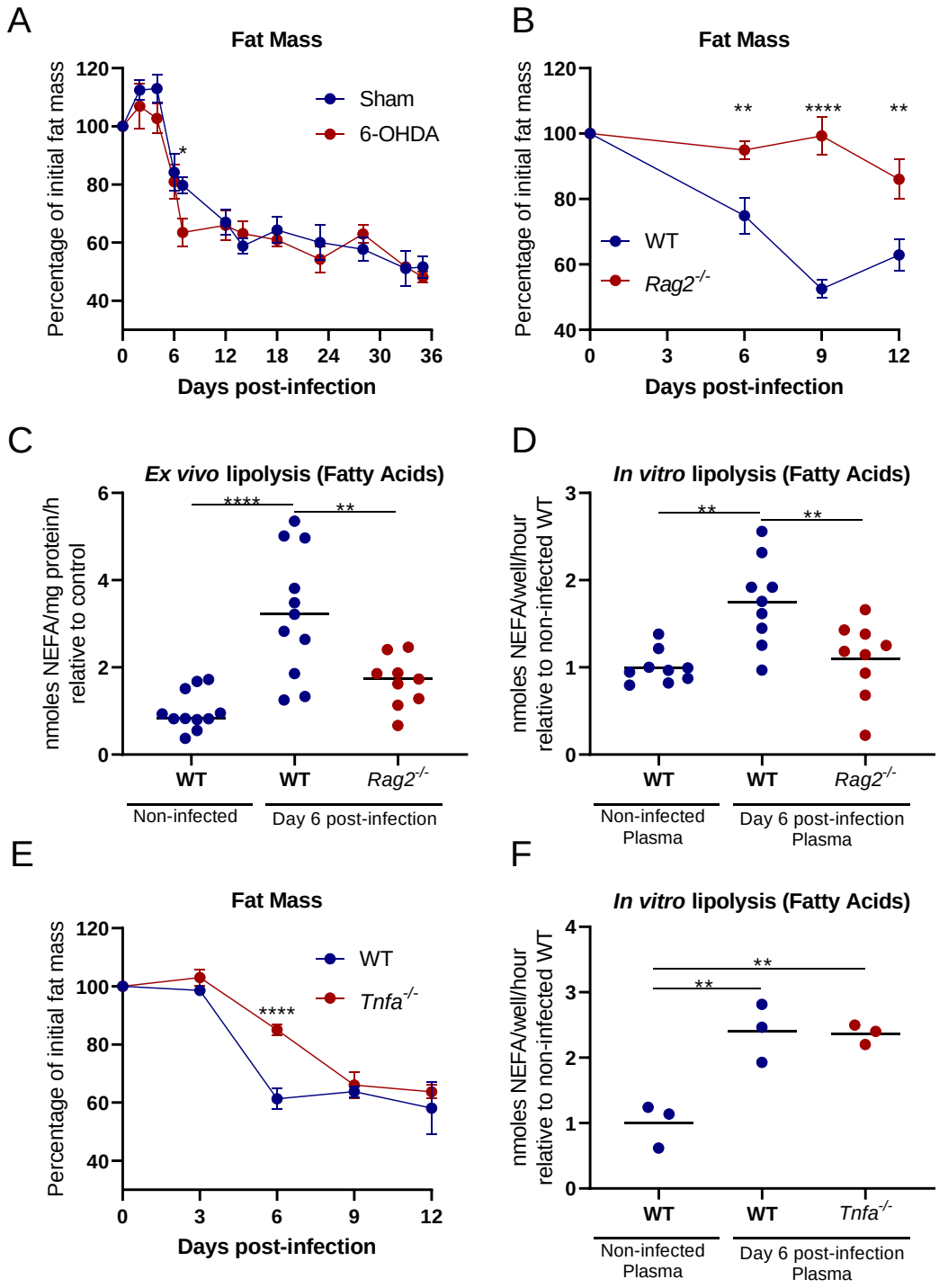

Figure 27 – *T. brucei* induced loss of fat mass is dependent on an adaptive immune response. (A) Fat mass relative to baseline of infected mice chemically sympathectomized with 6-OHDA and infected sham controls. Fat mass relative to baseline of **B)** *Rag2*$^{-/-}$ and **(E)** *Tnfa*$^{-/-}$ mice and WT controls. **(C)** Release of fatty acids from gonadal AT explants of infected WT and Rag2$^{-/-}$ mice normalized to non-infected WT controls. Fatty acid release from 3T3-L1 adipocytes stimulated for 24 h with 10% plasma from infected **(D)** *Rag2*$^{-/-}$ and **(F)** *Tnfa*$^{-/-}$ or with plasma from WT infected and non-infected controls.. Error bars represent the SEM (**(A/B/C/E)** n= 4-6 mice per group). Statistical analysis was performed with **(A/B/E)** Two-way ANOVA and (**C/D/F)** One-way ANOVA using Sidak's test for multiple comparisons. *, P<0.05; **, P<0.01; ***, P<0.001; ****, P<0.0001.

These data suggest that activation of adipocyte lipolysis and ensuing loss of fat mass during a *T. brucei* infection are primarily induced by a soluble immune factor(s) produced by T and/or B lymphocytes.

3.3. Parasite-adipocyte interactions induce lipolysis

Unlike most infectious agents, *T. brucei* shows a disproportionately high accumulation in the interstitial spaces of the AT. This places the parasite in a privileged position to perform direct cell-cell interactions with the host's adipocytes. As described for other pathogens, it is feasible that *T. brucei* derived PAMPs may engage adipocyte PRRs leading to downstream activation of lipolysis. However, this hypothesis is challenging to study in an *in vivo* setting, as concomitant with these parasite-adipocyte interactions a myriad of other lipolysis-inducing signals are being modulated (*e.g.* immune signals).

To circumvent confounding factors, we established a co-culture system of differentiated 3T3-L1 adipocytes that allows for parasite growth and enables the assessment of lipolytic rates in the absence of host-derived confounding factors. Accordingly, we incubated 3T3-L1 adipocytes for 24 h with 10^7 *T. brucei* parasites and then replaced the culture media with lipolysis assay medium, as described previously for the *ex vivo* lipolysis assay.

Adipocytes co-cultured with *T. brucei* showed a significant increase in the release of fatty acids and glycerol. As observed during an *in vivo* infection, this *T. brucei* induced lipolysis was dependent on ATGL activity, as treatment of atglistatin (*i.e.* mouse ATGL inhibitor) abrogated the increase of both lipolysis end-products (Fig. 28A and 28B).

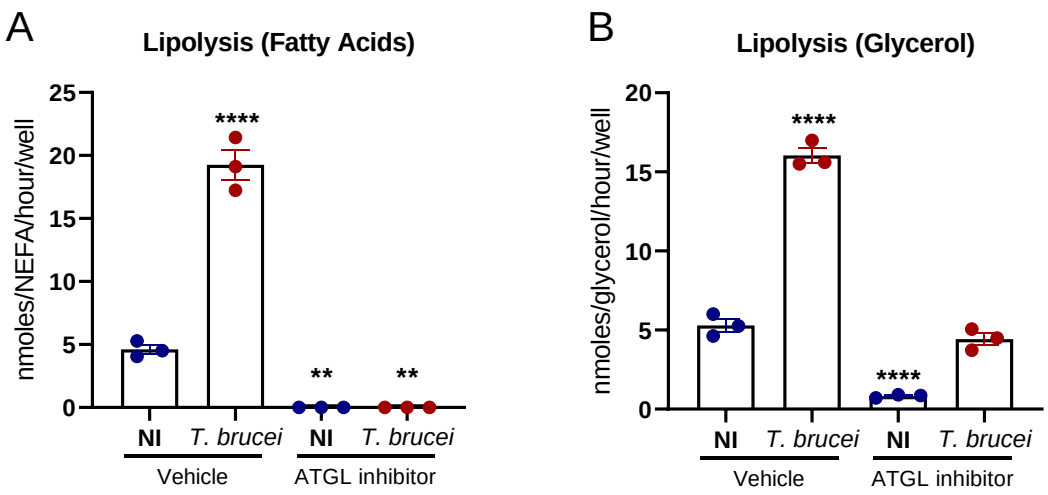

Figure 28 – *T. brucei*-adipocyte interactions are sufficient to induce ATGL-dependent lipolysis. Release of **(A)** fatty acids and **(B)** glycerol from 3T3-L1 adipocytes incubated for 24 h with 10^7 Lister 427 *T. brucei* and non-infected controls in the presence or absence of 50µM of the ATGL inhibitor atglistatin. Error bars represent the SEM (n= 3 cultures per group). Statistical analysis was performed with One-way ANOVA using Sidak's test for multiple comparisons. *, P<0.05; **, P<0.01; ***, P<0.001; ****, P<0.0001.

3.4. Adipocyte lipolysis is induced by a secreted *T. brucei* factor

We then questioned whether direct cell-cell contact is required for *T. brucei*-induced lipolysis in a co-culture setting. To assess this we used a transwell system with 0.4 µm pore diameter. In this setting, adipocytes are differentiated on the bottom of the culture plate and the parasites are placed inside the transwell insert (*i.e.* no contact with adipocytes) or outside the transwell insert (*i.e.* direct contact with adipocytes) (Fig. 29A). As parasites have a width between 2 and 3 µm, we selected a pore size that allows for unrestricted exchange of soluble factors but does not allow parasite traversal.

As shown previously, *T. brucei* co-cultured for 24 h in direct contact with adipocytes was still able to induce a robust increase in adipocyte release of fatty acids and glycerol (Fig. 29B and 29C). However, direct contact was not essential for *T. brucei* induced adipocyte lipolysis. Indeed, parasites cultured inside the transwell insert were able to induce a significant increase in adipocyte lipolysis, although this increase was lower than that induced by parasites cultured outside the insert (Fig. 29B and 29C). Accordingly, these data suggest that a soluble *T. brucei* secreted factor(s) is sufficient to induce adipocyte lipolysis.

A soluble factor could induce lipolysis via a ligand-receptor interaction. Alternatively, the presence of parasites in the same culture as the adipocytes could lead to a metabolite competition and modulate adipocyte metabolism. To distinguish between these two possible effects, we reasoned that a crude lysate of *T. brucei* would contain the soluble factor, but would not compete for metabolites in the medium. To test this, we prepared crude *T. brucei* lysates through repeated flash freeze and thaw cycles and stimulated 3T3-L1 adipocytes for 24 h with lysates equivalent to $5x10^6$ lysed *T. brucei* parasites.

As hypothesized, lysate-treated adipocytes showed a significant increase in both fatty acid and glycerol release when compared to non-treated/infected controls (Fig. 29D and 29E). The fact that lipolytic effect is not as strong as in live parasites could be due to multiple reasons, including partial loss of the soluble factor during lysate preparation, soluble factor may form non-physiological interactions during lysate preparation, partial degradation or loss of activity, among others.

In sum, these data show that *in vivo* activation of adipocyte lipolysis and loss of fat are independent of changes in feeding behavior and modulation of sympathetic input and occurs primarily through activation by immune factors produced by lymphocytes. Concomitantly, high parasite burdens may also induce adipocyte lipolysis through yet unknown parasite-adipocyte interactions, whose relevance in vivo remains to be elucidated.

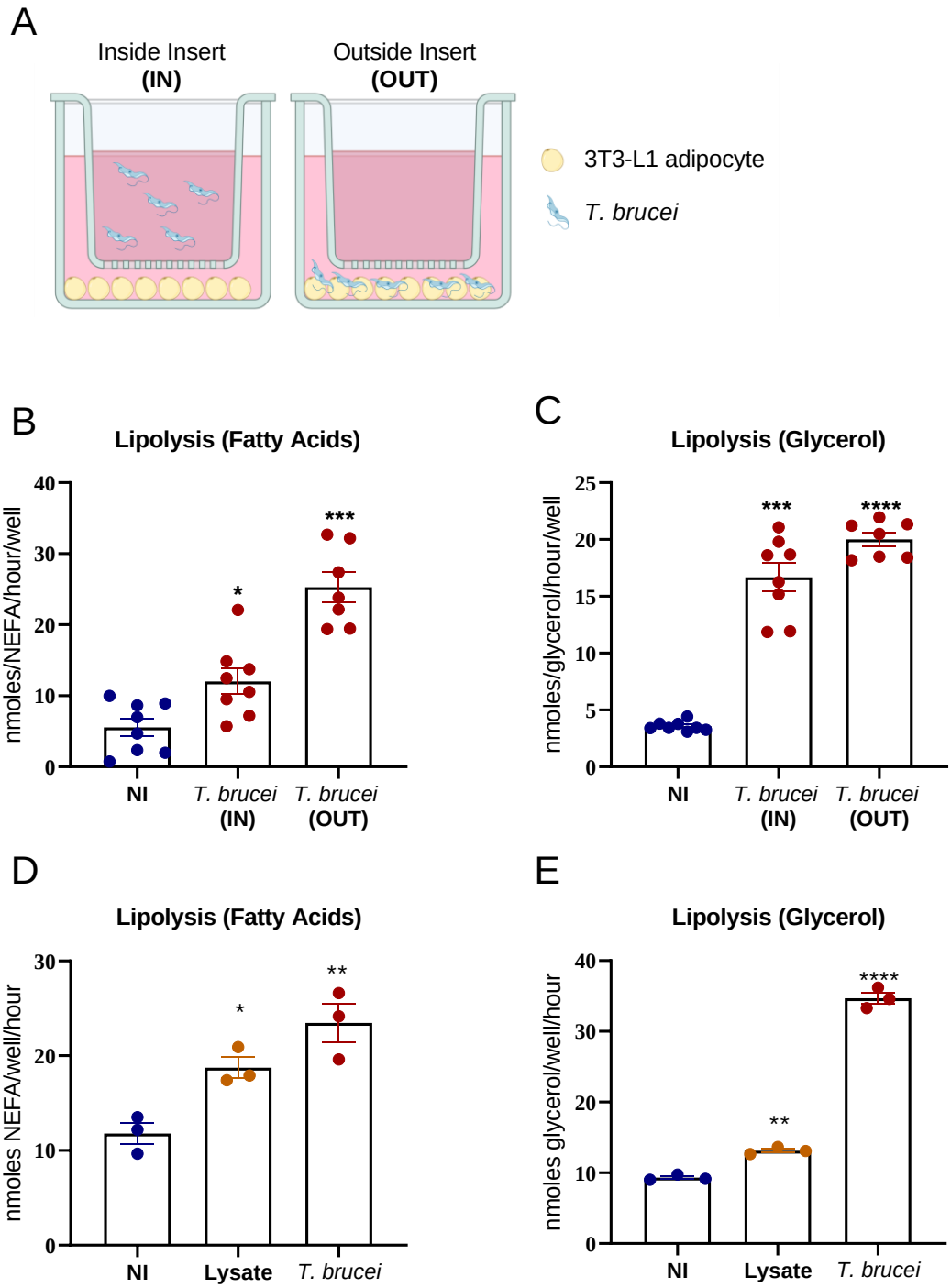

Figure 29 – Soluble *T. brucei* factors are sufficient to induce adipocyte lipolysis. (A) Schematic representation of 3T3-L1 - *T. brucei* co-cultures using a transwell setting (figure created using BioRender.com). Release of **(B)** fatty acids and **(C)** glycerol from 3T3-L1 adipocytes incubated for 24 h with 10^7 Lister 427 *T. brucei* parasites inside or outside the transwell insert and non-infected controls. Release of **(D)** fatty acids and **(E)** glycerol from 3T3-L1 adipocytes incubated for 24 h with 10^7 Lister 427 *T. brucei* parasites or stimulated with cell lysates equivalent to $5x10^6$ Lister 427 *T. brucei* parasites and non-infected controls. Error bars represent the SEM (n= 3-4 cultures per group). Statistical analysis was performed with One-way ANOVA using Sidak's test for multiple comparisons. *, P<0.05; **, P<0.01; ***, P<0.001; ****, P<0.0001.

4. Effect of adipocyte lipolysis on parasite burdens

4.1. Adipocyte lipolysis contributes to the reduction of adipose tissue parasite burden

Finally, we questioned whether adipocyte lipolysis *per se* is able to modulate the number of parasites. As previously shown, neither *Adipoq*$^{Cre/+}$*-Atgl*$^{fl/fl}$ nor *Adipoq*$^{Cre/+}$*-Hsl*$^{fl/fl}$ mice showed different blood parasite burdens when compared to littermate controls. This indicates that adipocyte lipolysis is insufficient to modulate number of parasites on a systemic level, but this does not exclude the existence of tissue-specific effects. Indeed, *Adipoq*$^{Cre/+}$*-Atgl*$^{fl/fl}$ mice present a transient 10-fold increase in parasite number within the gonadal AT by day 10 post-infection (Fig. 30A). To remove any bias due to a higher AT mass typically observed in *Adipoq*$^{Cre/+}$*-Atgl*$^{fl/fl}$ compared to *Atgl*$^{fl/fl}$ mice (*i.e.* due to loss of AT mass in *Atgl*$^{fl/fl}$ mice), we also plotted the number of parasites per milligram (mg) of tissue (Fig. 30B). After this normalization, *Adipoq*$^{Cre/+}$*-Atgl*$^{fl/fl}$ mice present on average a 7-fold increase in the number of parasites in the gonadal AT compared to *Atgl*$^{fl/fl}$ controls.

This transiently higher parasite burden appears to be restricted to the AT, as no significant differences were found between the livers, spleens of lungs of *Atgl*$^{fl/fl}$ and *Adipoq*$^{Cre/+}$*-Atgl*$^{fl/fl}$ mice (Fig. 30C).

Together, these data suggest that adipocyte lipolysis induces a local host-protective effect, limiting parasite numbers. This protective effect may be due to a multitude of factors. On the one hand, released fatty acids and glycerol may exert an immunomodulatory effect that increased the trypanocydal capacity of the local immune response. Alternatively, these lipolytic products may directly modulate the parasite's cell cycle, promote differentiation between slender and stumpy forms, or even exert a direct trypanocydal effect (*e.g.* lipotoxicity).

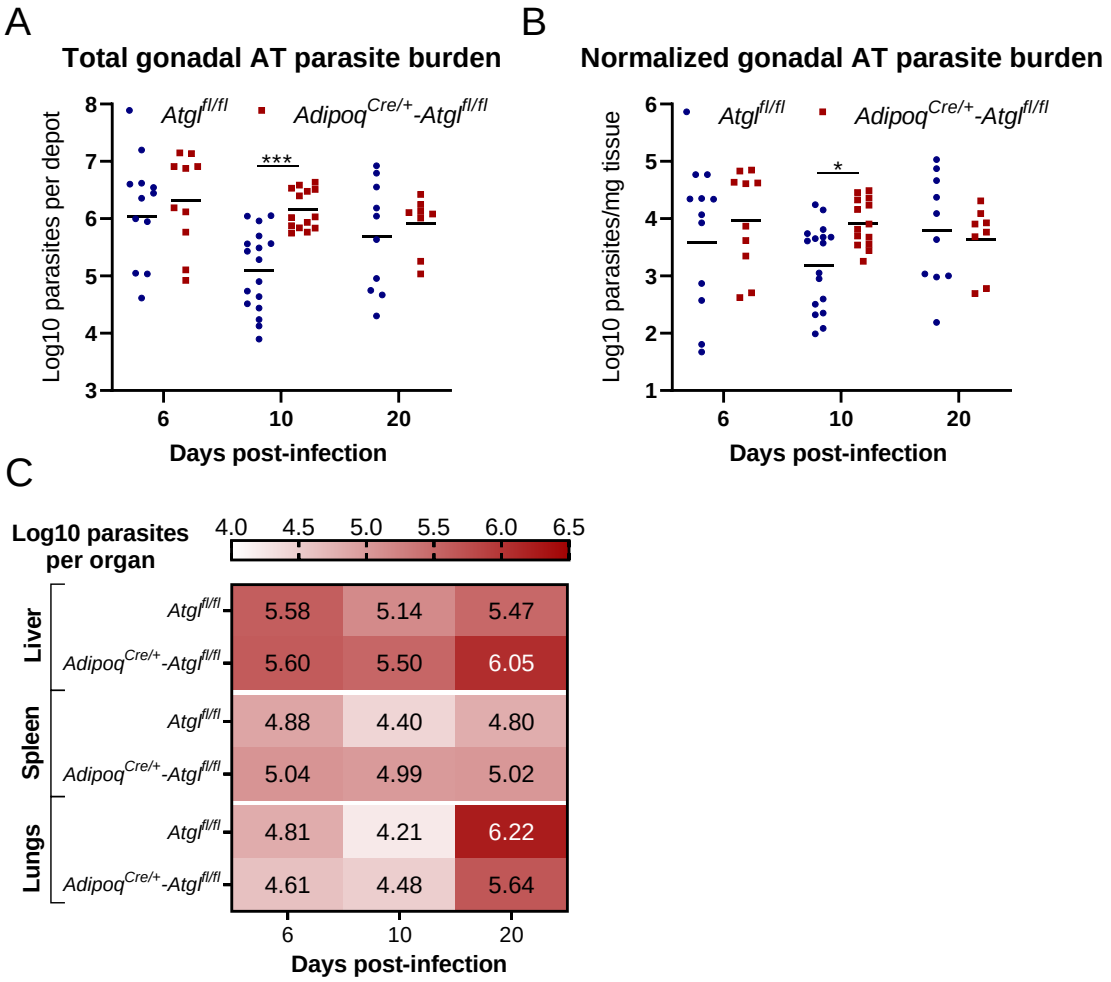

Figure 30 – ATGL-dependent adipocyte lipolysis impacts adipose tissue parasite burden. Log10 number of *T. brucei* parasites at different time-points post-infection per **(A)** depot or **(B)** milligram of gonadal AT of *Atgl*$^{fl/fl}$ and *Adipoq*$^{Cre/+}$*-Atgl*$^{fl/fl}$ mice. **(C)** Heatmap of number of *T. brucei* parasites in the liver, spleen and lungs of *Atgl*$^{fl/fl}$ and *Adipoq*$^{Cre/+}$*-Atgl*$^{fl/fl}$ mice at different time-points post-infection. Error bars represent the SEM (**(A-B-)** n= 5-17 and **(C)** n=4-7 mice per group). Statistical analysis was performed with Two-way ANOVA using Sidak's test for multiple comparisons. *, P<0.05; **, P<0.01; ***, P<0.001; ****, P<0.0001.

4.2. Chemical induction of adipocyte lipolysis prevents *T. brucei* growth

To test whether adipocyte lipolysis is able to directly control the number of parasites, we co-cultured *T. brucei* with adipocytes and chemically induced adipocyte lipolysis with the AC activator forskolin (Fig. 31A-B). Two distinct *T. brucei* cell lines were used for this purpose: the pleomorphic AnTaT1.1 (*i.e.* in which proliferative parasites

(slender forms) are able to differentiate into non-replicative transmissible parasites (stumpy forms)) and the monomorphic Lister427 (*i.e.* unable to differentiate into *bona fide* stumpy forms).

Strikingly, pleomorphic *T. brucei* co-cultured with forskolin-treated adipocytes were unable to proliferate (Fig. 31C), while monomorphic *T. brucei* were able to proliferate, albeit with a significant growth impairment (Fig. 31D). These effects were not due to a direct effect of forskolin on the parasite, as axenic *T. brucei* cultures were not affected by this compound (Fig. 31E-F).

This difference in behavior between pleomorphic and monomorphic parasite cell lines prompted us to study whether adipocyte lipolysis could induce parasite differentiation from replicative slender forms to cell cycle arrested stumpy forms. To do this, we used the AnTat1.1E 90–13 GFP::PAD1utr reporter cell line, which allows for identification of stumpy forms by detection of fluorescence emitted by GFP[234].

We co-cultured 3T3-L1 adipocytes with $5x10^4$ parasites, a density insufficient to trigger stumpy differentiation through parasite quorum sensing, in the presence or absence of forskolin. We then quantified the percentage of GFP+ parasites at 4, 8 and 24 h post-inoculation by flow cytometry. Unlike anticipated, while no significant differences were observed between conditions at 4 and 8 h post-inoculation, after 24 h parasites co-cultured with forskolin-treated adipocytes showed a lower percentage of stumpy forms than vehicle-treated controls (16 vs 26%) (Fig. 32A). This result suggests that not only does adipocyte lipolysis fail to promote stumpy differentiation, it may even inhibit this differentiation process.

We then sought to identify whether adipocyte lipolysis was able to modulate stumpy differentiation in an *in vivo* context. To do this, we infected *Atgl*$^{fl/fl}$ and *Adipoq*$^{Cre/+}$-*Atgl*$^{fl/fl}$ mice with the same reporter cell line and isolated parasites from the gonadal AT (*i.e.* ATFs) of these mice at day 6 post-infection.

ATFs extracted from the gonadal AT of *Atgl*$^{fl/fl}$ showed on average 20% of stumpy forms, which is line with previously published data for the same time-point using WT mice[19] (Fig. 32B). Interestingly, on average 60% of ATFs extracted from the gonadal AT of *Adipoq*$^{Cre/+}$-*Atgl*$^{fl/fl}$ were stumpy forms, supporting the an inhibitory role for adipocyte lipolysis in stumpy differentiation.

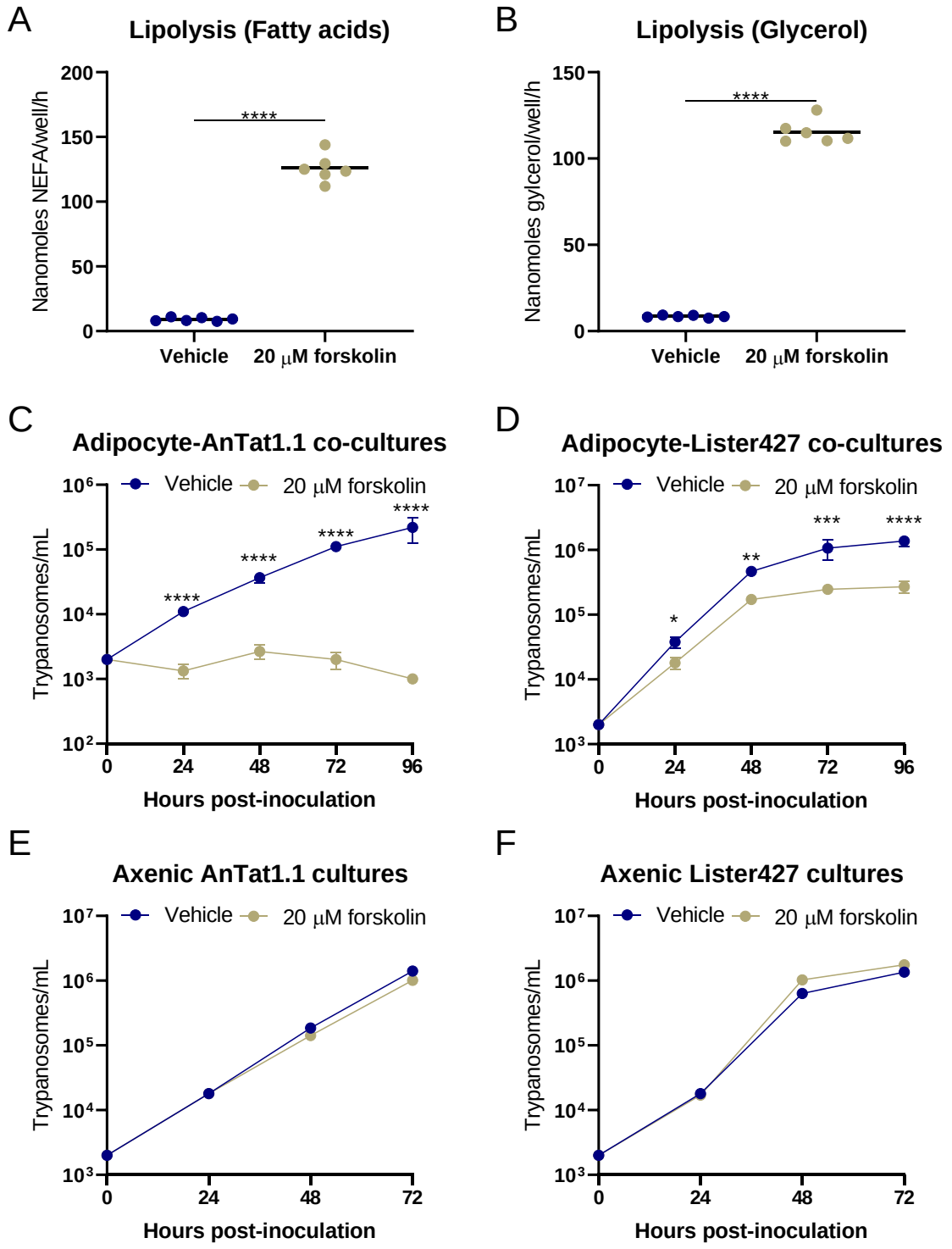

Figure 31 – Chemical induction of adipocyte lipolysis impairs *T. brucei* growth. Effect of a 1 hour treatment with forskolin on the release of **(A)** fatty acids and **(B)** glycerol from 3T3-L1 adipocytes Number of **(C)** AnTat1.1 and **(D)** Lister427 *T. brucei* parasites co-cultured with 3T3-L1 adipocytes stimulated daily with 20 µM forskolin or vehicle. Number of **(E)** AnTat1.1 and **(F)** Lister427 *T. brucei* parasites cultured in HMI-11 medium stimulated daily with 20 µM forskolin or vehicle. Error bars represent the SEM (**C-F**: n=3 wells per group). Statistical analysis was performed with **(A-B)** unpaired t test or **(C-F)** Two-way ANOVA using Sidak's test for multiple comparisons. *, P<0.05; **, P<0.01; ***, P<0.001; ****, P<0.0001. Data is representative of 3 independent experiments.

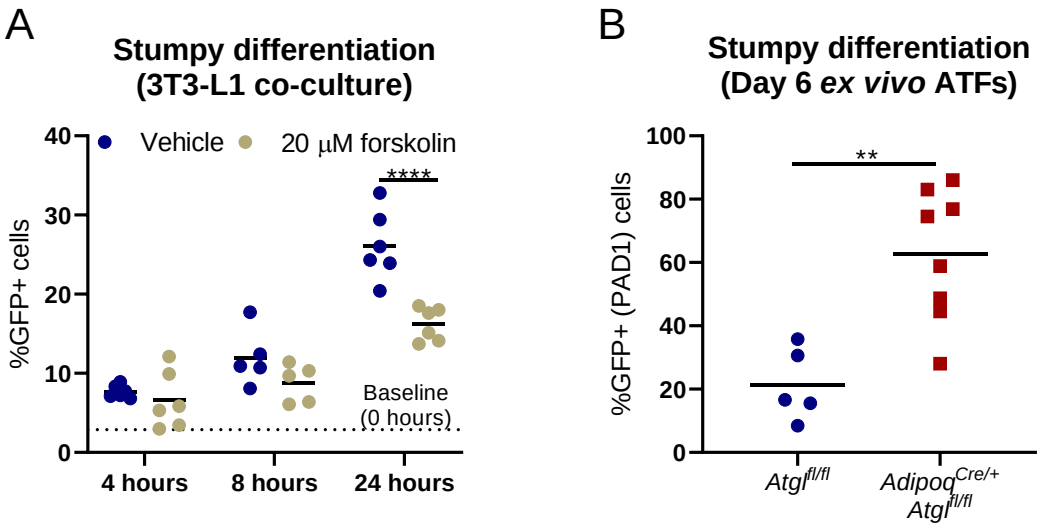

Figure 32 – Adipocyte lipolysis does not promote stumpy differentiation. (A) Percentage of stumpy forms (GFP+ cells) in co-cultures of 3T3-L1 adipocytes infected with $5x10^4$ AnTat1.1E 90–13 GFP::PAD1utr parasites and treated with 20 μM forskolin or vehicle (DMSO). Dashed line denotes the percentage of GFP+ events (≈ 3%) in the inoculum used to infected 3T3-L1 adipocyte cultures. **(B)** Percentage of stumpy forms (GFP+ cells) in AnTat1.1E 90–13 GFP::PAD1utr parasites isolated from the gonadal AT of *Atgl*$^{fl/fl}$ and *Adipoq*$^{Cre/+}$-*Atgl*$^{fl/fl}$ mice at day 6 post-infection. Error bars represent the SEM (**A**: n=5-6 wells per group; **B**: 5-8 mice per group) Statistical analysis was performed with **(A)** Two-way ANOVA using Sidak's test for multiple comparisons or **(B)** two-tailed unpaired t-test. *, P<0.05; **, P<0.01; ***, P<0.001; ****, P<0.0001.

Together, data from these *in vivo* and *in vitro* infections indicate that adipocyte lipolysis limits parasite growth through a mechanism that is independent of stumpy differentiation.

Discussion of Part 2

The role of the AT in whole-organism homeostasis has become an important study in a multitude of pathologies. It is now acknowledged that the function of the AT is not solely that of an inert storage of fat. Indeed, dysregulation of AT function has systemic consequences and has thus been implicated in the establishment of metabolic syndrome, in the increased incidence of multiple malignancies as well as cardiovascular disease[31]. Epidemiological and fundamental research data point towards an important role for AT function in the pathogenesis of infectious diseases.

However, in most studies, this impact of AT function in disease progression does not stem from a disruption of these tissues' homeostasis by the infectious agent *per se* but are rather the consequence of a pre-existing comorbidity or condition, usually obesity and/or metabolic syndrome.

A likely exception to these cases may be found in pathogens that actively colonize the AT. Among these, *T. brucei* infection is an interesting, and perhaps unique, case where a high pathogen burden and pronounced immune response are found in the AT. Both AT parasite burden and ensuing immune response are bound to disrupt normal adipocyte function, which in turn affect pathogenesis.

Impact of ATGL-dependent adipocyte lipolysis on body fat

In this work we have shown that during a *T. brucei* infection adipocytes become progressively smaller, in a process that correlates with an increase in ATGL-dependent lipolysis. Other studies have shown a similar role for ATGL in the loss of fat mass. Specifically, fully ATGL-deficient mice are protected from fat loss induced by Lewis lung carcinoma or B16 melanoma cells[116]. Moreover, burn injury-induced loss of body weight and adipocyte volume was partially prevented in *Adipoq*$^{Cre/+}$*-Atgl*$^{fl/fl}$ mice[235]. Interestingly, in a model of lymphocytic choriomeningitis virus infection, where significant loss of AT and total weight occur, *Adipoq*$^{Cre/+}$*-Atgl*$^{fl/fl}$ mice were not protected from loss of total weight[236]. This suggests the relative relevance of ATGL in fat mass retention is disease-specific.

Increased adipocyte lipolysis is likely one among metabolic alterations occurring simultaneously. Indeed, previous work in the early 1980s using rabbits experimentally infected with *T. brucei* has established a link between hyperlipidemia and reduced LPL activity due to increased TNF-α levels[237]. Here, inhibition of LPL

prevented the export of lipids contained in lipoproteins from circulation and into the AT, leading to decreased lipogenesis.

Elevated TNF-α levels are often found in pathological conditions where a wasting phenotype, or cachexia, develops[238,239]. Moreover, treatment of several cell types, including adipocytes, with this cytokine promotes the upregulation of catabolic processes in detriment of anabolic ones, a phenotype often termed as cellular cachexia[233].

Although never formally tested, this collective body of work led to the logic conclusion that inhibition of lipogenesis may be central in the progressive emaciation phenotype observed in natural and experimental *T. brucei* infections.

Recently, a greater appreciation of the complex inflammatory profile leading to the development of cachexia has re-framed the role of TNF-α as one of many inflammatory cytokines in the development and progression of wasting syndromes[115].

Although it remains to be elucidated exactly how relevant LPL activity is in the loss of fat mass during a *T. brucei* infection, our data suggests that TNF-α is not sufficient to induce fat loss. Consistently, TNF-α deficient mice, which should retain significant LPL activity, showed only a small delay in loss of fat mass (Fig. 27C). Indeed, our data show that fat loss and adipocyte volume reduction require the activation of adipocyte lipolysis (Fig. 24D). This dominance of increased adipocyte lipolysis over reduced lipogenesis in fat loss has also been reported in the context of CAC[240].

Ablation of adipocyte-ATGL significantly impaired loss of whole-organism fat mass, however it was unable to completely abolish it (Fig. 23D). On the one hand, even in absolute absence of adipocyte-lipolysis, a significant loss of total fat mass would still be expected, as most cells are capable of storing fats within cytosolic lipid droplets, which may then be consumed during infection. On the other hand, it is possible that even in absence of adipocyte-ATGL during a *T. brucei* infection, TAG may still be hydrolyzed at a slower rate by HSL. This lipase is able to hydrolyze TAG, despite having 10-fold higher affinity for DAG[241]. Moreover, if at any point acid lipolysis is activated in adipocytes during infection, LAL would be able to fully catalyze the conversion of TAG into free fatty acids and glycerol without requiring the activity of any neutral lipase[65].

Altogether, our data show that activation of adipocyte lipolysis is a central, but not exclusive, pathway in fat loss and emaciation during *T. brucei* infections. To the best of our knowledge, this is the first report showing that adipocyte-ATGL activity is involved in loss of fat mass in the context of an infectious disease.

Induction of adipocyte lipolysis

In this work, we attempted to isolate the specific signal(s) that induce adipocyte lipolysis during a *T. brucei* infection. We were partially successful in this. We found that both host-derived and parasite-derived factors are capable of inducing adipocyte lipolysis. Among host-derived factors, T and B cell-secreted cytokines (or secreted by other cells after T and/or B cell-dependent activation) are the best candidates for adipocyte lipolysis inducers.

This immune-centric hypothesis is supported by the reduced loss of fat mass observed in infected Rag2$^{-/-}$ mice (Fig. 27B), by their low *ex vivo* AT lipolysis upon infection (Fig. 27B), and by the inability of their plasma, unlike plasma from infected WT mice, to induce lipolysis on *in vitro* grown adipocytes (Fig. 27C).

In the future, assessing which cytokines are increased in the sera of infected WT mice when compared to infected Rag2$^{-/-}$ mice will provide us with a list of lipolysis inducing candidates. These can then be selectively depleted from the plasma of infected mice and then tested for their capacity to induce *in vitro* lipolysis. Ultimately, this strategy should yield a short list of lipolysis-inducing cytokines that can be tested further using *in vivo* models.

Although our data suggest that immune cues are the overarching inducers of adipocyte lipolysis *in vivo*, we were able to show that *T. brucei* is also able to induce adipocyte lipolysis in a co-culture system containing only parasites and adipocytes (Fig. 29). This induction is higher upon direct parasite-adipocyte contact; however, it also occurs to a lesser extent when parasite-adipocyte communication is limited to soluble factors.

The nature of these parasite factors, their route of delivery (*i.e.* secretion, EV-loading and exocytosis, surface-surface ligand-receptor interactions) as well as their adipocyte interacting partners remain to be identified. The relevance of these

interactions in an *in vivo* context are still a matter of speculation. It is possible that early *T. brucei*-adipocyte interactions, preceding the formation of an immune response, contribute to the upregulation of lipolysis in individual adipocytes. These interactions could contribute to an early modulation of the microenvironment of the AT (and other tissues containing adipocytes) to the parasite's benefit.

Effect of adipocyte lipolysis on pathology

Mice deficient for ATGL-dependent adipocyte lipolysis showed a significant reduction in survival when compared to WT littermate controls (Fig. 22A). These differences were not due to changes in parasitemia, as *Adipoq*$^{Cre/+}$*-Atgl*$^{fl/fl}$ mice were equally able as *Atgl*$^{fl/fl}$ to clear the successive parasitemia peaks, suggesting that adipocyte lipolysis does not impact systemic parasite elimination (Fig. 22B).

Attempts to identify differential cause of death between *Atgl*$^{fl/fl}$ and *Adipoq*$^{Cre/+}$*-Atgl*$^{fl/fl}$ mice were thus far inconclusive, as all organs submitted to pathology analysis showed comparable immunopathology, irrespective of host genotype (Fig. 23E). This does not rule out a differential cause of death in *Adipoq*$^{Cre/+}$*-Atgl*$^{fl/fl}$ mice, or a faster progression towards the same cause of death of *Atgl*$^{fl/fl}$ mice. Accordingly, a future assessment of hematological, clinical chemistry and urinalysis parameters of infected *Atgl*$^{fl/fl}$ and *Adipoq*$^{Cre/+}$*-Atgl*$^{fl/fl}$ mice throughout infection may help identify specific organ/system failures[242]. In turn, this will useful to further characterize the impact of adipocyte lipolysis in overall disease progression.

Local parasite burden control by adipocyte lipolysis

The abundant availability of fatty acids and glycerol in the AT milieu may provide the parasite with additional substrates for energy production through β-oxidation and glycolysis. It is thus puzzling that increasing the availability of these metabolites through upregulation of adipocyte lipolysis leads to a significantly reduced local parasite burden.

Our data indicate that increased stumpy differentiation is not responsible for this reduction in parasite numbers. In fact, data from two distinct models support a model where increased adipocyte lipolysis exerts an inhibitory effect on stumpy differentiation. Specifically, chemical induction of lipolysis on *T. brucei*-3T3-L1

adipocyte co-cultures yields a significantly lower percentage of stumpy forms after 24 h of co-culture (Fig. 32A). Moreover, parasites extracted from the AT of lipolysis deficient *Adipoq*$^{Cre/+}$*-Atgl*$^{fl/fl}$ mice at day 6 post-infection are predominantly stumpy forms, unlike those extracted from WT littermate controls (Fig. 32B).

A likely scenario is that lipolysis is not directly modulating stumpy differentiation. Instead, lipolysis may be limiting parasite growth through an alternative mechanism, resulting in lower parasite densities, thus preventing activation of the density-dependent parasite quorum sensing mechanism that governs stumpy differentiation. Here, the parasite secretes two peptidases (*i.e.* Tb927.11.12850 and Tb927.11.2500) that cleave host proteins into oligopeptides that induce stumpy differentiation upon uptake[7].

Another possible mechanism through which parasite density is limited by adipocyte lipolysis relies on fatty acid induced lipotoxicity. Here, excessive fatty acid endocytosis by *T. brucei* may exceed the parasite's capacity to catabolize these species through β-oxidation or to anabolize them into relatively stable acylglycerol species stored into lipid droplets. This form of lipid-mediated parasite killing has been elegantly shown in *Toxoplasma gondii*, where excessive supplementation of unsaturated C18 and C16 fatty acids or inhibition of *T. gondii* DGAT-1 (*i.e.* inhibiting lipid droplet formation) led to a marked reduction of doubling time and parasite viability[243].

Although lipid droplet formation has is yet to be thoroughly addressed in mammalian stages of *T. brucei*, there is compelling evidence that their formation is essential for procyclic from survival[244]. Here, ablation of TbLpn, (Tb927.7.5450) a lipin that converts phosphatidic acid into diacylglycerol, leads to defective lipid droplet formation, mitochondrial abnormalities and reduced parasite viability under culture conditions[244]. Considering the impact of lipid droplet formation in both *T. brucei* procyclic forms and in mammalian infective *T. gondii*, it is tempting to speculate that similar lipotoxicity phenotypes may occur with mammalian stages of *T. brucei* in the interstitial spaces of the AT upon upregulation of adipocyte lipolysis.

Interestingly, the putative *T. brucei* DGAT-1 enzyme Tb927.3.1700[245] is significantly upregulated in parasites extracted from the AT when compared to parasites extracted from the blood[19]. This suggests that in the AT the parasite requires a

higher conversion rate of DAG into TAG to remove excessive FFAs. It is thus possible that under conditions of prolonged adipocyte lipolysis, the parasite's ability to transform FFAs into TAG or its overall storage capacity will be exceeded, resulting in a lipotoxic effect.

Overall, further study on how adipocyte lipolysis improves host control over *T. brucei* may lead to the identification of new mechanisms that may be useful in our understanding of the pathology of trypanosomiasis and in the development novel therapies against African trypanosomiasis.

In a broader view, and although further research is needed, this work suggest that ATGL (and potentially other lipases) in adipocytes can play a microbicidal role. In the future, it would be interesting to study whether and how adipocyte lipolysis affects the pathogen burden of different microorganisms know to colonize the AT. This is especially important because depending on the pathogen, adipocyte lipolysis may promote distinct effects on pathogen proliferation. Specifically, it has been shown that inhibition of ATGL or HSL inhibits intracellular *Chlamydia pneumonia* growth in 3T3-L1 adipocytes[121].This work is important for a general understanding of the role for AT function in the pathogenesis of infectious diseases. Loss of fat mass is a common clinical feature of many infectious diseases and may play a more central role in pathogenesis than previously anticipated. Even in the absence of any AT-associated disease (*e.g.* type 2 diabetes or obesity), we show that AT metabolism can significantly impacts host survival. It remains to be clarified whether other infectious diseases are similarly affected by modulation of AT metabolism, especially those where the AT is a site of active infection (*e.g. T. cruzi*, *M. tuberculosis*, HIV).

Importantly, pharmacological interventions aimed at managing type 2 diabetes and/or obesity ultimately affect adipocyte metabolism. The use of these drugs is becoming more widespread in response to the increasing in prevalence of metabolic diseases. Accordingly, a greater understanding of how AT metabolism affects the pathogenesis of different infectious diseases may be invaluable in the proper treatment of infected patients concomitantly being treated with drugs that modulate adipocyte metabolism.

General Discussion

The study of extravascular colonization of tissues by *T. brucei*, and of properties of each tissue that determine the extent of parasite colonization is just in its infancy. Here, we attempted to understand which properties of the AT make it a preferential target for colonization by *T. brucei*.

We found no evidence of a defective immune response in the AT, which could provide the parasite with a niche where it escape the strong immune response observed in the blood. In fact, we observed that an immune response is mounted in the AT upon a *T. brucei* infection, and that this immune response contains protective T and B cells, as well as VSG-specific antibodies. In turn, this local immune response is able to clear extravascular parasites. However, a clear limitation of this study is the inability to precisely assess the contribution of the local immune response to local parasite elimination. This stems from the inability to disassociate the effect of circulating immune factors (*e.g.* cytokines and antibodies) from those locally produce in the AT.

Interestingly, in addition to parasite elimination, the immune response mounted during a *T. brucei* infection is the central player behind the loss of fat mass. This effect appears to be mediated by T and or B cells and occurs through ATGL-dependent adipocyte lipolysis. In turn, inhibition of lipolysis promotes accumulation of higher parasite burden, while activation of lipolysis prevents parasite growth. This suggests in the context of a *T. brucei* infection, adipocyte lipolysis in the AT is a trypanocidal mechanism.

The reason why parasites accumulate so extensively in the AT tissue remains to be elucidated. One possible hypothesis stemming from this work is that colonization of the AT promotes activation of ATGL-dependent adipocyte lipolysis, which in turn prolongs host survival. In naturally occurring infections this would be advantageous for the parasite, as increased host survival provides the parasite with more chances of being taken up by a tsetse fly.

Another possible scenario is that the high parasite burdens observed in visceral and subcutaneous AT depots are actually secondary events of another evolutionarily selected trait. Specifically, *T. brucei* is known to accumulate in the vicinity of, and interact with, dermal adipocytes[27,246]. Chemotaxis-based homing of parasites to these adipocytes would place them in a privileged anatomical position to be taken

up the tsetse vector. As parasitemia is often undetectable in natural infections[247,248], and thus transmission through blood uptake inefficient, alternative strategies to increase transmission would pose a strong evolutionary driving force for the parasite. Here, parasite homing to the AT has been shown to be partially dependent on CD36[18], which, in addition to being ubiquitously expressed in adipocytes, is also highly expressed in the skin[249].

Several outstanding questions remain to be answered. First, which lymphocytes are responsible for the loss of fat mass? This can be answered by performing adoptive transfer of either CD4+ T cells, CD8+ T cells or B cells into *Rag2*$^{-/-}$ mice, enabling us to determine the relative contribution of each of these cell types in the loss of fat mass. Second, which cytokine(s) induce adipocyte lipolysis during infection? To answer this, we will probe which cytokines are increased in WT infected mice when compared to *Rag2*$^{-/-}$ infected mice. These cytokines can then be antibody-depleted from the plasma of infected WT mice and then tested for its capacity to induce lipolysis in *in vitro* grown adipocytes.

Another outstanding question pertains to the requirement for parasite colonization of the interstitial spaces of the AT for lipolysis induction to occur. Unfortunately, this is currently challenging to study using *T. brucei*, as no efficient way to block AT colonization without significant systemic consequences has been found. A possible alternative would be to compare mice infected with either *T. brucei* or *T. congolense*. The latter is a close relative of *T. brucei* and also causes a chronic disease characterized by successive waves of parasitemia while exclusively occupying intravascular spaces[250]. Accordingly, studying AT inflammation and metabolism during a *T. congolense* infection may yield important data to understand *T. brucei* biology.

Lastly, it remains to be elucidated how adipocyte-lipolysis helps control *T. brucei* burden. In the future, assessing the parasite's response to different concentrations of fatty acids with varying lengths and saturations, as well as glycerol, will elucidate which lipolytic component(s) enables parasite control.

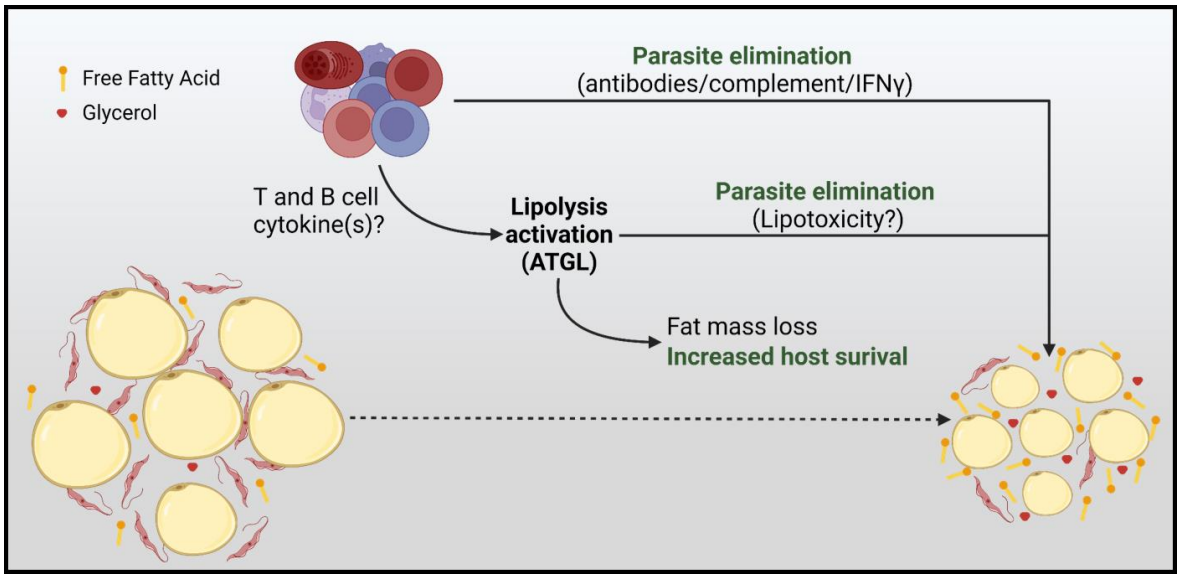

Figure 33 – A coordinated immuno-metabolic response protects the host at the expense of fat mass. *T. brucei* infection induces immune cell recruitment to the adipose tissue. In turn, these immune cells secrete inflammatory signals and antibodies that promote immune clearance of the parasite and induce ATGL activity in adipocytes. Activation of ATGL improves host survival and promotes loss of fat mass. Increased extracellular levels of fatty acids and glycerol resulting from ATGL activity promote local parasite elimination, possibly through lipotoxicity. Figure created using BioRender.com.

References

1. Büscher, P., Cecchi, G., Jamonneau, V. & Priotto, G. Human African trypanosomiasis. *Lancet* **390**, 2397–2409 (2017).

2. Morrison, L. J., Vezza, L., Rowan, T. & Hope, J. C. Animal African Trypanosomiasis: Time to Increase Focus on Clinically Relevant Parasite and Host Species. *Trends Parasitol.* **32**, 599–607 (2016).

3. Spickler, A. R. African Animal Trypanosomiasis African Animal Trypanosomiasis. http://www.cfsph.iastate.edu/ DiseaseInfo/factsheets.php. (2018).

4. Vickerman, K. Developmental cycles and biology of pathogenic trypanosomes. *Br. Med. Bull.* **41**, 105–114 (1985).

5. Vassella, E., Reuner, B., Yutzy, B. & Boshart, M. Differentiation of African trypanosomes is controlled by a density sensing mechanism which signals cell cycle arrest via the cAMP pathway. *J. Cell Sci.* **110**, 2661–2671 (1997).

6. Tettey, M. D., Rojas, F. & Matthews, K. R. Extracellular release of two peptidases dominates generation of the trypanosome quorum-sensing signal. *Nat. Commun.* **13**, 1–14 (2022).

7. Rojas, F. *et al.* Oligopeptide Signaling through TbGPR89 Drives Trypanosome Quorum Sensing. *Cell* **176**, 306-317.e16 (2019).

8. Black, S. J., Jack, R. M. & Morrison, W. I. Host-parasite interactions which influence the virulence of Trypanosoma (Trypanozoon) brucei brucei organisms. *Acta Trop.* **40**, 11–18 (1983).

9. Turner, C. M. R. Replication, differentiation, growth and the virulence of Trypanosoma brucei infections. *Parasitology* **111**, 289–300 (1995).

10. Rico, E. *et al.* Bloodstream form pre-adaptation to the tsetse fly in Trypanosoma brucei. *Front. Cell. Infect. Microbiol.* **4**, 1–15 (2013).

11. Schuster, S. *et al.* Unexpected plasticity in the life cycle of Trypanosoma brucei. *Elife* **10**, 1–25 (2021).

12. Hee Lee, S., Stephens, J. L. & Englund, P. T. A fatty-acid synthesis mechanism specialized for parasitism. *Nat. Rev. Microbiol.* **5**, 287–297

(2007).

13. Franco, J. R., Simarro, P. P., Diarra, A. & Jannin, J. G. Epidemiology of human African trypanosomiasis. *Clin. Epidemiol.* **6**, 257–275 (2014).

14. World Health Organization. No Title. *Trypanosomiasis, human African (sleeping sickness)* https://www.who.int/news-room/fact-sheets/detail/trypanosomiasis-human-african-(sleeping-sickness) (2019).

15. WHO. *Ending the neglect to attain the Sustainable Development Goals: a road map for neglected tropical diseases 2021–2030. Geneva: World Health Organization (https://www.who.int/neglected_diseases/Revised-DraftNTD-Roadmap-23Apr2020.pdf)*. *Word Health Organization* (2020).

16. Kennedy, P. G. E. Clinical features, diagnosis, and treatment of human African trypanosomiasis (sleeping sickness). *Lancet. Neurol.* **12**, 186–94 (2013).

17. Pereira, S. S., Trindade, S., De Niz, M. & Figueiredo, L. M. Tissue tropism in parasitic diseases. *Open Biol.* **9**, (2019).

18. De Niz, M. *et al.* Organotypic endothelial adhesion molecules are key for Trypanosoma brucei tropism and virulence. *Cell Rep.* **36**, (2021).

19. Trindade, S. *et al.* Trypanosoma brucei Parasites Occupy and Functionally Adapt to the Adipose Tissue in Mice. *Cell Host Microbe* **19**, 837–848 (2016).

20. Tanowitz, H. B., Scherer, P. E., Mota, M. M. & Figueiredo, L. M. Adipose Tissue: A Safe Haven for Parasites? *Trends in Parasitology* vol. 33 276–284 (2017).

21. Mott, F. W. *Reports of the Sleeping Sickness Commission No. VII*. *Search* (1907).

22. Calwell, H. G. The pathology of the brain in rhodesian trypanosomiasis. *Trans. R. Soc. Trop. Med. Hyg.* **30**, (1937).

23. Giroud, C. *et al.* Murine models for Trypanosoma brucei gambiense disease progression - From silent to chronic infections and early brain tropism. *PLoS Negl. Trop. Dis.* **3**, (2009).

24. Forrester, J. V., McMenamin, P. G. & Dando, S. J. CNS infection and immune privilege. *Nat. Rev. Neurosci.* **19**, 655–671 (2018).

25. Crump, A. J. & Brady, J. Circadian activity patterns in three species of tsetse fly: Glossina palpalis, austeni and morsitans. *Physiol. Entomol.* **4**, 311–318 (1979).

26. McGovern, T. W. Cutaneous Manifestations of African Trypanosomiasis. *Arch. Dermatol.* **131**, 1178 (1995).

27. Capewell, P. *et al.* The skin is a significant but overlooked anatomical reservoir for vector-borne African trypanosomes. *Elife* **5**, 1–17 (2016).

28. Capewell, P. *et al.* Resolving the apparent transmission paradox of African sleeping sickness. *PLoS Biol.* **17**, 1–6 (2019).

29. Reuter, C. *et al.* Vector-borne Trypanosoma brucei parasites develop in artificial human skin and persist as skin tissue forms (Preprint). *bioRxiv* 2021.05.13.443986 (2021).

30. Szöör, B., Haanstra, J. R., Gualdrón-López, M. & Michels, P. A. M. Evolution, dynamics and specialized functions of glycosomes in metabolism and development of trypanosomatids. *Curr. Opin. Microbiol.* **22**, 79–87 (2014).

31. Rosen, E. D. & Spiegelman, B. M. What we talk about when we talk about fat. *Cell* **156**, 20–44 (2014).

32. Ahima, R. S. *et al.* Adipose tissue as an endocrine organ. *Trends Endocrinol. Metab.* **11**, 327–32 (2000).

33. Cook KS, Min HY, Johnson D, Chaplinsky RJ, Flier JS, Hunt CR, S. B. Adipsin : A Circulating Serine Protease Homolog. *Science* **237**, 402–5 (1987).

34. Mohamed-Ali, V. *et al.* Subcutaneous adipose tissue releases interleukin-6, but not tumor necrosis factor-α, in vivo. *J. Clin. Endocrinol. Metab.* **82**, 4196–4200 (1997).

35. Hotamisligil, G. S., Shargill, N. S. & Spiegelman, B. M. 9. H. Semb, J.

Peterson, J. Tavernier, T. Olivecrona, J. Biol. Chtem. 262, 8390 (1987). **259**, 87–92 (1993).

36. Chait, A. & den Hartigh, L. J. Adipose Tissue Distribution, Inflammation and Its Metabolic Consequences, Including Diabetes and Cardiovascular Disease. *Front. Cardiovasc. Med.* **7**, 1–41 (2020).

37. Torres, N., Vargas-Castillo, A. E. & Tovar, A. R. *Adipose Tissue: White Adipose Tissue Structure and Function*. *Encyclopedia of Food and Health* (Elsevier Ltd., 2015). doi:10.1016/B978-0-12-384947-2.00006-4.

38. Chang, E., Varghese, M. & Singer, K. Gender and Sex Differences in Adipose Tissue. *Curr. Diab. Rep.* **18**, (2018).

39. Cheong, L. Y. & Xu, A. Intercellular and inter-organ crosstalk in browning of white adipose tissue: Molecular mechanism and therapeutic complications. *J. Mol. Cell Biol.* **13**, 466–479 (2021).

40. Ameer, F., Scandiuzzi, L., Hasnain, S., Kalbacher, H. & Zaidi, N. De novo lipogenesis in health and disease. *Metabolism.* **63**, 895–902 (2014).

41. Solinas, G., Borén, J. & Dulloo, A. G. De novo lipogenesis in metabolic homeostasis: More friend than foe? *Mol. Metab.* **4**, 367–377 (2015).

42. Grabner, G. F., Xie, H., Schweiger, M. & Zechner, R. Lipolysis: cellular mechanisms for lipid mobilization from fat stores. *Nat. Metab.* **3**, 1445–1465 (2021).

43. Wang, Z., Wang, Q. A., Liu, Y. & Jiang, L. Energy metabolism in brown adipose tissue. *FEBS J.* **288**, 3647–3662 (2021).

44. Fedorenko, A., Lishko, P. V. & Kirichok, Y. Mechanism of fatty-acid-dependent UCP1 uncoupling in brown fat mitochondria. *Cell* **151**, 400–413 (2012).

45. Haman, F. & Blondin, D. P. Shivering thermogenesis in humans: Origin, contribution and metabolic requirement. *Temperature* **4**, 217–226 (2017).

46. Ikeda, K., Maretich, P. & Kajimura, S. The Common and Distinct Features of Brown and Beige Adipocytes. *Trends Endocrinol. Metab.* **29**, 191–200

(2018).

47. Wu, J. *et al.* Beige adipocytes are a distinct type of thermogenic fat cell in mouse and human. *Cell* **150**, 366–376 (2012).

48. Lee, M. K., Lee, B. & Kim, C. Y. Natural extracts that stimulate adipocyte browning and their underlying mechanisms. *Antioxidants* **10**, 1–17 (2021).

49. Lipke, K., Kubis-Kubiak, A. & Piwowar, A. Molecular Mechanism of Lipotoxicity as an Interesting Aspect in the Development of Pathological States—Current View of Knowledge. *Cells* **11**, (2022).

50. Tumova, J., Andel, M. & Trnka, J. Excess of free fatty acids as a cause of metabolic dysfunction in skeletal muscle. *Physiol. Res.* **65**, 193–207 (2016).

51. Liu, J., Han, L., Zhu, L. & Yu, Y. Free fatty acids, not triglycerides, are associated with non-alcoholic liver injury progression in high fat diet induced obese rats. *Lipids Health Dis.* **15**, 1–9 (2016).

52. Zhang, J. *et al.* Association between serum free fatty acid levels and nonalcoholic fatty liver disease: A cross-sectional study. *Sci. Rep.* **4**, 1–6 (2014).

53. Wueest, S., Rapold, R. A., Rytka, J. M., Schoenle, E. J. & Konrad, D. Basal lipolysis, not the degree of insulin resistance, differentiates large from small isolated adipocytes in high-fat fed mice. *Diabetologia* **52**, 541–546 (2009).

54. Kumari, A., Kristensen, K. K., Ploug, M. & Lund Winther, A. M. The importance of lipoprotein lipase regulation in atherosclerosis. *Biomedicines* **9**, 1–24 (2021).

55. Knowles, S. E., Jarrett, I. G., Filsell, O. H. & Ballard, F. J. Production and utilization of acetate in mammals. *Biochem. J.* **142**, 401–411 (1974).

56. Sone, H. *et al.* Acetyl-coenzyme A synthetase is a lipogenic enzyme controlled by SREBP-1 and energy status. *Am. J. Physiol. Metab.* **282**, E222–E230 (2002).

57. Takeuchi, K. & Reue, K. Biochemistry, physiology, and genetics of GPAT, AGPAT, and lipin enzymes in triglyceride synthesis. *Am. J. Physiol. -*

Endocrinol. Metab. **296**, (2009).

58. Liss, K. H. H. *et al.* Metabolic importance of adipose tissue monoacylglycerol acyltransferase 1 in mice and humans. *J. Lipid Res.* **59**, 1630–1639 (2018).

59. Harris, C. A. *et al.* DGAT enzymes are required for triacylglycerol synthesis and lipid droplets in adipocytes. *J. Lipid Res.* **52**, 657–667 (2011).

60. Strawford, A., Antelo, F., Christiansen, M. & Hellerstein, M. K. Adipose tissue triglyceride turnover, de novo lipogenesis, and cell proliferation in humans measured with 2H2O. *Am. J. Physiol. - Endocrinol. Metab.* **286**, 577–588 (2004).

61. Hsiao, W. Y. & Guertin, D. A. De Novo Lipogenesis as a Source of Second Messengers in Adipocytes. *Curr. Diab. Rep.* **19**, (2019).

62. Nagai, A., Sato, T., Akimoto, N., Ito, A. & Sumida, M. Isolation and identification of histone H3 protein enriched in microvesicles secreted from cultured sebocytes. *Endocrinology* **146**, 2593–2601 (2005).

63. Lee, H. *et al.* Compositional dynamics of the milk fat globule and its role in infant development. *Front. Pediatr.* **6**, (2018).

64. Flaherty, S. E. *et al.* A lipase-independent pathway of lipid release and immune modulation by adipocytes. *Science (80-.).* **363**, 989–993 (2019).

65. Zechner, R., Madeo, F. & Kratky, D. Cytosolic lipolysis and lipophagy: Two sides of the same coin. *Nat. Rev. Mol. Cell Biol.* **18**, 671–684 (2017).

66. Zimmermann, R. *et al.* Fat mobilization in adipose tissue is promoted by adipose triglyceride lipase. *Science (80-.).* **306**, 1383–1386 (2004).

67. Fredrikson, G., Strålfors, P., Nilsson, N. O. & Belfrage, P. Hormone-sensitive lipase of rat adipose tissue. Purification and some properties. *J. Biol. Chem.* **256**, 6311–6320 (1981).

68. Recazens, E., Mouisel, E. & Langin, D. Hormone-sensitive lipase: sixty years later. *Prog. Lipid Res.* **82**, 101084 (2021).

69. Vaughan, M., Berger, J. E. & Steinberg, D. Hormone-sensitive Lipase and Monoglyceride Lipase Activities in Adipose Tissue. *J. Biol. Chem.* **239**, 401–

409 (1964).

70. Tornqvist, H. & Belfrage, P. Purification and some properties of a monoacylglycerol hydrolyzing enzyme of rat adipose tissue. *J. Biol. Chem.* **251**, 813–819 (1976).

71. Karlsson, M., Contreras, J. A., Hellman, U., Tornqvist, H. & Holm, C. cDNA cloning, tissue distribution, and identification of the catalytic triad of monoglyceride lipase. Evolutionary relationship to esterases, lysophospholipases, and haloperoxidases. *J. Biol. Chem.* **272**, 27218–27223 (1997).

72. White, J. E. & Engel, F. L. A Lipolytic Action of Epinephrine and Norepinephrine on Rat Adipose Tissue in vitro. *Proc. Soc. Exp. Biol. Med.* **99**, 375–378 (1958).

73. Gasic, S., Tian, B. & Green, A. Tumor necrosis factor α stimulates lipolysis in adipocytes by decreasing G(i) protein concentrations. *J. Biol. Chem.* **274**, 6770–6775 (1999).

74. Van Hall, G. *et al.* Interleukin-6 stimulates lipolysis and fat oxidation in humans. *J. Clin. Endocrinol. Metab.* **88**, 3005–3010 (2003).

75. Zhang, W. *et al.* Adipocyte lipolysis-stimulated interleukin-6 production requires sphingosine kinase 1 activity. *J. Biol. Chem.* **289**, 32178–32185 (2014).

76. Zhang, H. H., Halbleib, M., Ahmad, F., Manganiello, V. C. & Greenberg, A. S. Differentiated Human Adipocytes Through Activation of Extracellular Signal – Related Kinase and Elevation of Intracellular cAMP. *Diabetes* **51**, 2929–2935 (2002).

77. Oppenheimer, J. H., Schwartz, H. L., Lane, J. T. & Thompson, M. P. Functional relationship of thyroid hormone-induced lipogenesis, lipolysis, and thermogenesis in the rat. *J. Clin. Invest.* **87**, 125–132 (1991).

78. Chakrabarti, P. *et al.* Insulin Inhibits Lipolysis in Adipocytes via the Evolutionarily Conserved mTORC1-Egr1-ATGL-Mediated Pathway. *Mol. Cell. Biol.* **33**, 3659–3666 (2013).

79. Chernick, S. S., Spooner, P. M., Garrison, M. M. & Scow, R. W. Effect of epinephrine and other lipolytic agents on intracellular lipolysis and lipoprotein lipase activity in 3T3-L1 adipocytes. *J. Lipid Res.* **27**, 286–294 (1986).

80. Kawamura, M. *et al.* Hormone-sensitive lipase in differentiated 3T3-L1 cells and its activation by cyclic AMP-dependent protein kinase. *Proc. Natl. Acad. Sci. U. S. A.* **78**, 732–736 (1981).

81. Krintel, C., Mörgelin, M., Logan, D. T. & Holm, C. Phosphorylation of hormone-sensitive lipase by protein kinase A in vitro promotes an increase in its hydrophobic surface area. *FEBS J.* **276**, 4752–4762 (2009).

82. Kimmel, A. R. & Sztalryd, C. The Perilipins: Major Cytosolic Lipid Droplet-Associated Proteins and Their Roles in Cellular Lipid Storage, Mobilization, and Systemic Homeostasis. *Annu. Rev. Nutr.* **36**, 471–509 (2016).

83. Greenberg, A. S. *et al.* Stimulation of Lipolysis and Hormone-sensitive Lipase via the Extracellular Signal-regulated Kinase Pathway. *J. Biol. Chem.* **276**, 45456–45461 (2001).

84. Cullberg, K. B., Larsen, J. Ø., Pedersen, S. B. & Richelsen, B. Effects of LPS and dietary free fatty acids on MCP-1 in 3T3-L1 adipocytes and macrophages in vitro. *Nutr. Diabetes* **4**, e113 (2014).

85. Chi, W. *et al.* Bacterial peptidoglycan stimulates adipocyte lipolysis via NOD1. *PLoS One* **9**, 1–9 (2014).

86. Zu, L. *et al.* Bacterial endotoxin stimulates adipose lipolysis via toll-like receptor 4 and extracellular signal-regulated kinase pathway. *J. Biol. Chem.* **284**, 5915–5926 (2009).

87. Souza, S. C. *et al.* TNF-α induction of lipolysis is mediated through activation of the extracellular signal related kinase pathway in 3T3-L1 adipocytes. *J. Cell. Biochem.* **89**, 1077–1086 (2003).

88. Scherer, T. *et al.* Brain Insulin Controls Adipose Tissue Lipolysis and Lipogenesis. *Cell Metab.* **13**, 183–194 (2011).

89. Ji, Y. K., Tillison, K., Lee, J. H., Rearick, D. A. & Smas, C. M. The adipose

tissue triglyceride lipase ATGL/PNPLA2 is downregulated by insulin and TNF-α in 3T3-L1 adipocytes and is a target for transactivation by PPARγ. *Am. J. Physiol. - Endocrinol. Metab.* **291**, 115–127 (2006).

90. Petersen, M. C. & Shulman, G. I. Mechanisms of insulin action and insulin resistance. *Physiol. Rev.* **98**, 2133–2223 (2018).

91. DiPilato, L. M. *et al.* The Role of PDE3B Phosphorylation in the Inhibition of Lipolysis by Insulin. *Mol. Cell. Biol.* **35**, 2752–2760 (2015).

92. Hjelholt, A. J. *et al.* Temporal patterns of lipolytic regulators in adipose tissue after acute growth hormone exposure in human subjects: A randomized controlled crossover trial. *Mol. Metab.* **29**, 65–75 (2019).

93. Kopchick, J. J., Berryman, D. E., Puri, V., Lee, K. Y. & Jorgensen, J. O. L. The effects of growth hormone on adipose tissue: old observations, new mechanisms. *Nat. Rev. Endocrinol.* **16**, 135–146 (2020).

94. Sharma, R. *et al.* Growth hormone controls lipolysis by regulation of FSP27 expression. *J. Endocrinol.* **239**, 289–301 (2018).

95. Liu, L. R. *et al.* Serum amyloid a induces lipolysis by downregulating perilipin through ERK1/2 and PKA signaling pathways. *Obesity* **19**, 2301–2309 (2011).

96. Kaltenecker, D. *et al.* Adipocyte STAT5 deficiency promotes adiposity and impairs lipid mobilisation in mice. *Diabetologia* **60**, 296–305 (2017).

97. Kaltenecker, D. *et al.* STAT5 is required for lipid breakdown and beta-adrenergic responsiveness of brown adipose tissue. *Mol. Metab.* **40**, 101026 (2020).

98. Chen, J., Lu, Y., Tian, M. & Huang, Q. Molecular mechanisms of foxo1 in adipocyte differentiation. *J. Mol. Endocrinol.* **62**, R239–R253 (2019).

99. Caron, A., Richard, D. & Laplante, M. The Roles of mTOR Complexes in Lipid Metabolism. *Annu. Rev. Nutr.* **35**, 321–348 (2015).

100. Sun, C. *et al.* Adipose Snail1 Regulates Lipolysis and Lipid Partitioning by Suppressing Adipose Triacylglycerol Lipase Expression. *Cell Rep.* **17**,

2015–2027 (2016).

101. Roy, D. *et al.* Coordinated transcriptional control of adipocyte triglyceride lipase (Atgl) by transcription factors Sp1 and peroxisome proliferator-activated receptor γ (PPARγ) during adipocyte differentiation. *J. Biol. Chem.* **292**, 14827–14835 (2017).

102. Yogosawa, S., Mizutani, S., Ogawa, Y. & Izumi, T. Activin receptor-like kinase 7 suppresses lipolysis to accumulate fat in obesity through downregulation of peroxisome proliferator-activated receptor γ and C/EBPα. *Diabetes* **62**, 115–123 (2013).

103. Fujimoto, Y. *et al.* TFE3 Controls Lipid Metabolism in Adipose Tissue of Male Mice by Suppressing Lipolysis and Thermogenesis. *Endocrinology* **154**, 3577–3588 (2013).

104. Gambo, Y., Matsumura, M. & Fujimori, K. Triiodothyronine enhances accumulation of intracellular lipids in adipocytes through thyroid hormone receptor α via direct and indirect mechanisms. *Mol. Cell. Endocrinol.* **431**, 1–11 (2016).

105. Stenson, B. M. *et al.* Liver X Receptor (LXR) regulates human adipocyte lipolysis. *J. Biol. Chem.* **286**, 370–379 (2011).

106. Singh, R. *et al.* Autophagy regulates lipid metabolism. *Nature* **458**, 1131–1135 (2009).

107. Garcia, E. J., Vevea, J. D. & Pon, L. A. Lipid droplet autophagy during energy mobilization, lipid homeostasis and protein quality control. *Front. Biosci. (Landmark Ed.* **23**, 1552–1563 (2018).

108. Cui, W. *et al.* Lipophagy-derived fatty acids undergo extracellular efflux via lysosomal exocytosis. *Autophagy* **17**, 690–705 (2021).

109. Lettieri Barbato, D., Tatulli, G., Aquilano, K. & Ciriolo, M. R. FoxO1 controls lysosomal acid lipase in adipocytes: Implication of lipophagy during nutrient restriction and metformin treatment. *Cell Death Dis.* **4**, 1–11 (2013).

110. Settembre, C. *et al.* TFEB controls cellular lipid metabolism through a starvation-induced autoregulatory loop. *Nat. Cell Biol.* **15**, 647–658 (2013).

111. Raben, N. & Puertollano, R. TFEB and TFE3: Linking Lysosomes to Cellular Adaptation to Stress∗. *Annu. Rev. Cell Dev. Biol.* **32**, 255–278 (2016).

112. Emanuel, R. *et al.* Induction of lysosomal biogenesis in atherosclerotic macrophages can rescue lipid-induced lysosomal dysfunction and downstream sequelae. *Arterioscler. Thromb. Vasc. Biol.* **34**, 1942–1952 (2014).

113. Baracos, V. E., Martin, L., Korc, M., Guttridge, D. C. & Fearon, K. C. H. Cancer-associated cachexia. *Nat. Rev. Dis. Prim.* **4**, 1–18 (2018).

114. Fearon, K. *et al.* Definition and classification of cancer cachexia: An international consensus. *Lancet Oncol.* **12**, 489–495 (2011).

115. Baazim, H., Antonio-Herrera, L. & Bergthaler, A. The interplay of immunology and cachexia in infection and cancer. *Nat. Rev. Immunol.* **22**, 309–321 (2022).

116. Das, S. K. *et al.* Adipose Triglyceride Lipase Contributes to Cancer-Associated Cachexia. *Science (80-.).* **333**, 233–238 (2011).

117. Ye, R. Z., Richard, G., Gévry, N., Tchernof, A. & Carpentier, A. C. Fat Cell Size: Measurement Methods, Pathophysiological Origins, and Relationships With Metabolic Dysregulations. *Endocr. Rev.* **43**, 35–60 (2022).

118. Morigny, P., Houssier, M., Mouisel, E. & Langin, D. Adipocyte lipolysis and insulin resistance. *Biochimie* **125**, 259–266 (2016).

119. Geng, Y., Faber, K. N., de Meijer, V. E., Blokzijl, H. & Moshage, H. How does hepatic lipid accumulation lead to lipotoxicity in non-alcoholic fatty liver disease? *Hepatol. Int.* **15**, 21–35 (2021).

120. Walenna, N. F. *et al.* Chlamydia pneumoniae infection-induced endoplasmic reticulum stress causes fatty acid-binding protein 4 secretion in murine adipocytes. *J. Biol. Chem.* **295**, 2713–2723 (2020).

121. Walenna, N. F. *et al.* Chlamydia pneumoniae exploits adipocyte lipid chaperone FABP4 to facilitate fat mobilization and intracellular growth in murine adipocytes. *Biochem. Biophys. Res. Commun.* **495**, 353–359 (2018).

122. Wang, C., Gao, D. & Kaltenboeck, B. Acute chlamydia pneumoniae reinfection accelerates the development of insulin resistance and diabetes in obese C57BL/6 mice. *J. Infect. Dis.* **200**, 279–287 (2009).

123. Fernández-Real, J. M. *et al.* Burden of infection and insulin resistance in healthy middle-aged men. *Diabetes Care* **29**, 1058–1064 (2006).

124. Neyrolles, O. *et al.* Is adipose tissue a place for Mycobacterium tuberculosis persistence? *PLoS One* **1**, (2006).

125. Beigier-Bompadre, M. *et al.* Mycobacterium tuberculosis infection modulates adipose tissue biology. *PLoS Pathog.* **13**, 1–24 (2017).

126. Oswal, N. *et al.* Host Metabolic Changes during Mycobacterium Tuberculosis Infection Cause Insulin Resistance in Adult Mice. *J. Clin. Med.* **11**, (2022).

127. Ayyappan, J. P. *et al.* Adipose Tissue Regulates Pulmonary Pathology during TB Infection. *MBio* **10**, 1–16 (2019).

128. Caron-Debarle, M., Lagathu, C., Boccara, F., Vigouroux, C. & Capeau, J. HIV-associated lipodystrophy: from fat injury to premature aging. *Trends Mol. Med.* **16**, 218–229 (2010).

129. Hommes, M. J., Romijn, J. A., Endert, E. & Sauerwein, H. P. Resting energy expenditure and substrate oxidation in human immunodeficiency virus (HIV)-infected asymptomatic men: HIV affects host metabolism in the early asymptomatic stage. *Am. J. Clin. Nutr.* **54**, 311–315 (1991).

130. Sharpstone, D. R., Ross, H. M. & Gazzard, B. G. The metabolic response to opportunistic infections in AIDS. *AIDS* **10**, 1529–1533 (1996).

131. Koethe, J. R. Adipose Tissue in HIV Infection. **7**, 1339–1357 (2017).

132. Agarwal, N. *et al.* HIV-1 Vpr Induces Adipose Dysfunction in Vivo Through Reciprocal Effects on PPAR / GR Co-Regulation. **164**, (2013).

133. Andrade, Z. A. & Silva, H. R. Parasitism of adipocytes by Trypanosoma cruzi. *Memórias do Instituto Oswaldo Cruz* vol. 90 521–522 (1995).

134. Combs, T. P. *et al.* The adipocyte as an important target cell for

Trypanosoma cruzi infection. *J. Biol. Chem.* **280**, 24085–24094 (2005).

135. Nagajyothi, F. *et al.* Response of adipose tissue to early infection with trypanosoma cruzi (Brazil Strain). *J. Infect. Dis.* **205**, 830–840 (2012).

136. Matos Ferreira, A. V. *et al.* Evidence for Trypanosoma cruzi in adipose tissue in human chronic Chagas disease. *Microbes Infect.* **13**, 1002–1005 (2011).

137. González, F. B. *et al.* Immune response triggered by Trypanosoma cruzi infection strikes adipose tissue homeostasis altering lipid storage, enzyme profile and adipokine expression. *Med. Microbiol. Immunol.* **208**, 651–666 (2019).

138. Lizardo, K. *et al.* Fat tissue regulates the pathogenesis and severity of cardiomyopathy in murine chagas disease. *PLoS Negl. Trop. Dis.* **15**, 1–19 (2021).

139. Lu, Y. *et al.* Microarray Analysis of lncRNA and mRNA Reveals Enhanced Lipolysis Along With Metabolic Remodeling in Mice Infected With Larval Echinococcus granulosus. *Front. Physiol.* **11**, (2020).

140. Onyilagha, C. & Uzonna, J. E. Host Immune Responses and Immune Evasion Strategies in African Trypanosomiasis. *Front. Immunol.* **10**, (2019).

141. Caljon, G. *et al.* Neutrophils enhance early Trypanosoma brucei infection onset. *Sci. Rep.* **8**, (2018).

142. Laveran, A. & Mesnil, F. *Trypanosomes et trypanosomiases*. *Trypanosomes et Trypanosomiases* (Libraires de l'Académie de Médecine, Paris (in French), 1912). doi:10.5962/bhl.title.939.

143. Thomson, R. & Finkelstein, A. Human trypanolytic factor APOL1 forms pH-gated cation-selective channels in planar lipid bilayers: Relevance to trypanosome lysis. *Proc. Natl. Acad. Sci.* **112**, 2894–2899 (2015).

144. Vanhamme, L. *et al.* Apolipoprotein L-I is the trypanosome lytic factor of human serum. *Nature* **422**, 83–87 (2003).

145. Raper, J., Nussenzweig, V. & Tomlinson, S. The main lytic factor of

Trypanosoma brucei brucei in normal human serum is not high density lipoprotein. *J. Exp. Med.* **183**, 1023–1029 (1996).

146. Capewell, P. *et al.* The TgsGP Gene Is Essential for Resistance to Human Serum in Trypanosoma brucei gambiense. *PLoS Pathog.* **9**, 2–7 (2013).

147. Uzureau, P. *et al.* Mechanism of Trypanosoma brucei gambiense resistance to human serum. *Nature* **501**, 430–434 (2013).

148. Van Xong, H. *et al.* A VSG expression site-associated gene confers resistance to human serum in Trypanosoma rhodesiense. *Cell* **95**, 839–846 (1998).

149. Lecordier, L. *et al.* C-terminal mutants of apolipoprotein L-I efficiently kill both Trypanosoma brucei brucei and Trypanosoma brucei rhodesiense. *PLoS Pathog.* **5**, (2009).

150. Horn, D. Antigenic variation in African trypanosomes. *Mol. Biochem. Parasitol.* **195**, 123–129 (2014).

151. Schwede, A., Jones, N., Engstler, M. & Carrington, M. The VSG C-terminal domain is inaccessible to antibodies on live trypanosomes. *Mol. Biochem. Parasitol.* **175**, 201–204 (2011).

152. Reinitz, D. M. & Mansfield, J. M. T-cell-independent and T-cell-dependent B-cell responses to exposed variant surface glycoprotein epitopes in trypanosome-infected mice. *Infect. Immun.* **58**, 2337–42 (1990).

153. Magez, S. *et al.* The role of B-cells and IgM antibodies in parasitemia, anemia, and VSG switching in Trypanosoma brucei-infected mice. *PLoS Pathog.* **4**, (2008).

154. Macaskill, J. A. *et al.* Immunological clearance of 75Se-labelled Trypanosoma brucei in mice. II. Mechanisms in immune animals. *Immunology* **40**, 629–35 (1980).

155. Lecordier, L. *et al.* The Trypanosoma Brucei KIFC1 Kinesin Ensures the Fast Antibody Clearance Required for Parasite Infectivity. *iScience* **23**, (2020).

156. Salmon, D. *et al.* Adenylate cyclases of Trypanosoma brucei inhibit the innate immune response of the host. *Science (80-.).* **337**, 463–466 (2012).

157. Kubagawa, H. *et al.* The long elusive IgM Fc receptor, FcμR. *J. Clin. Immunol.* **34 Suppl 1**, S35-45 (2014).

158. Skopnik, C. M. *et al.* expressed by innate immune cells. 1–4 (2022) doi:10.1038/s41467-022-29407-0.

159. Pan, W., Ogunremi, O., Wei, G., Shi, M. & Tabel, H. CR3 (CD11b/CD18) is the major macrophage receptor for IgM antibody-mediated phagocytosis of African trypanosomes: Diverse effect on subsequent synthesis of tumor necrosis factor α and nitric oxide. *Microbes Infect.* **8**, 1209–1218 (2006).

160. van Lookeren Campagne, M., Wiesmann, C. & Brown, E. J. Macrophage complement receptors and pathogen clearance. *Cell. Microbiol.* **9**, 2095–2102 (2007).

161. Jones, J. F. & Hancock, G. E. Trypanosomiasis in mice with naturally occurring immunodeficiencies. *Infect. Immun.* **42**, 848–851 (1983).

162. Magez, S., Pinto Torres, J. E., Obishakin, E. & Radwanska, M. Infections With Extracellular Trypanosomes Require Control by Efficient Innate Immune Mechanisms and Can Result in the Destruction of the Mammalian Humoral Immune System. *Front. Immunol.* **11**, 1–19 (2020).

163. Crotty, S. T Follicular Helper Cell Differentiation, Function, and Roles in Disease. *Immunity* **41**, 529–542 (2014).

164. Seed, J. R. The role of immunoglobulins in immunity to Trypanosoma brucei gambiense. *Int. J. Parasitol.* **7**, 55–60 (1977).

165. Sima, N., McLaughlin, E. J., Hutchinson, S. & Glover, L. Escaping the immune system by DNA repair and recombination in African trypanosomes. *Open Biol.* **9**, (2019).

166. Engstler, M. *et al.* Hydrodynamic Flow-Mediated Protein Sorting on the Cell Surface of Trypanosomes. *Cell* **131**, 505–515 (2007).

167. Krüger, T., Schuster, S. & Engstler, M. Beyond Blood: African

Trypanosomes on the Move. *Trends Parasitol.* **34**, 1056–1067 (2018).

168. Verdi, J. *et al.* Inducible Germline IgMs Bridge Trypanosome Lytic Factor Assembly and Parasite Recognition. *Cell Host Microbe* **28**, 79-88.e4 (2020).

169. Vincendeau, P. *et al.* Nitric oxide-mediated cytostatic activity on Trypanosoma brucei gambiense and Trypanosoma brucei brucei. *Exp. Parasitol.* **75**, 353–360 (1992).

170. Duleu, S. *et al.* Mouse Strain Susceptibility to Trypanosome Infection: An Arginase-Dependent Effect. *J. Immunol.* **172**, 6298–6303 (2004).

171. Olivera, G. C. *et al.* Nitric Oxide Protects against Infection-Induced Neuroinflammation by Preserving the Stability of the Blood-Brain Barrier. *PLoS Pathog.* **12**, 1–25 (2016).

172. Wong, P. & Pamer, E. G. CD8 T cell responses to infectious pathogens. *Annu. Rev. Immunol.* **21**, 29–70 (2003).

173. Liu, G. *et al.* Distinct contributions of CD4+ and CD8+ T cells to pathogenesis of trypanosoma brucei infection in the context of gamma interferon and interleukin-10. *Infect. Immun.* **83**, 2785–2795 (2015).

174. Rottenberg, M. E. *et al.* Differential susceptibilities of mice genomically deleted of CD4 and CD8 to infections with Trypanosoma cruzi or Trypanosoma brucei. *Infect. Immun.* **61**, 5129–5133 (1993).

175. Saravia, J., Chapman, N. M. & Chi, H. Helper T cell differentiation. *Cell. Mol. Immunol.* **16**, 634–643 (2019).

176. Vazquez, M. I., Catalan-Dibene, J. & Zlotnik, A. B cells responses and cytokine production are regulated by their immune microenvironment. *Cytokine* **74**, 318–326 (2015).

177. Namangala, B. *et al.* Attenuation of Trypanosoma brucei is associated with reduced immunosuppression and concomitant production of Th2 lymphokines. *J. Infect. Dis.* **181**, 1110–1120 (2000).

178. Namangala, B. *et al.* Alternative versus classical macrophage activation during experimental African trypanosomosis Abstract : The type I / type II

cytokine balance may type II cytokine production , wild type (WT) -in-response . In the present study , phenotype and ac- comp. *J. Leukoc. Biol.* **69**, 387–396 (2001).

179. Vanwalleghem, G., Morias, Y., Beschin, A., Szymkowski, D. E. & Pays, E. Trypanosoma brucei growth control by TNF in mammalian host is independent of the soluble form of the cytokine. *Sci. Rep.* **7**, 1–7 (2017).

180. Magez, S., Radwanska, M., Beschin, A., Sekikawa, K. & De Baetselier, P. Tumor necrosis factor alpha is a key mediator in the regulation of experimental Trypanosoma brucei infections. *Infect. Immun.* **67**, 3128–3132 (1999).

181. Hertz, C. J., Filutowicz, H. & Mansfield, J. M. Resistance to the African trypanosomes is IFN-gamma dependent. *J. Immunol.* **161**, 6775–83 (1998).

182. Namangala, B., Noël, W., De Baetselier, P., Brys, L. & Beschin, a. Relative contribution of interferon-gamma and interleukin-10 to resistance to murine African trypanosomosis. *J. Infect. Dis.* **183**, 1794–800 (2001).

183. Wu, H., Liu, G. & Shi, M. Interferon gamma in African trypanosome infections: Friends or foes? *Front. Immunol.* **8**, 4–10 (2017).

184. Sakaguchi, S. *et al.* Regulatory T Cells and Human Disease. *Annu. Rev. Immunol.* **38**, 541–566 (2020).

185. Schmidt, A., Oberle, N. & Krammer, P. H. Molecular Mechanisms of Treg-Mediated T Cell Suppression. *Front. Immunol.* **3**, 1–20 (2012).

186. Guilliams, M. *et al.* Experimental expansion of the regulatory T cell population increases resistance to African trypanosomiasis. *J. Infect. Dis.* **198**, 781–791 (2008).

187. De Trez, C. *et al.* A Critical Blimp-1-Dependent IL-10 Regulatory Pathway in T Cells Protects From a Lethal Pro-inflammatory Cytokine Storm During Acute Experimental Trypanosoma brucei Infection. *Front. Immunol.* **11**, 1–15 (2020).

188. Cardoso, F. *et al.* Neuro-mesenchymal units control ILC2 and obesity via a brain–adipose circuit. *Nature* **597**, 410–414 (2021).

189. Engstler, M. & Boshart, M. Cold shock and regulation of surface protein trafficking convey sensitization to inducers of stage differentiation in Trypanosoma brucei. *Genes Dev.* **18**, 2798–2811 (2004).

190. Hirumi, H. & Hirumi, K. Continuous cultivation of Trypanosoma brucei blood stream forms in a medium containing a low concentration of serum protein without feeder cell layers. *J. Parasitol.* **75**, 985–989 (1989).

191. Galarraga, M. *et al.* Adiposoft: Automated software for the analysis of white adipose tissue cellularity in histological sections. *J. Lipid Res.* **53**, 2791–2796 (2012).

192. Bolger, A. M., Lohse, M. & Usadel, B. Trimmomatic: A flexible trimmer for Illumina sequence data. *Bioinformatics* **30**, 2114–2120 (2014).

193. Andrew, S., Lindenbaum, P., Howard, B. & Ewels, P. FastQC: a quality control tool for high throughput sequence data. (2011).

194. Cox, M. P., Peterson, D. A. & Biggs, P. J. SolexaQA: At-a-glance quality assessment of Illumina second-generation sequencing data. *BMC Bioinformatics* **11**, 485 (2010).

195. Aslett, M. *et al.* TriTrypDB: A functional genomic resource for the Trypanosomatidae. *Nucleic Acids Res.* **38**, (2009).

196. Kim, D., Langmead, B. & Salzberg, S. L. HISAT: A fast spliced aligner with low memory requirements. *Nat. Methods* **12**, 357–360 (2015).

197. Zerbino, D. R. *et al.* Ensembl 2018. *Nucleic Acids Res.* **46**, D754–D761 (2018).

198. Liao, Y., Smyth, G. K. & Shi, W. FeatureCounts: An efficient general purpose program for assigning sequence reads to genomic features. *Bioinformatics* **30**, 923–930 (2014).

199. Love, M. I., Huber, W. & Anders, S. Moderated estimation of fold change and dispersion for RNA-seq data with DESeq2. *Genome Biol.* **15**, (2014).

200. Robinson, M. D., McCarthy, D. J. & Smyth, G. K. edgeR: A Bioconductor package for differential expression analysis of digital gene expression data.

Bioinformatics **26**, 139–140 (2009).

201. Ritchie, M. E. *et al.* Limma powers differential expression analyses for RNA-sequencing and microarray studies. *Nucleic Acids Res.* **43**, e47 (2015).

202. Huber, W. *et al.* Orchestrating high-throughput genomic analysis with Bioconductor. *Nat. Methods* **12**, 115–121 (2015).

203. R Core Team. R: A language and environment for statistical computing. (2018).

204. Alexa, A. & Rahnenfuhrer, J. topGO: topGO: Enrichment analysis for Gene Ontology. R package version 2.30.1. (2018) doi:10.18129/B9.bioc.topGO.

205. Gu, Z., Eils, R. & Schlesner, M. Complex heatmaps reveal patterns and correlations in multidimensional genomic data. *Bioinformatics* **32**, 2847–2849 (2016).

206. Wickham, H. *ggplot2*. (Springer International Publishing, 2016). doi:10.1007/978-3-319-24277-4.

207. Chen, Z. *et al.* seq-ImmuCC: Cell-centric view of tissue transcriptome measuring cellular compositions of immune microenvironment from mouse RNA-seq data. *Front. Immunol.* **9**, (2018).

208. Bourin, P. *et al.* Stromal cells from the adipose tissue-derived stromal vascular fraction and culture expanded adipose tissue-derived stromal/stem cells: A joint statement of the International Federation for Adipose Therapeutics and Science (IFATS) and the International So. *Cytotherapy* **15**, 641–648 (2013).

209. Deutsch, A., Feng, D., Pessin, J. E. & Shinoda, K. The impact of single-cell genomics on adipose tissue research. *Int. J. Mol. Sci.* **21**, 1–13 (2020).

210. Stijlemans, B. *et al.* Development of a pHrodo-Based Assay for the Assessment of In Vitro and In Vivo Erythrophagocytosis during Experimental Trypanosomosis. *PLoS Negl. Trop. Dis.* **9**, 1–21 (2015).

211. Drennan, M. B. *et al.* The Induction of a Type 1 Immune Response following a Trypanosoma brucei Infection Is MyD88 Dependent. *J. Immunol.* **175**,

2501–2509 (2005).

212. Chan, C. C. *et al.* Type I interferon sensing unlocks dormant adipocyte inflammatory potential. *Nat. Commun.* **11**, 1–15 (2020).

213. Campbell, G. H. & Phillips, S. M. Adoptive transfer of variant specific resistance to Trypanosoma rhodesiense with B lymphocytes and serum. *Infect. Immun.* **14**, 1144–1150 (1976).

214. Pan, A. A. *et al.* Clinical evaluation of an EIA for the sensitive and specific detection of serum antibody to trypanosoma cruzi (Chagas' disease). *J. Infect. Dis.* **165**, 585–588 (1992).

215. Frenkel, D. *et al.* Trypanosoma brucei Co-opts NK Cells to Kill Splenic B2 B Cells. *PLoS Pathog.* **12**, 1–29 (2016).

216. Jubel, J. M., Barbati, Z. R., Burger, C., Wirtz, D. C. & Schildberg, F. A. The Role of PD-1 in Acute and Chronic Infection. *Front. Immunol.* **11**, 1–15 (2020).

217. Zaragosi, L. E. *et al.* Neutrophils enhance early Trypanosoma brucei infection onset. *Immunology* **8**, 1–9 (2015).

218. Guilliams, M. *et al.* IL-10 Dampens TNF/Inducible Nitric Oxide Synthase-Producing Dendritic Cell-Mediated Pathogenicity during Parasitic Infection. *J. Immunol.* **182**, 1107–1118 (2009).

219. Laperchia, C. *et al.* Trypanosoma brucei Invasion and T-cell Infiltration of the Brain Parenchyma in Experimental Sleeping Sickness: Timing and Correlation with Functional Changes. *PLoS Negl. Trop. Dis.* **10**, 1–19 (2016).

220. Deleeuw, V. *et al.* Trypanosoma brucei brucei causes a rapid and persistent influx of neutrophils in the spleen of infected mice. *Parasite Immunol.* **41**, 1–5 (2019).

221. Bunker, J. J. *et al.* Natural polyreactive IgA antibodies coat the intestinal microbiota. *Science (80-.).* **358**, (2017).

222. Ferrante, A. & Allison, A. C. Alternative pathway activation of complement by

African trypanosomes lacking a glycoprotein coat. *Parasite Immunol.* **5**, 491–498 (1983).

223. Cheung, J. L. Y. *et al.* Blocking Synthesis of the Variant Surface Glycoprotein Coat in Trypanosoma brucei Leads to an Increase in Macrophage Phagocytosis Due to Reduced Clearance of Surface Coat Antibodies. *PLoS Pathog.* **12**, 1–27 (2016).

224. Stevens, D. R. & Moulton, J. E. Ultrastructural and immunological aspects of the phagocytosis of Trypanosoma brucei by mouse peritoneal macrophages. *Infect. Immun.* **19**, 972–982 (1978).

225. Ngaira, J. M., Nantulya, V. M., Musoke, A. J. & Hirumi, K. Phagocytosis of antibody-sensitized Trypanosoma brucei in vitro by bovine peripheral blood monocytes. *Immunology* **49**, 393–400 (1983).

226. Mugnier, M. R., Cross, G. A. M. & Papavasiliou, F. N. The in vivo dynamics of antigenic variation in Trypanosoma brucei. *Science (80-.).* **347**, 1470–1473 (2015).

227. Eisenthal, R. & Panes, A. The aerobic/anaerobic transition of glucose metabolism in Trypanosoma brucei. *FEBS Lett.* **181**, 23–27 (1985).

228. Michels, P. A. M., Bringaud, F., Herman, M. & Hannaert, V. Metabolic functions of glycosomes in trypanosomatids. *Biochim. Biophys. Acta - Mol. Cell Res.* **1763**, 1463–1477 (2006).

229. Morrison, L. J. *et al.* A major genetic locus in Trypanosoma brucei is a determinant of host pathology. *PLoS Negl. Trop. Dis.* **3**, 1–12 (2009).

230. Machado, H. *et al.* Trypanosoma brucei triggers a broad immune response in the adipose tissue. *PLoS Pathog.* **17**, 1–26 (2021).

231. Aresta-Branco, F., Sanches-Vaz, M., Bento, F., Rodrigues, J. A. & Figueiredo, L. M. African trypanosomes expressing multiple VSGs are rapidly eliminated by the host immune system. *Proc. Natl. Acad. Sci. U. S. A.* **116**, 20725–20735 (2019).

232. Cawthorn, W. P. & Sethi, J. K. TNF- a and adipocyte biology. *FEBS Lett.* **582**, 117–131 (2008).

233. Tracey, K. J. & Cerami, A. Metabolic responses to cachectin/TNF. A brief review. *Ann. N. Y. Acad. Sci.* **587**, 325–331 (1990).

234. Guegan, F. *et al.* A long noncoding RNA promotes parasite differentiation in African trypanosomes. *Sci. Adv.* **8**, eabn2706 (2022).

235. Kaur, S. *et al.* Adipose-specific ATGL ablation reduces burn injury-induced metabolic derangements in mice. *Clin. Transl. Med.* **11**, (2021).

236. Baazim, H. *et al.* CD8+ T cells induce cachexia during chronic viral infection. *Nat. Immunol.* **20**, 701–710 (2019).

237. Rouzer, C. A. & Cerami, A. Hypertriglyceridemia associated with Trypanosoma brucei brucei infection in rabbits: Role of defective triglyceride removal. *Mol. Biochem. Parasitol.* **2**, 31–38 (1980).

238. Ebadi, M. & Mazurak, V. C. Evidence and mechanisms of fat depletion in cancer. *Nutrients* **6**, 5280–5297 (2014).

239. Petruzzelli, M. & Wagner, E. F. Mechanisms of metabolic dysfunction in cancer-associated cachexia. *Genes Dev.* **30**, 489–501 (2016).

240. Delano, M. J. & Moldawer, L. L. The oriqins of cachexia in acute and chronic inflammatory diseases. *Nutr. Clin. Pract.* **21**, 68–81 (2006).

241. Lafontan, M. & Langin, D. Lipolysis and lipid mobilization in human adipose tissue. *Prog. Lipid Res.* **48**, 275–297 (2009).

242. *A Comprehensive Guide to Toxicology in Nonclinical Drug Development*. (Elsevier, 2017).

243. Nolan, S. J., Romano, J. D., Kline, J. T. & Coppens, I. Novel approaches to kill toxoplasma gondii by exploiting the uncontrolled uptake of unsaturated fatty acids and vulnerability to lipid storage inhibition of the parasite. *Antimicrob. Agents Chemother.* **62**, (2018).

244. Dawoody Nejad, L., Serricchio, M., Jelk, J., Hemphill, A. & Bütikofer, P. TbLpn, a key enzyme in lipid droplet formation and phospholipid metabolism, is essential for mitochondrial integrity and growth of Trypanosoma brucei. *Mol. Microbiol.* **109**, 105–120 (2018).

245. Smith, T. K. & Bütikofer, P. Lipid metabolism in Trypanosoma brucei. **172**, 66–79 (2010).

246. Caljon, G. *et al.* The Dermis as a Delivery Site of Trypanosoma brucei for Tsetse Flies. *PLoS Pathog.* **12**, 1–22 (2016).

247. Koffi, M. *et al.* Aparasitemic serological suspects in Trypanosoma brucei gambiense human African trypanosomiasis: A potential human reservoir of parasites? *Acta Trop.* **98**, 183–188 (2006).

248. Kanmogne, G. D., Asonganyi, T. & Gibson, W. C. Detection of Trypanosoma brucei gambiense, in serologically positive but aparasitaemic sleeping-sickness suspects in Cameroon, by PCR. *Ann. Trop. Med. Parasitol.* **90**, 475–483 (1996).

249. Uhlén, M. *et al.* Tissue-based map of the human proteome. *Science (80-.).* **347**, (2015).

250. Pereira, S. S. *et al.* congolense parasite sequestration cause acute cerebral trypanosomiasis. 1–32 (2022).

Annexes

S1 Table. Mapping information of RNA-Seq reads in samples from infected AT.

https://doi.org/10.1371/journal.ppat.1009933.s007

S1 File. RNA-seq raw counts and differential expression analysis.

(A) Raw counts and **(B)** reads per kilobase per million mapped reads from RNA-seq of AT from non-infected mice (D0), n = 3, day 6 post-infection (D6), n = 3 and day 26 post-infection (D26), n = 2. Differential expression analysis between **(C)** D0 and D6, **(D)** D0 and D26 and **(E)** D6 and D26.

https://doi.org/10.1371/journal.ppat.1009933.s008

S2 File. Significant GO terms list.

GO term analysis from RNA-seq of AT from non-infected mice (D0), n = 3, day 6 post-infection (D6), n = 3 and day 26 post-infection (D26), Up-regulated GO terms in the AT between **(A)** D6vsD0, **(B)** D26vsD0, **(C)** D26vsD6. Down-regulated GO terms in the AT between **(D)** D6vsD0, **(E)** D26vsD0, **(F)** D26vsD6.

https://doi.org/10.1371/journal.ppat.1009933.s009

S3 File. Effect of tissue weight on immune cell number and parasite number determination.

(A) Weight of spleens and ATs analysed. Data for entire organs and normalized to tissue weight **(B-C)** parasite burden, **(D-E)** CD45+ cells, **(F-G)** neutrophils, **(H-I)** macrophages, **(J-K)** monocytes, **(L-M)** effector CD4+ T cells, **(N-O)** effector CD8+ T cells and **(P-Q)** regulatory T cells.

https://doi.org/10.1371/journal.ppat.1009933.s010

S4 File. Effect of tissue weight on B cell number determination.

(A) Weight of spleens and ATs analysed. Data for entire organs and normalized to tissue weight **(B-C)** B cells and **(D-E)** activated B cells.

https://doi.org/10.1371/journal.ppat.1009933.s011

S5 File. Effect of tissue weight on parasite number determination.

Weight of organs used from infected **(A)** Rag2-/-, **(B)** Jht-/-, **(C)** Ifng-/-, **(D)** C3-/- and **(E)** anti-PD1 treated mice, with respective controls. Data for parasite numbers in the entire organ or normalized to tissue weight for infected **(F-G)** Rag2-/-, **(H-I)** Jht-/-, **(J-K)** Ifng-/-, **(L-M)** C3-/- and **(N-O)** anti-PD1 treated mice, with respective controls.

https://doi.org/10.1371/journal.ppat.1009933.s012

List of publications during this thesis:

1. **Henrique Machado***, Tiago Bizarra-Rebelo*, Mariana Costa-Sequeira, Sandra Trindade,Tânia Carvalho, Filipa Rijo-Ferreira, Barbara Rentroia-Pacheco, Karine Serre, Luisa M. Figueiredo. Trypanosoma brucei triggers a broad immune response in the adipose tissue. PLoS Pathogens. 17, 1–26 (2021).

   https://doi.org/10.1371/journal.ppat.1009933

   *Equal contribution.

2. **Henrique Machado**, Luisa M. Figueiredo. Polyreactive Antibodies Bridge Immunity Particles to Pathogen. Trends in Parasitology. (2020).

   https://doi.org/10.1016/j.pt.2020.07.012

Contributions for Part 1 of this work

Figure 9:	No contribution.
Figure 10:	Conceptualization and data analysis.
Figure 11:	Data analysis.
Figure 12:	No contribution.
Figure 13:	Data analysis.
Figure 14:	Data analysis.
Figure 15:	No contribution.
Figure 16:	Conceptualization, data acquisition and analysis.
Figure 17:	Conceptualization, data acquisition and analysis.
Figure 18:	Conceptualization, data acquisition and analysis.
Figure 19:	Data analysis.

PLOS PATHOGENS

RESEARCH ARTICLE

Trypanosoma brucei triggers a broad immune response in the adipose tissue

Henrique Machado[1☯], Tiago Bizarra-Rebelo[1☯], Mariana Costa-Sequeira[1], Sandra Trindade[1], Tânia Carvalho[1], Filipa Rijo-Ferreira[2], Barbara Rentroia-Pacheco[1], Karine Serre[1‡*], Luisa M. Figueiredo[1‡*]

1 Instituto de Medicina Molecular João Lobo Antunes, Faculdade de Medicina, Universidade de Lisboa, Lisbon, Portugal, **2** Department of Neuroscience, Peter O'Donnell Jr. Brain Institute, University of Texas Southwestern Medical Center, Dallas, Texas, United States

☯ These authors contributed equally to this work.
‡ KS and LMF also contributed equally to this work.
* karineserre@medicina.ulisboa.pt (KS); lmf@medicina.ulisboa.pt (LMF)

Check for updates

OPEN ACCESS

Citation: Machado H, Bizarra-Rebelo T, Costa-Sequeira M, Trindade S, Carvalho T, Rijo-Ferreira F, et al. (2021) *Trypanosoma brucei* triggers a broad immune response in the adipose tissue. PLoS Pathog 17(9): e1009933. https://doi.org/10.1371/journal.ppat.1009933

Editor: Stefan Magez, Vrije Universiteit Brussel, BELGIUM

Received: April 14, 2021

Accepted: August 31, 2021

Published: September 15, 2021

Peer Review History: PLOS recognizes the benefits of transparency in the peer review process; therefore, we enable the publication of all of the content of peer review and author responses alongside final, published articles. The editorial history of this article is available here: https://doi.org/10.1371/journal.ppat.1009933

Copyright: © 2021 Machado et al. This is an open access article distributed under the terms of the Creative Commons Attribution License, which permits unrestricted use, distribution, and reproduction in any medium, provided the original author and source are credited.

Data Availability Statement: RNA-Seq data is publicly available in the ArrayExpress database under the accession number E-MTAB-4061 and E-MTAB-7596.

Abstract

Adipose tissue is one of the major reservoirs of *Trypanosoma brucei* parasites, the causative agent of sleeping sickness, a fatal disease in humans. In mice, the gonadal adipose tissue (AT) typically harbors 2–5 million parasites, while most solid organs show 10 to 100-fold fewer parasites. In this study, we tested whether the AT environment responds immunologically to the presence of the parasite. Transcriptome analysis of *T. brucei* infected adipose tissue revealed that most upregulated host genes are involved in inflammation and immune cell functions. Histochemistry and flow cytometry confirmed an increasingly higher number of infiltrated macrophages, neutrophils and CD4+ and CD8+ T lymphocytes upon infection. A large proportion of these lymphocytes effectively produce the type 1 effector cytokines, IFN-γ and TNF-α. Additionally, the adipose tissue showed accumulation of antigen-specific IgM and IgG antibodies as infection progressed. Mice lacking T and/or B cells (*Rag2*$^{-/-}$, *Jht*$^{-/-}$), or the signature cytokine (*Ifng*$^{-/-}$) displayed a higher parasite load both in circulation and in the AT, demonstrating the key role of the adaptive immune system in both compartments. Interestingly, infections of *C3*$^{-/-}$ mice showed that while complement system is dispensable to control parasite load in the blood, it is necessary in the AT and other solid tissues. We conclude that *T. brucei* infection triggers a broad and robust immune response in the AT, which requires the complement system to locally reduce parasite burden.

Author summary

African trypanosomiasis is a neglected disease with significant socio-economic burden in sub-Saharan Africa. The protozoan parasite *Trypanosoma brucei*, a causative agent of African trypanosomiasis, can be found in the blood and extra-vascular spaces of the infected host. For an unknown reason, *T. brucei* accumulates in adipose tissue (AT) in very high numbers. Here we used a multidisciplinary approach to assess whether an immune response was mounted in AT during a *T. brucei* infection. We found that as

Funding: This work was supported by the European Research Council (FatTryp, ref. 771714) awarded to LMF, by Fundação para a Ciência e Tecnologia (CEECIND/03322/2018) awarded to LMF, (PTDC/MED-IMU/30948/2017 and CEECIND/00697/2018) awarded to KS, (PD/BD/128286/2017) awarded to HM, (SFRH/BPD/89833/2012) awarded to ST, (IMM/BI/83-2017 through PTDC/BIM-MET/4471/2014) awarded to TB-R and by the National Institutes of Health (NIGMS K99GM132557) awarded to FR-F. The funders had no role in study design, data collection and analysis, decision to publish, or preparation of the manuscript.

Competing interests: The authors have declared that no competing interests exist.

infection progresses, a broad variety of immune cells and antibodies accumulate in the AT. We also found that this broad immune response is partially able to control parasite numbers in the AT. Our study provides evidence that *T*. *brucei* parasites present in the AT are subjected to immune surveillance. The reason why *T*. *brucei* accumulates to such a high extent in AT remains to be elucidated.

Introduction

Trypanosoma brucei is an extracellular protozoan parasite that causes sleeping sickness in humans and nagana in cattle, diseases that still hold a significant socio-economic impact in sub-Saharan Africa[1, 2]. *T*. *brucei* transmission to a mammalian host occurs upon the bite of an infected tsetse fly (*Glossina* spp). During such blood meal, parasites are released into the circulation and quickly differentiate into bloodstream forms (BSFs) that proliferate and invade the interstitial spaces of many organs[3]. In primate hosts, most African trypanosome species are rapidly eliminated by an innate immune trypanosome lytic factor (TLF)[4, 5]. This TLF is delivered by germline-encoded antibodies[6] and promotes complete parasite elimination before the onset of disease.

In non-primate mammalian hosts, or in primates infected TLF-resistant *T*. *brucei*, most parasite elimination does not occur through direct humoral mediated lysis and instead requires internalization by the host's phagocytes, mainly monocytes and macrophages. Optimal phagocytosis of *T*. *brucei* requires antibody and complement mediated opsonization[7]. These antibodies are produced by B cells, particularly plasmocytes (plasmablasts and plasma cells), activated during infection and are directed primarily at the parasite's variant surface glycoprotein (VSG)[7, 8]. This allows for direct Fc receptor-mediated phagocytosis and for the classical activation of the complement system, followed by phagocytosis.

Activation of both macrophages/monocytes and B cells is promoted by a T cell response comprising CD4+ T cells and CD8+ T cells[9]. Macrophages/monocytes respond to cytokines produced by T cells, such as interferon gamma (IFN-γ) and tumour necrosis factor alpha (TNF-α), by increasing phagocytic capacity, phagosome acidification and production of microbicidal reactive nitrogen species[10, 11]. Additionally, CD4+ T cells play an important role in B cell survival and maturation, which allows for the production of higher affinity antibodies via B cell class switching and affinity maturation[12]. Although this immune response is capable of largely limiting the number of parasites, it does so at the cost of severe immunopathology. To limit this deleterious effect, the immune system partially downregulates itself through the production of anti-inflammatory cytokines such as interleukin (IL)-10 which is highly expressed by regulatory T (Treg) cells[13, 14].

These host-parasite interactions, together with the capacity of parasites to switch VSGs by antigenic variation[15] and to undergo terminal differentiation to transmissible forms[16], leads to the characteristic oscillating waves of parasitemia displayed throughout the disease[17].

Most studies on the immune response against *T*. *brucei* have focused on blood and lymphoid organs. However, *T*. *brucei* occupies several extra-vascular tissues, including the brain, skin[18], testis[19, 20] and adipose tissue (AT)[21], which may present distinct immune responses[22] and even be immune privileged sites. A study from our laboratory showed that the AT is not only one of the major parasite reservoirs, reaching levels comparable to the blood, but also that parasites in this tissue (adipose tissue forms–ATFs) present a gene expression signature different from bloodstream forms[21].

For a long time, the role of the AT was believed to be exclusively of lipid storage, exerting important roles in energy homeostasis and thermogenesis[23]. It is now recognized that the AT is an immunologically active[24] endocrine organ[25], as adipocytes secrete a wide variety of immunomodulatory molecules[26]. *T. brucei* is not the only parasite that accumulates in the AT. *Neospora caninum*[27], *Plasmodium berghei* and *Trypanosoma cruzi* also reside in this tissue[28].Some protozoan parasites can even challenge the anti-inflammatory balance in AT or take advantage of such an environment to establish a successful infection. For instance, upon infection, *N. caninum* was reported to trigger a shift towards a pro-inflammatory environment, promoting pathogen elimination from AT[27]. On the contrary, *T. cruzi* was described to induce an anti-inflammatory macrophage polarization in a diet-induced obesity model, contributing to tissue homeostasis and parasite survival[29].

Given the importance of tissue immunity in a wide variety of conditions such as in infections[30] and cancer[31], here we compared the circulating, splenic and AT type of immune responses mounted against *T. brucei*. We show that the AT is a favorable location where an effective protective immune response is mounted, with both innate and adaptive immune cells that control parasite load in this tissue. We conclude that like in the blood, in the AT parasites require active mechanisms of immune evasion.

Results

Transcriptome of infected adipose tissue reveals a strong inflammatory response

A local immune response typically consists in the accumulation of myeloid and lymphoid cells sensing determinants of inflammation and/or determinants specific to the pathogen in order to control the infection and regulate the immune response itself. Given that the signature profile of immune cells is unique and different from all other resident cells of AT (adipocytes, endothelial cells, and mesenchymal stromal cells)[32, 33], we postulated that a transcriptome analysis of infected versus non-infected AT should provide a first glimpse of the type of immune response that is mounted in this tissue. We performed RNA sequencing (RNA-Seq) analysis of mice gonadal AT depots at early and late stages of infection. Total RNA was extracted from this tissue at day 0 (n = 3), 6 (n = 3) and 26 (n = 2) post-infection. Most sequence reads mapped to the mouse genome (between 86% and 96%) and the 1%-10% of reads that mapped to the parasite were not considered in this analysis (S1 Table).

Unbiased clustering of the expression profiles of the analysed samples showed that non-infected and infected AT clustered separately. Furthermore, the cluster of infected AT was divided in 2 sub-clusters separating samples of early and late infection time points (Fig 1A). This indicates significant alterations of transcript abundances in AT upon and during a *T. brucei* infection. To identify the genes differentially expressed, we used three distinct algorithms. Genes significant in at least 2 of them (adjusted p-value < 0.01) and having a fold-change higher than 2 were considered differentially expressed. At day 6 post-infection, 2678 genes were differentially expressed compared with non-infected AT. From these, 1770 genes were upregulated while the remaining 908 were downregulated at day 6 post-infection (S1C File). When comparing AT at day 26 post-infection with non-infected AT, 3684 genes were differentially expressed, from which 2264 were upregulated and 1420 downregulated (S1D File). Between AT at day 6 and day 26 post-infection, we identified 941 differentially expressed genes, 503 upregulated and 438 downregulated at day 26 post-infection (S1E File).

Gene ontology (GO) enrichment analysis was conducted to determine which GO terms were over-represented among the differentially expressed genes (Fisher's exact test, p-value < 0.01). Enrichment tests on the upregulated genes in infected AT (both on day 6

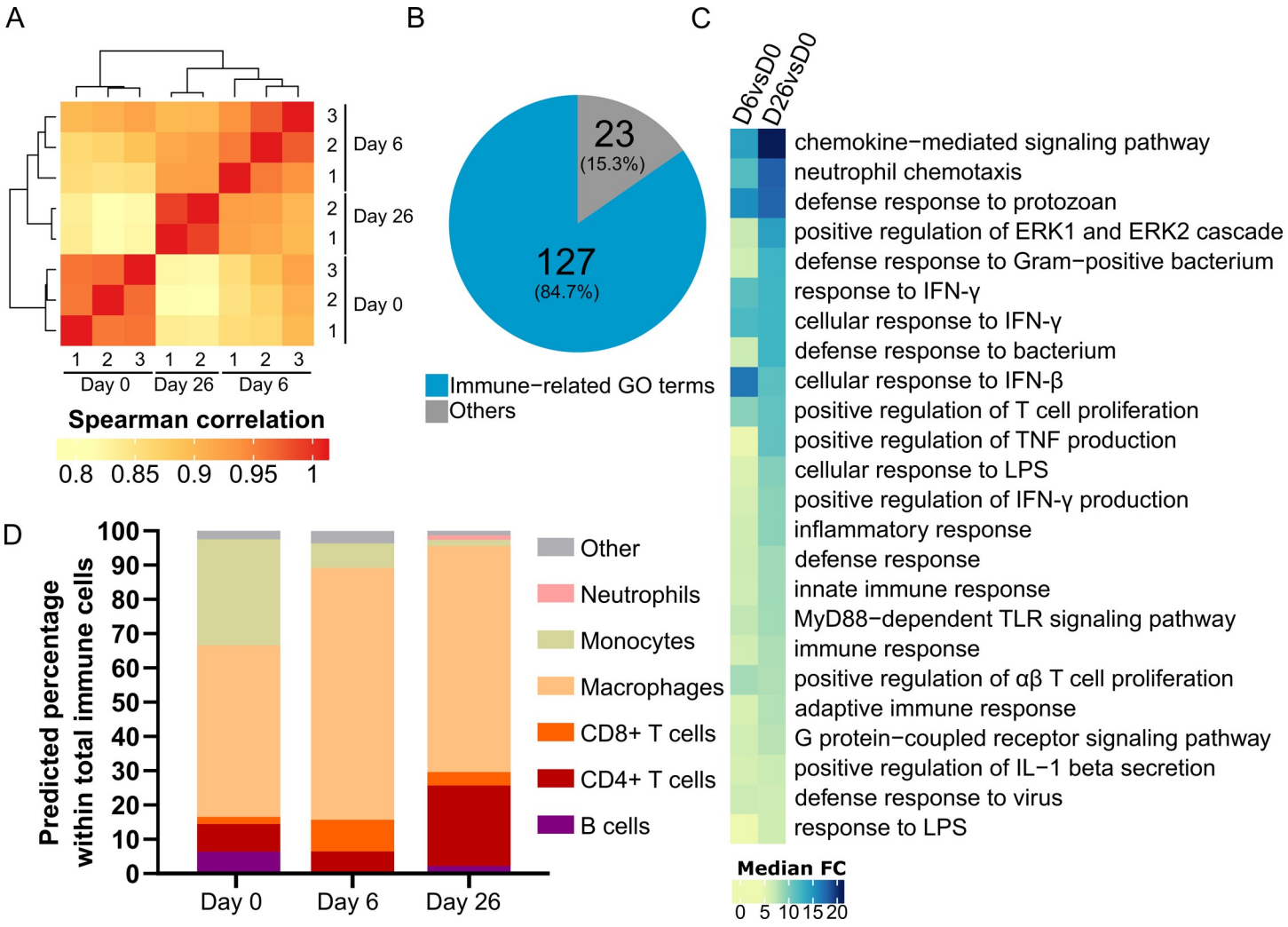

Fig 1. Transcriptome of *T. brucei* infected AT shows a strong immune response. (A) Heat map of hierarchical clustering of Spearman correlations of Reads per kilobase per million mapped reads (RPKM) levels from non-infected (D0), n = 3 and infected AT at early (D6), n = 3 and late (D26), n = 2 time points. **(B)** Pie chart of most significant biological processes GO term families. **(C)** Heat map view of median fold change (FC) of genes associated to the top 20 Biological Process GO terms in day 6 and day 26 of infection versus non-infected AT (D6 vs D0 and D26 vs D0, respectively) **(D)** Prediction of immune cell distribution based on immuCC RNA-seq deconvolution.

https://doi.org/10.1371/journal.ppat.1009933.g001

and day 26 versus day 0) revealed a strong inflammatory profile, with 84.7% of the top 150 (127/150) most significant Biological Process GO-terms related to immunity (Fig 1B and S2 File). Also, the median fold-change of the genes associated to the top 20 Biological Process GO-terms in infected versus non-infected AT (p-value $< 1x10^{-5}$) increased from day 6 to day 26 (Fig 1C), suggesting that the immune response taking place in AT increases in magnitude as infection progresses. Conversely, most downregulated genes were involved in metabolite biosynthesis (*e.g.* fatty acid biosynthetic processes) and other metabolic changes (*e.g.* fatty acid beta-oxidation) (S1 and S2D and S2E Files). Interestingly, differential expression analysis showed a marked and significant upregulation of T helper 1 (Th1) signature genes (*e.g. Tbx21*, *Eomes*, *Il12r1b*, *Ifng*, *Tnf*, *Nos2*, *Stat1*, *Stat4)* both on day 6 and day 26 versus day 0 (S1A Fig and S1C and S1D File), which are associated with a protective immune response against *T. brucei*. This profile was not observed for non-protective Th2 response associated genes (*e.g. Gata3*, *Il4*, *Il5*, *Il13*, *Stat5*, *Stat6)*, which were either not detected or

not differentially expressed in all conditions assessed (S1B Fig and S1 File). In addition to Th1 signature genes, the infected AT showed an overall upregulation of pro-inflammatory genes such as *Gzma*, *Gzmb*, *Il1a and Il6* (S1A Fig). In turn, this was accompanied by the upregulation of genes such as *Il10*, *Il10ra*, *Ctla4*, *Foxp3* and *Pdcd1* which are associated with the suppression of an active immune response (S1B Fig).

To assess whether the changes in transcriptomic profile of the AT could be due to an alteration of the cellular makeover of the tissue, we performed a cellular deconvolution analysis using the immuCC algorithm[34]. This analysis predicted that during a *T*. *brucei* infection the relative proportions of innate and adaptive immune cells were variable (Fig 1D). Specifically, these data predicted a relative increase of macrophages and CD8+ T cells between days 0 and 6 post-infection, while the prediction for monocytes and B cells was a relative decrease in the same period. Lastly, by day 26 post-infection this deconvolution model predicted a sizeable increase of the CD4+ T cell response, with a predicted 3 to 4-fold relative increase when compared to days 0 and 6 post-infection. Overall, the transcriptome of the AT of infected mice revealed signs of intense inflammation and an ongoing active immune response.

Adipose tissue shows a gradual accumulation of immune cells during infection

Bulk RNA-seq provides a strong indication of broad changes in the inflammatory profile immune cell milieu of the AT, however it does not allow to identify the absolute accumulation of immune cells and determine their selective *in situ* effector functions. To investigate this, and to compare the extent of systemic to AT immune responses, we quantified the number of parasites and immune cells in the spleen and the AT. The spleen was used as a proxy for the systemic immune response as it filters bloodborne pathogens and is a major site for lymphocyte activation and proliferation. Quantifications were performed at key time-points of the murine *T*. *brucei* infection, encompassing the formation and resolution of the first and second peaks of parasitemia as well as the chronic stage of infection.

In the blood, the progression of parasitemia throughout infection exhibited its characteristic pattern (Fig 2A): a first peak around day 5 post-infection; undetectable parasitemia between days 9 and 13 post-infection; followed by a fluctuating number of parasites that differs in each mouse until day 28 post-infection. In the spleen, the number of parasites reached the peak at day 5 post-infection and dropped 32-fold from 6 to 9 days post-infection, when the lowest parasite load was detected (Fig 2B). From day 14 post-infection, the number of parasites fluctuated at around 10^5 parasites per organ. Remarkably, in the gonadal AT, the number of parasites peaked at day 6 post-infection (one day later than in blood/spleen) and it suffered only a 6-fold reduction from 6 to 9 days post-infection (Fig 2B). From day 14 post-infection onward, the number of parasites fluctuated at around 10^6 parasites, which is an approximate constant 10-fold more than in the spleen or any other organ assessed, as we have previously reported[21].

At the same key time-points of infection, immune cells from spleen and AT were analysed by flow cytometry. Using an anti-CD45 antibody to gate all immune cells (S2 Fig), we observed a striking gradual accumulation in the gonadal AT with a 16-fold increase in the number of immune cells per tissue from days 0 to 28 post-infection (Fig 2C). Conversely, and despite a large increase in spleen mass (S4A Fig), no significant changes were observed in the total number of splenic immune cells. This suggests that the increase in spleen weight may be largely due to the accumulation of damaged red blood cells undergoing eythrophagocytosis[35], which is known to occur during *T*. *brucei*-induced anemia[36].

Interestingly, while the number of parasites in the AT peaks on day 6 post-infection and oscillates afterwards, the immune cells are recruited and/or proliferate in AT with different dynamics,

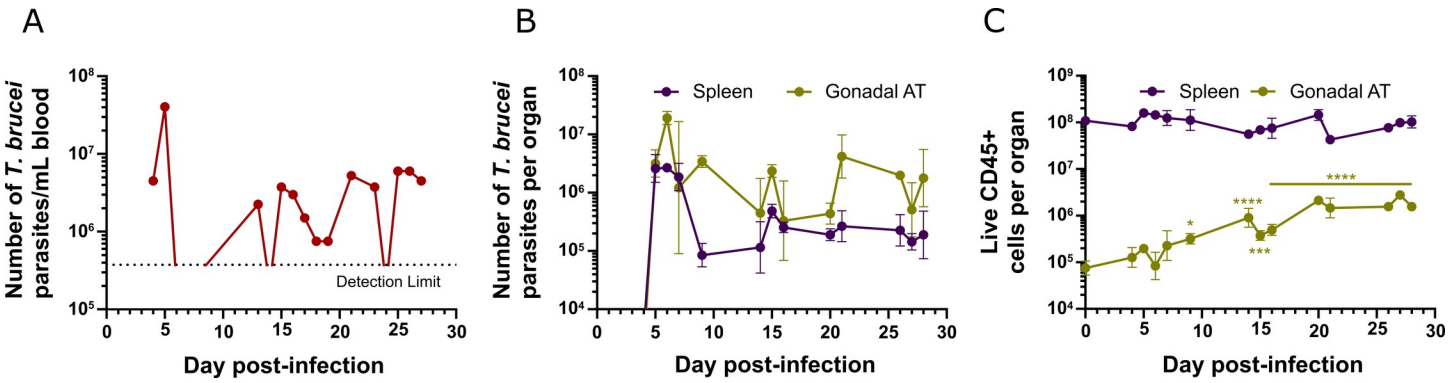

Fig 2. Dynamics of *T. brucei* parasites and immune cells throughout infection. (A) Number of *T. brucei* parasites per mL of blood of a single representative mouse, quantified using a hemocytometer. Dashed line represents the detection limit ($3.75x10^5$ parasites/mL of blood). **(B)** Total number of *T. brucei* parasites in the spleen and gonadal AT, quantified by qPCR. **(C)** Number of live immune cells in spleen and gonadal AT. **(B-C)** Error bars represent the standard error of the mean (SEM) (n = 2–6 mice per group). Statistical analysis was performed with a two-way analysis of variance (ANOVA) using Sidak's test for multiple comparisons. * refers to statistical differences within the groups in each time-point and the non-infected group. *, P<0.05; **, P<0.01; ***, P<0.001; ****, P<0.0001.

https://doi.org/10.1371/journal.ppat.1009933.g002

increasing steadily as infection progresses. The fact that the spleen has a higher proportion of immune cells than the AT is not surprising due to its nature as a secondary lymphoid organ.

To assess the distribution of the inflammatory cell infiltrates and the morphological changes of the AT, we performed immunohistochemistry for parasites (anti-VSG antibody), macrophages (anti-F4/80 antibody) and T cells (anti-CD3 antibody) in sections of gonadal AT on days 6 and 26 post-infection. Consistent with the analysis by flow cytometry, a significant increase was observed in the number of infiltrating macrophages and T cells, mainly during the later time-points of infection (Fig 3A). Inflammatory cells were distributed diffusely in the tissue, often associated with parasites or parasite debris. By transmission electron microscopy (TEM), parasites were also detected intracellularly, in the cytoplasm of phagocytes (most likely macrophages) (Fig 3B). These intracellular parasites were often surrounded by membranous whorls, suggesting they had been phagocytosed.

In conclusion, our analysis shows that the AT is not an immune silent tissue, but instead that it actively responds to a *T. brucei* infection. It is important to mention that these data were acquired in an intraperitoneal infection model and that Tsetse fly transmitted or intradermally injected *T. brucei* may lead to significant differences in immune response.

Adipose tissue is populated by effector innate and adaptive immune cells

To experimentally characterize the immune response that is mounted against *T. brucei* in the AT, we isolated gonadal fat pads and spleen of infected animals at different time-points of the infection, and we identified and quantified the main immune cell subsets by flow cytometry. On the one hand we followed the dynamics of neutrophils, monocytes, and macrophages to assess the innate myeloid immunity branch. On the other hand, to assess the adaptive immunity branch, we followed T cell subsets (helper T cells (CD4+) and killer T cells (CD8+)) and evaluated whether these T cells were activated and responding to the infection by assessing their expression of two main pro-inflammatory cytokines, IFN-γ and TNF-α. Additionally, we analysed the frequency of Treg cells, a key immunosuppressive subset. The gating strategies for all the populations are presented in the S2 Fig.

As infection progressed, while the total number of immune cells of all subtypes assessed increased in the AT, the same was not observed for the spleen (Fig 4). As expected for the innate immune response, neutrophils (Fig 4A) and monocytes (Fig 4B) are the first to be

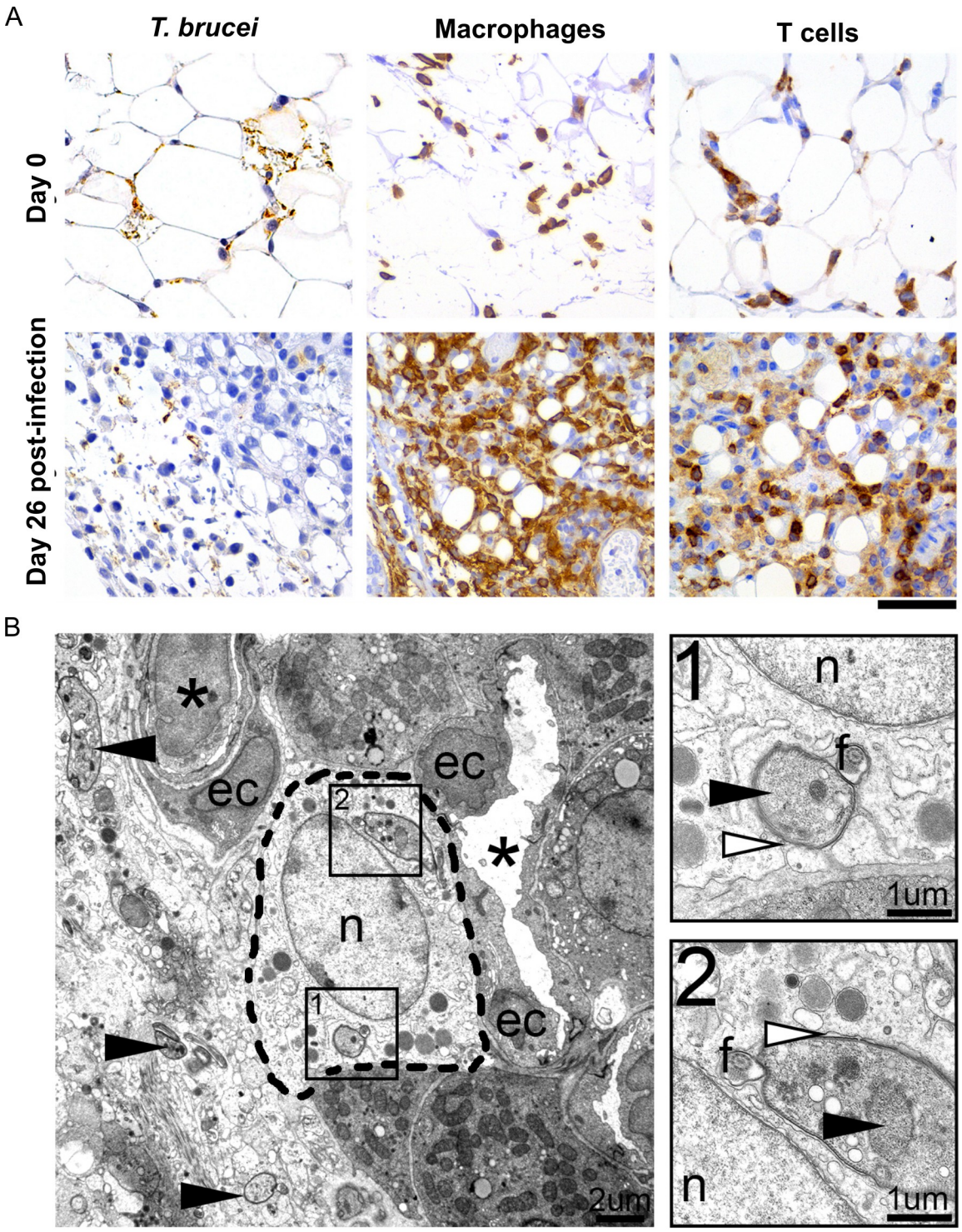

Fig 3. Inflammatory cell response in the adipose tissue. (A) Immunohistochemistry reveals a large number of *T. brucei* parasites (anti-VSG antibody) accompanied by marked infiltration by macrophages (anti-F4/80 antibody) and moderate infiltration by T cells (anti-CD3 antibody), at a later stage post-infection (day 26). (n = 4–6 per time-point); DAB counterstained with hematoxylin, original magnification 40x (Scale bar, 50μm). **(B).** Representative electron micrograph of the perirenal adipose tissue of the mouse, 26 days post-infection, showing various extracellular tangential and cross-sectional profiles of trypanosomes (arrowhead) and also intracellular parasites, in the cytoplasm of a phagocyte [most probably a macrophage (inside dashed line)]. Asterisk, vessel; ec, endothelial cell; n, nucleus, f, flagellum. **B-1, B-2.** Insets of the phagocytized trypanosomes, with well-defined nucleus (black arrowhead) and pseudopodia (white arrowhead), consisting of multiple membranous whorls extended by the phagocyte around the parasite.

https://doi.org/10.1371/journal.ppat.1009933.g003

recruited to the AT, presenting an increase of 68-fold and 49-fold from days 6 to 9 post-infection, respectively. Few neutrophils were detected in the gonadal AT prior to infection with $8.45x10^2$ cells, however they increased nearly 100-fold by day 28 post-infection (Fig 4A). Similarly, the number of neutrophils in the spleen increased significantly, presenting a 38-fold increase from days 0 to 28 post-infection (Fig 4A).

Prior to infection, few monocytes were present in the spleen and AT. During *T*. *brucei* infection, monocytes accumulated in both tissues, increasing 39-fold in the spleen and 12-fold in the gonadal AT by day 28 post-infection (Fig 4B).

Macrophages were the most abundant myeloid population in both tissues in control mice. Interestingly, this population was kept at relatively stable numbers throughout infection in the spleen, as the only significant change observed was a moderate 2.7-fold increase by day 28 post-infection (Fig 4C). In the gonadal AT, the number of macrophages was significantly increased from day 20 post-infection onward, presenting a 10-fold increase by day 28 post-infection (Fig 4C).

CD4+ and CD8+ T cell subsets showed a similar overall increase in the AT, while the spleen showed no changes in CD4+ T cells and an overall decrease for CD8+ T cells (S3B and S3C Fig). Within the total pool of T cells, we assessed the fraction that differentiated into effector T cells expressing IFN-γ, TNF-α or both pro-inflammatory cytokines. During the infection, we observed that the number of effector CD4+ T cells presented a modest incremental trend in the spleen, reaching a 3.8-fold increase by day 28 post-infection (Fig 4D). A higher relative increase in effector CD4+ T cells was observed in gonadal AT, with significant accumulation from day 14 post-infection onwards, showing a 14.6-fold increase by day 28 post-infection (Fig 4D). A distinct profile between the spleen and gonadal AT was observed for effector CD8 + T cells. There was a trend for a modest reduction in number of this effector cell in the spleen (Fig 4E). In contrast, a significant increase in the number of effector CD8+ T cells in the gonadal AT was observed from day 16 post-infection onwards, reaching a 8.7-fold increase by day 28 post-infection. This profile of effector T cells is in agreement with the high expression of TNF-α and IFN-γ in gonadal AT revealed at the transcriptomic level (S1 Fig and S1C and S1D File), confirming the accumulation of effector T cells in the AT and propagating a Th1 type of response. The number of Treg cells showed an overall decrease in the spleen while increasing 4-fold in gonadal AT (Fig 4F), which is in agreement with the increased expression of FOXP3, CTLA-4 and IL-10 at the transcriptomic level (S1 Fig and S1C and S1D File). This suggests that Treg cells recruited to AT may contribute to control an excessive inflammatory response and could favor the persistence of *T*. *brucei* parasites in AT.

This flow cytometry analysis in the AT is mostly consistent with changes observed in transcriptomic data (Fig 1C) and predicted by immuCC (Fig 1D). Specifically, we confirmed a similar relative variation for many immune subsets such as CD4+ T cells, CD8+ T cells, monocytes and neutrophils. Macrophages were the only population for which flow cytometry did not confirm the immuCC predictions (S2 Fig). This overestimation of the macrophage population by immuCC could be due to the fact that immune activation of adipocytes unlocks a gene expression signature that highly resembles that of macrophages[37]. Overall, during a *T*. *brucei* infection the AT accumulates cells of the innate and adaptive immunity branches. Importantly, there is a significant increase of immune cells described as protective against a *T*. *brucei* infection (*i.e.* IFN-γ+CD4+Th1 cells and macrophages).

Adipose tissue presents a strong humoral response

Effective immunity against *T*. *brucei* requires a humoral immune response in addition to a strong cellular immune response[8]. The importance of antibody-mediated *T*. *brucei* clearance

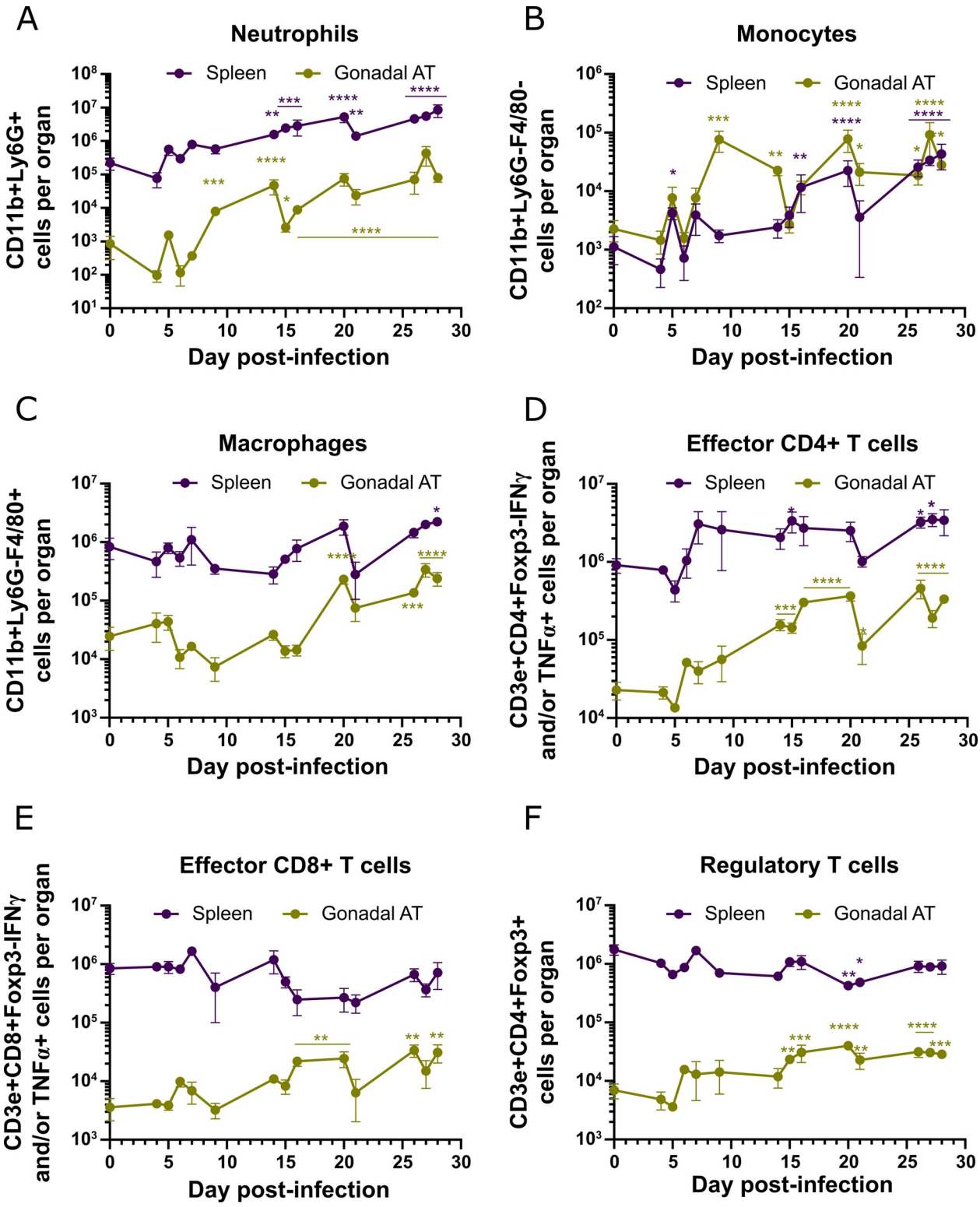

Fig 4. Dynamics of immune cells during infection. **(A-F)** Number of **(A)** neutrophils, **(B)** monocytes, **(C)** macrophages, **(D)** effector CD4+ T cells, **(E)** effector CD8+ T cells and **(F)** regulatory T cells in the spleen and gonadal AT. Error bars represent the SEM (n = 2–6 mice per group). Statistical analysis was performed with a two-way ANOVA using Sidak's test for multiple comparisons. * refers to statistical differences within the groups in each time-point and the non-infected group. *, $P<0.05$; **, $P<0.01$; ***, $P<0.001$; ****, $P<0.0001$.

https://doi.org/10.1371/journal.ppat.1009933.g004

is well documented. Indeed, B cell and antibody deficiencies lead to increased susceptibility to T. *brucei*[38] and passive transfer of VSG-specific antibodies grants variant-specific protection [39, 40].

To assess if a humoral response was ongoing in solid tissues and in AT in particular, we quantified the levels of antigen-specific IgM, IgG and IgA by ELISA, using plates coated with purified VSG AnTat1.1 (S5 Fig). A series of 10-fold dilutions of serum samples and 2-fold dilutions of cell-free suspensions from tissues were tested for anti-VSG AnTat1.1 immunoglobulins. For each sample, the antibody titer was determined as the highest dilution with an OD 450nm higher than the cutoff value (0.13x average of positive control + average of negative control) (S5D Fig)[41].

We collected samples from mice on days 0, 6 and 9 post-infection from the serum (reference of circulating immunoglobulins), spleen (reference of an active site of immunoglobulin production), AT and kidney (an example of low parasitised organ). These timepoints were chosen because in wild-type (WT) mice there is a significant drop in AT parasite burden between days 6–9 (Fig 2B) and we questioned if B cell responses could play a local role. As expected, circulating antibodies against VSG AnTaT1.1 increased in infected mice when compared to non-infected mice (*i.e.* 10 to 100-fold increase (Fig 5A). This effect was also observed in the interstitial fluid, albeit in an organ specific manner. Specifically, the antibody titer of IgM in the AT increased upon infection but was lower than in the kidney and spleen at day 6 post-infection (6.6 and 88-fold respectively) and to a lesser extent at day 9 post-infection (4.6 and 6.3-fold). Moreover, the antibody titer for IgG in the AT was similar that of the kidney at day 6 post-infection but was 107-fold lower than that of the spleen. By day 9 post-infection the AT presented a 3-fold lower anti-VSG IgG titer compared to the kidney and 14-fold lower than the spleen. Additionally, anti-VSG IgA was not detected in the AT and presented low titers in the spleen. Interestingly, kidney titers for anti-VSG IgA were high but were independent of infection, as titers from non-infected mice were equally elevated as those of infected mice.

Next, we assessed whether this humoral response in the AT was accompanied by a local B cell response. There was an increase in the numbers of B cells in spleen and AT (Fig 5E), as well as an increase in the number of activated, (IgD-CD19+ cells), and proliferating (Ki67+) B cells (Fig 5F). Specifically, by day 9 post-infection total B cells showed a 3.55-fold increase in the spleen and a 8.45-fold increase in the AT, relative to non-infected controls. This increase was also observed for activated B cells, as their number presented a 16.29-fold increase in the spleen and a 9.24-fold increase in the AT in the same period. We then assessed whether plasmocytes (*i.e.* main immunoglobulin producing cells) were present in the AT. CD138 (also known as syndecan-1) is an excellent marker of plasmacytic differentiation, however it is sensitive to the collagenase treatment used for flow cytometry analysis of AT digestion, and thus we applied immunohistochemistry to AT (Fig 5G–5I). Relative to non-infected mice, the number of CD138+ cells increased 3.7-fold and 17.4-fold at days 6 and 9 post-infection, respectively (Fig 5J), indicating that the AT harbors plasmocytes that secrete immunoglobulins.

Collectively, these data show that a humoral response takes place in the AT and suggest that the increase of immunoglobulin levels is likely the result of the infiltration of circulating immunoglobulins (serum), but also partially due to increased local production by antibody-producing plasmocytes in the AT. Altogether, we conclude that the components of a protective immune response against *T. brucei* are present in the AT.

Parasite load in adipose tissue depends on systemic effectors

Parasites infiltrate and accumulate in the AT, even though a host-protective acute (that turns chronic) immune response is mounted in response to the infectious agent, as revealed by the

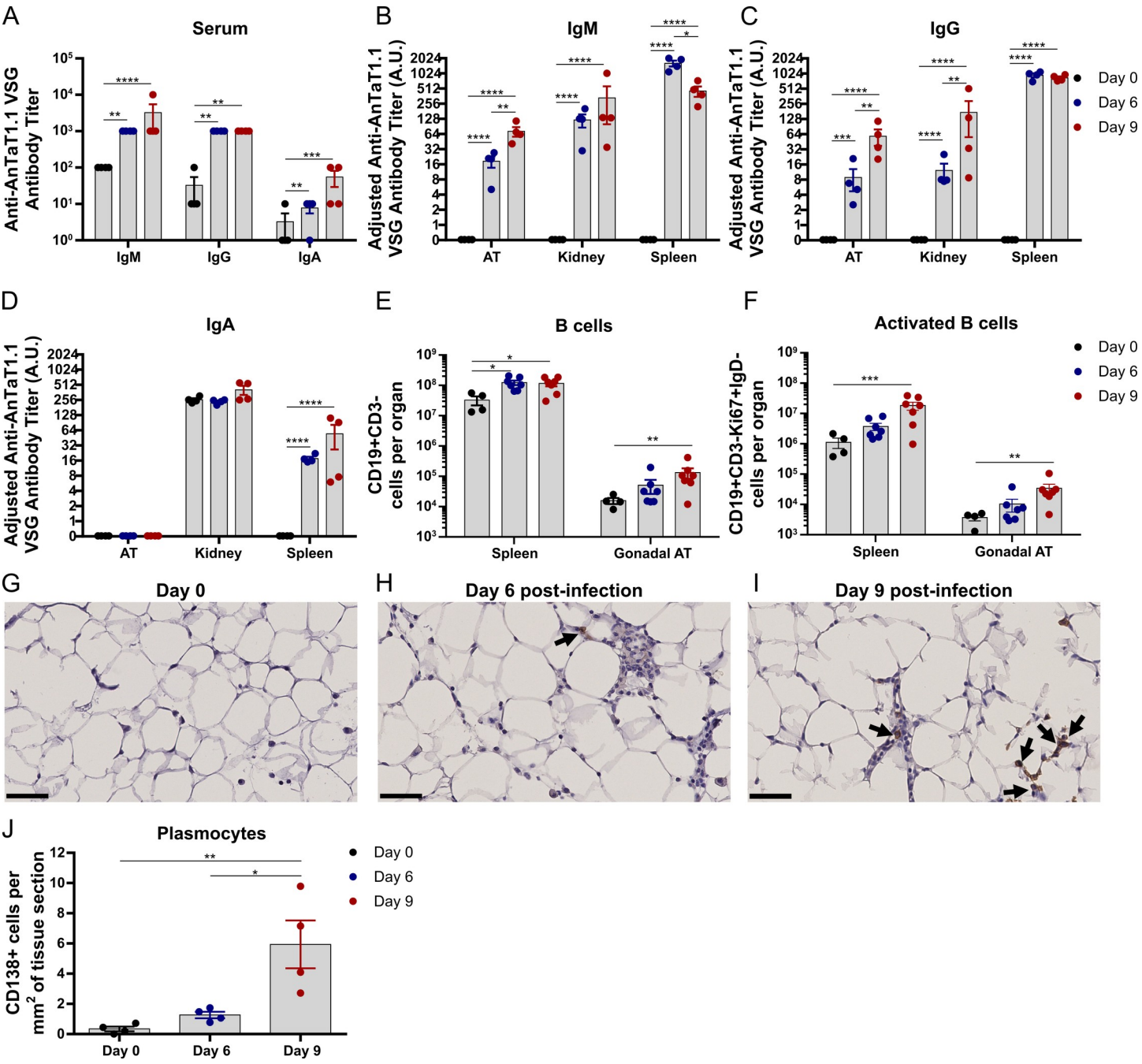

Fig 5. Dynamics of immunoglobulins, B cells and plasmocytes during infection. **(A)** Antibody titers of anti-AnTaT1.1 VSG in the serum. Antibody titer normalized to tissue mass used to prepare cell-free suspensions in arbitrary units (A.U.) of **(B)** IgM, **(C)** IgG and **(D)** IgA. Number of **(E)** total B cells and **(F)** activated B cells in the spleen and gonadal AT. Immunohistochemistry detection of (anti-CD138 antibody) plasmocytes at days **(G)** 0, **(H)** 6 and **(I)** 9 post-infection. **(J)** Quantification of plasmocytes in tissue sections. **(G-I)** Black arrows indicate CD138+ cells and scale bars represent 50 μm, original magnification 40x. Statistical analysis was performed with **(A-F)** two-way ANOVA and **(J)** one-way ANOVA using Sidak's test for multiple comparisons. *, P<0.05; **, P<0.01; ***, P<0.001; ****, P<0.0001.

https://doi.org/10.1371/journal.ppat.1009933.g005

dramatic accumulation of myeloid cells and lymphoid effector subsets (Figs 3 and 4). Thus, we decided to undertake a systematic approach and test the importance of several immune cells and soluble factors key in the control of *T. brucei*. For this, we performed infections in several immunocompromised mouse mutants, and collected organs on days 6 and 9 post-infection.

Specifically, we infected mice that lack T and B lymphocytes (deficient in the recombination activation gene 2 (*Rag2*$^{-/-}$)), (Fig 6A and 6B) mice that lack selectively B lymphocytes (*Jht*$^{-/-}$) (Fig 6C and 6D), mice that lack IFN-γ (*Ifng*$^{-/-}$) (Fig 6E and 6F), and mice that lack complement component 3 (C3$^{-/-}$) (Fig 6G and 6H). These cells or factors have been previously implicated in the parasite elimination. Here, we hypothesized that if one of these factors was ineffective solely in the clearance of parasites in the AT, its absence would have little impact on the elimination of AT parasites, but it would prevent parasite elimination in the blood and other organs.

Upon infection with *T*. *brucei*, in both *Rag2*$^{-/-}$ and *Jht*$^{-/-}$ mice, parasitemia increased until day 6 post-infection, but instead of undergoing a quick reduction, parasite numbers persisted at very high levels (Fig 6A and 6C). While WT mice were able to reduce parasite burden from the spleen and AT between days 6 and 9 by roughly 10-fold, neither *Rag2*$^{-/-}$ nor *Jht*$^{-/-}$ showed a significant decrease in the parasite burden of these organs in the same period (Fig 6B and 6D). These data show that efficient parasite elimination between days 6 and 9 post-infection in the AT requires a B and T cell responses, similarly to parasitemia clearance in the blood. Given that the infection promoted the generation of a high frequency of IFN-γ-producing CD4+ and CD8+ T effectors in AT (Fig 4D and 4E), the contribution of IFN-γ was assessed by infecting *Ifng*$^{-/-}$ mice. Unlike WT controls, *Ifng*$^{-/-}$ mice were not able to eliminate parasites from the blood nor from all tested solid tissues (Fig 6E and 6F). These results suggest that *T*. *brucei* is controlled by IFN-γ both systemically and within the tissues, highlighting the key role of Th1-dependent immune response in the control of the infection.

As previously shown, albeit with different kinetics[42], mice with defective complement system (C3-/-), were able to control the first peak of T. *brucei* parasitemia, suggesting that complement opsonization is not essential in the blood (Fig 6G). Interestingly, these mutant mice were partially impaired in controlling the number of parasites in the AT, between days 6 and 9 post-infection (4.3-fold reduction vs 32-fold reduction in WT mice) (Fig 6H). This impairment was also observed in the heart, where *C3*$^{-/-}$ showed virtually no parasite elimination (1.6-fold) whereas WT mice presented an 8.4-fold decrease between days 6 and 9 post-infection. These results suggest that the complement system may have a more active role in parasite elimination from some tissues than from the blood.

We then questioned whether an overarching immunosuppressive mechanism was reducing overall parasite clearance and allowing for higher parasite accumulation in the AT, when compared to other organs. Among these, the programmed cell death protein 1 (PD-1) and the programmed cell death ligand 1 (PD-L1) interactions are well described as inhibitors of T cell effector functions in several contexts, including infection[43]. The interaction between PD-1 on the surface of a T cell and PD-L1 on the surface of an antigen presenting cell, leads to the decreased activation, proliferation and cytokine secretion of the T cell. Although we observed by flow cytometry an upregulation of PD-1 in both CD4+ and CD8 + T cells (S6A and S6B Fig) and in *Pdcd1* gene expression (S1B Fig and S1C File) during the acute phase of infection, its antibody-mediated blockade failed to enhance parasite clearance in AT (S6C and S6D Fig).

Overall, the infections in immunocompromised mice revealed the parasite burden in the AT depends on several systemic components (B cells, T cells, IFN-γ and complement system). We conclude that the AT does not provide a niche devoid of immune surveillance for *T*. *brucei*.

Discussion

The relevance of tissue invasion and colonization by *T*. *brucei* is only now being elucidated in the context of pathogenesis, persistence, and drug resistance. Each tissue presents a specific immune environment that may impact a pathogen's ability to colonize and persist in each

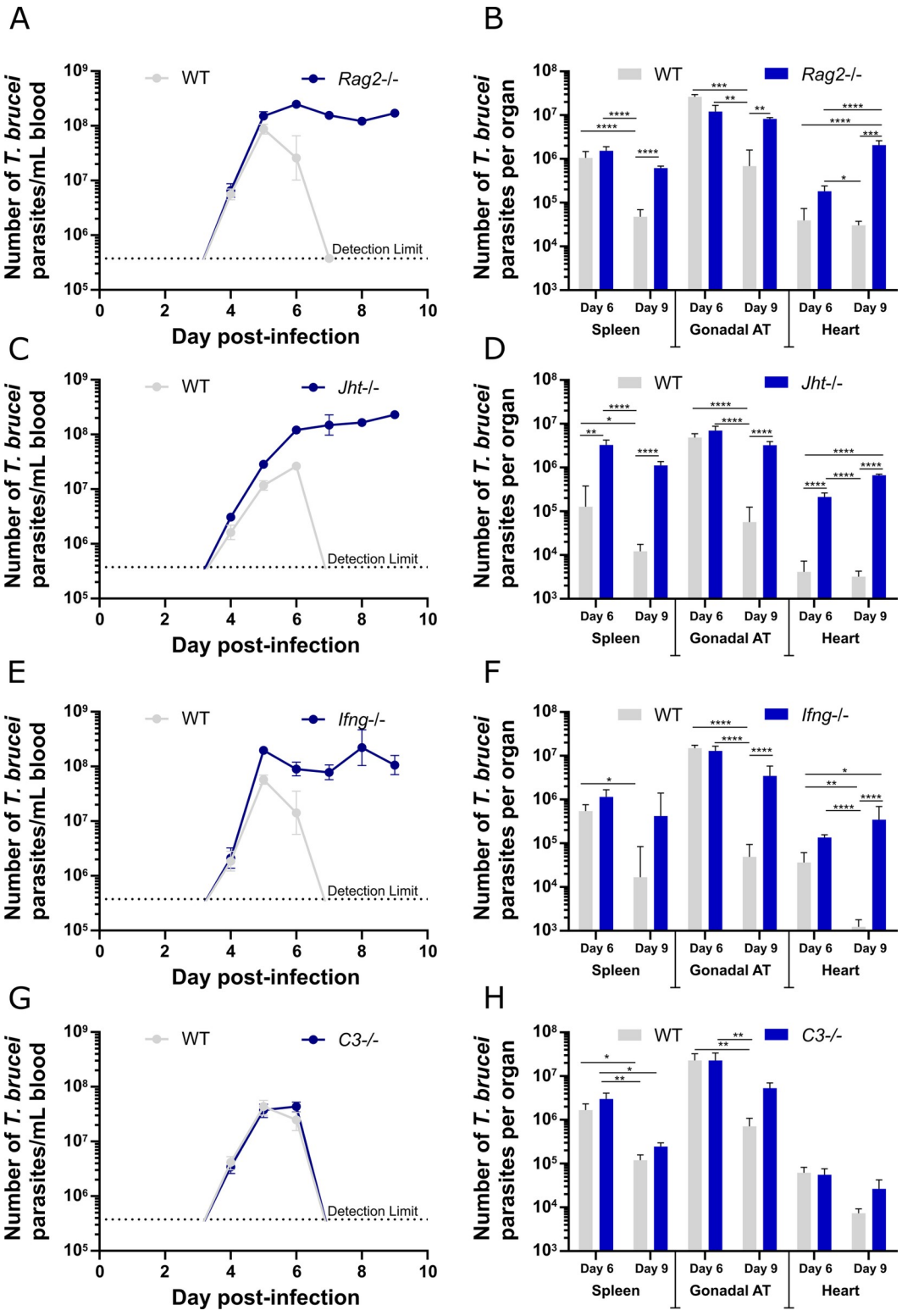

Fig 6. Assessment of the role of immune cells/factors in parasite control. Infection of WT and **(A-B)** *Rag2*$^{-/-}$, **(C-D)** *Jht*$^{-/-}$, **(E-F)** *Ifng*$^{-/-}$, **(G-H)** *C3*$^{-/-}$ **(A-H)** Error bars represent the SEM (n = 3–7 mice per group). **(Left)** Parasitemia of mice infected with *T. brucei*, quantified in a hemocytometer. Dashed line represents the limit of detection ($3.75x10^5$ parasites/mL of blood). **(Right)** Number of *T. brucei* parasites quantified by qPCR in spleen, gonadal AT and heart, 6 and 9 days post-infection. Statistical analysis was performed with a two-way ANOVA using Sidak's test for multiple comparisons. *, $P<0.05$; **, $P<0.01$; ***, $P<0.001$; ****, $P<0.0001$.

https://doi.org/10.1371/journal.ppat.1009933.g006

anatomical location. The increasing evidence of persistence of evolutionarily diverse pathogens in the AT raises the question of its immune competence. Given the extensive accumulation of *T*. *brucei* in the AT we sought to elucidate whether an effective immune response was mounted in this tissue and how different it was from the better described systemic responses observed in the blood and spleen (where the parasites also reside).

Adipose tissue immunity against *T. brucei*

Here, we show that upon *T*. *brucei* infection the AT acquires a marked immune transcriptomic phenotype. Within this immune phenotype, a marked Th1 signature is observed, which unlike a Th2 signature, is associated with protection against *T*. *brucei*. This shift in transcriptomic profile is likely the result of *in situ* activation of resident immune cells as well as of the recruitment of additional immune cells throughout infection. Accordingly, during infection we observed both by immunohistochemistry and flow cytometry a large accumulation of myeloid and lymphoid cells. Indeed, although with distinct kinetics, similar accumulations of neutrophils[44], monocytes[44, 45] and T cells[46, 47] have been reported for other active sites of *T*. *brucei*, such as the skin[44], liver[45, 47] and brain[46]. Comparison of the AT and spleen leukocyte accumulation kinetics reveals a sharp contrast between these tissues. The AT presents an overall sustained increase throughout time of all the immune cell types assessed.

While starting with a much higher number of immune cells, the spleen shows an overall maintenance of the total number of immune cells (Fig 2C). This maintenance of the total number of splenic immune cells does not represent a static immune environment and it is in fact the result of opposing variations in individual immune subsets. Among the few similarities found between the spleen and AT is the overall increase in monocyte and neutrophil numbers (Fig 4A and 4B), which is in accordance with previously published data for the spleen[48]. Although an active immune response is taking place in both the spleen and AT, the differences in their immune kinetics, especially in the T cell compartment, suggest that parasites in the spleen and in AT may be subjected to distinct immune responses.

The immune response mounted in the AT is likely to actively participate in the reduction of the number of parasites. Classically, parasites are described to be eliminated by antibody-dependent phagocytosis that can be assisted by IgM-mediated complement opsonization[9]. Our observation by TEM of phagocytosed parasites in the AT suggests that local elimination of the parasite is ongoing. This phagocytic clearance is consistent with the accumulation of antigen-specific IgM and IgG (Fig 5B and 5C) in the tissue, and macrophages that are activated by innate signals delivered by the presence of the parasite as well as adaptive signals such as the local production of IFN-γ by CD4+ Th1 cells (Fig 4D). This is supported by the observed abrogation of parasite clearance from the AT in infected mice deficient for T and/or B cells, or IFN-γ (Fig 6). Given the hyperparasitemia presented by these mutant mice, we cannot exclude the possibility that the high number of parasites in AT 9 days post-infection is partially due to a spill in effect from circulating parasites (although in some mutants and in some organs a tendency for higher parasite load is already detectable 6 days post-infection). However, the inability to remove immune cells/factors exclusively from the AT prevents the study of the contribution of circulating parasites that may excessively cross into tissues.

The dynamics of anti-VSG immunoglobulins show a protective humoral response in the AT, although at significantly lower levels than the spleen. Compared to the kidney, the AT shows comparable anti-VSG IgG titers and modestly lower IgM titers. Interestingly, while the AT shows no detectable anti-VSG IgA titer, the kidney has elevated titers even in non-infected mice. These are likely natural polyreactive IgAs [49] whose relevance in Trypanosomiasis, if any, remains to be elucidated. Although our data show the presence of plasmocytes and thus

suggest that local immunoglobulin production in the AT is likely occurring (Fig 5G–5J), how important this production is for the overall humoral response requires further investigation.

The observation that *C3*$^{-/-}$ mice are not as efficient at reducing parasite load in non-lymphoid solid tissues on day 9 is intriguing (Fig 6G and 6H). It has been previously reported that, while the parasite is at least partially resistant to complement-mediated lysis[50–52], the complement system is important for *T*. *brucei* opsonization and killing via phagocytosis[7, 52]. In the absence of complement opsonization, macrophages can still phagocytose *T*. *brucei*, albeit less efficiently[52–54]. Classical activation of the complement system requires IgM or IgG binding the parasite to initiate binding of complement components to the Fc-region. Unlike IgG, opsonization by IgM alone does not promote macrophage phagocytosis, as these cells lack the FcμR[55]. Hence, IgM-promoted phagocytosis requires opsonization by the complement system. Given that in the AT, anti-VSG IgM and IgG titers are significantly lower than in the spleen (a proxy for the blood) (Fig 5), it is tempting to speculate that the parasite control in AT (and perhaps other solid organs) is more dependent on complement opsonization, while in the spleen the faster accumulation of specific IgG could reduce complement-dependency. Further studies are required to better understand the role of the complement system in *T*. *brucei* infection, including a quantitative analysis of the complement components and immunoglobulins in multiple tissue types throughout infection.

Parasite immune evasion in the AT could also be achieved by an increased activity of immunosuppressive effectors when compared to other organs. Our transcriptomic data show an upregulation of multiple immune-suppressive genes (S1B Fig), which is further validated by a progressive accumulation of Treg cells (Fig 4F). This suppressive response serves to prevent overactivation of the immune system and reduce immunopathology but can be exploited by pathogens to reduce immune pressure on them. In this scenario it is possible that one or multiple of these suppressive mechanisms prevent sterile tissue immunity. As such, we sought to disrupt the immunosuppressive PD-1/PD-L1 axis which shows evidence of being upregulated in the AT during infection. This disruption led to no significant alterations in the number of parasites in the AT (S6D Fig). Thus, it is unlikely that this immunosuppressive axis is a determining factor for parasite colonization of the AT.

How do parasites evade the immune response in the AT?

Antigenic variation is the hallmark immune evasion strategy used by African trypanosomes. At any given time during infection a small subset of VSGs is dominant among the BSF population[56], leading to the mounting of VSG-specific IgM responses. These IgM responses are efficient at eliminating parasites expressing their cognate VSG but exert no effect on parasites expressing a different VSG coat. It is possible that when parasites colonize solid tissues, they adapt VSG gene regulation to fine tune antigenic variation. If for example, VSG switching occurred more frequently, perhaps the tissues could be the source of new VSG variants that escape more efficiently the immune response. This hypothesis remains to be investigated.

Another immune evasion strategy employed by *T*. *brucei* is its ability to remove VSG-bound antibodies through endocytosis of the VSG-Ig complex. This process requires a hydrodynamic drag force to propel the VSG-Ig complex towards the parasite's flagellar pocket and protects the parasite from Ig-mediated opsonization until a critical antibody threshold is reached[51]. Factors affecting this hydrodynamic drag force include the milieu's viscosity, the parasites swimming speed and the interstitial fluid's flow speed[51, 57]. It is possible that these and other biophysical factors may vary between the blood and interstitia of different organs [57], thus granting the parasite a varying capacity to neutralize antibody responses. This could confer to parasites an immune-independent resistance to antibody-mediated phagocytosis.

In summary, we show that an active immune response is mounted in the AT against *T. brucei*, where parasite burden is controlled using the same overarching components of the systemic immune response. Whether these host-protective components are as effective in the AT as in other tissues and the blood requires further study.

Methods

Ethics statement

All experimental animal work was performed in accordance with the Federation of European Laboratory Animal Science Associations (FELASA) guidelines and was approved by the Animal Care and Ethical Committee of the Instituto de Medicina Molecular (under the license AWB_2016_07_LF_Tropism).

RNA isolation and RNA-Seq analysis

Mice infected for 0, 6 and 26 days were euthanized and perfused, gonadal fat depots were collected, RNA extracted by TRIzol (Invitrogen) and its integrity assessed by TapeStation (Agilent). Poly-A mRNA library was prepared as recommended by the manufacturer (Illumina TruSeq) and the samples were sequenced in Illumina HiSeq2000 platform (EMBL and BGI). Sequenced reads were 49bp single-end for samples D0.1, D6.1, D26.1 and D26.2 and 100bp paired-end for the remaining ones. To reduce differences between single and paired-end RNA-Seq datasets, the second read of each mate-pair in paired-end samples was discarded. Also, the first read of each mate-pair was trimmed to the first 49 bases using Trimmomatic (version 0.38)[58].

Read quality was evaluated with FastQC quality control tool (version 0.11.5)[59] and raw reads were trimmed to improve mapping with SolexaQA (version 3.1.7.1)[60]. First, reads were cropped to their longest continuous segment whose PHRED score was higher than 28 and then reads smaller than 25 bp were discarded. Trimmed reads were aligned to the *T. brucei* TREU927 genome (TriTrypDB version 33)[61] using HISAT2 (version 2.0.0-beta)[62] without spliced alignments. Reads mapping to *T. brucei* were discarded and the unmapped reads aligned to the *M. musculus* genome (GRCm38 release 92)[63] using HISAT2 with default parameters. Unique read counts were computed using featureCounts (version 1.6.2)[64] and lowly expressed genes were discarded by keeping genes having a minimum of 10 read counts in at least 2 replicates of the same condition (D0, D6 or D26). In total, 19,488 genes were used to perform differential expression analysis by DESeq2 (version 1.18.1)[65], edgeR (version 3.20.9)[66] and limma (version 3.34.9)[67] from Bioconductor (version 3.5)[68] in the R software environment (version 3.4.4)[69]. Genes having an adjusted p-value < 0.01 in at least 2 algorithms and a fold-change > 2 in all were considered differentially expressed.

GO term overrepresentation on differentially expressed genes was performed with the topGO (version 2.30.1)[70] R package, using the weight01 algorithm and Fisher's exact test (p-value < 0.01) for terms with at least 5 annotated genes.

Heat maps were created using the package ComplexHeatmap (version 1.17.1)[71] and ggplot2 (version 3.0.0)[72] was used to create the remaining plots.

Relative immune cell compositions in infected AT were estimated with seq-ImmuCC deconvolution tool[34]. As in differential expression analysis, only genes having a minimum of 10 read counts in at least 2 replicates of the same condition were used. Then, read counts were processed following the authors script in Github[34]: the read counts of each V, D and J gene segments in both T and B cell receptors merged and a quantile normalization performed. The quantile normalized read counts were uploaded in ImmuCC server using the SVR algorithm.

RNA-Seq data from the samples of day 6 post-infection AT were made publicly available in the ArrayExpress database under the accession number E-MTAB-4061. The remaining RNA--Seq sequence data have also been submitted to the ArrayExpress database under the accession number E-MTAB-7596.

Animals

In vivo experiments were performed with male C57BL/6J mice, from Charles River Laboratories International, unless otherwise stated. *Rag2*-deficient (*Rag2*$^{-/-}$) and *Jht*-deficient (*Jht*$^{-/-}$) mice, generated on a C57BL/6J background, were obtained from Instituto Gulbenkian de Ciência (IGC, Portugal). Ifng-deficient (*Ifng*$^{-/-}$), generated on a C57BL/6J background, were kindly provided by Bruno Silva-Santos laboratory from Instituto de Medicina Molecular (iMM, Portugal). C3-deficient (*C3*$^{-/-}$), generated on a C57BL/6J background, were kindly provided by Miguel Prudêncio laboratory from Instituto de Medicina Molecular (iMM, Portugal). All experimental mice were 7–9 weeks old, unless otherwise stated. *Jht*-deficient mice were 9–21 weeks old, as well as the WT controls in such experiment. Mice were housed in a Specific-Pathogen-Free barrier facility, at iMM, under standard laboratory conditions: 21 to 22˚C ambient temperature and a 12h light/12h dark cycle. Chow and water were available *ad libitum*.

Parasite lines

Experiments were performed using parasites derived from *T*. *brucei* AnTat 1.1E, a pleomorphic clone derived from the EATRO1125 strain. AnTat 1.1E 90–13 is a transgenic cell-line encoding the tetracyclin repressor and T7 RNA polymerase[73]. AnTat1.1E 90–13 GFP::PAD1$_{utr}$ derives from AnTat1.1E 90–13 in which the green fluorescent protein (GFP) is coupled to PAD1 3'UTR.

Infection

T. *brucei* cryostabilates were thawed and parasite viability by its motility was confirmed under an optic microscope. Mice were infected by intraperitoneal (i.p.) injection of 2,000 *T*. *brucei* parasites. At selected time-points post-infection, animals were euthanized by CO_2 narcosis and immediately perfused transcardially with pre-warmed heparinised saline (50mL phosphate buffered saline (PBS) with 250 μL of 5000 I.U./mL heparin). Organs were collected and either snap frozen in liquid nitrogen; used immediately to prepare single cell suspensions for flow cytometry staining; or immersion-fixed in formalin or glutaraldehyde for histopathology or electron microscopy, respectively. To block PD-1/PD-L1 axis, mice were injected intravenously (i.v.) with 300μg of αPD-1 (clone RMP1-14, InVivoMab, BioXcell), immediately before infection and at days 3, 5 and 7 post-infection.

Histopathology and Electron Microscopy

Formalin-fixed gonadal adipose tissue was paraffin-embedded and sectioned at 4 μm. Immunohistochemistry for the identification of trypanosomes and inflammatory cells (macrophages and T cells) was performed using a non-purified rabbit serum anti-*T*. *brucei* VSG13 antigen (cross-reactive with most *T*. *brucei* VSGs because it is not CRD-depleted, produced in-house), anti-F4/80 antibodies (Abcam, ab6640), anti-CD3 (Dako, A0452), and anti-CD138 (BD, 553712) following conventional protocols. Briefly, antigen retrieval slides was performed in PT Link module (DAKO) at low-Ph, followed by incubation with the primary antibodies. EnVision Link horseradish peroxidase/DAB visualization system (DAKO) was used and

counterstained with Harris hematoxylin. For Transmission Electron Microscopy, samples were fixed with a solution containing 2.5% glutaraldehyde (Electron Microscopy Sciences, EMS) plus 0.1% formaldehyde (Thermo Fisher) in 0.1 M cacodylate buffer (Sigma), pH7.3 for 1 h. After fixation, these were washed and treated with 0.1% Millipore filtered cacodylate buffered (Sigma), post-fixed with 1% Millipore-filtered osmium tetroxide (EMS) for 30 min, and stained *en bloc*, with 1% Millipore-filtered uranyl acetate (Agar Scientific). Samples were dehydrated in increasing concentrations of ethanol, infiltrated and embedded in EMBed-812 medium (EMS). Polymerization was performed at 60˚C for 2 days, and ultrathin sections were cut in a Reichert supernova microtome, stained with uranyl acetate and lead citrate (Sigma) and examined in a H-7650 transmission electron microscope (Hitachi) at an accelerating voltage of 100 kV. Electron micrographs were obtained using a XR41M bottom mount AMT digital camera (Advanced Microscopy Techniques Corp). Acquisition of immunohistochemistry images was done in a Nanozoomer-SQ (Hamamatsu Photonics) and analysed using NDP. view2 (Hamamatsu Photonics).

Parasite quantification in blood and organs

For parasitemia quantification, blood samples were taken daily from the tail vein and diluted 1:150. Parasites were counted manually in a Neubauer haemocytometer (0.1 mm^3, detection limit is $3.75x10^5$ parasites per mL of blood). When applicable, the total number of parasites was determined by multiplying by the total volume of blood, considering that a mouse has 58.5 mL of blood per kg of bodyweight.

For parasite quantification in organs, genomic DNA (gDNA) was extracted using NZY tissue gDNA isolation kit (NZYTech, Portugal). The amount of *T*. *brucei* 18S rDNA was measured by quantitative PCR (qPCR), using the primers 5'-ACGGAATGGCACCACAAGAC–3' and 5'–GTCCGTTGACGGAATCAACC–3', and converted into number of parasites using a calibration curve, as previously described by Trindade *et al*. [15]. Number of parasites per mg of organ (parasite density) was calculated by dividing the number of parasites by the mass of organ used for qPCR. The total amount of parasites in the organ was estimated by multiplying parasite density by the total mass of the organ. Parasite burden normalized to tissue mass and corresponding organ masses are available in the S3 and S5 Files.

Preparation of single cell suspensions

Gonadal AT samples were incubated at 37˚C in Dulbecco's Modified Eagle Medium (DMEM, GIBCO) with Collagenase I (0.4mg/mL, Whortington LS004196), Collagenase IV (1mg/mL, Whortington LS004188) and DNAse (10μg/mL) for 30 minutes, under 1100 rpm agitation. Single cell suspensions from the spleen, heart and digested gonadal AT were obtained by sieving them through a 40μm-pore-size nylon cell strainer (BD Biosciences) with a syringe plunger. Spleen cells were treated with erythrocyte lysis buffer (BioLegend 420301) to lyse red blood cells. Both spleen and gonadal AT cells were resuspended in complete Roswell Park Memorial Institute medium (cRPMI, RPMI supplemented with 1% sodium pyruvate 100mM, 1% MEM non-essential amino acids, 1% HEPES 1M, 1% Pen-Strep, 0.1% gentamycin 50mg/mL, 0.1% β-mercaptoethanol 50mM and 10% fetal calf serum (all from Gibco)) to use for flow cytometry analysis. Live cells in single cell suspensions were counted after trypan blue staining in a haemocytometer.

Flow cytometry

Stainings of myeloid and lymphoid cells were performed separately. In isolated spleen cells, stainings were performed in $5x10^6$ cells. Stainings of cells isolated from the gonadal AT were

performed with the highest number of cells possible, by diving the cell suspension equally between each staining (never exceeding $5x10^6$ cells).

For myeloid staining of surface determinants, cells were incubated for 45 minutes at 25˚C in cRPMI, in the presence of 5% normal mouse serum (NMS), with the following antibodies: F4/80-FITC (clone BM8, BioLegend), Ly6G-PerCP/Cy5.5 (clone 1A8, BioLegend), CD274-PE/Cy7 (PD-L1, clone 10F.9G2, BioLegend), CD11b-APC/Cy7 (clone M1/70, BioLegend), CD45-Brilliant Violet (BV) 510 (clone 30-F11, BioLegend) and Ly6C-BV605 (clone HK1.4, BioLegend). To stain non-viable cells, Zombie Violet Fixable Viability Kit (BioLegend) was used, incubating cells in PBS with 5% NMS, for 15 minutes at 25˚C. Finally, stained cells were resuspended in cRPMI for flow cytometry acquisition.

For lymphoid staining, cells were first incubated in cRPMI with phorbol 12-myristate 13-acetate (20ng/mL, PMA) and ionomycin (1μg/mL) to stimulate cytokine production by T cells, for 1h45 at 37˚C. Next, to block cytokine secretion, brefeldin A (10μg/mL) and monensin (5μM), were added for the final 1h at 37˚C of incubation. Staining of surface determinants was performed by incubating cells for 45 minutes at 25˚C in cRPMI with 5% NMS and the following antibodies: CD3-FITC (clone 17A2, BioLegend), CD279-PE (PD-1, clone J43, eBioscience), CD45-BV510 (clone 30-F11, BioLegend), CD4-BV605 (clone RM4-5, BioLegend) and CD8-BV711 (clone 53–6.7, BioLegend). To stain non-viable cells, LIVE/DEAD Fixable Near-IR Dead Cell Stain Kit (Invitrogen) was used, incubating cells in PBS with 5% NMS, for 15 minutes at 4˚C. For staining of intracellular antigens, fixation and permeabilization of cells was performed using Foxp3/Transcription Factor Staining Buffer Set (eBioscience) and the following antibodies: IFN-γ-PerCP/Cy5.5 (clone XMG1.2, BioLegend), Foxp3-APC (clone FJK-16s, eBioscience) and TNF-α-eFluor450 (clone MP6-XT22, eBioscience). Finally, stained cells were resuspended in cRPMI for flow cytometry acquisition.

For staining of B cell surface determinants, cells were incubated for 45 minutes at 25˚C in cRPMI, in the presence of 5% normal mouse serum (NMS), with the following antibodies: CD45-BV510 (clone 30-F11, BioLegend), IgD-APC (clone 12-26c, eBioscience) and CD19-APC/Cy7 (clone 6D5, Biolegend). For staining of intracellular antigens, fixation and permeabilization of cells was performed using Foxp3/Transcription Factor Staining Buffer Set (eBioscience) and the following antibody Ki67-PE (clone 16A8, eBioscience). Samples were analysed on a BD LSRFortessa flow cytometer with FACSDiva 6.2 Software. All data were analysed using FlowJo software version 10.0.7r2. A schematic of the gating strategy used is represented in S2 Fig. Immune cell populations normalized to tissue mass and corresponding organ masses are available in the S3 and S4 Files.

Soluble VSG isolation and identification

Approximately $5x10^8$ AnTat1.1E parasites cultured in HMI-11 were centrifuged at 2500g at 4˚C for 10 minutes and washed twice in trypanosome dilution buffer (TDB). Trypanosomes were then resuspended and incubated for 3 minutes at 37˚C in 3 mL of 10mM sodium phosphate (NaH_2PO_4) buffer pH 8.0 containing a protease inhibitor cocktail (P8340, Sigma). Cells were then incubated for 3 minutes on an ice water bath, centrifuged at 4000g for 5 minutes and the supernatant purified through a diethylaminoethyl Sepharose column (GE Healthcare). Protein quantification was performed using a BCA Protein Assay Kit (A53225, ThermoFisher Scientific) according to the manufacturer's instructions.

The protein sample was run through SDS-PAGE, stained with Coomassie blue and the protein band of interest was isolated, destained, reduced, alkylated and digested with trypsin (Promega) overnight at 37˚C. The tryptic peptides were desalted and concentrated using POROS C18 (Empore, 3M) and eluted directly onto the MALDI plate using 1 μL of in 50% (v/v)

acetonitrile and 5% (v/v) formic acid. The data were acquired in positive reflector MS and MS/MS modes using a 5800 MALDI-TOF/TOF (AB Sciex) mass spectrometer and using TOF/TOF Series Explorer software v.4.1.0 (Applied Biosystems). External calibration was performed using a CalMix5 standard (Protea). The 25 most intense precursor ions from the MS spectra were selected for MS/MS analysis. The raw MS and MS/MS data were analysed using Protein Pilot software v.4.5 (ABSciex) with the Mascot search engine (MOWSE algorithm). For the search parameters were as follows: monoisotopic peptide mass values were considered, maximum precursor mass tolerance (MS) of 50 ppm and a maximum fragment mass tolerance (MS/MS) of 0.3 Da. The search was performed against the SwissProt protein sequence database without taxonomy restriction. Carboxyamidomethylation of cysteines was set as fixed modifications, oxidation of methionines and N-Pyro Glu of the N-terminal Q were set as variable modifications. Protein identification was accepted only when significant protein homology scores were obtained ($P < 0.05$) and at least one peptide was fragmented with a significant individual ion score ($P < 0.05$). The MS data were generated by the Mass Spectrometry Unit (UniMS), ITQB/iBET, Oeiras, Portugal.

Antibody quantification

Antigen-specific antibody titers were determined by ELISA. Assay plates (423501, BioLegend) were coated overnight with 2 μg/mL purified VSG AnTat1.1 (10 mM sodium phosphate buffer, pH 8.0) at 4˚C. Assay plates were blocked with blocking buffer (3% BSA in PBS with 0.05% Tween20). Secondary antibody solutions were prepared by diluting 1:1000 anti-mouse IgM-HRP (lab0372, Covalab), anti-mouse IgG-HRP (lab0365, Covalab) and anti-mouse IgA-biotin (clone RMA-1, BioLegend). Wells with biotinylated antibodies were incubated with SAv-HRP (BioLegend). Assay plates were developed with TMB substrate set (BioLegend), subsequently stopped with a 1M sulfuric acid solution and the OD 450 nm values were read in a TECAN Infinite M200 microplate reader using 570 nm as the reference wavelength. All washing steps were performed with PBS with 0.05% Tween20. The OD cut-off value used for antibody titer was determined according to the formula $[\text{Cut-off} = X_{neg} + 0.13(X_{pos})]$sssss, where X_{neg} is the average of the assay wells loaded with PBS and X_{pos} is the average of the wells loaded with the most concentrated samples from mice infected for 9 days Antibody titers for AT, kidney and spleen were normalized to the organ masses used to prepare cell-free suspensions.

Statistical analysis

The values presented are mean ± SEM. Parasite and immune cell numbers were transformed into their respective Log base 10 values to achieve linearization prior to statistical analysis. Statistical differences were assessed using two-way ANOVA and one-way ANOVA with Sidak's test for multiple comparisons. P values lower than 0.05 were considered to be statistically significant.

Supporting information

S1 Fig. Immune activatory and suppressive transcriptomic signature. Heat map of the differential expression of genes associated with immune response **(A)** activation and **(B)** suppression at days 6 and 26 post-infection relative to non-infected. Gene expression change in Log2 units is denoted in red for up-regulation and in blue for down-regulation.
(TIF)

S2 Fig. Gating strategy for flow cytometry analysis. (A) Myeloid gating strategy: live immune cells were gated based on positive expression of CD45 and absence of viability dye

signal. Single cells were then identified using SSC-W vs FSC-A gating. Total myeloid cells were selected based on CD11b expression and then subdivided into neutrophils and other myeloid cells based on Ly6G gating. Within the remaining myeloid cells, macrophages and monocytes were identified using F4/80 vs Ly6C gating. **(B)** Lymphoid gating strategy: single live immune cells were identified as described above and then T cells were identified based on the co-expression of CD3 and CD4 or CD3 and CD8. CD4+ T cells were further subdivided into conventional CD4+ T cells or regulatory T cells based on FoxP3 expression. Effector T cells were identified by gating single or dual expression of TNF-α and IFN-γ within CD3+CD4+FoxP3- or CD3+CD8+ cells **(C)** B cell gating strategy: Live immune cells were identified as before and then B cells were identified based on expression of CD19 and lack of CD3 expression. Activated B cells were identified based on positive Ki67 expression and absence of IgD expression.
(TIF)

S3 Fig. Comparison of flow cytometry and immuCC data. Variation of immune cell subsets between days 0, 6 and 26 post-infection. Data are scaled between 0 and 1, where 1 corresponds to the highest percentual value within each group. **(A)** B cells, **(B)** CD4+ T cells, **(C)** CD8+ T cells, **(D)** Macrophages, **(E)** monocytes, **(F)** neutrophils and **(G)** other immune cells.
(TIF)

S4 Fig. Organ mass and T cell dynamics. **(A)** Spleen and gonadal AT mass. **(B)** CD4+ T cells. **(C)** CD8+ T cells. Error bars represent the standard error of the mean (n = 2–6 mice per group). Statistical analysis was performed with a two-way ANOVA using Sidak's test for multiple comparisons. * refers to statistical differences between the group in each time-point and the non-infected group. *, $P<0.05$; **, $P<0.01$; ***, $P<0.001$; ****, $P<0.0001$.
(TIF)

S5 Fig. Purified soluble VSG identification. **(A)** Coomassie stained SDS-PAGE of purified soluble VSG solution denoting a single preeminent band within the predicted size range of VSG. **(B)** Best peptide match within the SwissProt database (sp|P06015|VSA1_TRYBB, Variant surface glycoprotein AnTaT 1.1 OS = Trypanosoma brucei brucei OX = 5702 PE = 2 SV = 1) with matching peptides depicted in bold red. **(C)** Summary of protein identification. Protein score is -10*Log(P), where P is the probability that the observed match is a random event. Protein scores greater than 70 are significant ($p<0.05$). Protein scores are derived from ions scores as a non-probabilistic basis for ranking protein hits. **(D)** Measurement of anti-VSG IgM titers by ELISA depicting optical density (OD) curves and antibody titer cut off determination.
(TIF)

S6 Fig. Assessment of the role of PD-1 expression in parasite control. Percentage of PD1+ **(A)** CD4+ T cells and **(B)** CD8+ T cells. Effect of anti-PD-1 treatment on **(C)** parasitemia of mice infected with *T. brucei*, quantified in a hemocytometer and **(D)** number of T. brucei parasites quantified by qPCR in spleen, gonadal AT and heart, 6 and 9 days post-infection. Error bars represent the SEM (n = 5 mice per group). Statistical analysis was performed with a two-way ANOVA using Sidak's test for multiple comparisons. **(A-B)** * refers to statistical differences between groups. *, $P<0.05$; **, $P<0.01$; ***, $P<0.001$; ****, $P<0.0001$.
(TIF)

S1 Table. Mapping information of RNA-Seq reads in samples from infected AT.
(DOCX)

S1 File. RNA-seq raw counts and differential expression analysis. **(A)** Raw counts and **(B)** reads per kilobase per million mapped reads from RNA-seq of AT from non-infected mice

(D0), n = 3, day 6 post-infection (D6), n = 3 and day 26 post-infection (D26), n = 2. Differential expression analysis between **(C)** D0 and D6, **(D)** D0 and D26 and **(E)** D6 and D26.
(XLSX)

S2 File. Significant GO terms list. GO term analysis from RNA-seq of AT from non-infected mice (D0), n = 3, day 6 post-infection (D6), n = 3 and day 26 post-infection (D26), Up-regulated GO terms in the AT between **(A)** D6vsD0, **(B)** D26vsD0, **(C)** D26vsD6. Down-regulated GO terms in the AT between **(D)** D6vsD0, **(E)** D26vsD0, **(F)** D26vsD6.
(XLSX)

S3 File. Effect of tissue weight on immune cell number and parasite number determination. (A) Weight of spleens and ATs analysed. Data for entire organs and normalized to tissue weight **(B-C)** parasite burden, **(D-E)** CD45+ cells, **(F-G)** neutrophils, **(H-I)** macrophages, **(J-K)** monocytes, **(L-M)** effector CD4+ T cells, **(N-O)** effector CD8+ T cells and **(P-Q)** regulatory T cells.
(PDF)

S4 File. Effect of tissue weight on B cell number determination. (A) Weight of spleens and ATs analysed. Data for entire organs and normalized to tissue weight **(B-C)** B cells and **(D-E)** activated B cells.
(PDF)

S5 File. Effect of tissue weight on parasite number determination. Weight of organs used from infected **(A)** *Rag2*$^{-/-}$, **(B)** *Jht*$^{-/-}$, **(C)** *Ifng*$^{-/-}$, **(D)** *C3*$^{-/-}$ and **(E)** anti-PD1 treated mice, with respective controls. Data for parasite numbers in the entire organ or normalized to tissue weight for infected **(F-G)** *Rag2*$^{-/-}$, **(H-I)** *Jht*$^{-/-}$, **(J-K)** *Ifng*$^{-/-}$, **(L-M)** *C3*$^{-/-}$ and **(N-O)** anti-PD1 treated mice, with respective controls.
(PDF)

Acknowledgments

We are grateful to Bruno Silva-Santos (iMM) for the helpful discussion and for providing experimental materials. We thank Andreia Pinto, Ana Margarida Biscaia Santos and Ana Rita Pires from the Histology and Comparative Pathology Laboratory of the iMM for expert technical assistance. We also thank the staff of the Rodent facility of the iMM and Catarina Correia and Isabel Abreu of the Mass Spectrometry Unit (UniMS) of ITQB/iBET.

Author Contributions

Conceptualization: Tiago Bizarra-Rebelo, Karine Serre, Luisa M. Figueiredo.

Data curation: Henrique Machado, Tiago Bizarra-Rebelo, Mariana Costa-Sequeira, Barbara Rentroia-Pacheco.

Formal analysis: Henrique Machado, Tiago Bizarra-Rebelo, Mariana Costa-Sequeira, Barbara Rentroia-Pacheco.

Funding acquisition: Karine Serre, Luisa M. Figueiredo.

Investigation: Henrique Machado, Tiago Bizarra-Rebelo, Sandra Trindade, Tânia Carvalho, Filipa Rijo-Ferreira, Karine Serre.

Methodology: Tiago Bizarra-Rebelo, Mariana Costa-Sequeira, Tânia Carvalho, Barbara Rentroia-Pacheco.

Project administration: Karine Serre, Luisa M. Figueiredo.

Resources: Karine Serre, Luisa M. Figueiredo.

Software: Mariana Costa-Sequeira, Barbara Rentroia-Pacheco.

Supervision: Karine Serre, Luisa M. Figueiredo.

Validation: Henrique Machado, Tiago Bizarra-Rebelo, Karine Serre, Luisa M. Figueiredo.

Visualization: Henrique Machado, Tiago Bizarra-Rebelo, Mariana Costa-Sequeira.

Writing – original draft: Henrique Machado, Tiago Bizarra-Rebelo, Tânia Carvalho, Karine Serre, Luisa M. Figueiredo.

Writing – review & editing: Henrique Machado, Tiago Bizarra-Rebelo, Tânia Carvalho, Karine Serre, Luisa M. Figueiredo.

References

1. Bukachi SA, Wandibba S, Nyamongo IK. The socio-economic burden of human African trypanosomiasis and the coping strategies of households in the South Western Kenya foci. PLoS Negl Trop Dis. 2017; 11: e0006002. https://doi.org/10.1371/journal.pntd.0006002 PMID: 29073144
2. Shaw A, Robays J, Fèvre EM, Lutumba P, Boelaert M. The Burden of Human African Trypanosomiasis. Handbook of Disease Burdens and Quality of Life Measures. New York, NY: Springer New York; 2010. pp. 1433–1442. https://doi.org/10.1007/978-0-387-78665-0_83
3. Kennedy PGE. Clinical features, diagnosis, and treatment of human African trypanosomiasis (sleeping sickness). Lancet Neurol. 2013; 12: 186–194. https://doi.org/10.1016/S1474-4422(12)70296-X PMID: 23260189
4. Raper J, Nussenzweig V, Tomlinson S. The main lytic factor of Trypanosoma brucei brucei in normal human serum is not high density lipoprotein. J Exp Med. 1996; 183: 1023–1029. https://doi.org/10.1084/jem.183.3.1023 PMID: 8642243
5. Vanhamme L, Paturiaux-Hanocq F, Poelvoorde P, Nolan DP, Lins L, Van Den Abbeele J, et al. Apolipoprotein L-I is the trypanosome lytic factor of human serum. Nature. 2003; 422: 83–87. https://doi.org/10.1038/nature01461 PMID: 12621437
6. Verdi J, Zipkin R, Hillman E, Gertsch RA, Pangburn SJ, Thomson R, et al. Inducible Germline IgMs Bridge Trypanosome Lytic Factor Assembly and Parasite Recognition. Cell Host Microbe. 2020; 28: 79-88.e4. https://doi.org/10.1016/j.chom.2020.04.012 PMID: 32416060
7. Macaskill JA, Holmes PH, Whitelaw DD, McConnell I, Jennings FW, Urquhart GM. Immunological clearance of 75Se-labelled Trypanosoma brucei in mice. II. Mechanisms in immune animals. Immunology. 1980; 40: 629–35. https://doi.org/10.1016/0001-706x(89)90003-x PMID: 7429544
8. Reinitz DM, Mansfield JM. T-cell-independent and T-cell-dependent B-cell responses to exposed variant surface glycoprotein epitopes in trypanosome-infected mice. Infect Immun. 1990; 58: 2337–42. https://doi.org/10.1128/iai.58.7.2337-2342.1990 PMID: 1694824
9. Onyilagha C, Uzonna JE. Host Immune Responses and Immune Evasion Strategies in African Trypanosomiasis. Front Immunol. 2019;10. https://doi.org/10.3389/fimmu.2019.00010 PMID: 30723470
10. Schroder K, Hertzog PJ, Ravasi T, Hume DA. Interferon-γ: an overview of signals, mechanisms and functions. J Leukoc Biol. 2004; 75: 163–189. https://doi.org/10.1189/jlb.0603252 PMID: 14525967
11. Parameswaran N, Patial S. Tumor necrosis factor-α signaling in macrophages. Crit Rev Eukaryot Gene Expr. 2010; 20: 87–103. https://doi.org/10.1615/critreveukargeneexpr.v20.i2.10 PMID: 21133840
12. Walker LSK, Gulbranson-Judge A, Flynn S, Brocker T, Raykundalia C, Goodall M, et al. Compromised OX40 function in CD28-deficient mice is linked with failure to develop CXC chemokine receptor 5-positive CD4 cells and germinal centers. J Exp Med. 1999; 190: 1115–1122. https://doi.org/10.1084/jem.190.8.1115 PMID: 10523609
13. De Trez C, Stijlemans B, Bockstal V, Cnops J, Korf H, Van Snick J, et al. A Critical Blimp-1-Dependent IL-10 Regulatory Pathway in T Cells Protects From a Lethal Pro-inflammatory Cytokine Storm During Acute Experimental Trypanosoma brucei Infection. Front Immunol. 2020; 11: 1–15. https://doi.org/10.3389/fimmu.2020.00001 PMID: 32038653
14. Namangala B, Noël W, De Baetselier P, Brys L, Beschin A. Relative Contribution of Interferon-g and Interleukin-10 to Resistance to Murine African Trypanosomosis. J Infect Dis. 2000. Available: https://academic.oup.com/jid/article/183/12/1794/2191258

15. Hovel-Miner G, Mugnier M, Papavasiliou FN, Pinger J, Schulz D. A host–pathogen interaction reduced to first principles: Antigenic variation in T. Brucei. Results Probl Cell Differ. 2015; 57: 23–46. https://doi.org/10.1007/978-3-319-20819-0_2 PMID: 26537376

16. MacGregor P, Savill NJ, Hall D, Matthews KR. Transmission stages dominate trypanosome within-host dynamics during chronic infections. Cell Host Microbe. 2011; 9: 310–318. https://doi.org/10.1016/j.chom.2011.03.013 PMID: 21501830

17. Ross R, Thomson D. A Case o f Sleeping Sickness studied by Precise Methods: Further Observations. Roy Soc Proc B. 1910; 83: 187–205.

18. Capewell P, Cren-Travaillé C, Marchesi F, Johnston P, Clucas C, Benson RA, et al. The skin is a significant but overlooked anatomical reservoir for vector-borne African trypanosomes. Elife. 2016; 5: 1–17. https://doi.org/10.7554/eLife.17716 PMID: 27653219

19. Claes F, Vodnala SK, Van Reet N, Boucher N, Lunden-Miguel H, Baltz T, et al. Bioluminescent imaging of Trypanosoma brucei shows preferential testis dissemination which may hamper drug efficacy in sleeping sickness. PLoS Negl Trop Dis. 2009; 3: 1–10. https://doi.org/10.1371/journal.pntd.0000486 PMID: 19621071

20. Carvalho T, Trindade S, Pimenta S, Santos AB, Rijo-Ferreira F, Figueiredo LM. Trypanosoma brucei triggers a marked immune response in male reproductive organs. PLoS Negl Trop Dis. 2018; 12: 1–15. https://doi.org/10.1371/journal.pntd.0006690 PMID: 30110342

21. Trindade S, Rijo-Ferreira F, Carvalho T, Pinto-Neves D, Guegan F, Aresta-Branco F, et al. Trypanosoma brucei Parasites Occupy and Functionally Adapt to the Adipose Tissue in Mice. Cell Host Microbe. 2016; 19: 837–848. https://doi.org/10.1016/j.chom.2016.05.002 PMID: 27237364

22. Pereira SS, Trindade S, De Niz M, Figueiredo LM. Tissue tropism in parasitic diseases. Open Biol. 2019;9. https://doi.org/10.1098/rsob.190036 PMID: 31088251

23. Rosen ED, Spiegelman BM. What we talk about when we talk about fat. Cell. 2014; 156: 20–44. https://doi.org/10.1016/j.cell.2013.12.012 PMID: 24439368

24. Grant RW, Dixit VD. Adipose tissue as an immunological organ. Obesity. 2015; 23: 512–518. https://doi.org/10.1002/oby.21003 PMID: 25612251

25. Ahima RS, Flier JS. Adipose tissue as an endocrine organ. Trends Endocrinol Metab. 2000; 11: 327–332. https://doi.org/10.1016/s1043-2760(00)00301-5 PMID: 10996528

26. Vielma SA, Klein RL, Levingston CA, Young MRI. Adipocytes as immune regulatory cells. Int Immunopharmacol. 2013; 16: 224–231. https://doi.org/10.1016/j.intimp.2013.04.002 PMID: 23587489

27. Teixeira L, Moreira J, Melo J, Bezerra F, Marques RM, Ferreirinha P, et al. Immune response in the adipose tissue of lean mice infected with the protozoan parasite Neospora caninum. Immunology. 2015; 145: 242–257. https://doi.org/10.1111/imm.12440 PMID: 25581844

28. Tanowitz HB, Scherer PE, Mota MM, Figueiredo LM. Adipose Tissue: A Safe Haven for Parasites? Trends in Parasitology. Elsevier Ltd; 2017. pp. 276–284. https://doi.org/10.1016/j.pt.2016.11.008 PMID: 28007406

29. Cabalén ME, Cabral MF, Sanmarco LM, Andrada MC, Onofrio LI, Ponce NE, et al. Chronic Trypanosoma cruzi infection potentiates adipose tissue macrophage polarization toward an anti-inflammatory M2 phenotype and contributes to diabetes progression in a diet-induced obesity model. Oncotarget. 2016; 7: 13400–13415. https://doi.org/10.18632/oncotarget.7630 PMID: 26921251

30. Hu W, Pasare C. Location, location, location: tissue-specific regulation of immune responses. J Leukoc Biol. 2013; 94: 409–421. https://doi.org/10.1189/jlb.0413207 PMID: 23825388

31. Salmon H, Remark R, Gnjatic S, Merad M. Host tissue determinants of tumour immunity. Nat Rev Cancer. 2019; 19: 215–227. https://doi.org/10.1038/s41568-019-0125-9 PMID: 30867580

32. Bourin P, Bunnell BA, Casteilla L, Dominici M, Katz AJ, March KL, et al. Stromal cells from the adipose tissue-derived stromal vascular fraction and culture expanded adipose tissue-derived stromal/stem cells: A joint statement of the International Federation for Adipose Therapeutics and Science (IFATS) and the International So. Cytotherapy. 2013; 15: 641–648. https://doi.org/10.1016/j.jcyt.2013.02.006 PMID: 23570660

33. Deutsch A, Feng D, Pessin JE, Shinoda K. The impact of single-cell genomics on adipose tissue research. Int J Mol Sci. 2020; 21: 1–13. https://doi.org/10.3390/ijms21134773 PMID: 32635651

34. Chen Z, Quan L, Huang A, Zhao Q, Yuan Y, Yuan X, et al. seq-ImmuCC: Cell-centric view of tissue transcriptome measuring cellular compositions of immune microenvironment from mouse RNA-seq data. Front Immunol. 2018;9. https://doi.org/10.3389/fimmu.2018.00009 PMID: 29403493

35. Stijlemans B, Cnops J, Naniima P, Vaast A, Bockstal V, De Baetselier P, et al. Development of a pHrodo-Based Assay for the Assessment of In Vitro and In Vivo Erythrophagocytosis during Experimental Trypanosomosis. PLoS Negl Trop Dis. 2015; 9: 1–21. https://doi.org/10.1371/journal.pntd.0003561 PMID: 25742307

36. Drennan MB, Stijlemans B, Van Den Abbeele J, Quesniaux VJ, Barkhuizen M, Brombacher F, et al. The Induction of a Type 1 Immune Response following a Trypanosoma brucei Infection Is MyD88 Dependent. J Immunol. 2005; 175: 2501–2509. https://doi.org/10.4049/jimmunol.175.4.2501 PMID: 16081822

37. Chan CC, Damen MSMA, Moreno-Fernandez ME, Stankiewicz TE, Cappelletti M, Alarcon PC, et al. Type I interferon sensing unlocks dormant adipocyte inflammatory potential. Nat Commun. 2020; 11: 1–15. https://doi.org/10.1038/s41467-019-13993-7 PMID: 31911652

38. Magez S, Schwegmann A, Atkinson R, Claes F, Drennan M, De Baetselier P, et al. The role of B-cells and IgM antibodies in parasitemia, anemia, and VSG switching in Trypanosoma brucei-infected mice. PLoS Pathog. 2008;4. https://doi.org/10.1371/journal.ppat.1000122 PMID: 18688274

39. Campbell GH, Phillips SM. Adoptive transfer of variant specific resistance to Trypanosoma rhodesiense with B lymphocytes and serum. Infect Immun. 1976; 14: 1144–1150. https://doi.org/10.1128/iai.14.5.1144-1150.1976 PMID: 1086289

40. Seed JR. The role of immunoglobulins in immunity to Trypanosoma brucei gambiense. Int J Parasitol. 1977; 7: 55–60. https://doi.org/10.1016/0020-7519(77)90025-x PMID: 858657

41. Pan AA, Rosenberg GB, Hurley MK, Schock GJH, Chu VP, Aiyappa A. Clinical evaluation of an EIA for the sensitive and specific detection of serum antibody to Trypanosoma cruzi (Chagas' disease). J Infect Dis. 1992; 165: 585–588. https://doi.org/10.1093/infdis/165.3.585 PMID: 1538165

42. Frenkel D, Zhang F, Guirnalda P, Haynes C, Bockstal V, Radwanska M, et al. Trypanosoma brucei Co-opts NK Cells to Kill Splenic B2 B Cells. PLoS Pathog. 2016; 12: 1–29. https://doi.org/10.1371/journal.ppat.1005733 PMID: 27403737

43. Jubel JM, Barbati ZR, Burger C, Wirtz DC, Schildberg FA. The Role of PD-1 in Acute and Chronic Infection. Front Immunol. 2020; 11: 1–15. https://doi.org/10.3389/fimmu.2020.00001 PMID: 32038653

44. Caljon G, Mabille D, Stijlemans B, De Trez C, Mazzone M, Tacchini-Cottier F, et al. Neutrophils enhance early Trypanosoma brucei infection onset. Sci Rep. 2018;8. https://doi.org/10.1038/s41598-017-18329-3 PMID: 29311689

45. Guilliams M, Movahedi K, Bosschaerts T, VandenDriessche T, Chuah MK, Hérin M, et al. IL-10 Dampens TNF/Inducible Nitric Oxide Synthase-Producing Dendritic Cell-Mediated Pathogenicity during Parasitic Infection. J Immunol. 2009; 182: 1107–1118. https://doi.org/10.4049/jimmunol.182.2.1107 PMID: 19124754

46. Laperchia C, Palomba M, Seke Etet PF, Rodgers J, Bradley B, Montague P, et al. Trypanosoma brucei Invasion and T-cell Infiltration of the Brain Parenchyma in Experimental Sleeping Sickness: Timing and Correlation with Functional Changes. PLoS Negl Trop Dis. 2016; 10: 1–19. https://doi.org/10.1371/journal.pntd.0005242 PMID: 28002454

47. Guilliams M, Bosschaerts T, Hérin M, Hünig T, Loi P, Flamand V, et al. Experimental expansion of the regulatory T cell population increases resistance to African trypanosomiasis. J Infect Dis. 2008; 198: 781–791. https://doi.org/10.1086/590439 PMID: 18627271

48. Deleeuw V, Phạm HTT, De Poorter I, Janssens I, De Trez C, Radwanska M, et al. Trypanosoma brucei brucei causes a rapid and persistent influx of neutrophils in the spleen of infected mice. Parasite Immunol. 2019; 41: 1–5. https://doi.org/10.1111/pim.12664 PMID: 31325372

49. Bunker JJ, Erickson SA, Flynn TM, Henry C, Koval JC, Meisel M, et al. Natural polyreactive IgA antibodies coat the intestinal microbiota. Science (80-). 2017;358. https://doi.org/10.1126/science.aan6619 PMID: 28971969

50. Ferrante A, Allison AC. Alternative pathway activation of complement by African trypanosomes lacking a glycoprotein coat. Parasite Immunol. 1983; 5: 491–498. https://doi.org/10.1111/j.1365-3024.1983.tb00763.x PMID: 6634218

51. Engstler M, Pfohl T, Herminghaus S, Boshart M, Wiegertjes G, Heddergott N, et al. Hydrodynamic Flow-Mediated Protein Sorting on the Cell Surface of Trypanosomes. Cell. 2007; 131: 505–515. https://doi.org/10.1016/j.cell.2007.08.046 PMID: 17981118

52. Cheung JLY, Wand N V., Ooi CP, Ridewood S, Wheeler RJ, Rudenko G. Blocking Synthesis of the Variant Surface Glycoprotein Coat in Trypanosoma brucei Leads to an Increase in Macrophage Phagocytosis Due to Reduced Clearance of Surface Coat Antibodies. PLoS Pathog. 2016; 12: 1–27. https://doi.org/10.1371/journal.ppat.1006023 PMID: 27893860

53. Stevens DR, Moulton JE. Ultrastructural and immunological aspects of the phagocytosis of Trypanosoma brucei by mouse peritoneal macrophages. Infect Immun. 1978; 19: 972–982. https://doi.org/10.1128/iai.19.3.972-982.1978 PMID: 640740

54. Ngaira JM, Nantulya VM, Musoke AJ, Hirumi K. Phagocytosis of antibody-sensitized Trypanosoma brucei in vitro by bovine peripheral blood monocytes. Immunology. 1983; 49: 393–400. PMID: 6852873

55. Kubagawa H, Oka S, Kubagawa Y, Torii I, Takayama E, Kang D-W, et al. The long elusive IgM Fc receptor, FcμR. J Clin Immunol. 2014; 34 Suppl 1: S35–45. https://doi.org/10.1007/s10875-014-0022-7 PMID: 24793544

56. Mugnier MR, Cross GAM, Papavasiliou FN. The in vivo dynamics of antigenic variation in Trypanosoma brucei. Science (80-). 2015; 347: 1470–1473. https://doi.org/10.1126/science.aaa4502 PMID: 25814582

57. Krüger T, Schuster S, Engstler M. Beyond Blood: African Trypanosomes on the Move. Trends Parasitol. 2018; 34: 1056–1067. https://doi.org/10.1016/j.pt.2018.08.002 PMID: 30181072

58. Bolger AM, Lohse M, Usadel B. Trimmomatic: A flexible trimmer for Illumina sequence data. Bioinformatics. 2014; 30: 2114–2120. https://doi.org/10.1093/bioinformatics/btu170 PMID: 24695404

59. Andrew S, Lindenbaum P, Howard B, Ewels P. FastQC: a quality control tool for high throughput sequence data. 2011. Available: https://www.bioinformatics.babraham.ac.uk/projects/fastqc/

60. Cox MP, Peterson DA, Biggs PJ. SolexaQA: At-a-glance quality assessment of Illumina second-generation sequencing data. BMC Bioinformatics. 2010; 11: 485. https://doi.org/10.1186/1471-2105-11-485 PMID: 20875133

61. Aslett M, Aurrecoechea C, Berriman M, Brestelli J, Brunk BP, Carrington M, et al. TriTrypDB: A functional genomic resource for the Trypanosomatidae. Nucleic Acids Res. 2009; 38: 457–462. https://doi.org/10.1093/nar/gkp851 PMID: 19843604

62. Kim D, Langmead B, Salzberg SL. HISAT: A fast spliced aligner with low memory requirements. Nat Methods. 2015; 12: 357–360. https://doi.org/10.1038/nmeth.3317 PMID: 25751142

63. Zerbino DR, Achuthan P, Akanni W, Amode MR, Barrell D, Bhai J, et al. Ensembl 2018. Nucleic Acids Res. 2018; 46: D754–D761. https://doi.org/10.1093/nar/gkx1098 PMID: 29155950

64. Liao Y, Smyth GK, Shi W. FeatureCounts: An efficient general purpose program for assigning sequence reads to genomic features. Bioinformatics. 2014; 30: 923–930. https://doi.org/10.1093/bioinformatics/btt656 PMID: 24227677

65. Love MI, Huber W, Anders S. Moderated estimation of fold change and dispersion for RNA-seq data with DESeq2. Genome Biol. 2014;15. https://doi.org/10.1186/s13059-014-0550-8 PMID: 25516281

66. Robinson MD, McCarthy DJ, Smyth GK. edgeR: A Bioconductor package for differential expression analysis of digital gene expression data. Bioinformatics. 2009; 26: 139–140. https://doi.org/10.1093/bioinformatics/btp616 PMID: 19910308

67. Ritchie ME, Phipson B, Wu D, Hu Y, Law CW, Shi W, et al. Limma powers differential expression analyses for RNA-sequencing and microarray studies. Nucleic Acids Res. 2015; 43: e47. https://doi.org/10.1093/nar/gkv007 PMID: 25605792

68. Huber W, Carey VJ, Gentleman R, Anders S, Carlson M, Carvalho BS, et al. Orchestrating high-throughput genomic analysis with Bioconductor. Nat Methods. 2015; 12: 115–121. https://doi.org/10.1038/nmeth.3252 PMID: 25633503

69. R Core Team. R: A language and environment for statistical computing. Vienna, Austria: R Foundation for Statistical Computing; 2018.

70. Alexa A, Rahnenfuhrer J. topGO: topGO: Enrichment analysis for Gene Ontology. R package version 2.30.1. 2018. https://doi.org/10.18129/B9.bioc.topGO

71. Gu Z, Eils R, Schlesner M. Complex heatmaps reveal patterns and correlations in multidimensional genomic data. Bioinformatics. 2016; 32: 2847–2849. https://doi.org/10.1093/bioinformatics/btw313 PMID: 27207943

72. Wickham H. ggplot2. Cham: Springer International Publishing; 2016. https://doi.org/10.1007/978-3-319-24277-4

73. Engstler M, Boshart M. Cold shock and regulation of surface protein trafficking convey sensitization to inducers of stage differentiation in Trypanosoma brucei. Genes Dev. 2004; 18: 2798–2811. https://doi.org/10.1101/gad.323404 PMID: 15545633

In summary, the findings of Harrison *et al*. nicely highlight the structural basis underlying the interaction of RIFINs with the prominent inhibitory immune receptor LILRB1. Importantly, this dampening function of RIFINs is ensured by a dedicated LILRB1-binding surface that commonly displays strong antigenic variation to avoid immune detection. This enlightening article provides additional evidence that the *P. falciparum* multigene families of adhesins have evolved to disrupt the activation of immune cells, thereby mimicking the structure of the natural ligand of LILRB1, that is, MHC class I molecules. This study points out once again how *P. falciparum* parasites have deployed a plethora of strategies to survive in the human host and sustain their life cycle in endemic areas.

[1]Unité Génétique du Paludisme et Résistance, Département de Parasites et Insectes Vecteurs, Institut Pasteur, Paris, France
[2]AP-HP, Hôpital Bichat, Laboratoire de Parasitologie-Mycologie, UMR261 Merit, Université de Paris, Paris, France
[3]Host–Pathogen Interaction Study Group (GEIHP, EA 3142), UNIV Angers, UNIV Brest, Angers, France
[4]Federative Structure of Research 'Cellular Interactions and Therapeutic Applications', SFR 4208 ICAT, Univ Angers, Angers, France

*Correspondence:
didier.menard@pasteur.fr (D. Ménard) and
sandrine.houze@aphp.fr (S. Houzé).

https://doi.org/10.1016/j.pt.2020.07.017

© 2020 Elsevier Ltd. All rights reserved.

References

1. WHO (2019) *World Malaria Report 2019*, World Health Organization
2. White, N.J. *et al.* (2014) Malaria. *Lancet* 383, 723–735
3. Glennon, E.K.K. *et al.* (2018) Opportunities for host-targeted therapies for malaria. *Trends Parasitol.* 34, 843–860
4. Feachem, R.G.A. *et al.* (2019) Malaria eradication within a generation: ambitious, achievable, and necessary. *Lancet* 394, 1056–1112
5. Scherf, A. *et al.* (2008) Antigenic variation in *Plasmodium falciparum*. *Annu. Rev. Microbiol.* 62, 445–470
6. Wahlgren, M. *et al.* (2017) Variant surface antigens of *Plasmodium falciparum* and their roles in severe malaria. *Nat. Rev. Microbiol.* 15, 479–491
7. Tan, J. *et al.* (2016) A LAIR1 insertion generates broadly reactive antibodies against malaria variant antigens. *Nature* 529, 105–109
8. Pieper, K. *et al.* (2017) Public antibodies to malaria antigens generated by two LAIR1 insertion modalities. *Nature* 548, 597–601
9. Saito, F. *et al.* (2017) Immune evasion of *Plasmodium falciparum* by RIFIN via inhibitory receptors. *Nature* 552, 101–105
10. Harrison, T.E. *et al.* (2020) Structural basis for RIFIN-mediated activation of LILRB1 in malaria. *Nature.* Published online July 10, 2020. https://doi.org/10.1038/s41586-020-2530-3

Spotlight

Polyreactive Antibodies Bridge Immunity Particles to Pathogen

Henrique Machado[1] and Luisa M. Figueiredo[1,*]

Humans are protected from most African trypanosomes via high-density lipoproteins, known as trypanosome lytic factor (TLF). In humans, IgM antibodies are found associated with TLF. The recent work by Verdi *et al*. studied the origin of these antibodies and their binding partners, suggesting a new model for TLF uptake.

For over a century we have known that human blood contains a trypanosome lytic factor (TLF) capable of lysing most animal-infecting African trypanosomes, the notable exceptions being the human-infective *Trypanosoma brucei rhodesiense* and *T. b. gambiense* parasites [1]. TLF is a high-density lipoprotein (HDL) containing apolipoprotein L-1 (APOL1), apolipoprotein A-I (APOAI), and the hemoglobin (HB)-binding haptoglobin-related protein (HPR) present in several primates, including humans [2]. The size of TLF, or TLF1, is roughly 500 kDa. A larger TLF particle of ≈1400 kDa is also found in human serum [3]. TLF2 has an IgM molecule associated with the TLF complex (i.e., TLF2 = TLF1 + IgM). In both TLF1 and TLF2 complexes, APOL1 is the lytic component [2,4]. APOL1 binds to the endosomal membranes of *T. brucei* at acidic pH, forming cation-selective channels. These are activated by pH neutralization during exposure to an extracellular milieu, which occurs upon endosome fusion to the plasma membrane during endosomal recycling. Activated APOL1-formed channels allow sodium influx, resulting in potassium efflux, chloride and water influx, and subsequent osmotic swelling and lysis [2].

TLF1 is endocytosed by the parasite when the HPR–HB complex binds to the parasite's [5] haptoglobin–hemoglobin receptor (HPHBR). HPR competes with circulating haptoglobin (HP) for hemoglobin and it has been shown that TLF1 endocytosis is inhibited by physiological levels of HP [6]. This hemoglobin dependence may mean that TLF1 has a limited lytic activity *in vivo* [6]. Notable exceptions may be situations in which circulating free hemoglobin is highly increased (e.g., hemolysis). By contrast, the endocytosis of TLF2 is partially independent from HPHBR through a thus far unidentified pathway [5]. The recently published work from Verdi and colleagues sheds light on how TLF2 finds its way into the parasite [3]. The authors show that host natural IgM antibodies can bind to the TLF particle and to the parasite surface, which could facilitate the binding of this innate immunity particle to the pathogen.

Natural antibodies are produced by the host without requiring prior exposure to foreign antigens and some are even present during prenatal development [7]. They are predominantly of the IgM isotype and have a germline structure, presenting no nontemplated nucleotides nor somatic hypermutation. A hallmark feature of these IgMs is their polyreactivity, being able to recognize a wide array of epitopes in self and foreign antigens [7]. These antibodies are of high biological significance, presenting functions such as immunity to infectious agents, clearance of apoptotic

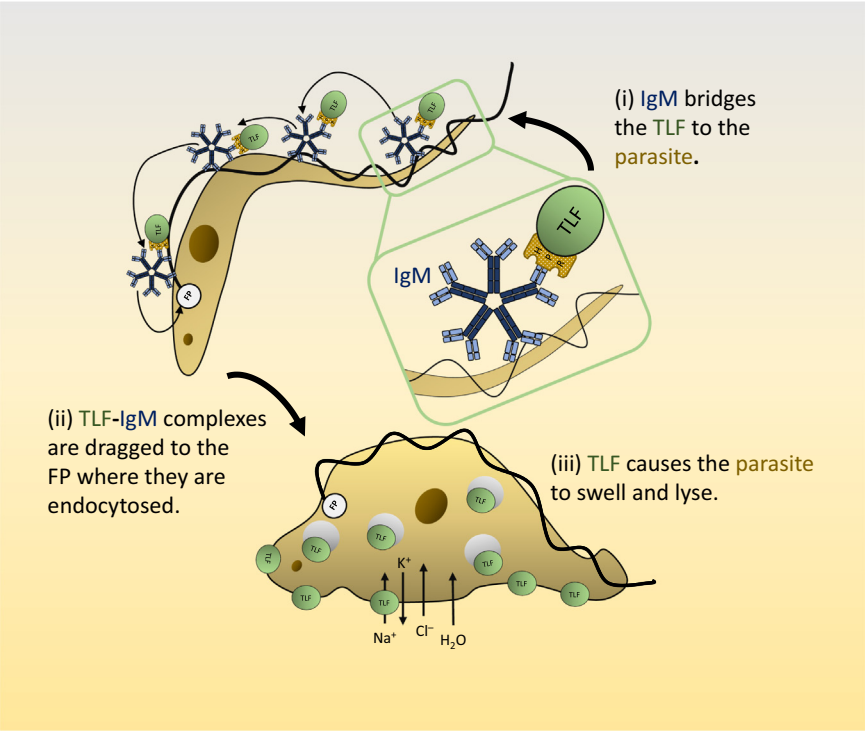

Figure 1. Model of TLF2 Delivery to African Trypanosomes. (i) The simultaneous binding of an autoreactive IgM to the parasite (i.e., VSG protein, not depicted) and to the HPR portion of TLF creates a stable interaction between the parasite and TLF. (ii) The large IgM–TLF complexes bound to the parasite's VSG are pushed towards the FP by a hydrodynamic drag force created by the parasite's forward swimming movement. Once in the flagellar pocket, the IgM–TLF–VSG complexes are endocytosed through a receptor-independent mechanism. (iii) TLF is disassembled into its components in the endosomal compartment, and the lytic component is inserted into endosomal membranes. Endosome recycling delivers the lytic component of TLF to the plasma membrane, allowing sodium influx and resulting in osmotic imbalance and lysis. The large and small brown circles represent the nucleus and mitochondrial DNA, respectively. The gray circles containing TLF represent endosomes. Abbreviations: FP, flagellar pocket; HPR, haptoglobin-related protein; TLF, trypanosome lytic factor; VSG, variant surface glycoprotein.

debris, and regulation of B cell development and responses [7].

In theory, owing to their pentameric structure, IgMs can bind up to ten epitopes simultaneously. Interestingly, Verdi and colleagues demonstrated that IgMs extracted from TLF2 complexes were able to bind to both the TLF2 particle and to the parasite. Within the TLF2 particle, IgM recognizes the HPR component (Figure 1), but not the APOL1. By contrast, IgM recognizes several proteins from total lysates of *T. brucei*. Importantly, these IgMs have been proven to be capable of binding – albeit with varying affinity – to at least three different variant surface glycoproteins (VSGs), the dominant surface protein of *T. brucei* that is responsible for its immune evasion. The simultaneous binding of an IgM to the HPR in the TLF2 particle and to the VSG in the parasite could lead to a rapid internalization of TLF2 by hijacking the molecular sail mechanism [8] (Figure 1). This mechanism allows *T. brucei* to direct antibody–VSG complexes towards the flagellar pocket due to the hydrodynamic drag force exerted on the antibody complex during the parasite's forward swimming movement [8] (Figure 1). Indeed, the proposed mechanism would direct the TLF–antibody–VSG complexes to the flagellar pocket, facilitating endocytosis of the TLF particle and subsequent lysis of the parasite by APOL1 (Figure 1). Altogether, this model proposes a fast and HPHBR-independent route of TLF2 internalization and suggests that the HPR-bound IgM may prevent HPHBR–HPR–HB interaction via steric obstruction. Although an enticing prospect, this model requires future validation. It would also be interesting to be able to visualize the TLF–antibody–VSG complex with methods such as cryogenic electron microscopy.

Healthy individuals present almost 20 times more TLF1 than TLF2; however, people infected with *T. b. rhodesiense* present a ratio of TLF1:TLF2 closer to one. This correlates well with the fact that total IgM levels are roughly 50 times higher in these patients than in healthy controls. Together with the fact that *T. b. rhodesiense* infection does not seem to change plasma APOL1 levels suggests that the TLF1:TLF2 ratio is determined by the amount of circulating IgM. It remains to be elucidated whether this is due to natural antibodies that arise via clonal expansion of many polyreactive IgM-producing B cells or whether there is an actual expansion and somatic hypermutation of B cells resulting in IgMs specific to *T. b. rhodesiense*. If the latter situation occurs, and IgMs with increased affinity for VSG are generated, would this affect their ability to recognize HPR? And would this change the time-course of the infection? It is conceivable that the stability of these TLF2 complexes may differ in stability to those formed with natural antibodies. In the future, it would be interesting to assess whether TLF2 complexes from naïve individuals differ in stability and lytic capacity from those of infection-cured individuals.

Acknowledgments

L.M.F. is an investigator of the Fundação para a Ciência e Tecnologia (IF/01050/2014) and the laboratory is funded by ERC (FatTryp, ref. 771714). H.M. is

funded by Fundação para a Ciência e Tecnologia (PD/BD/128286/2017).

[1]Instituto de Medicina Molecular, Faculdade de Medicina, Universidade de Lisboa, 1649-048 Lisboa, Portugal

*Correspondence:
lmf@medicina.ulisboa.pt (L.M. Figueiredo).

https://doi.org/10.1016/j.pt.2020.07.012

© 2020 Elsevier Ltd. All rights reserved.

References

1. Laveran, A. and Mesnil, F. (1912) *Trypanosomes et trypanosomiases* (10th edn), Libraires de l'Académie de Médecine, Paris
2. Thomson, R. and Finkelstein, A. (2015) Human trypanolytic factor APOL1 forms pH-gated cation-selective channels in planar lipid bilayers: Relevance to trypanosome lysis. *Proc. Natl. Acad. Sci. U. S. A.* 112, 2894–2899
3. Verdi, J. *et al.* (2020) Inducible germline IgMs bridge trypanosome lytic factor assembly and parasite recognition. *Cell Host Microbe* 28, 79–88.e4
4. Vanhamme, L. *et al.* (2003) Apolipoprotein L-I is the trypanosome lytic factor of human serum. *Nature* 422, 83–87
5. Vanhollebeke, B. *et al.* (2008) A haptoglobin-hemoglobin receptor conveys innate immunity to *Trypanosoma brucei* in humans. *Science* 320, 677–681
6. Raper, J. *et al.* (1996) The main lytic factor of *Trypanosoma brucei brucei* in normal human serum is not high density lipoprotein. *J. Exp. Med.* 183, 1023–1029
7. Holodick, N.E. *et al.* (2017) Defining natural antibodies. *Front. Immunol.* 8, 872
8. Engstler, M. *et al.* (2007) Hydrodynamic flow-mediated protein sorting on the cell surface of trypanosomes. *Cell* 131, 505–515